Technical Report

New Method for Dual-Axis Fatigue Testing of Large Wind Turbine Blades Using Resonance Excitation and Spectral Loading

Darris White

NREL

National Renewable Energy Laboratory
1617 Cole Boulevard, Golden, Colorado 80401-3393
303-275-3000 • www.nrel.gov

New Method for Dual-Axis Fatigue Testing of Large Wind Turbine Blades Using Resonance Excitation and Spectral Loading

Darris White

National Renewable Energy Laboratory

Available electronically at http://www.osti.gov/bridge

Available for a processing fee to U.S. Department of Energy
and its contractors, in paper, from:
       U.S. Department of Energy
       Office of Scientific and Technical Information
       P.O. Box 62
       Oak Ridge, TN 37831-0062
       phone: 865.576.8401
       fax: 865.576.5728
       email: mailto:reports@adonis.osti.gov

Available for sale to the public, in paper, from:
       U.S. Department of Commerce
       National Technical Information Service
       5285 Port Royal Road
       Springfield, VA 22161
       phone: 800.553.6847
       fax: 703.605.6900
       email: orders@ntis.fedworld.gov
       online ordering: http://www.ntis.gov/ordering.htm

Table of Contents

List of Figures

Chapter 1. Background and Introduction

This chapter provides background information on the research that was conducted throughout the course of this study. An introduction is given on the objectives of this research and its importance. Additionally, an overview of the study that was conducted and its presentation are provided.

1.1 Background

1.1.1 Historical Review of Wind Energy

The purpose of the research conducted for this project is the advancement of knowledge and capabilities in the area of wind turbine blade fatigue testing. It is not possible to properly discuss the contributions made by this research without first introducing the reader to wind turbine blade testing. Prior to discussion of the current wind systems, a historical review of the use of wind energy will be presented.

The Persians built the first (recorded) windmills around 900 A.D. [1-4]. These vertical axis windmills were not very efficient at capturing the wind's power and particularly susceptible to damage during high winds. During the Middle Ages, wind turbines began to appear in Europe [5-7]. These turbines resembled the 4-bladed horizontal axis windmill typically associated with Holland. The applications of windmills in Europe included water pumping, grinding grain, sawing wood and powering tools. Like modern wind turbines, the early European systems had a yaw degree of freedom that allowed the turbine to turn into the wind to capture the most power. The use of windmills in Europe reached their height in the 19th century just before the onset of the Industrial Revolution. At this time, windmill designs were beginning to include some of the same features found on modern wind turbines including yaw drive systems, air foil shaped blades and a power limiting control systems [8-10].

With the advent of the steam engine, the use of windmills as a power source began to decline. Wind turbines continued to evolve but without much application until after World War II. During the 1950's, Johannes Juul developed the Gedser turbine [11-13]. This 3-bladed upwind turbine was the predecessor of modern wind turbines including such features as aerodynamic stall regulation of power, an electromechanical yaw drive and asynchronous power generation.

Public and private interest in wind energy increased in the 1960's as environmental concerns about fossil fuels and pollutions began to emerge. Significant wind energy research was not conducted in the U.S. until the Oil Crisis of the mid-1970s. Under the Carter administration, the Department of Energy sponsored several wind energy research programs [14, 15] but in the early 1980's, these programs were cancelled due to changing political ideologies. Following the California Wind Rush (1980-1985) during which thousands of wind turbines were installed in California, there was a decline in U.S. involvement in the wind industry. Most activity related to the development of wind energy shifted toward Europe where subsidies in Denmark and Germany have resulted in significant increases in the installed wind energy capacity since the mid-1990s.

Wind turbines have continued to evolve over the past 20 years and the overall cost of energy required to produce electricity from wind is now competitive with traditional fossil fuel energy sources [16, 17]. This reduction in wind energy cost is the result of; improved aerodynamic designs, advanced materials, improved power electronics, advanced control strategies and rigorous component testing. This research will focus on improving current component testing methods. This project will help to reduce the cost required to produce energy from wind by improving upon current testing methods and introducing a test loading method to properly perform fatigue testing of wind turbine blades. Additionally, the research conducted for this project will make it feasible and more economical to test the next generation of wind turbine blades.

1.1.2 Historical Review of Blade Fatigue Testing

As shown by the previous section, modern wind energy technologies are still very new. Although the idea of using wind to produce power has existed for centuries, modern wind turbines have only existed for approximately 25 years. The next section will show that the evolution of wind turbines on going. Similarly, the methods used to test wind turbine blades are rapidly evolving. The purpose of this research project is to develop an advanced testing method, to gain a better understanding of the interaction between the flap and lead-lag forces and to evaluate the impact that this interaction can have on fatigue testing. Each topic is important and their contributions will be discussed below.

1.1.2.1 History of Fatigue Testing Methods

The blades of a wind turbine are generally considered to be the most critical component of the wind turbine system [18]. The fundamental purpose of performing fatigue tests on wind turbine blades is to demonstrate that a blade, when manufactured to a certain set of specifications, has the prescribed reliability and service life [19-22]. Historically, only a limited number of full-scale fatigue tests are conducted for any specific blade design and this evaluation is not intended to replace the detailed analysis required to manufacture reliable blades. Practical and economic considerations have traditionally prevented test conditions from representing load cases that were evaluated analytically. In most cases, a single equivalent load case is applied during testing. The equivalent load case is calculated from experimental or design load conditions and includes magnification factors to account for factors not accounted for during fatigue testing [23]. Worldwide there are only five facilities that perform full-scale structural blade testing. These facilities employ only two testing systems; a single-axis resonance excitation system and a dual-axis forced-displacement system [24-26].

Wind energy research began at the National Renewable Energy Laboratory (then called the Solar Energy Research Institute) in 1976. In 1990, NREL began structural testing wind turbine blades [24]. By 1994, a new test facility capable of testing 28-meter blades was operating at NREL. As shown in section 1.1.3, the typical size of wind turbine blades has grown past the current testing capabilities at NREL. For smaller wind turbine blades, the bending moment in the flap direction is the predominate fatigue factor [27, 28]. As blades have increased in size, the lead-lag bending moment, influenced primarily by blade weight, became a significant factor in damage

calculations. In response, NREL developed a dual-axis fatigue test system in 1999 [29]. This system, like the previous single-axis test system, uses constant amplitude displacements to apply the damage cycles. At the beginning of this research project, NREL's dual-axis fatigue test system represented the most advanced system in use for testing wind turbine blades. NREL's fatigue test system is very similar to systems used by several other testing facilities, such as Delft University [30, 31]. The current test systems will be described in more detail in section 1.3 and Chapter 5.

The first wind turbine blade testing facility was built in the early 1980's in Denmark [25, 32]. RISO National Laboratory built a blade test system that uses resonance excitation to apply damage cycles to the blade in a single direction. This same single-axis concept is still used by RISO to test larger modern blades despite the fact that the lead-lag and flap forces are similar in magnitude and international blade fatigue testing standards state that a dual-axis testing is more accurate [23].

Structural testing is not a discipline unique to the wind turbine industry. Automotive, infostructure and aerospace industries also perform structural testing [33-35]. Single-axis resonance tests have been used in the aerospace industry to test wings in the past [NACA (1938), 36] but both the automotive and aerospace industries began applying spectral loads for fatigue testing years ago [(1968), 37]. Current test methods in these fields are much more sophisticated. Typical aerospace structural fatigue tests are conducted by measuring loads during operating conditions and then applying the filtered load time history directly to the structure at multiple locations [38]. For automotive fatigue testing, the same procedure is used except that the loads can be applied to the vehicle via a test track designed with specific loads histories or by using hydraulic actuators [39-41]. The duration of the tests is reduced either by increasing the load magnitudes (based on a damage model), increasing the frequency of load application or both. These test methods are more representative of operating conditions than the method currently used to determine equivalent loads for wind turbine blade tests. Economic considerations have prevented the use of similar test methods for use with wind turbine blade testing.

1.1.2.2 History of Stochastic Wind Load Research

Wind applies deterministic and stochastic loads to many structures including buildings, bridges and, of course, wind turbines. For wind turbines, the deterministic component of the wind loads includes wind shear, and aerodynamic forces [18]. The stochastic component is created by turbulence [42]. Turbulence is accounted for in analysis by simulating a three-dimensional wind velocity vector using programs such as SWING4 (Stochastic WINd Generator [43]), SNLWIND-3D (1993 [44, 45]) or the updated version of SNLWIND-3D called SNWIND (2001 [46]). These programs are based on the von Karman neutral flow energy spectrum [47] in combination with Taylor's frozen turbulence hypothesis [48], as directed by the IEC standard [23]. Other energy spectra are being considered to represent the turbulent wind loading [49] but the above method represents the current industry standard approach for turbulence effects and has been used in this analysis.

Based on experimental evaluations of stochastic wind loading, loading spectra for wind turbines were created as early as 1987 [50]. The WISPER (WInd SPEctrum Reference) spectrum was

developed to simulate loading in the flap direction (normal to the plane of rotation) [50]. This spectrum was based on load measurements taken at nine different wind turbine locations around Europe. This spectrum included a large number of test cycles that caused little damage. As a result, this spectrum required long test durations in order to apply the appropriate damage that would be expected during operation. A new version of the spectrum, WISPERX, was created by removing 90% of the least damaging load cases from the WISPER spectrum [51]. This spectrum was later compared to data collected from U.S. wind sites and found to be compatible [52]. The WISPERX spectrum has been used for a number of purposes in the design and evaluation of wind turbine blades and related materials. One area were this loading has been used is in the prediction of design loads for the next generation of wind turbines blades [53-60]. For this analysis, Palmgren-Miner's rule is normally used to evaluate the spectrum's effect on damage. The WISPERX load spectrum has also been used is for the experimental evaluation of material coupons [61-63]. This experimental work has lead to a number of questions about using load spectra for full-scale testing. The results of the experimental coupon tests indicate that load sequencing is important but Miner's rule [64] is not capable of addressing this issue. Without an industry accepted damage accumulation model capable of accounting for sequence effects, full-scale testing with spectra loads has not been widely accepted. Another issue surrounding load spectra is that the test load magnitudes are generally increased to result in the desired amount of damage at a specific number of cycles (e.g. 3 million cycles). Amplifying the entire WISPERX spectrum so that the cumulative damage is equal to a targeted value may result in some loads that are greater than the static strength of the blade. Truncating the larger loads (and amplifying the loads to compensate) results in a narrow load spectrum. Typically, a constant amplitude load case is used with a magnification factor applied to account for the absence of a load spectrum [23]. The same procedure is used to account for aspects such as humidity, temperature and light exposure, which are not controlled during fatigue testing.

Given that wind loads contribute a stochastic input to wind turbine blade damage, this aspect cannot and is not ignored for the design [65-67]. Since Miner's rule is used to analyze the damage accumulation during the design phase, it is possible to evaluate the influences of spectra loading during the design phase without considering sequence effects.

With that said, it is important to recognize that all of the analysis conducted up to this point with respect to spectral loading has been conducted in the flap direction only. The purpose of this research project is to evaluate the effects of real time variations of the interaction between the flap and lead-lag forces as they relate to full-scale blade fatigue testing. This aspect of the problem has not been considered before and will be addressed by the research presented in this document.

1.1.2.3 History of Flap and Lead-Lag Load Coupling

Since wind turbine fatigue testing systems have only recently begun to include both axes (as discussed above), it is not surprising that the influence of the interaction between the flap and lead-lag forces on the damage accumulation is not well understood. In general, it is understood that the phase angle between the sinusoidal flap test loads and the sinusoidal lead-lag test loads is important, but prior to the research project presented in this dissertation, there had been no analysis conducted to determine the actual phase angle experienced during operating conditions.

Also, no detailed analysis had been computed on how varying the phase angle during testing would affect damage accumulation. In fact, there did not exist a definition with which to even evaluate the phase angle during operating conditions before this project. The phase angle between two sinusoidal functions (as with the test loads) is easily defined but, as will be shown in Chapter 3, the operating loads are not sinusoidal. As such, a definition for phase angle was created and will be present in Chapter 3. Prior to this research, the only previous work regarding the influence of load phase angle was an experimental study performed by Musial et al. (2001, [68]) where two fatigue tests were performed on the same blade using a 0-degree phase angle and then a 90-degree phase angle. The test conducted with a 0-degree phase angle resulted in failure an order of magnitude earlier than the test conducted with a 90-degree phase angle.

The phase angle between the flap and lead-lag forces is certainly important for testing but is not a term that would be relevant for the analysis of the design. For the analysis of a wind turbine blades design, the time histories of the forces in the flap and lead-lag directions are applied simultaneously to a finite element model of the blade [66]. So, the influence of the interaction between the flap and lead-lag forces on the accumulated damage is accounted for during the design process. The discrepancy in the current test method is that this interaction is not properly accounted for during the fatigue testing of wind turbine blades. Without the financial resources and overall industry maturity to be able implement the fatigue testing systems used by the aerospace and automotive industries, the wind turbine blade industry has simplified the loads to two constant amplitude forces with a constant phase angle between the loads throughout the entire endurance test. As this research will demonstrate, this is an oversimplification of the problem that results in non-conservative test results. As the wind energy industry continues evolve, it will become increasingly critical to test wind turbine blades accurately so that reduced cost of energy targets can be achieved.

1.1.3 Introduction to Modern Wind Energy

Over the past 20 years, wind turbines have evolved and are now cost competitive with traditional energy sources. By increasing the swept area of the turbine, improving manufacturing processes, and taking advantage of recent technological advances, the cost required to generate power from wind turbines has decreased from 40 cents per kilowatt-hour in 1979 to as low as 4 cents per kilowatt-hour in 2000 [69, 70].

This cost decline for wind power has been accompanied by a rise in environmental concerns surrounding conventional sources of energy. Together these two factors have spurred the demand for wind power. As shown in Figure 1-1, the cumulative wind power generation capacity in the world has grown steadily. Wind energy is the fastest-growing energy source with a worldwide annual growth rate of 29% over the past five years [71]. Wind energy constitutes a global market of $5 billion (U.S. Dollars) in annual sales. European countries such as Germany and Denmark have been responsible for a large portion of the increase.

5
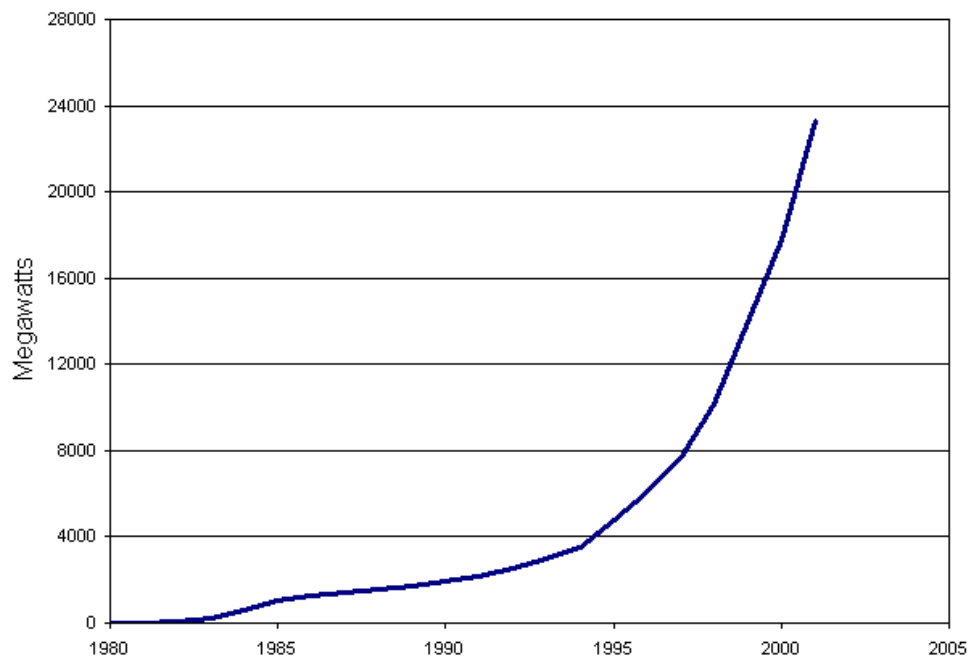
Sources: BTM Consult, AWEA, EWEA, Windpower Monthly

Figure 1-1. Worldwide wind energy generating capacity: 1981-2001

Advances in technology and materials have contributed to greater efficiency of wind turbines. Part of this efficiency has been achieved by increasing the size of modern wind turbines.

Figure 1-2. Typical wind turbine (NREL/PIX09990)

Like the 1.5-MW wind turbine shown in Figure 1-2, most turbines have a horizontally mounted hub with two or three blades. As the blades become longer to capture more power, the static and dynamic loads on the blades and other components increase. In general, a blade for a 1.5-MW turbine is 34 meters in length or greater and weighs as much as 6,000 kg (13,200 lbs).

As shown in Figure 1-3, current trends indicate that wind turbines will continue to increase in size. The primary motivation for ever-larger rotors is the push to develop offshore wind turbine generation. Offshore wind generation sites are especially of interest in Europe where land-based sites are more rare. Offshore turbines have fewer transportation and erection constraints with respect to land-based systems, and due to high offshore foundation costs, larger rotors are advantageous. As the market for offshore systems has developed, land-based systems have thus far followed suit. Designs for 5-MW turbines are currently being developed, and larger machines may follow. Longer blades will encounter greater loads, which will exceed the capacity of current testing facilities.
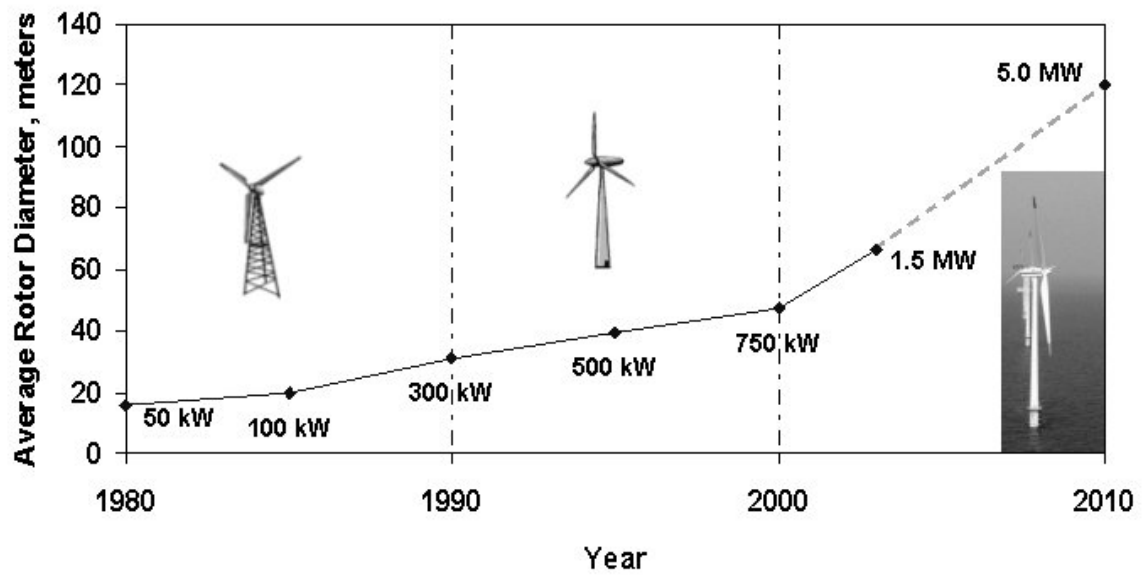
Figure 1-3. Wind turbine power and rotor diameter trends

1.2 Wind Turbine Blade Construction

Most wind turbine blades are fabricated using reinforced fiberglass composite materials with epoxy or vinyl ester matrices. Single or double shear webs are usually combined with planks of unidirectional laminates to form integral I-beam or box beam structures that carry the loads along the blade's span. Wide panels use foam or balsa sandwich construction to prevent buckling instabilities. The blade structure transmits aerodynamic and inertial forces along the span into a steel hub that connects to the rotating drive system. A composite airfoil shape generally transitions to a circular section near the blade root, which comprises some method for joining the blade and hub. The culmination of high bending loads, rapid geometry changes, thick laminates, varying materials, and wide panels make the root area particularly vulnerable to both fatigue and buckling failures. Full scale testing has become the prudent means of reducing the risk of undetected structural problems in production.

Until recently, hand lay-up fabrication was the dominant manufacturing method. Resin infusion, prepreg, and vacuum-assisted resin transfer molding (VARTM) processes are quickly displacing the wet lay-up methods. This trend is being driven by a maturation of the industry, which now recognizes the benefits of controlling construction tolerances, overall part consistency, and reduced emissions without large cost penalties in industrialized countries. Wind turbine standards organizations have also played a part by making the path to blade design certification easier when advanced manufacturing processes are used.

As blades grow longer, power production increases with the swept area of the rotor disc, or by the square of the blade length. For the same blade design, scaling studies predict that blade weight will grow by a power of 2.9. However, actual blade weight has grown historically at a power of 2.4 with respect to blade length [72]. The attenuation of this trend has been attributed directly to the application of more efficient designs and new technologies, such as improvements in manufacturing. Nevertheless, blades are becoming heavier. If the trend toward larger rotors and longer blades is to continue, further innovations in materials (e.g. carbon fiber), manufacturing, and load-relieving designs must be introduced to reduce weight. All these innovations will require blade test validation.

1.3 Blade Fatigue Testing

In an effort to improve the reliability of wind turbines, a variety of tests are conducted at research facilities around the world. Testing is conducted on material samples, components such as the gearboxes and blades, and the complete wind turbine system. Coupons tests are used to evaluate new and different composite materials that are used in the construction of wind turbine blades. This information is generally applied to finite element models to evaluate and modify the overall blade design. Structural testing of the complete wind turbine blade is used to validate the blade properties used in the FE model,

determine if manufacturing defects may exist in the blade, and potentially to certify the blade design.

As blades have become longer, heavier, and more expensive, the importance of fatigue testing has also increased. At the same time, test methods that were developed for smaller blades have become more expensive and less effective. Single-axis fatigue tests were developed for the testing of smaller blades by several research facilities. For small relatively light wind turbine blades, wind loads in the flap direction are much greater than gravity loads, which occur in the lead-lag direction. As a result, strain profiles for a single-axis fatigue test should approximate the actual design loads for smaller blades. By taking advantage of a blade's resonant response, it is possible to conduct single-axis fatigue tests more accurately, cheaper and faster. As a result, some research facilities developed a single-axis fatigue test using an electric motor spinning an eccentric mass. As blades have increased in length and weight, gravity loads have increased at a faster rate than wind loads [73]. Subsequently, the flap and lead-lag loads are now of the same scale and it is not prudent to disregard either of the loads. In order to accurately test the blades, at least one research facility has developed a dual-axis fatigue test capable of testing blades up to 37 meters long. The dual-axis test system uses hydraulic actuator to apply loads at a single blade span station in the flap and lead-lag directions. The displacements of the tip in the flap and lead-lag directions are constant amplitude sinusoids with a constant phase angle between them.

As a result of the research conducted in this thesis, a new method of testing wind turbine blades had been developed. The new method uses resonance excitation in the flap direction to reduce the cost and time required to perform a full-life fatigue test. By using hydraulic actuators instead of an eccentric mass to excite the blade in the flap direction, the new system will be able to regulate the blade flap displacement independently of the excitation frequency. This allows the new test method to combine resonance excitation and dual-axis fatigue testing for the first time. After an in-depth analysis of blade loads, a progressive time history of the phase angle between the flap and lead-lag displacements has been developed that will provide more realistic testing conditions than the current constant phase angle.

1.4 Scope

The primary goals of this research are to:
1. Determine appropriate wind turbine size to be used in this analysis,
2. Obtain simulated wind turbine blade bending moment time histories in the flap and lead-lag directions,
3. Create a definition for the relationship between the two blade loads,
4. Evaluate the phase relationship between the flap and lead-lag bending moments for the target wind turbine blade size for various wind speeds and determine an aggregate phase angle distribution representative of general operating conditions,
5. Use a finite element model of the target blade to evaluate the influence of the phase relationship between the bending moments on the nodal strains,

6. Use Miner's Rule to determine the possible impact on fatigue lifetime predictions of switching from the constant phase angle fatigue tests currently used by the wind turbine industry to a variable phase angle fatigue test representative of the phase angle distribution determined by this research project,
7. Determine an appropriate phenomenological fatigue damage model for composite blade material and determine the appropriate model parameters using the Department of Energy material database,
8. Evaluate the influence of phase sequencing on the accumulation of fatigue damage,
9. Optimize the phase time history with respect to total damage accumulation using a conjugate method optimization routine,
10. Propose a phase time history for use with variable phase angle fatigue testing,
11. Analyze current blade fatigue testing methods and their performance,
12. Determine blade properties (EI, damping ratio, etc.) for target wind turbine blade and build a beam finite element model of the blade in the test configuration,
13. Analyze a new fatigue testing method that has been developed as part of this research project and compare its performance to current testing systems,
14. Perform an optimization of the new test system with respect to test bending moment distributions,
15. Create a dynamic model of the blade and test system,
16. Design and evaluate the performance of a PID controller for constant phase angle fatigue tests and for variable phase angle fatigue tests,
17. Design and evaluate the performance of a full-state feedback controller for constant phase angle fatigue tests and for variable phase angle fatigue tests,
18. Analyze, design and build the new test system and related hardware,
19. Evaluate the new test systems performance on an actual blade,
20. Establish the limitation of this analysis and make recommendations for future analysis and testing improvements.

1.5 Thesis Organization

This thesis consists of eight chapters.
- Chapter 1 covers the introduction, background and research objectives.

- Chapter 2 evaluates the challenges associated with the wind industry, evaluates the data ultimately used in this analysis and explains how the data was created. The wind industry is still in its developmental stages and modern horizontal axis turbines are changing to meet industry demands. The formative nature of the industry is illustrated by the fact that until 1996 research was still being conducted on vertical axis wind turbines called Darrieus turbines. It is within this continually evolving environment that this project has been conducted. With these considerations, a snapshot of the current loading conditions on wind turbine blades has been presented and evaluated. This analysis shows that the simulated

data used for this research project is representative of data for turbines of similar scale.

- Since Chapter 2 shows that the data sets used in this analysis is a valid representation of blade loads, the data sets were used to evaluate the relationship between the flap and lead-lag forces. Chapter 3 presents the analysis and results of the relationship and its potential influence on full-scale fatigue testing. Since a similar analysis has never been conducted before this research project, a term to define the relationship between the loads has been created. As such, the term "phase angle" was used for this research and was defined to mean the change in rotor angle between the occurrence of the maximum flap bending moment and the maximum lead-lag bending moment. From this research, it has been determined that the phase angle has an approximately Gaussian distribution for each wind speed. When the results are complied into a single aggregate distribution, the mean and standard deviation of the phase angles are 72 degrees and 54 degrees. Since current full-scale blade fatigue tests are conducted using a single-phase angle, it was expected that a variable phase angle test based on the newly determined phase angle distribution would produce significantly different damage accumulation results. This expectation was confirmed by analyzing the two test configurations using a three-dimensional finite element model of a 1.5 Mega-Watt wind turbine blade. The results indicate that the single-phase angle fatigue test is non-conservative compared to the variable phase angle fatigue test and the single-phase angle test has a lower probability of detecting material defects.

- Throughout Chapter 3, the influence of variable phase angle testing was compared to that of single-phase angle testing with the application of Palmgren-Miner's rule. Chapter 4 further analyzes the influence of variable phase angle testing but with respect to sequence effects. In order to perform this analysis, a nonlinear damage accumulation model was derived that is capable of demonstrating the influence of phase angle sequencing. The nonlinear model was tuned by fitting the model parameters based on the material database maintained for the Department of Energy (DOE). The results of this analysis indicate that lumping similar phase angles together will produce less damage than spreading out the phase angles throughout the complete fatigue test. It should be noted that this results is dependent on the exponent used for the nonlinear model. For glass-fiber composites, the model exponent has been experimentally determined to be less than 1.0. If another material is used and the model exponent for the new material is greater than 1.0, the most damaging case will occur when similar phase angles are lumped together.

- Chapter 5 describes current fatigue testing systems used to test wind turbine blades and a new test system developed as part of this project. This chapter details the reasons why a new system is needed as well as the design and benefits of the new system. Using a beam finite element model of a target blade and an optimization routine written for this project, the new test system has been demonstrated to perform as well or better than any existing test system. Based on

this analysis the new test system will reduce the energy required to perform a full-scale fatigue test of a wind turbine blade by more than 60% (i.e., the energy savings per test is sufficient to power over 100 households for one year).

- Chapter 6 describes the dynamic model used to simulate the new test system, as well as the design and analysis of the controller. A beam finite element model was used to calculate the first two eigenvalues of the system. The nonlinear interaction between the flap and lead-lag actuators was modeled and included in the dynamic analysis. A PID controller was simulated for the single-phase angle and variable phase angle test conditions and shown to be stable for the single-phase angle test condition only. A full-state feedback controller was designed for the variable phase angle test condition and was shown to be stable once the eigenvalues were properly placed using pole placement.

- The analysis in Chapter 6 shows that a dual-axis test system using resonance excitation is possible while the analysis in Chapter 5 shows that the envisioned system is more accurate and practical than any existing system. These hypotheses were experimentally validated by building and testing the new system. As shown in Chapter 7, the new test system can replicate the strain measurements of the current forced-displacement test system while using a fraction of the energy consumption. Also shown is that the response of the system using a PID controller is stable during normal operation.

- In Chapter 8, the summary, conclusions and recommendations for future research are presented.

Chapter 2. Wind Turbine Overview and Wind Turbine Blade Loads

This chapter provides information on basic wind turbine terminology, applicable loads, and some of research programs currently being conducted. Data simulated as part of the WindPACT program will be used to analyze blade deflections. A basic analysis of loads and factors effecting wind turbines have been conducted to demonstrate that the data set used for analysis in this research is representative of operating conditions.

2.1 Introduction

Power stored as kinetic energy in wind is the result of solar heating of the earth. The sun heats the earth's surface unevenly resulting in air flowing from high-pressure zones to low-pressure zones. Using wind turbines, it is possible to convert the kinetic energy into electricity. As shown by Equation 2.1, the amount of wind power stored in a circular cross-section of air with perpendicular wind speed depends on the wind speed, air density and cross-section area [74].

$$P = \frac{1}{2}\rho v^3 \pi r^2 \tag{2.1}$$

Where,

P = power
ρ = air density
v = wind speed
r = rotor radius

From the above equation, it can be seen that the power available varies cubically with wind speed but linearly with area. In order to collect the most power from a given wind turbine, the turbine should be placed in a location where high winds frequently occur. However, the locations where high winds typically occur are not necessarily the same location where most electricity is consumed. As shown in Figure 2-1, high wind speeds (shown in dark) occur infrequently. Locations with class 5 or higher wind conditions occur on approximately 1% of the contiguous U.S.

UNITED STATES ANNUAL AVERAGE WIND POWER
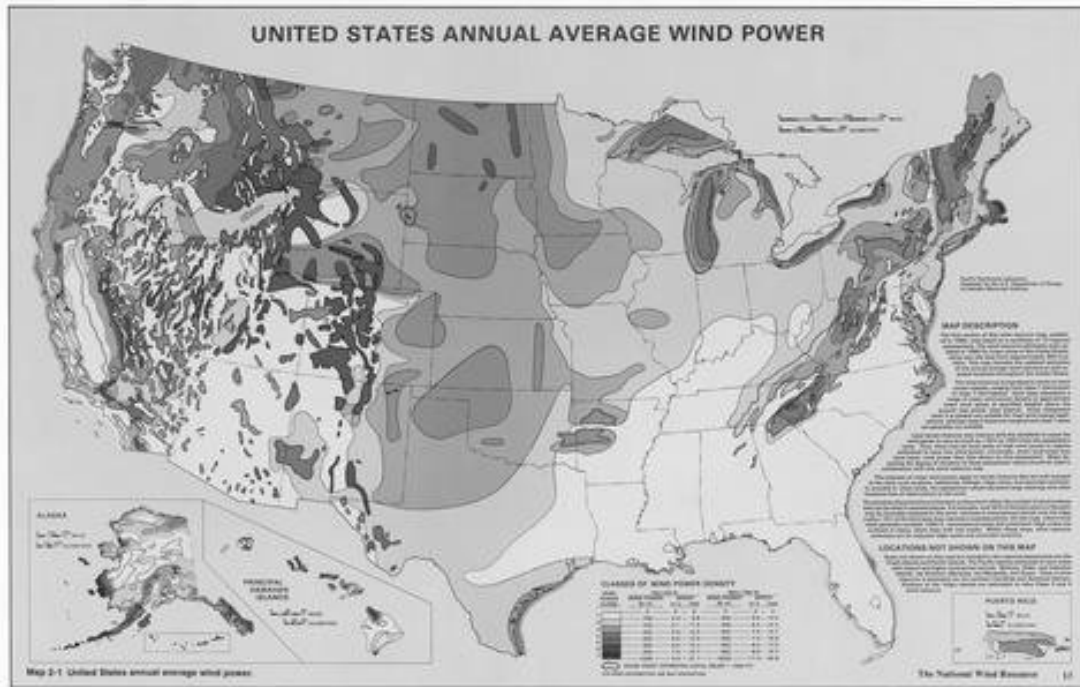
Figure 2-1. Average wind power distribution [75]

Production of electricity represents only part of the problems facing the wind industry. Once electricity has been produced, it must be transmitted from the place of origin to the place of consumption. As shown by Equation 2.2, the transmission loss of power increases linearly with the transmission distance.

$$P_{loss} = I^2 \frac{\rho l}{A}$$ (2.2)

Where,

P_{loss} = power lost to heat
I = electrical current
ρ = resistivity of power line
A = cross-sectional area of power line

As shown in Figure 2-2, the locations of consistently high wind speeds (shown above) are generally not located near locations of peak energy consumption (large population centers). As a result, wind turbines placed at locations of high wind speeds will require long transmission distances and subsequently higher transmission losses than wind turbines placed near large population centers.

Figure 2-2. Contiguous U.S. population distribution (750,000 people per dot) [76]

While modern wind turbines can produce electricity for approximately 4¢ per kWh at class 6 wind sites (6.7 meter/second average wind speed), the average distance from class 6 wind sites to major population centers is approximately 500 miles. Although class 4 wind sites (5.8 meter/second average wind speed) cannot produce as much power per wind turbine as class 6 sites, they are much more common and have an average distance to major population centers of 100 miles. The desire to make lower wind speed regions more economically advantageous is one reason that wind turbines have continued to increase in size. As shown in Equation 2.1 above, the swept area of the wind turbine must increase in order to capture the same amount of power for a slower wind speed.

As shown in Figure 2-3, improvements in technology and design have reduced the cost of wind energy substantially during the past 10 years. Further research and testing of wind turbines and their components will make wind energy even more competitive.
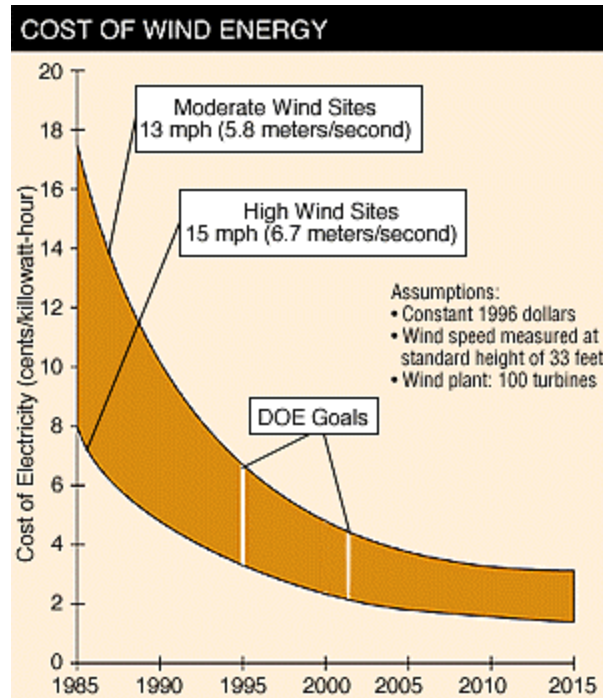
Figure 2-3. Wind energy cost trends [77]

2.1.1 Wind Turbine Designs

Wind turbine designs are typically broken down into two major categories; horizontal axis and vertical axis. Vertical axis turbines are not commonly used to produce power but they do exist and have some advantages for specific uses. There are two types of vertical axis turbines; drag-based and lift-based. Drag-based vertical axis turbines consist of radially mounted shapes that have higher drag coefficients in one direction than the other. Drag-based turbines are limited in application because the tip speed of the turbine cannot exceed the wind speed. As shown in Figure 2-4, a cup anemometer, commonly used to measure wind speed, is a good example of a drag-based vertical axis turbine.

Figure 2-4. Cup anemometer

Lift-based vertically axis turbines have been studied and commercially built for power generation. As shown in Figure 2-5, the Darrieus turbine has radially positioned airfoils that use lift to generate tip speeds greater than the wind speed. The generator for this system is located at ground level which reduces maintenance costs. This system is prone to vibration problem resulting from the resonance frequency for the airfoil structures being at or below the operating frequency. Also, the torque at start up is very low and the turbine may require an initial boost to start operation.

Figure 2-5. Darrieus vertical axis wind turbine [78]

As shown in Figure 2-6, lift generated by the airfoils has a tangent component resulting in a turning moment. Using lift allows the turbine to operate with tip speed greater than 3 times the wind speed. The shapes of the airfoils on the Darrieus turbine are designed to minimize bending moments during operation. While this turbine design has some advantages, it has not been generally accepted by the wind industry and it does not appear that this turbine will be widely used in the future.
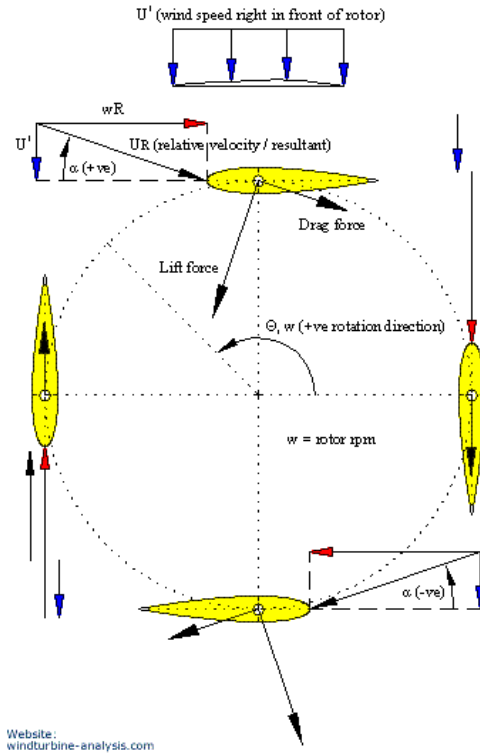
Figure 2-6. Darrieus turbine lift and drag forces

All utility scale wind turbine currently being installed are horizontal axis machines. This style of turbine also comes in two varieties; upwind and downwind turbines. Downwind turbines are cheaper than upwind turbines for several reasons. Upwind turbines require yaw drives to position the propeller into the wind. Also, upwind turbines must have stiffer blades to prevent them from hitting the turbine's tower during high winds. Figure 2-7 shows a schematic of a downwind turbine. Downwind turbines typically have a yaw bearing that allows the nacelle to rotate like a weathervane into the best position for power production. This is called "free yaw." Pitching the blades controls the rotational speed of the rotor and the operating efficiency.
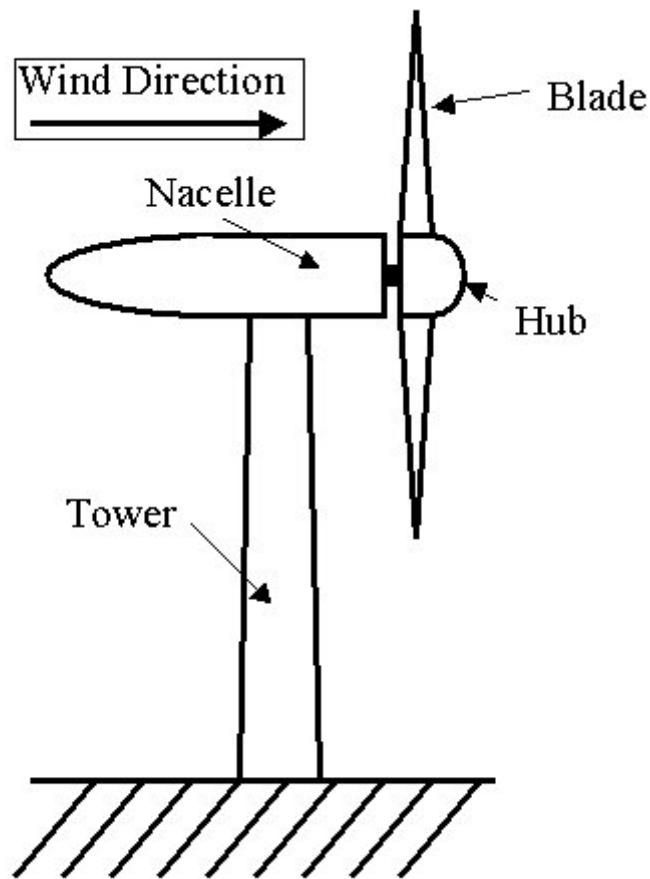
Figure 2-7. Horizontal axis downwind wind turbine

Upwind horizontal axis turbines operate in a similar manner as the downwind variety except that they require additional hardware and design constraints. As shown in Figure 2-8, upwind turbines are controlled using a yaw drive system located between the tower and nacelle. Upwind turbines have the advantage of capturing the wind energy before it passes through the tower. Wake turbulence generated by the tower reduces the amount of power that can be captured by downwind turbines and increases the dynamic load on downwind turbine blades. Low frequency noise generated by the blades passing through the tower wake has stigmatized this concept.
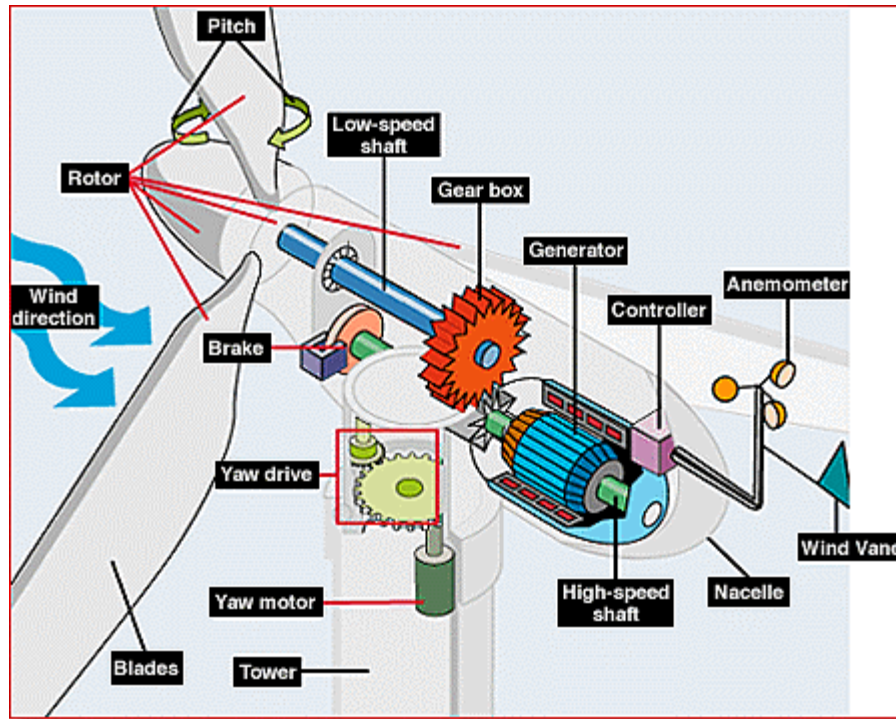
Figure 2-8. Horizontal axis upwind turbine [79]

Horizontal axis turbines generally are produced with two or three blades. Two-bladed systems have periodic variations in some dynamic properties such as the yaw moment of inertia and require larger rotor diameters or higher rotor speeds to generate the same power as three-bladed systems. Two-bladed systems are also less expensive and lighter than three-bladed system. Since the installation cost of wind turbines is a primary deterrent for even greater wind power installations in the U.S., two-bladed systems are currently being carefully considered. Three-bladed systems have been used with good success in Europe and the U.S. and represent most of the current commercial technology.

2.2 WindPACT Program

Some of the data used for the research project described in this thesis was generated as part of the WindPACT (Wind Partnerships for Advanced Component Technology) program. WindPACT is a DOE (Department of Energy) sponsored research program with the objective of reducing the COE (cost of energy) of wind energy by conducting research on wind turbine components [80]. This research is primarily intended to help reduce the COE for class 4 wind sites to 3¢/kWh by 2007. The stated goals for the WindPACT program are to reduce the cost of wind energy through technological advancements, determine the probable scale of future utility-scale wind turbines in the U.S., evaluated advanced concepts that are needed to meet WindPACT objectives, identify and resolve obstacles that might block industry from embracing promising technology, design, fabricate and test selected advanced components, and to support the U.S. wind industry by transferring technology from DOE labs.

21

As discussed in Chapter 1, wind turbines continue to grow in size. As such, the WindPACT project has studied the impact of larger turbine sizes on wind turbine components including wind turbine blades. As part of this analysis, a 1.5 MW wind turbine blade was modeled using FAST (an aeroelastic analysis code for horizontal-axis wind turbines) and a finite model was created using ANSYS. Since 1.5 MW blades are the maximum size that can be tested at the NREL facility, these models were used for part of the research described in this thesis.

2.3 FAST Turbine Model

FAST (Fatigue, Aerodynamics, Structures and Turbulence) is a computer code used to simulate the dynamic loads on two- and three-bladed horizontal-axis wind turbines [81]. The code was developed as part of a contract between NREL and Oregon State. The wind turbine is modeled as a combination of rigid and flexible bodies. The earth, nacelle and hub are modeled as rigid bodies, while the blades, tower and drive shaft are modeled as flexible bodies. The blades are modeled using two flapwise bending modes and one edgewise bending mode. The model has several degrees of freedom including tower bending, blade bending, nacelle yaw, nacelle pitch, rotor teeter, rotor speed and drive shaft torsion. FAST uses the AeroDyn computer code developed by Windward Engineering to simulate aerodynamic forces along the blade. Accuracy of the FAST model was verified by comparing the simulated results from FAST with the simulated results of ADAMS. The results of this verification were published at the 2001 AIAA/ASME Wind Energy Symposium [82].

For the research presented in this thesis, the results of FAST simulations for a 1.5 MW wind turbine were used. The simulations were conducted as part of the WindPACT program described above. For this analysis, FAST calculated the dynamic displacement of the 1.5 MW wind turbine blades under specific wind speeds and turbulence intensity factors. These displacements were used for the phase angle analysis described later in this chapter.

2.4 Wind and Gravity Loads

2.4.1 Terminology

Wind turbine blades are primarily subjected to two types of loads; aerodynamic loads such as shear, drag, lift, etc., and inertial loads such as gravity, blade dynamics, etc. These forces generally occur in orthogonal bending directions; flap and lead-lag. Flap forces are forces out of the hub plane of rotation. Lead-lag forces are those in the rotor plane of rotation. For a given blade pitch and blade station, the flap and lead-lag directions are shown in Figure 2-9. The relative angle between the airfoil chord and plane of rotation vary radially along the blade length. Since the blade travels in a circle, the tangential speed of the blade varies radially along the blade and the twist angle varies to control the relative angle of attack.
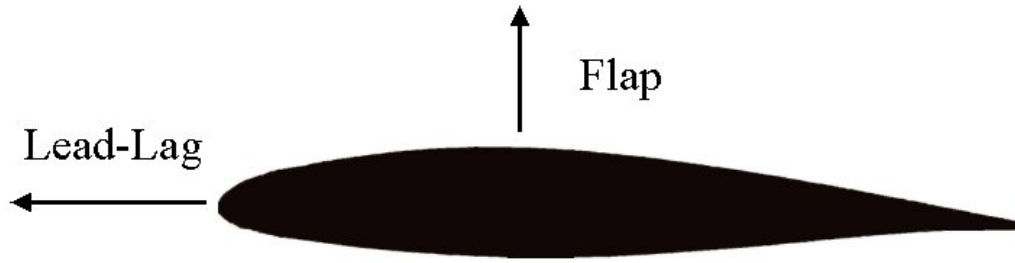
Figure 2-9. Blade bending moment directions

2.4.2 Wind Loads

Blade bending moments induced by wind loads typically occur in the flap direction. As shown in Figure 2-10, flap forces have stochastic and deterministic components [83].
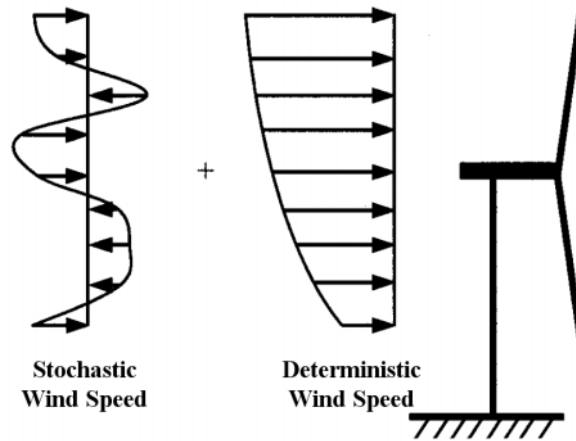
Figure 2-10. Flap forces

The stochastic component comes from the variability of the wind, as well as turbulence from nearby objects. The stochastic nature of wind is significant and may not be ignored even though this component of the force is considered to have a zero mean. The deterministic component is time invariant, and increases monotonically with height in accordance to boundary layer characterization. Equation 2.3 shows a typical boundary layer formula used to calculate the deterministic wind speed as a function of height [84,85]. This equation provides a representation of how wind speed changes with height.

$$v = v_{ref} \frac{\ln(z/z_0)}{\ln(z_{ref}/z_0)}$$

(2.3)

where,

$$v = \text{wind speed at height } z$$
$$v_{ref} = \text{reference wind speed at height } z_{ref}$$
$$z_0 = \text{boundary layer model tuning parameter}$$

As a result of the deterministic loads, the average location for the maximum bending moment should occur when a blade is directly above the hub. Since the deflection of the blade is of primary interest for this analysis, it is important to note that the maximum deflection does not necessarily coincide with the maximum force because of inertial response time.

2.4.3 Gravity Loads

For smaller blades, gravity loads were not considered a major source of fatigue. As blades have gotten larger and heavier, the effects of gravity can no longer be ignored. Blades for one-megawatt or greater wind turbines weigh more than 4500 kg (10,000 lbs). As shown in Figure 2-11, gravity forces and generator torques result in lead-lag loads. Additional lead-lag bending moments may be induced by generator torque. Blade loads in this direction have a larger deterministic component. Because of the airfoil shape, wind turbine blades are typically very stiff in the lead-lag direction and higher bending moments in the outboard sections are tolerable in this direction compared to flap bending moments.

Figure 2-11. Lead-lag forces

2.5 Blade Deflections

Blade deflections were calculated for a 1.5 mega-watt wind turbine model using the FAST computer simulation. The blade model used for this simulation was created for the WindPACT program and does not represent a specific manufacturers blade. A variety of

24

wind speeds and turbulence intensity factors were considered in this analysis. For each wind speed, the maximum turbulence intensity factor based on IEC (International Electrotechnical Commission) standards was calculated and used for the simulations [84].

The IEC orders external wind conditions into several WTGS (Wind Turbine Generator Set) classes. The classes are defined in terms of wind speed and turbulence parameters. The values for wind speeds and turbulence parameters are meant to represent many different sites and do not represent a specific location. For the analysis described later in this chapter, a class 1A wind class was selected. This class represents winds with the highest speeds and strongest turbulence of the eight standard classes. The turbulence intensity factor for each wind speed used was calculated using the IEC standard formula shown by Equation 2.4. For WTGS class IA, the parameters a and I_{15} are 2 and 0.18, respectively.

$$TI = I_{15}(15 + aV_{hub})/[V_{hub}(a+1)] \qquad (2.4)$$

Where,

TI = Turbulence Intensity factor

I_{15} = IEC Standard Turbulence Parameter

a = IEC Standard Turbulence Parameter

V_{hub} = Wind Speed at Rotor Height

For class IA wind sites, the turbulence intensity factor is shown in Figure 2-12. The parameters used for the FAST simulations used these turbulence intensity factors rounded to the nearest 0.02.

Turbulence Intensity Factor for IEC Standard Classs IA Wind Sites
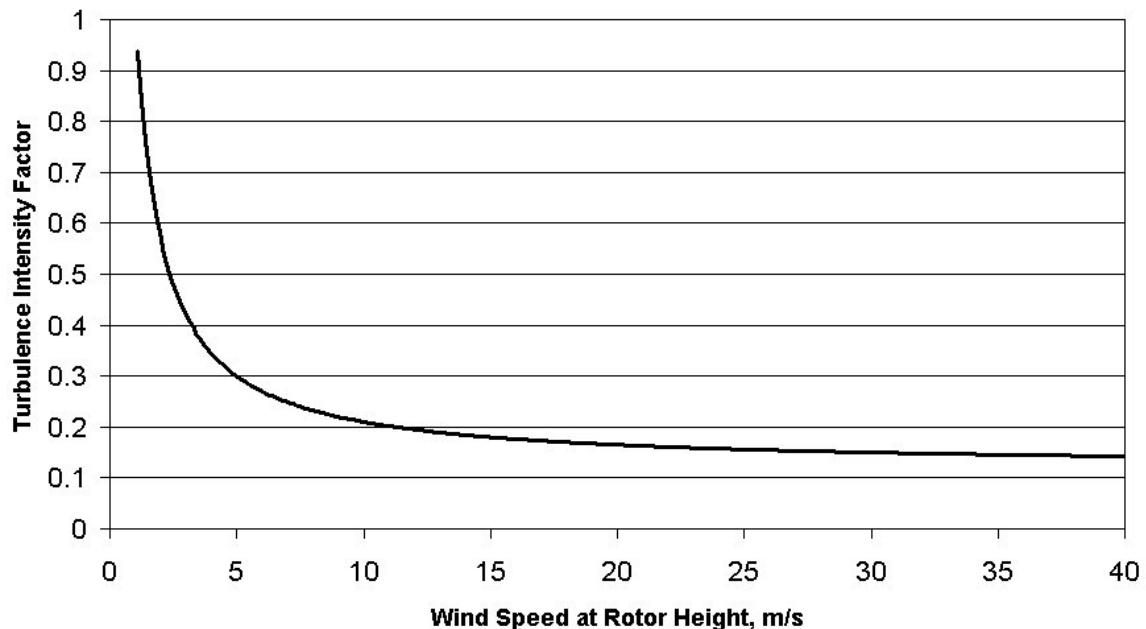
Figure 2-12. Turbulence Intensity Factor for WTGS Class IA

2.5.1 Bending Moment Time Series Analysis

Blade bending deflections in the flap and lead-lag direction were simulated using FAST for various wind speeds at the specified turbulence intensity factors. For this analysis a variable speed wind turbine model has been used. Since FAST is a dynamic simulation, the bending deflections were calculated as a function of time simultaneously with many other parameters including the azimuth angle. The azimuth angle is defined as the angle of rotation around the hub axis with zero azimuth defined as the line directly above the hub. Since wind speed is not a constant input parameter into the model, the rotor azimuth position is not a linear function with time. In order to compare the blade bending moments impartially, the azimuth angle is used as the reference variable.

As shown in Figures 2-13 and 2-14, bending moment in the flap direction are dependent on wind speed. The bending moments for these plots were simulated using FAST to reproduce strain gauge measurements. As a result, the actual bending moments may differ from the simulated bending moments. A sample size of three rotor revolutions has been shown in the following plots out of the 1800 revolutions available.

**Flap Blade Response to Bending Moment for 1.5 Mega-Watt
WindPACT Turbine and 9 m/s Average Wind Speed**
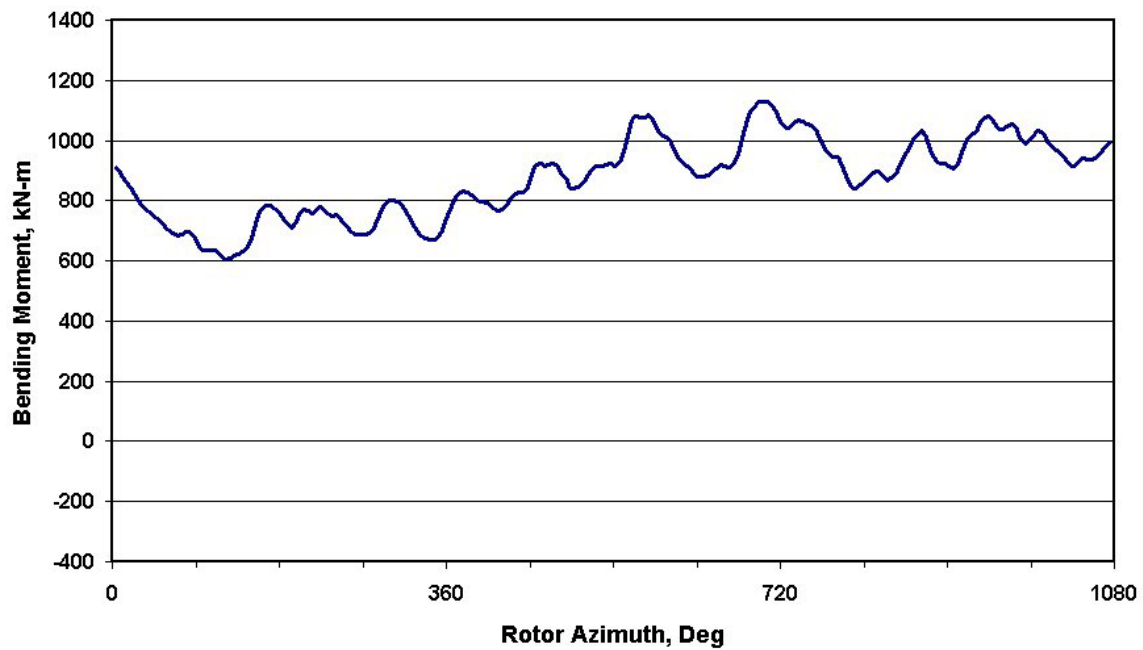
Figure 2-13. Flap bending moment at 9 m/s

The mean flap bending moment is lower for an average wind speed of 20 meters per second than for an average wind speed of 9 meters per second because the wind turbine model uses pitch control to regulate power.

Flap Blade Response to Bending Moment for 1.5 Mega-Watt WindPACT Turbine and 20 m/s Average Wind Speed
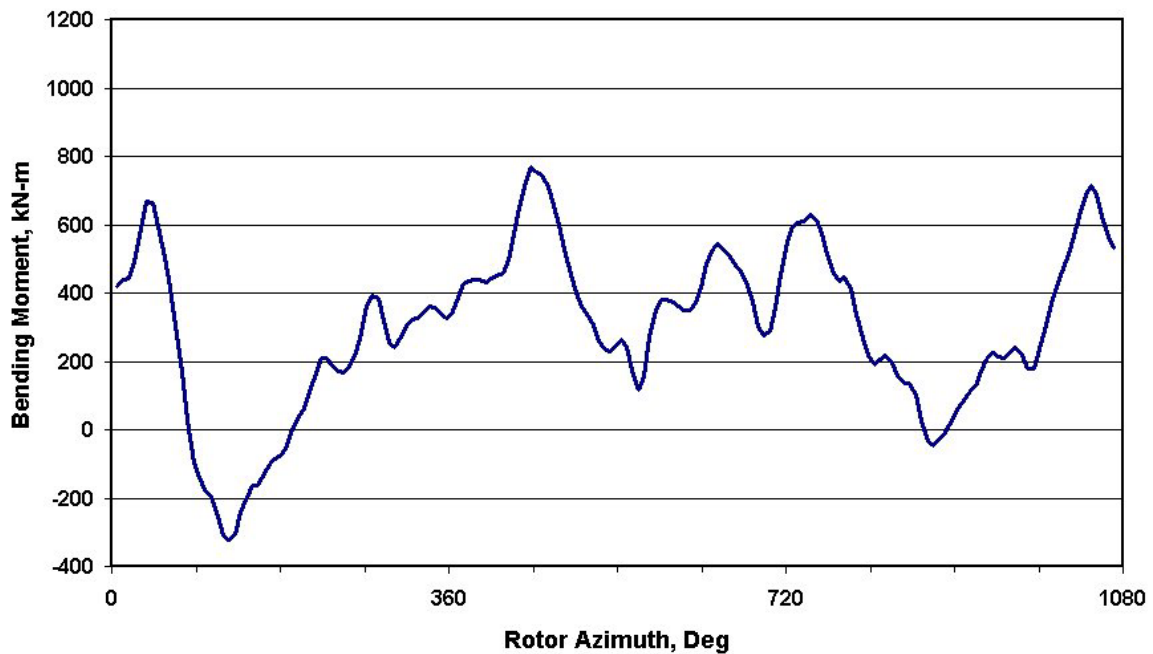
Figure 2-14. Flap bending moment at 20 m/s

Wind turbines operate at a variety of wind conditions. As shown in Figure 2-15, these conditions are generally classified in three operating conditions. In region 1, the wind speeds are too low to compensate for internal friction and power loss during operation. In region 2, the wind turbine attempts to capture as much power as possible. In order to reduce fatigue on the wind turbine and its components, the blades are pitch during region 3 to discard some of the power available in the wind. As a result, mean flap loads are actually lower in the flap direction in region 3 than in region 2. The standard deviation goes up with wind speed.
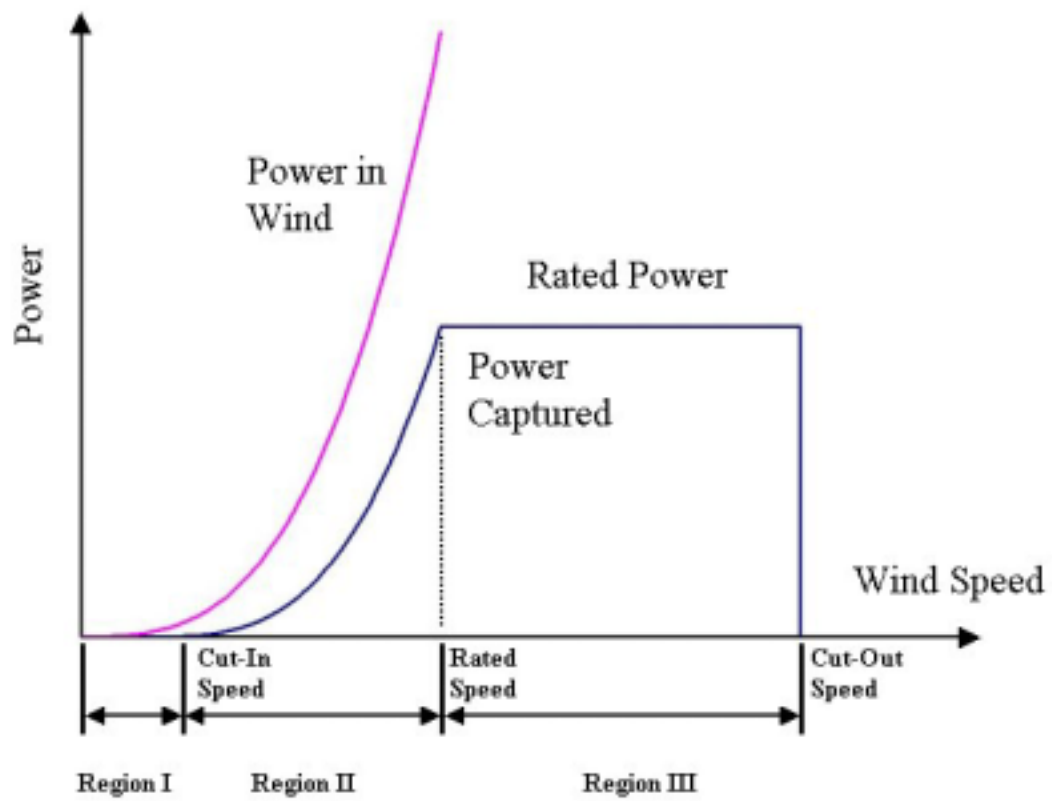
Figure 2-15. Regions of turbine operation

As shown in Figure 2-16, the WindPACT simulation supports this analysis. The mean bending moment in the flap direction continues to decrease as the blades are pitched to higher degrees.

Mean Flap Bending Moment as a Function of Wind Speed
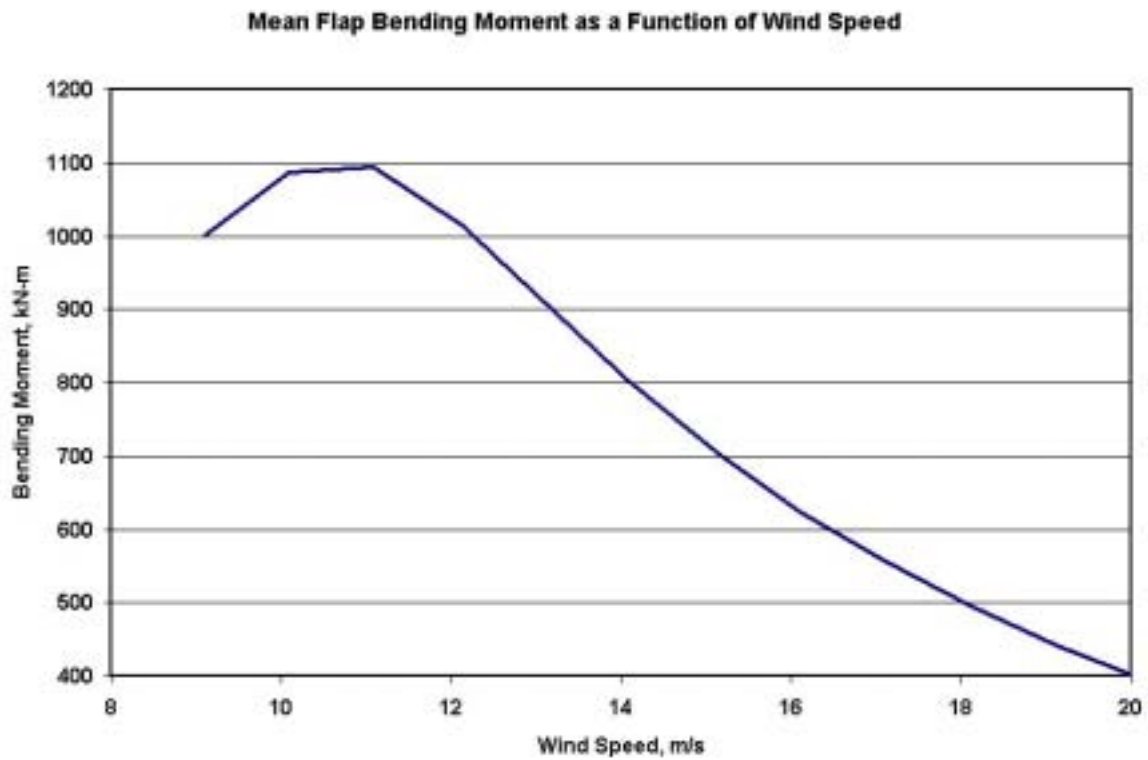
Figure 2-16. Mean flap bending moment for WindPACT pitch controlled turbine

As shown in Figure 2-17, the lead-lag bending moment exhibits more deterministic behavior than the flap bending moments. The frequency of the bending moment is equal to the rotor speed (i.e., 1P).

Lead-Lag Blade Response to Bending Moment for 1.5 Mega-Watt WindPACT Turbine and 9 m/s Average Wind Speed
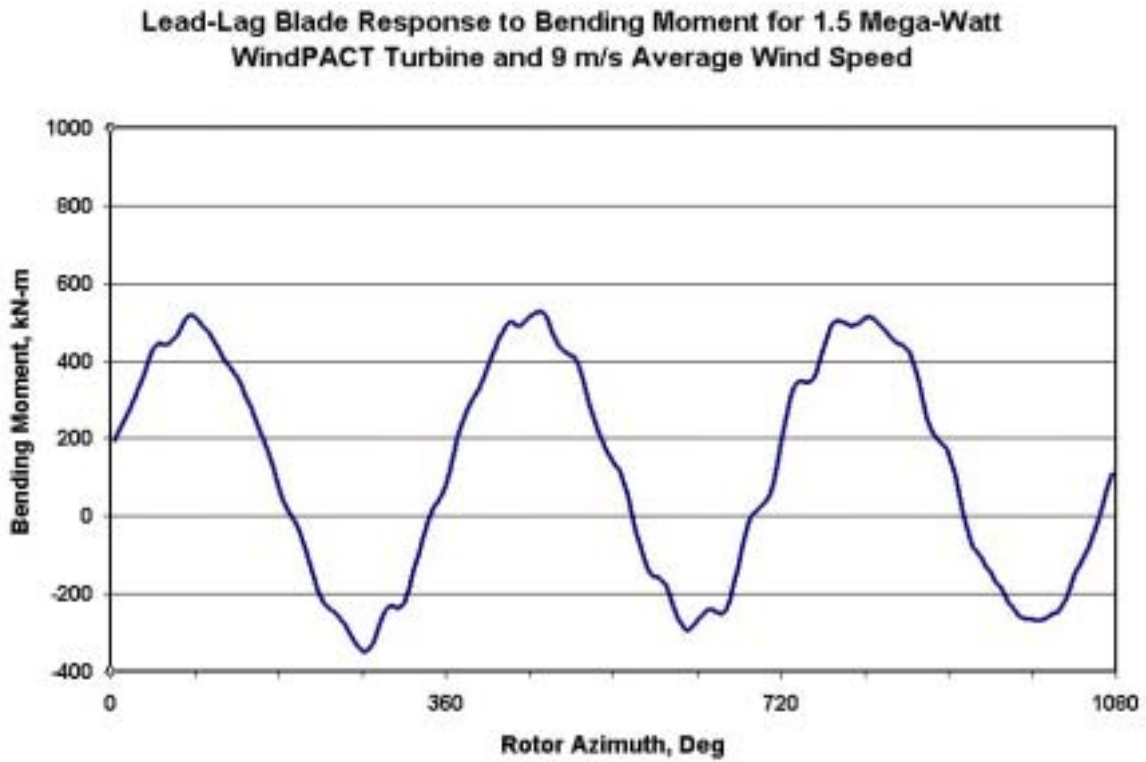
Figure 2-17. Lead-lag bending moment at 9 m/s wind speed

As shown in Figure 2-18, the mean lead-lag bending moment is higher at 20 meters-per-second than 9 meters-per-second. The mean lead-lag moment is closely associated with the power being captured. As a result, the mean lead-lag bending moment in region 2 will be lower than the mean moment in region 3.
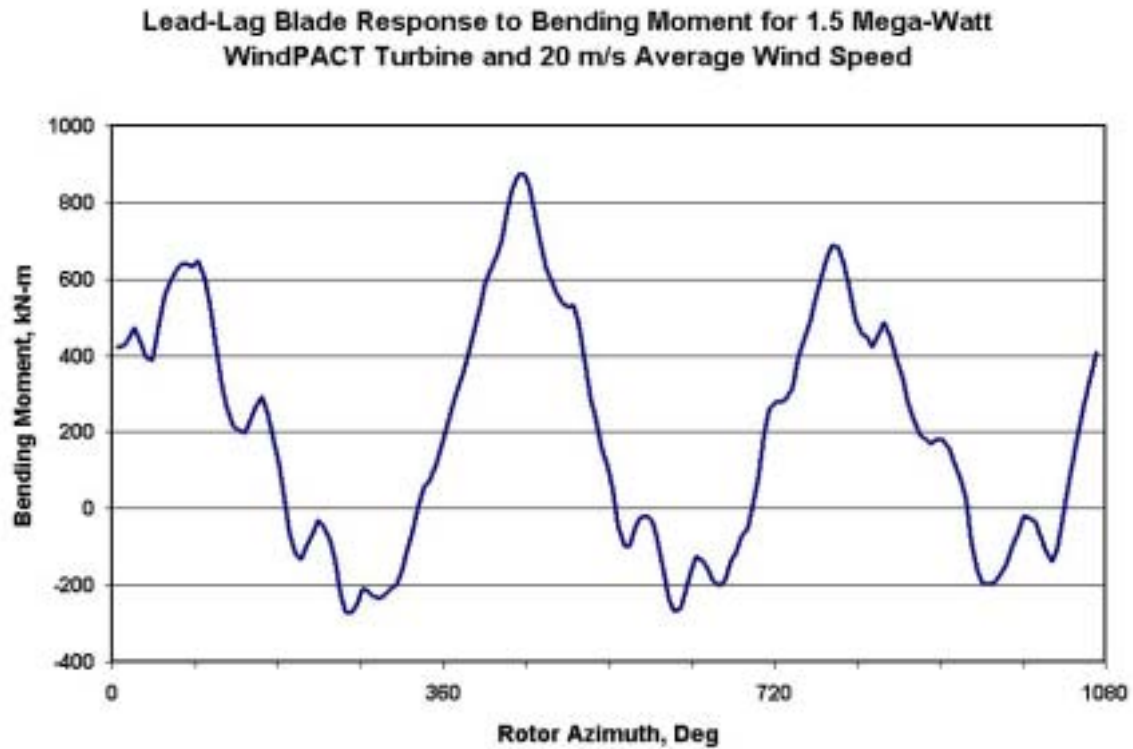
Figure 2-18. Lead-lag bending moment for 20 m/s

As shown in Figure 2-19, the mean lead-lag bending moment actually goes down slightly for higher wind speed within region 3. Ideally, the mean bending moment in region 3 would remain constant for all wind speeds. However, it is clear that lead-lag bending moment for region 2 wind speeds are lower than for region 3 wind speeds.

Mean Lead Lag Bending Moment as a Function of Wind Speed
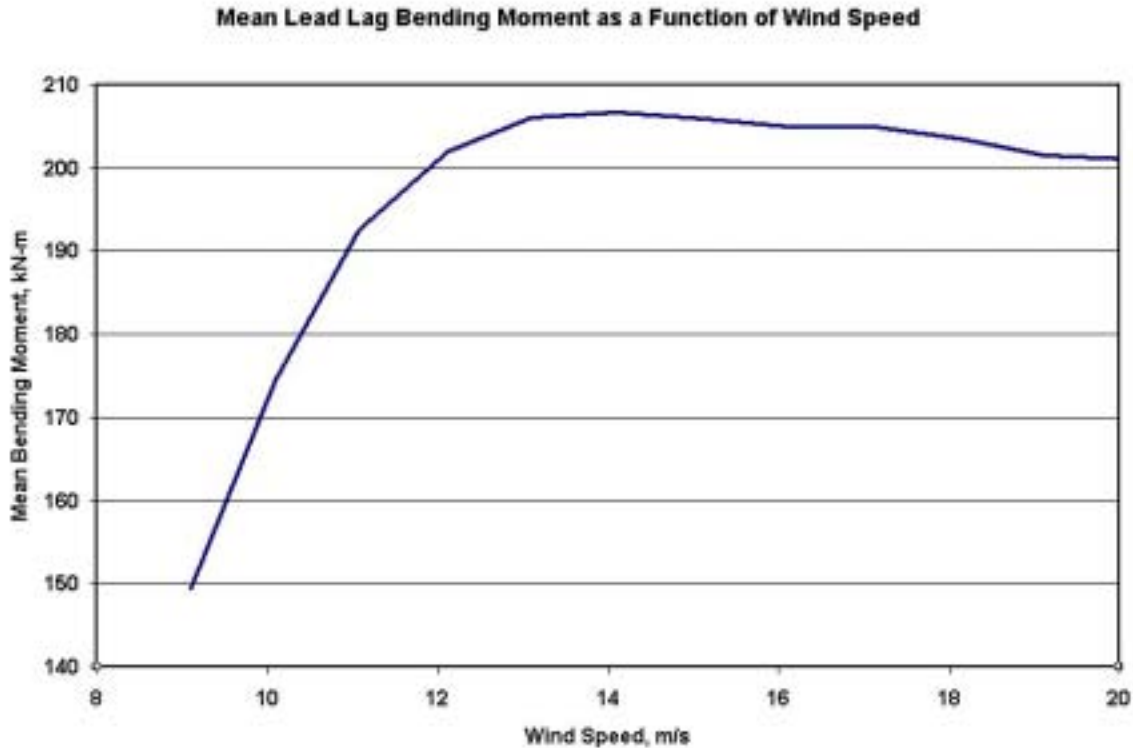
Figure 2-19. Mean lead-lag bending moment for pitch controlled wind turbine

As part of this analysis, the bending moment distributions have been analyzed in a several number of ways. The data above indicates typical behavior of the system during a range of operating conditions. This data is further evaluated in the frequency domain and using rainflow counting.

2.5.2 Bending Moment Frequency Domain Analysis

From the lead-lag time series data, it is clear that harmonic forces are present in the system. A frequency analysis of the flap and lead-lag forces has been conducted to determine which frequencies are important and how they vary with wind speed. The data was originally created with a sampling frequency of 20 Hz; however, the input forces are generally dependent on the blade position rather than time. Since the target wind turbine operates with a variable rotor speed, the change in azimuth angle is not linear with respect to time. Due to changes in wind speed and turbulence, the angular velocity of the rotor changes to capture the most power without overstressing the turbine's components. As shown in Figure 2-20, the rotor angular velocity varies with time. The data shown represents approximately 72 complete rotor revolutions.

33

1.5 MW WindPACT Rotor Velocity for 9 m/s Average Wind Speed at IEC Class IA Standard Turbulence Intensity
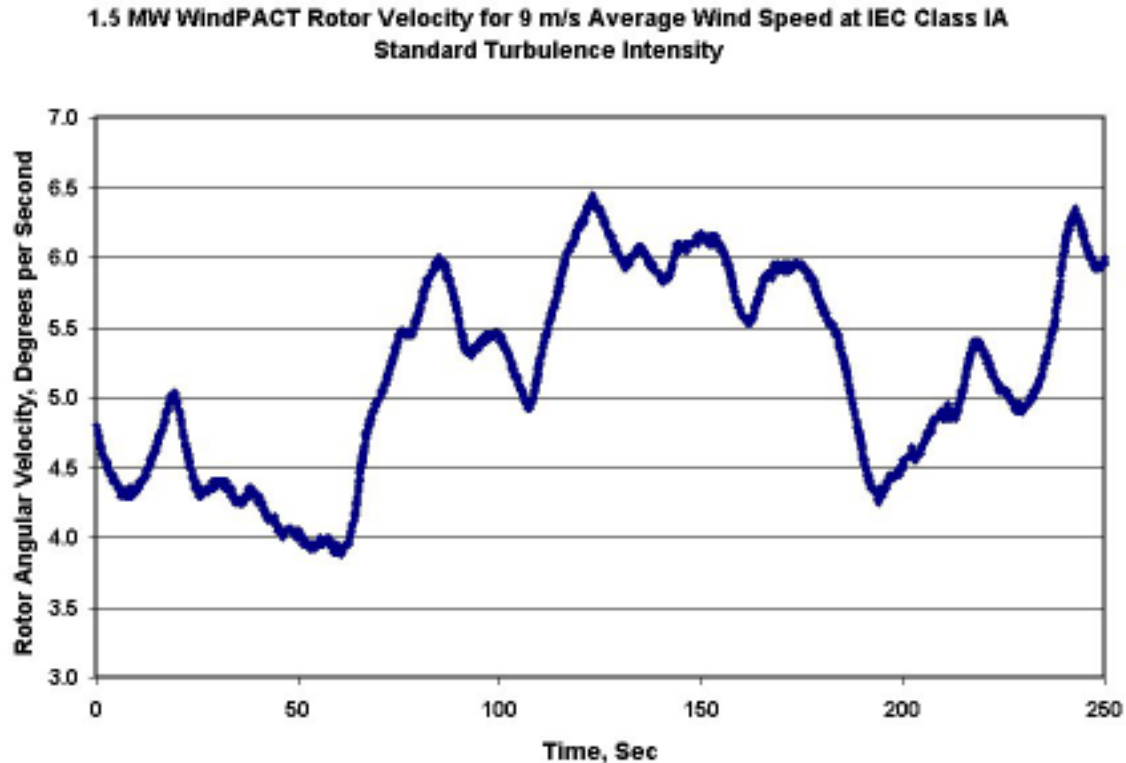
Figure 2-20: Sample rotor velocity data for an average wind speed of 9 m/s

Performing a frequency analysis on the time-sampled data results in useful information. The forces acting on the turbine blades are dependent more on the position of the blade than with time but since time and rotor position are roughly coupled, it is possible to perform a frequency analysis on the data and scale the frequency axis based on the average rotor speed. This will disperse the some of the peaks on the spectral density plot since a variable speed turbine has been modeled. As shown in Figure 2-21, scaling the frequency axis by the average rotor speed shows a peak at 1 cycle per revolution only. For each power spectrum described below, a Hanning window and block averaging were applied using 1024-sample blocks and the overall mean for each data set was set to zero.
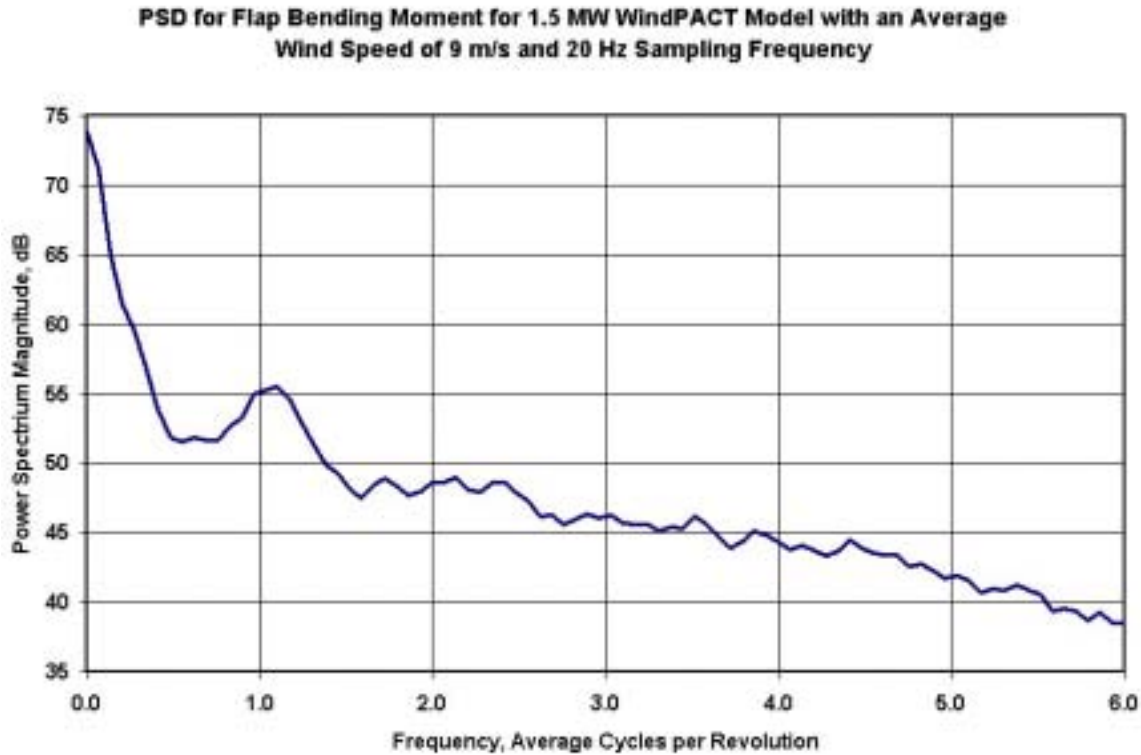
Figure 2-21. PSD of time-sampled flap bending moment for 9 m/s wind speed

Since the bending moment variations are largely determined more by spatial relationships than time, it was decided to resample the flap and lead-lag bending moment data with respect to rotor azimuth angle. The original time-sampled data was sampled at a frequency of 20 Hertz. For an average wind speed of 9 m/s, this sampling rate results in an average spatial frequency of 70.5 samples per revolution. The spatially uniform data was created by re-sampling the original data at a rate of 100 samples per revolution. The new dataset was generated using linear interpolation. As shown in Figure 2-22, the spatially sampled data demonstrates distinct peaks at various rotor speed harmonics. While the overall spectral density has not changed from the time-sampled data to the spatially sampled data, re-sampling the data has reduced the scatter of the frequency content. While a distinct and significant peak occurs at 1 cycle per revolution, this peak does not dominate the spectra. This behavior can probably be attributed to the stochastic nature of the wind forces.

PSD for Flap Bending Moment for 1.5 MW WindPACT Model with an Average
Wind Speed of 9 m/s and 100 Samples per Revolution Sampling Frequency
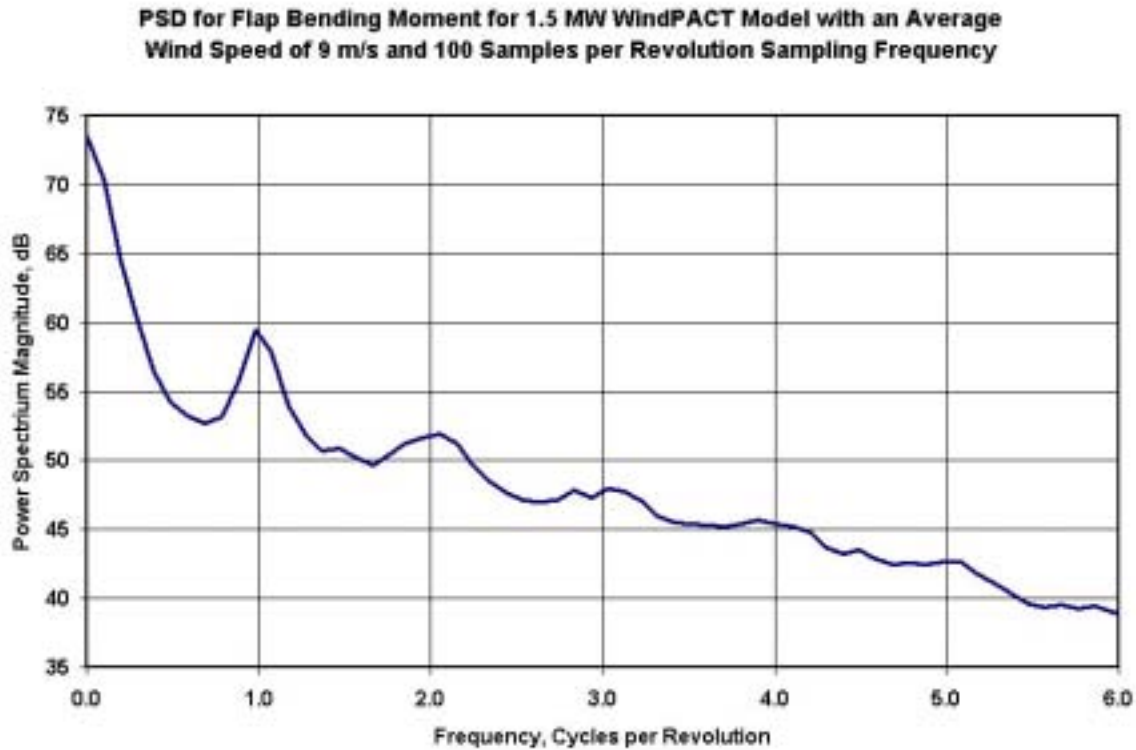
Figure 2-22. PSD of spatially sampled flap bending moment for 9 m/s wind speed

The same comparison between spatially re-sampled data and azimuth-averaged data was made for lead-lag loads. As shown in Figure 2-23, the lead-lag bending moments that were spatially uniform with respect to the rotor azimuth angle have more clearly defined spectral peaks than the original lead-lag bending moments. The spatially uniform data shows a clearly defined peak at 2 cycles per revolution while the chronologically uniform data does not. The frequency analysis also shows that the majority of spectral energy for the lead-lag bending moments occurs at 1 cycle per revolution. Since a significant portion of the forces in this direction can be associated with gravitational forces, the large amount of spectral content at 1 cycle per revolution is expected.

PSD for Lead-Lag Bending Moment for 1.5 MW WindPACT Model with an Average Wind Speed of 9 m/s with Time-Sampled and Azimuth-Sampled Data
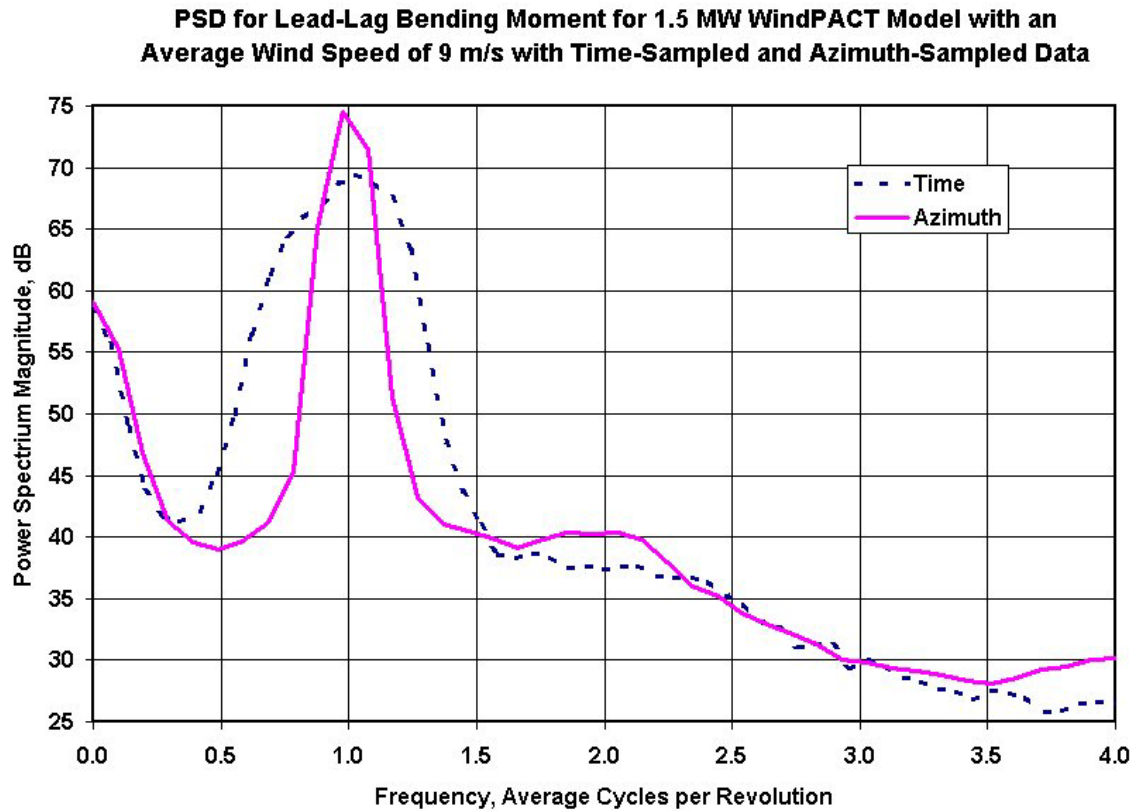
Figure 2-23. PSD of lead-lag bending moments for 9 m/s wind speed

Since re-sampling the bending moment data resulted in less dispersed spectra, only the newly sampled data will be discussed for the frequency analysis below. Clearly, there is a lot of frequency content located at one cycle per revolution for both the flap and lead-lag data for an average wind speed of 9 m/s. As shown in Figure 2-24, higher wind speeds increase the relative spectral energy content located at 1 cycle per revolution for flap bending.

PSD for Flap Bending Moment for 1.5 MW WindPACT Model with an Average Wind Speed of 20 m/s
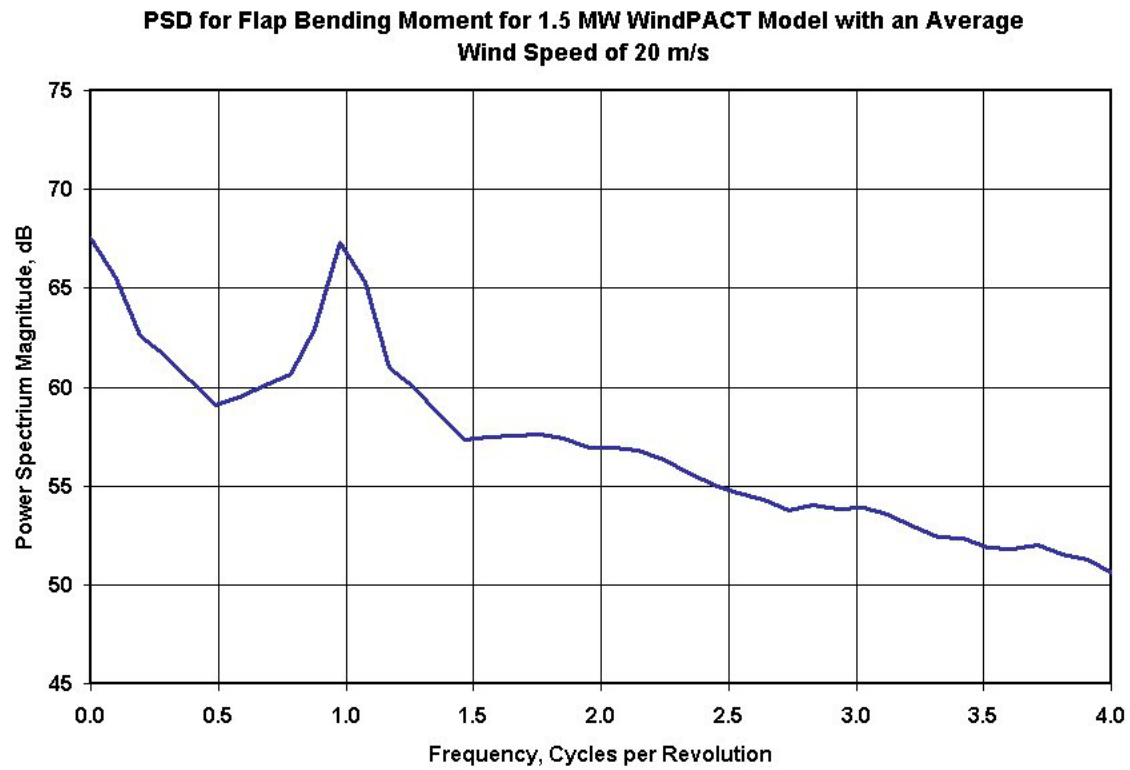
Figure 2-24. PSD of flap bending moments for 20 m/s wind speed

As shown in Figure 2-25, the lead-lag bending moment also shows a relative increase in the frequency content at 1 cycle per revolution.

PSD for Lead-Lag Bending Moment for 1.5 MW WindPACT Model with an Average Wind Speed of 20 m/s
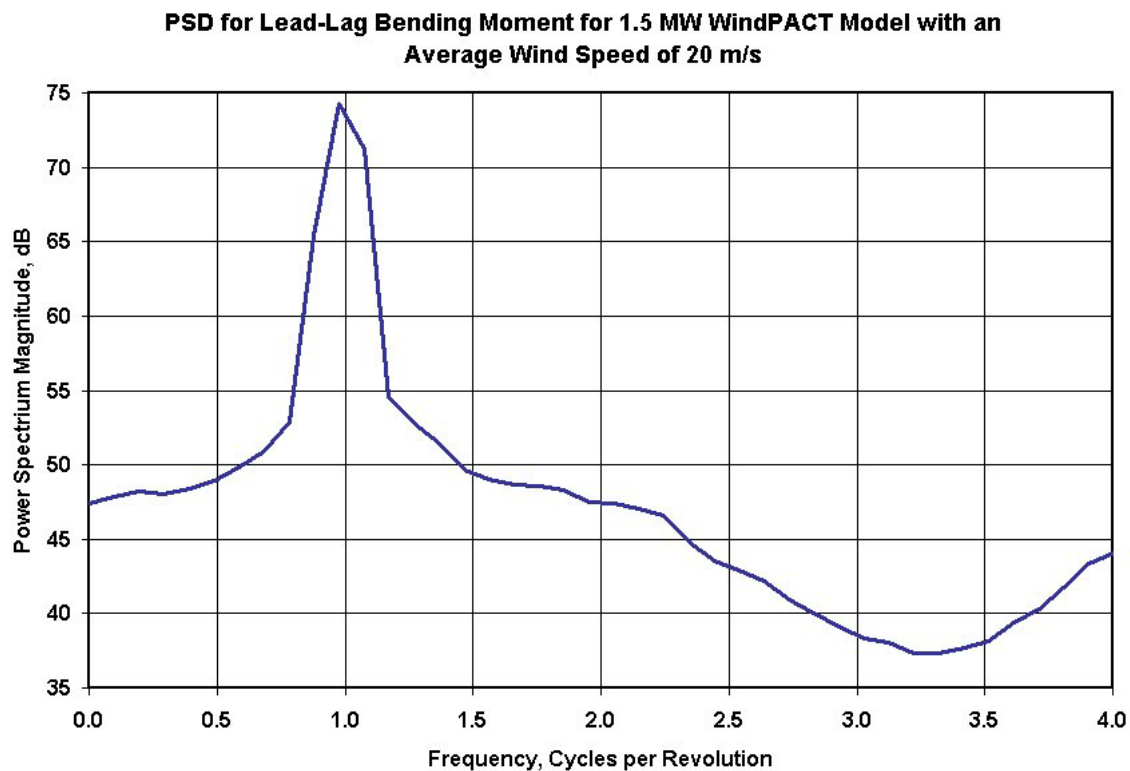
Figure 2-25. PSD of lead-lag bending moments for 20 m/s wind speed

While the frequency analysis indicates that both the flap and lead-lag bending moment have a lot of content located at the same frequency, this analysis does not indicate anything about the relative phase between the two bending moments or how much damage each load cycle contributes to the cumulative total. Additional analysis techniques were used to evaluate the coupling of the mean and alternating loads as well as the relative phase between the two loads. Before the relationship between the two data sets is discussed, the results of rainflow counting will be briefly considered.

2.5.3 Rainflow Count

When fatigue is considered, the relationship between the mean and alternating loads are important. Typically, rainflow counting is used to determine the relationship between the mean and alternating loads. This information is then transferred into equivalent strains using a Goodman diagram and compiled into an accumulated damage value using a fatigue damage model. The presented analysis shows the rainflow distribution for the simulated data but does not perform the damage analysis. This analysis has been performed to demonstrate that the simulated data has a typical rainflow distribution. In order to perform the rainflow count, the time-sampled data was reduced to include only the peak and valley loads. In some algorithms, a predetermined threshold must separate the peaks and valleys in order to be considered, but, this condition was not imposed for this data analysis. Once the time series data was manipulated into peak-valley data, the mean and range of each load cycle was calculated considering hysteresis. The mean and range data for each cycle was then binned. For this analysis, each cycle was equally biased regardless of the potential fatigue damage.

The rainflow counting process is designed to show relationship between the mean load and range of loads [67, 86-89]. As such, the dependence of the mean and standard deviation of the bending moments on wind speed described above is also evident in the rainflow distributions. Since this point is better made using statistics in another section, it will not be further discussed here.

As shown in Figure 2-26, the rainflow distribution for the flap bending moment is approximately Gaussian in both the mean and range dimensions. The mean bending moment for this distribution was approximately 1000 kN-m. This distribution agrees with field data collected on operating wind turbines [90].

Figure 2-26. Flap bending moment rainflow distribution

The lead-lag bending moment distribution was more complex. As shown in Figure 2-27, the lead-lag bending moment has three distinct load distributions. Gravitational forces produce a distribution with a large range and approximately zero mean. The other distributions can be attributed to the distribution of the wind. While the behavior of the wind would typically exhibit a single Gaussian distribution, the method used for rainflow counting tends to collect all cycles with the same mean into a single distribution around the larger range cycles. This behavior is the result of the peak-valley data reduction where intermediate values are discarded in favor of extrema. This distribution also agrees with field data collected on operating wind turbines [91].

Rainflow Count for 1.5 MW WindPACT Lead-Lag Bending Moment (9 m/s Wind)
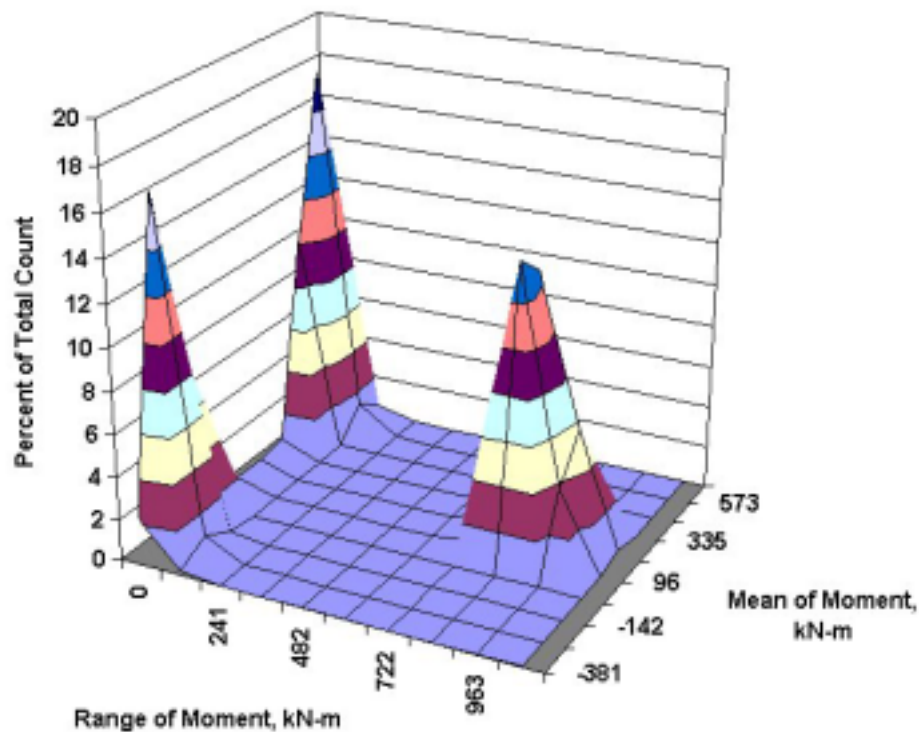
Figure 2-27. Lead-lag bending moment rainflow distribution

The distributions displayed in Figures 2-26 and 2-27 are generally representative of the distributions for other wind speeds and agree with rainflow distributions obtained using data for other wind turbines [92]. This type of analysis has been conducted for wind turbine blades prior to this study but this analysis does not consider the relative phase between the flap and lead-lag bending moments.

The analysis shown here demonstrates that the simulated data has a typical rainflow count distribution for wind turbine blades. This analysis also gives the reader an understanding of the underlying bending moment distributions that govern the following analysis on the phase angle between the flap and lead-lag bending moments that will be discussed later.

2.6 Summary

As an emerging technology, wind energy is continuing to evolve and mature. The basic nature and design of the wind turbine continues to converge to a more reliable and cost effective source of renewable energy and this evolution creates a continual demand for new structural and dynamic tests. In an effort to improve the way wind turbine blades are tested, the forces experienced by the blades have been analyzed. The analysis conducted in this chapter demonstrates that the simulated data is a valid representation of operating

conditions and can be used for further analysis. The relationship between the flap and lead-lag forces will be evaluated in chapter 3.

Chapter 3. Relationship Between Flap and Lead-Lag Blades Forces and Effect on Fatigue Damage

This chapter analyzed the phase angle relationship between the flap and lead-lag bending moments applied to wind turbines during operation. A relationship between the flap and lead-lag forces is defined (called the "phase angle") and statistically evaluated for a range of wind speeds. An aggregate phase angle distribution has been created from simulated wind turbine response data for a 1.5 MW pitch controlled variable speed turbine subjected to IEC class Ia wind conditions. This distribution has been used to evaluate the effects on fatigue life predictions of a variable phase angle fatigue test compared to that of a constant phase angle fatigue test. As part of the analysis, a three-dimensional finite element model of a 1.5 mega-Watt wind turbine blade was used to evaluate FEM nodal blade strains for specified loading conditions. This information was used to calculate the accumulated damage for a three million-cycle fatigue test with constant and variable phase angles. The results of this analysis show that the phase angle between the flap and lead-lag loads is very important to the accurate prediction and testing of fatigue damage. The results also show that when a material defect is present on the blade, a variable phase angle fatigue test has a higher probability of detecting the problem than a constant phase angle fatigue test.

3.1 Objective of Variable Phase Angle Testing

Since the purpose of performing fatigue tests is to reduce the overall wind turbine operating costs by improving reliability and providing manufacturers with accurate data from which to design the next generation of blades, it is imperative that the fatigue test accurately represent operational conditions. It is well known that the loads applied to wind turbine blades during operation are subject to variations [93]. But, current dual-axis wind turbine blade fatigue tests are conducted with a constant phase angle between the flap displacement and the lead-lag displacement [91]. As a result, the same regions of the blade are tested for each cycle. As the blade accumulates damage, the strain profile around the blade may move but will generally remain very similar throughout test. As will be shown in this chapter, the actual phase angle experienced by the blade during operation is not constant. Since the constant phase angle fatigue loads may produce a different degree of damage accumulation at certain locations than normal operating loads, the current test method may not detect some blade defects that could cause failures during operation. In an effort to improve the accuracy of blade tests, the effects of varying the phase angle have been analyzed and are presented below. Since the purpose of performing fatigue tests on entire blades is to validate and in some cases certify the blade design, the effects of varying the phase angle were considered for the theoretically perfect blade and with a material defect exists that was not been considered in the FEM. These results show that a fatigue test that varies the phase angle during operation has a higher probability of detecting material defects during testing than a constant phase angle test.

3.2 Assumptions and Limitations

For over a decade, researchers have been investigating the impact of differing load sequences on wind turbine blade materials [94-105]. In these cases, the magnitude of the load and displacement varies throughout the simulations and testing. A proposed load magnitude spectrum for fatigue testing, WisperX, has been proposed for wind turbine blades [23]. As discussed earlier, the size of the modern blades requires large amounts of energy to achieve the targeted displacement during testing. In most cases, the technology and equipment required to accurately perform dynamic spectra variable amplitude loading on a system of this size is very costly. By varying the phase angle throughout the fatigue test, it is possible to apply a simplified spectral loading to each blade location without increasing equipment costs. The analysis described in this chapter is meant to determine the practicality and impact of varying the phase angle during testing using the most accurate tools available. The damage accumulation and life predictions discussed below are not intended to be used to predict the quality or life expectancy of any specific blade. This research is meant to predict the difference in fatigue between potentially viable testing methods and determine which changes to current testing methods will have the most impact. The cases studied here include the current method for fatigue testing blades (constant phase angle) and variable phase angle testing.

3.3 Phase Angle

Based on an extensive literature search and discussions with blade testing experts, a previous study has not been conducted to determine the properties of the relative phase between the flap and lead-lag bending moments. While most agree that the phase angle is an important property to consider for testing, the variation of the phase angle with respect to wind speed and statistical variations has been generally overlooked. Since there were no publications found on the topic, the precise meaning of term 'phase angle' may be unclear to some. As such, a clear description of the phase angle used for this analysis will be presented. Research presented in chapter 5 will discuss the significance of phase angle variations with respect to fatigue analysis and testing.

3.3.1 Definition

The phase angle between the flap bending moment and a lead-lag bending moment is defined as the change in rotor angle between the maximum flap bending moment and maximum lead-lag bending moment for a given rotor revolution. Only one phase angle is recorded per rotor revolution. This angle is illustrated in Figure 3-1.
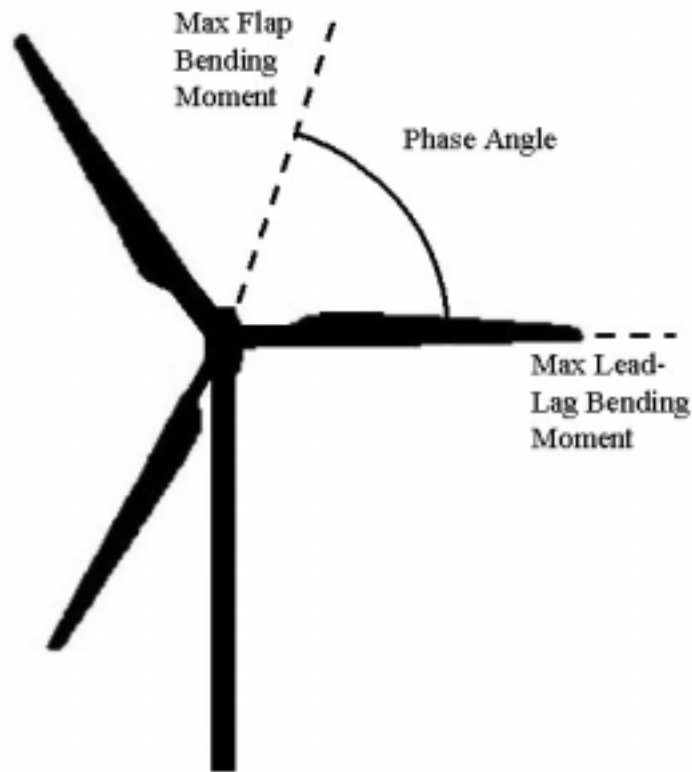
Figure 3-1. Phase angle definition

3.3.2 Phase Angle Time Series Analysis

In order to calculate the phase angle for each wind speed, the flap and lead-lag bending moments were broken up into data segments of one complete rotor revolution. For each bending moment, the rotor azimuth angle corresponding to the maximum bending moment was recorded. Figure 3-2 shows a sample of the flap and lead-lag bending moment data and demonstrates how the phase angles were calculated. The change in rotor position between the maximum flap and the maximum lead-lag bending moment was calculated for each complete rotor revolution and for each wind speed.

Normalized Flap and Lead-Lag Bending Moments for 9 m/s Wind Speed
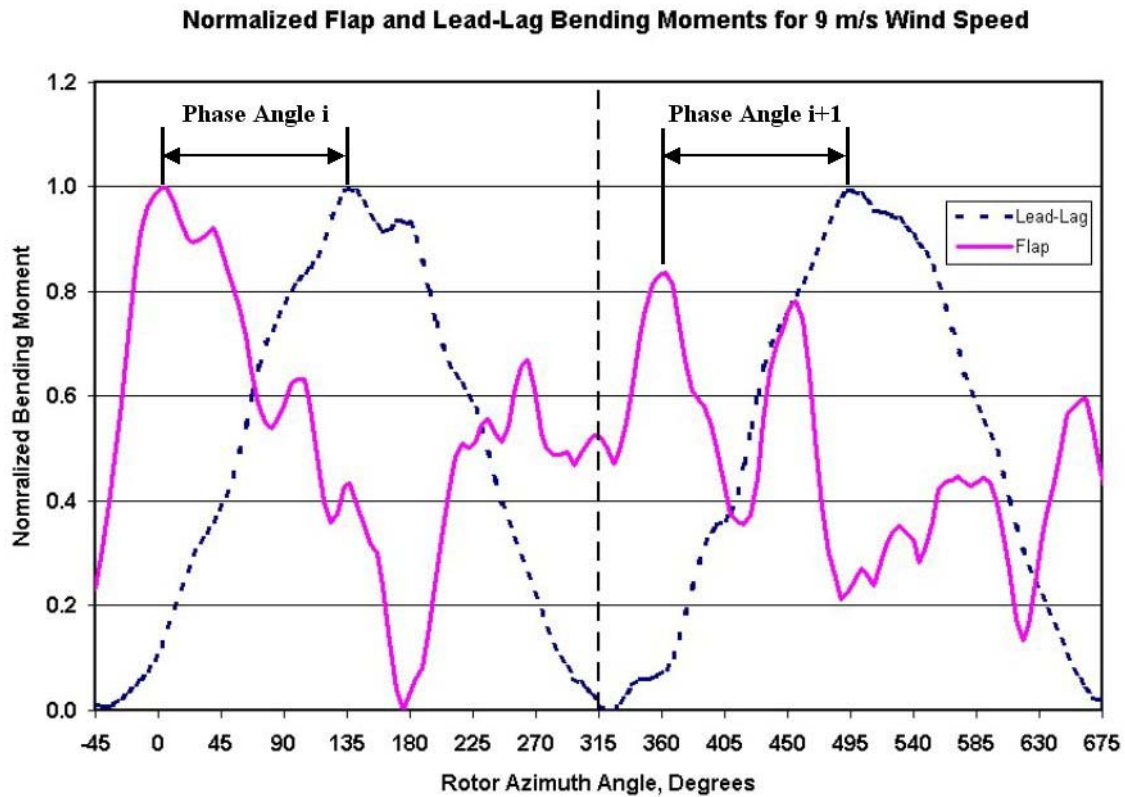
Figure 3-2. Sample calculation of phase angle for two rotor revolutions

While the phase angle may appear stable over short periods of time, its value may also experience large changes from one rotor cycle to the next. As shown in Figure 3-3, the phase angle between the flap and lead-lag bending moment has a range of nearly 360 degrees.

47

Phase Angle History for 9 m/s Average Wind Speed
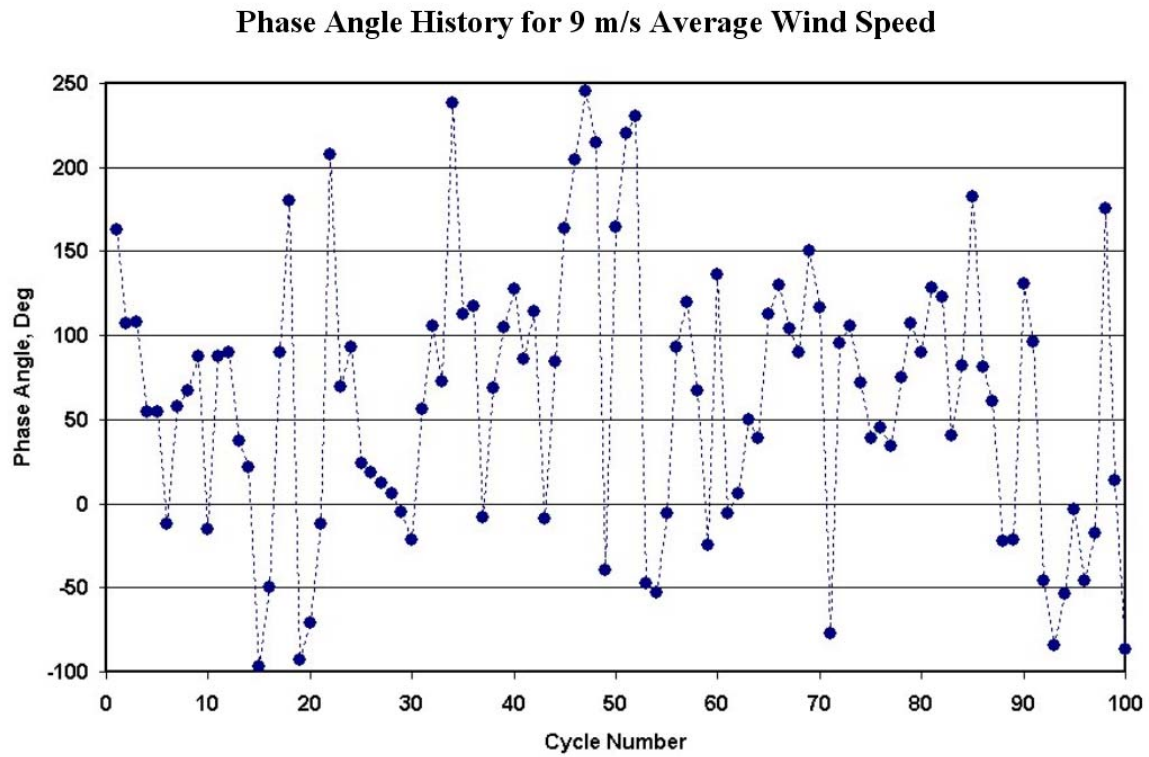
 Figure 3-3. Sample of phase angles calculated for an average wind speed of 9m/s

In order to better understand the nature of the phase angle variations, a statistical analysis of the data was performed.

3.3.3 Phase Angle Analysis

Once the phase angles for each wind speed and rotor cycle were calculated, the results were binned to create histograms. As shown in Figure 3-4, the phase angle data shows an approximately normal distribution for an average wind speed of 9 m/s. The average phase angle for this wind speed was 67 degrees.
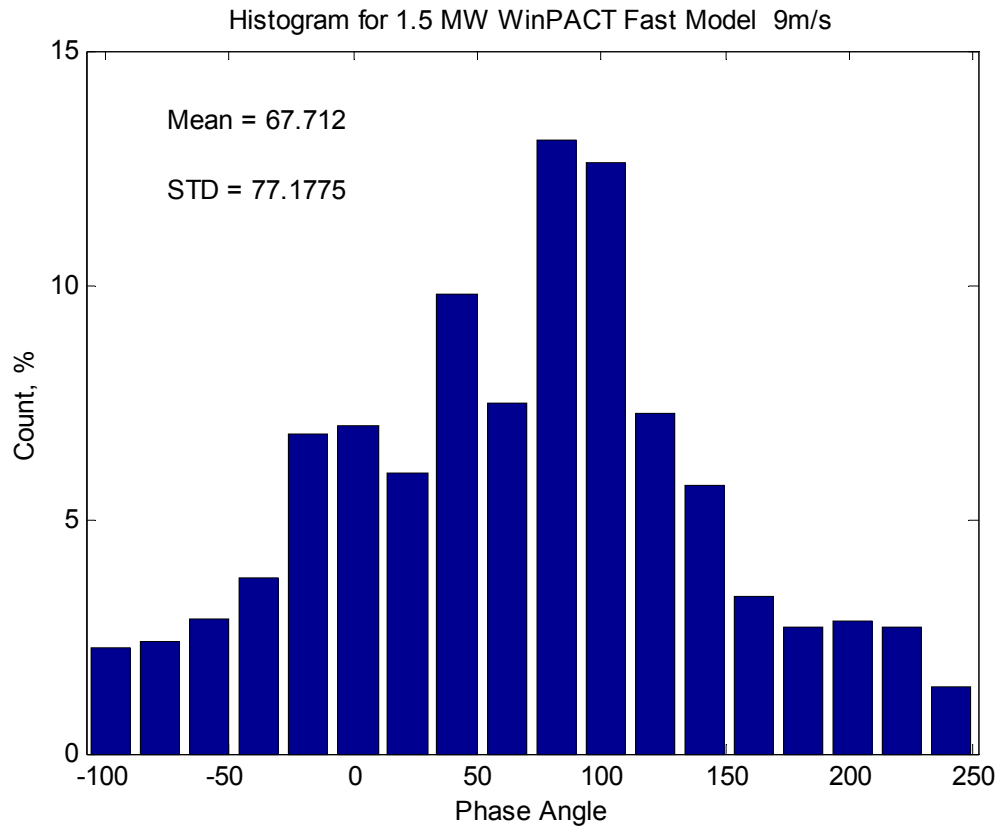
Figure 3-4. Phase angle histogram for an average wind speed of 9 m/s

Although not shown here, the histogram distribution was generated for the complete set of phase angle data and several subsets of the same data. By looking at 25 percent, 50 percent and 100 percent of the data, it was determined that the number of data samples did not influence the shape of the histogram distribution in this range. For higher wind speeds, the phase angle distribution remained approximately normal. As shown in Figure 3-5, the phase angle histogram distribution for an average wind speed of 20 m/s is also approximately normal.
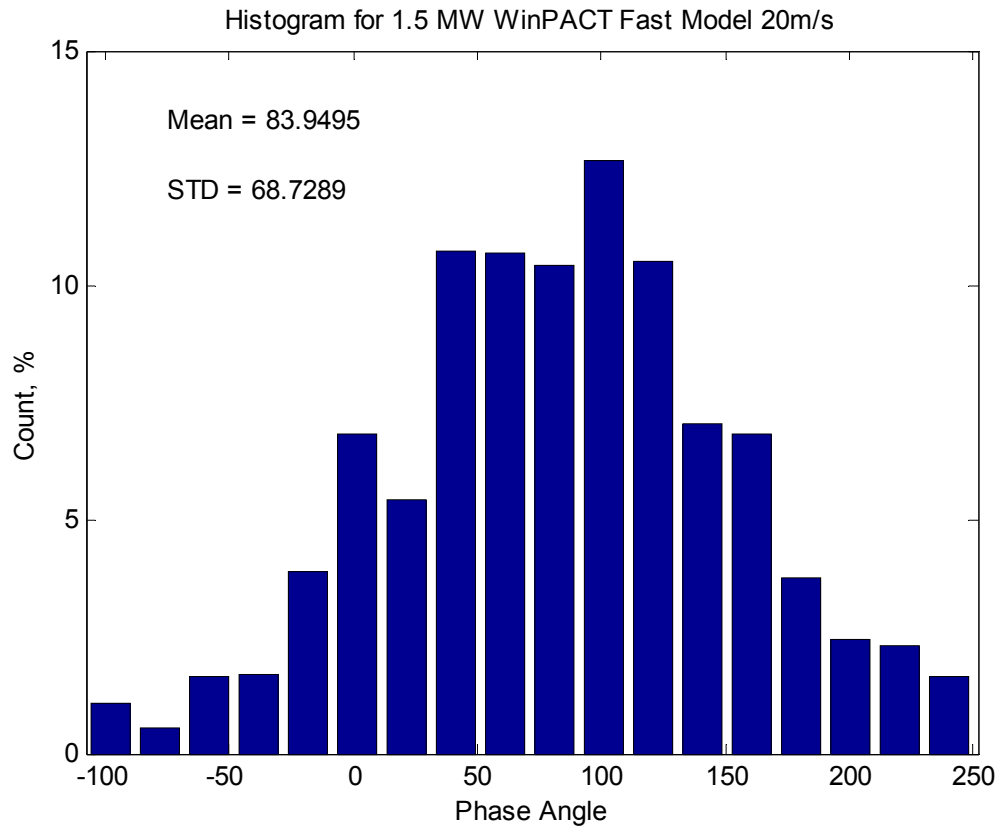
Figure 3-5. Phase angle histogram for an average wind speed of 20 m/s

Since the histogram distributions are approximately normal, the standard deviation of each data set was calculated. From the plots for 9 m/s and 20 m/s wind speeds, it is clear that the mean and standard deviation of the phase angles change with wind speed. As shown in Figure 3-6, the mean phase angle has an approximately linear relationship with wind speed. By curve fitting the data, an approximate slope of 1.69 degrees per m/s was obtained.
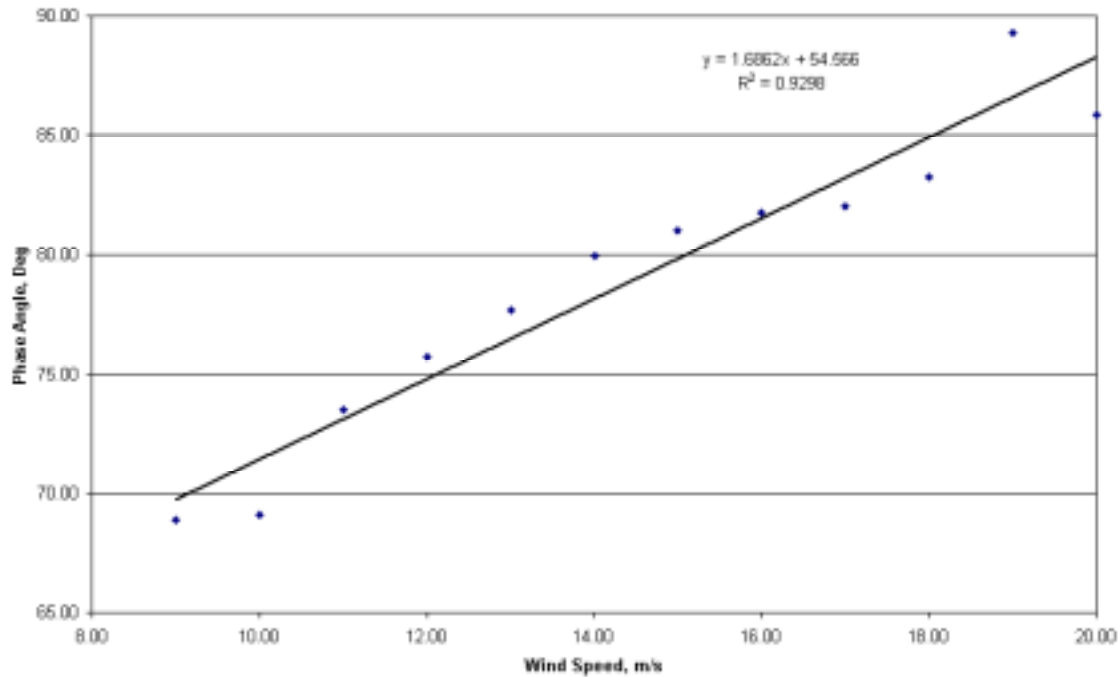
Figure 3-6. Effect of average wind speed on the mean phase angle

The increase in the mean phase angle as wind speed increases may be the result of increasing flap forces for higher wind speeds. Since the bending moment data is simulated from strain gauge measurements, any lag in the blade response due to inertia would appear in the data. As aerodynamic flap forces increase the lag response of the system will be reduced, because the inertially deterministic lead-lag forces do not increase with wind speed.

As shown in Figure 3-7, the standard deviation of the phase angle also changes linearly with wind speed. However, the standard deviation of the phase angle decreases for higher wind speed. This phenomenon could be the result of higher aeroelastic damping acting on the blade. The standard deviation is relatively large compared to the mean phase angle for all wind speeds.

51
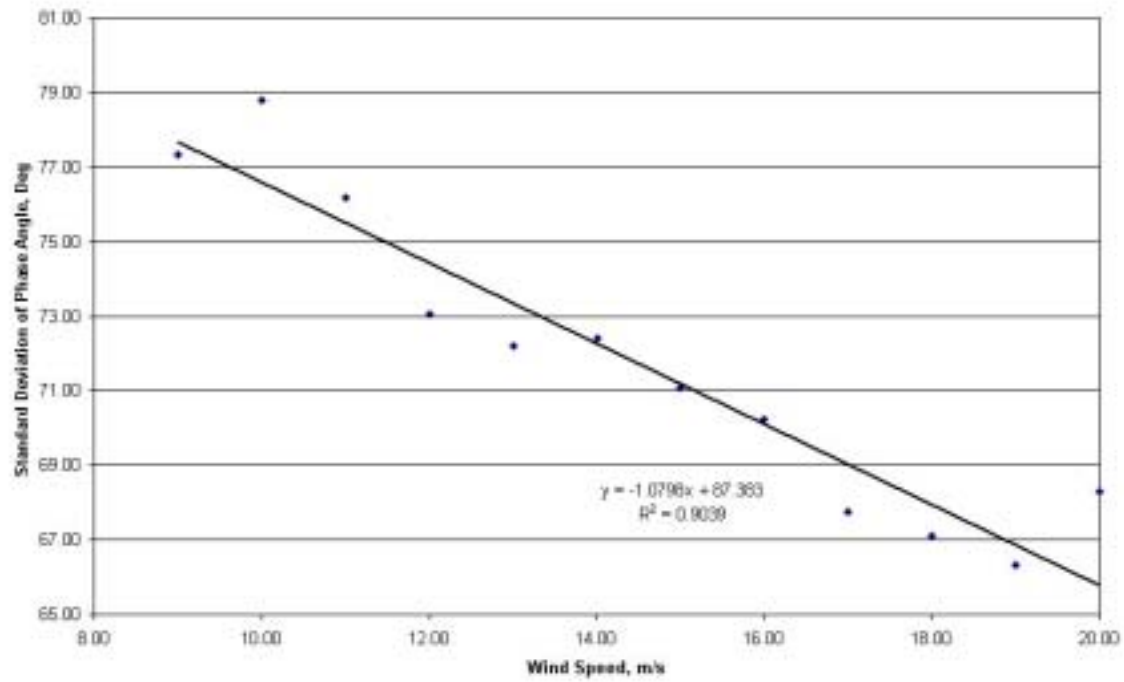
Figure 3-7. Effect of wind speed on the phase angle standard deviation

Ultimately, the goal of analyzing the phase angle characteristics is to determine a suitable distribution for fatigue tests or fatigue analysis. By determining the properties of the phase angle distribution for each wind speed, it is possible to develop a theoretical wind speed distribution.

3.3.4 Aggregate Distribution

While the phase angle properties at each individual wind speed are important, each blade fatigue test can have only one final phase angle distribution. In order to determine the best distribution to use for testing, the individual distributions at each wind speed must be weighted proportional to the frequency of occurrence. For this analysis the standard IEC wind speed distribution for class IA was used. The IEC standard uses either a Rayleigh or Weibull function distribution to describe the shape of the distribution. For this analysis a Rayleigh distribution was used. The probability density function for the class IA is show in Equation 3.1.

$$P(V) = \frac{\pi}{2}\left(\frac{V}{V_{AVE}^2}\right)\exp\left[\frac{-\pi}{4}\left(\frac{V}{V_{AVE}}\right)^2\right] \tag{3.1}$$

Where,

$P(V)$ is the probability function
V is the wind speed
V_{AVE} is the Average Wind Speed (from IEC Standard)

Using this Equation to calculate the wind speed probability results in the distribution shown in Figure 3-8.
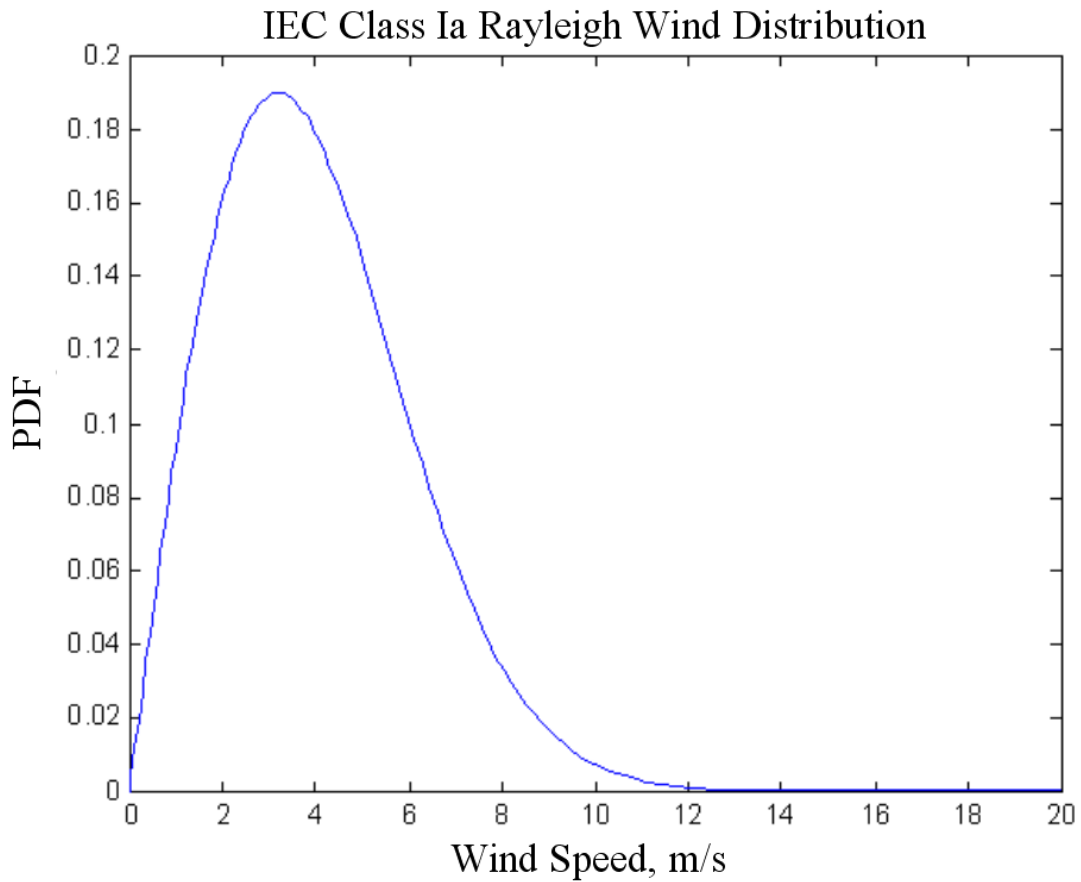
Figure 3-8. IEC wind speed distribution for standard class IA wind location

When the wind speed distribution is applied to the normal distributions for each wind speed, a three-dimensional probability distribution relating both the phase angle and wind speed is created. The new probability distribution was normalized so that the sum of the area under the curve is 1.0 and is shown in Figure 3-9.
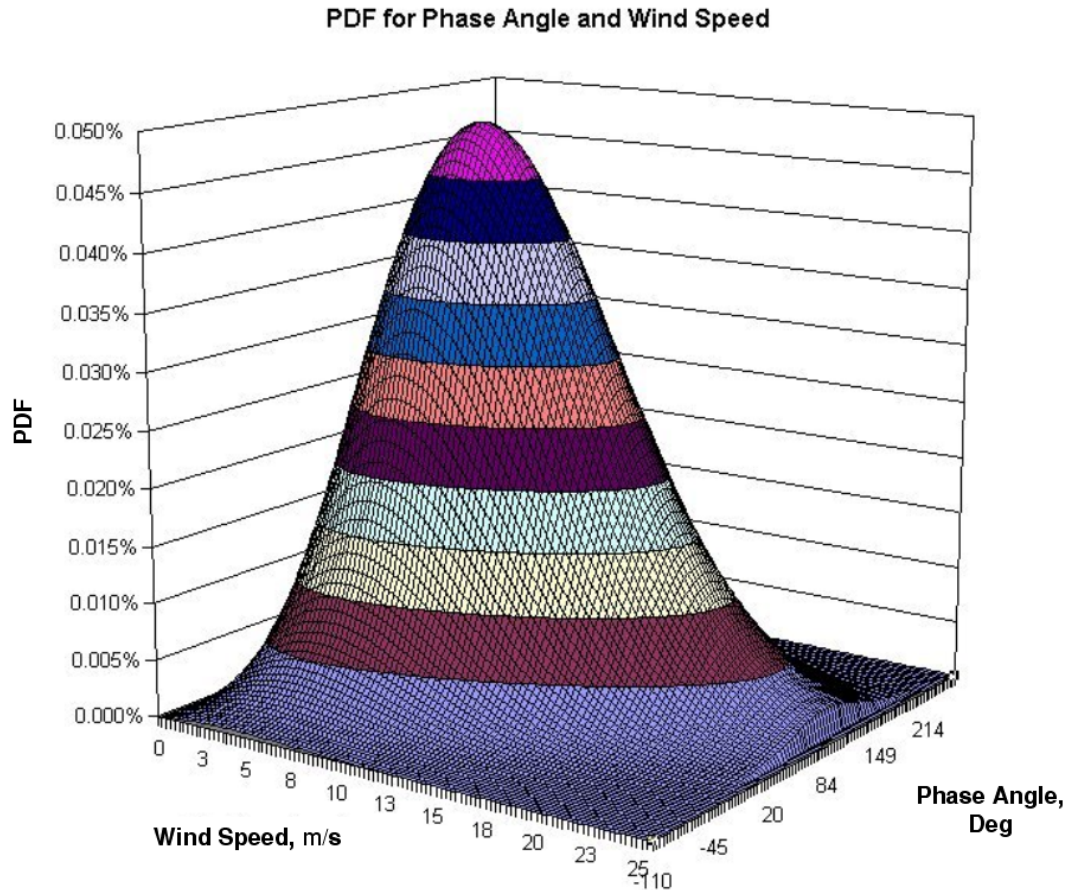
Figure 3-9. Normalized phase angle distribution

As discussed earlier, the fatigue test requires a single probability density function. In order to compress the three-dimensional probability distribution into a single distribution, the values for each wind speed were added together for a given phase angle. This procedure is equivalent to performing a weighted average of the normal phase angle distributions using the wind speed probability as the weighting function. Although the result of this method is not required to have a normal distribution, the aggregate distribution, shown in Figure 3-10, is approximately normal with a mean value of 72 degrees and a standard deviation of approximately 54 degrees. Since the system being modeled represents the dynamic response of a mechanical system, a smooth distribution was expected. The very minimal skewness and kurtosis shown by the distribution is a little surprising given the way the curve was derived. This indicates that a narrow range of wind speeds determine the shape of the distribution.

Aggregate Phase Angle Probability Distribution
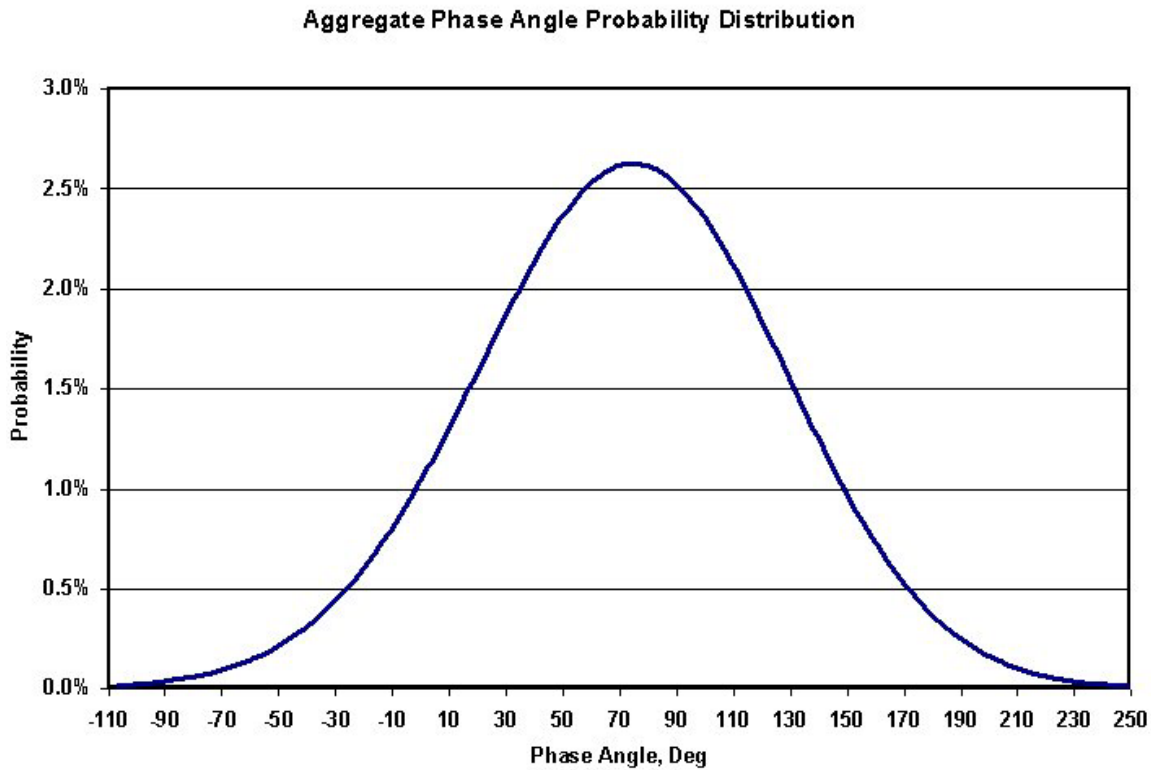
Figure 3-10. Probability distribution weighted by wind speed distribution

3.4 Structural Analysis

As discussed earlier, the Department of Energy (DOE) sponsored a research program designed to reduce the cost of energy (COE) for wind power called WindPACT (Wind Partnerships for Advanced Component Technology). This program consisted of a number of studies conducted by different research groups. The dynamic blade response data used for the analysis in Chapter 2 was generated by NREL as part of this program. As a separate part of the WindPACT program, Global Energy Concepts (GEC) developed a 3-D finite element model for a generic 1.5 mega-Watt turbine. The 3-D model was created using NuMAD (Numerical Manufacturing And Design tool developed by Sandia National Laboratories) [106]. NuMAD is a pre-processor and post-processor for the general FE code, ANSYS^{TM} designed specifically to reduce the model development time for wind turbine models.

3.4.1 FE Model Description

The 3-D finite element model used for this analysis is composed of 50 nodes located around the blade airfoil and 10 nodes located on the spar for each blade cross sections. The material properties for the blade model were calculated using generic wind turbine E-glass layer and resin properties. The material properties for the blade were compiled using NuMAD and used to create shell elements in ANSYS^{TM}. The node locations are shown in Figure 3-11 for the 3-D model.
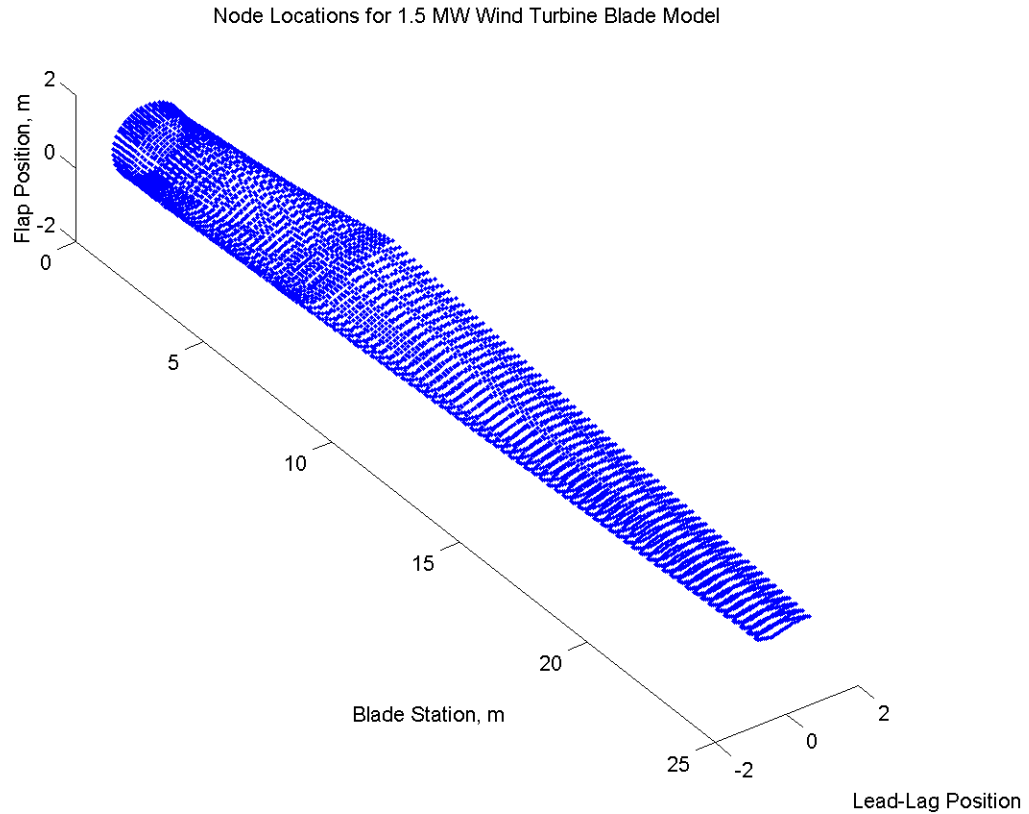
Figure 3-11. Finite element blade model airfoil nodes

Figure 3-12 shows the variation in chord length and overall blade thickness as a function of the blade station.
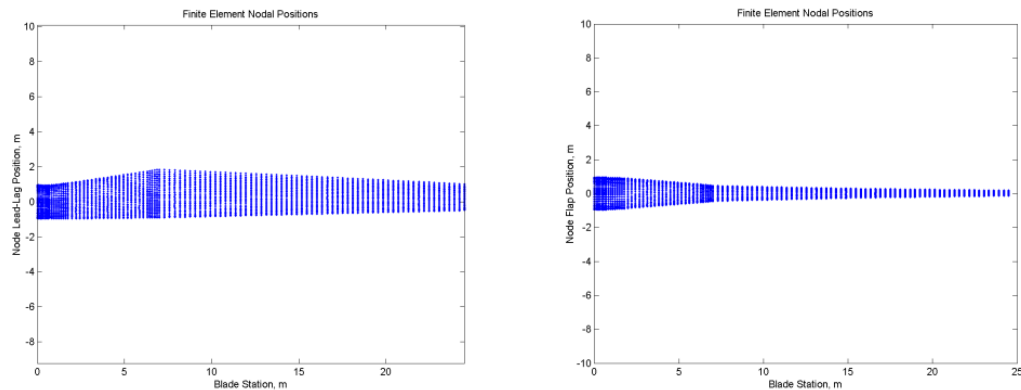
Figure 3-12. Blade lead-lag and flap shape

The shape of the airfoil and the chord length vary along the length of the blade. However, the nodes are numbered in the same manner for each blade station. As shown in Figure 3-13, the nodes are numbered one through 60 starting at the trailing edge. The leading edge is node number 26 while the vertical spar nodes are numbered 51 through 60. The material properties of the blade can be subdivided into two distinct regions

demonstrated by the red and blue color-coding. The detail of the material properties will be discussed later in this chapter.
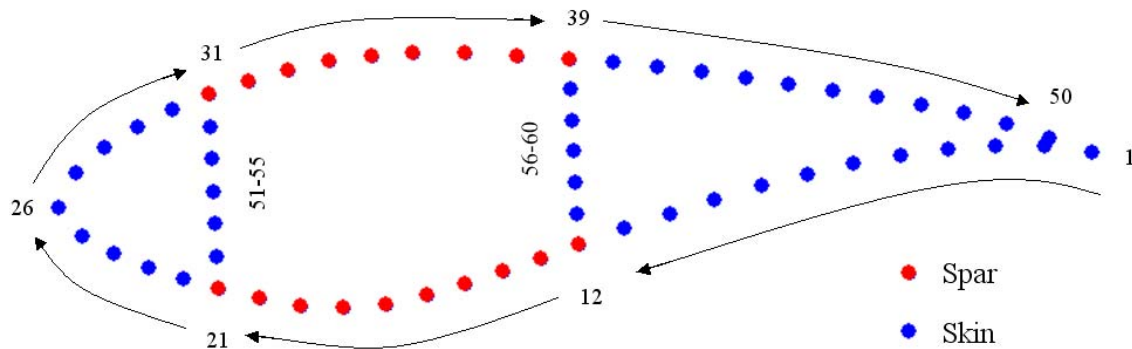
Figure 3-13. Finite element node numbers for each cross-section

3.4.2 Preliminary Results

In general, the research discussed in this chapter involves the specific and detailed analysis of individual blade stations. The amount of data and type of analyses conducted during this researched was much too computationally intensive to include all the information from the FEM model. However, it is possible to show some information for the global model. Figure 3-14 shows the axial strain for each node of the FEM when a unit lead-lag force is applied to the blade tip. The maximum axial strain coincides with the maximum chord length of the blade shown in Figure 3-1. This behavior has been observed in other blade models, during static testing and fatigue testing. At the 15.75-meter station, a dip in the strain profile boundary can be observed. This location coincides with a ply-drop.
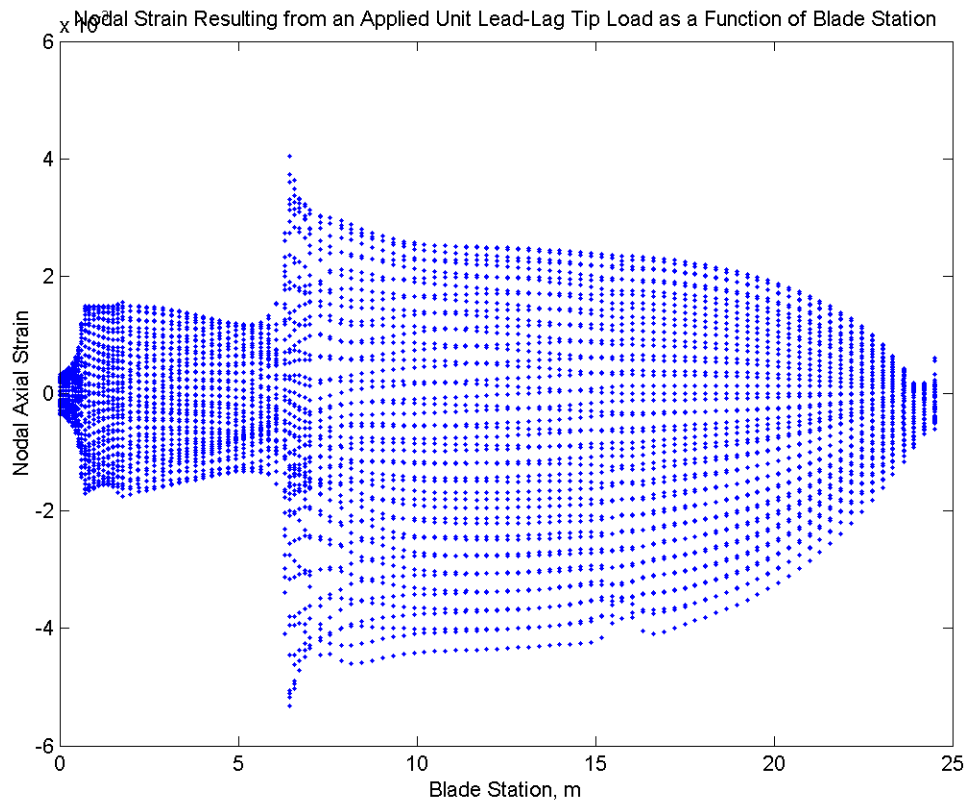
Figure 3-14. Axial strain profile for a unit load in the lead-lag direction

In an effort to determine if a change in phase angle could result in a noticeable change in the global strain profile, the strain profiles corresponding to the maximum resultant force for several phase angles were plotted. Figure 3-15 shows the global strain profile on the outer and lower surfaces resulting from the maximum resultant force occurring during a test cycle with a 72 degree phase angle between the flap and lead-lag actuators.
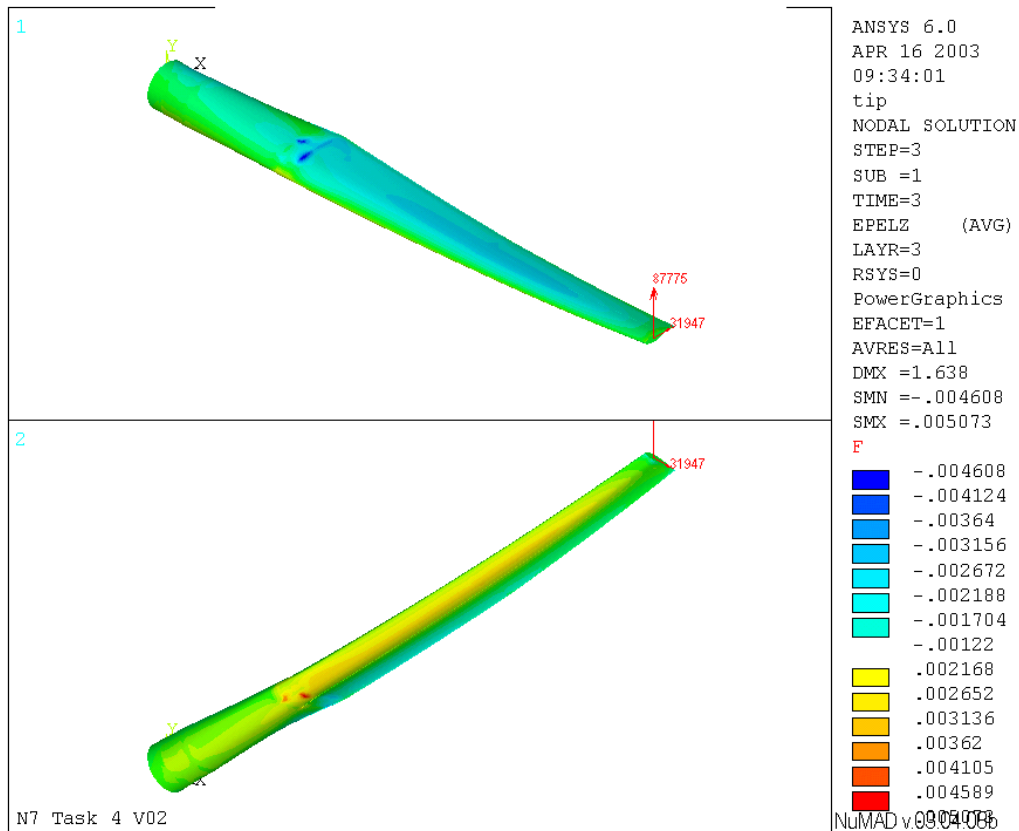
Figure 3-15. Strain profile for the maximum load for a 72 deg phase angle

A similar plot was generated for phase angles of 0 and 90 degrees. As shown in Figure 3-16, the strain profile for the maximum resultant force corresponding to a phase angle of zero degrees is noticeably different than the strain profile in Figure 3-15.
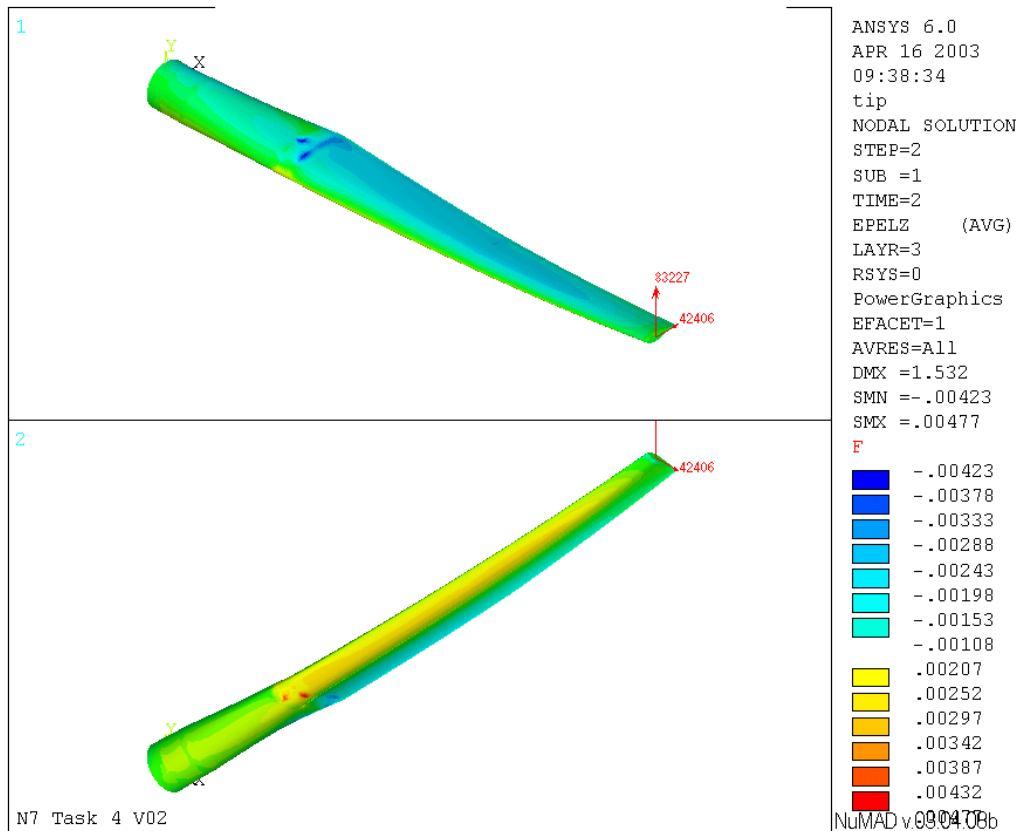
Figure 3-16. Strain profile for the maximum load for a 0 deg phase angle

3.4.3 Strain Profile Results

To calculate the effect of phase angle variations on fatigue, it is necessary to first create a predicted time history of the strain at each node location. To do this, the axial strain at each node was calculated using the 3-D FEM for unit loads in the flap and lead-lag direction. Time histories for the flap and lead-lag forces were created for all phase angle values. The axial strains calculated from the FEM were then multiplied by the flap and lead-lag force time histories and combined using superposition. The resulting axial strain time histories were then reduced using peak-valley detection to determine the mean and alternating strain values occurring at each node for each phase angle. Once cycle of a typical predicted strain time history is shown in Figure 3-17.

Example of Strain Time History for a Specified Node
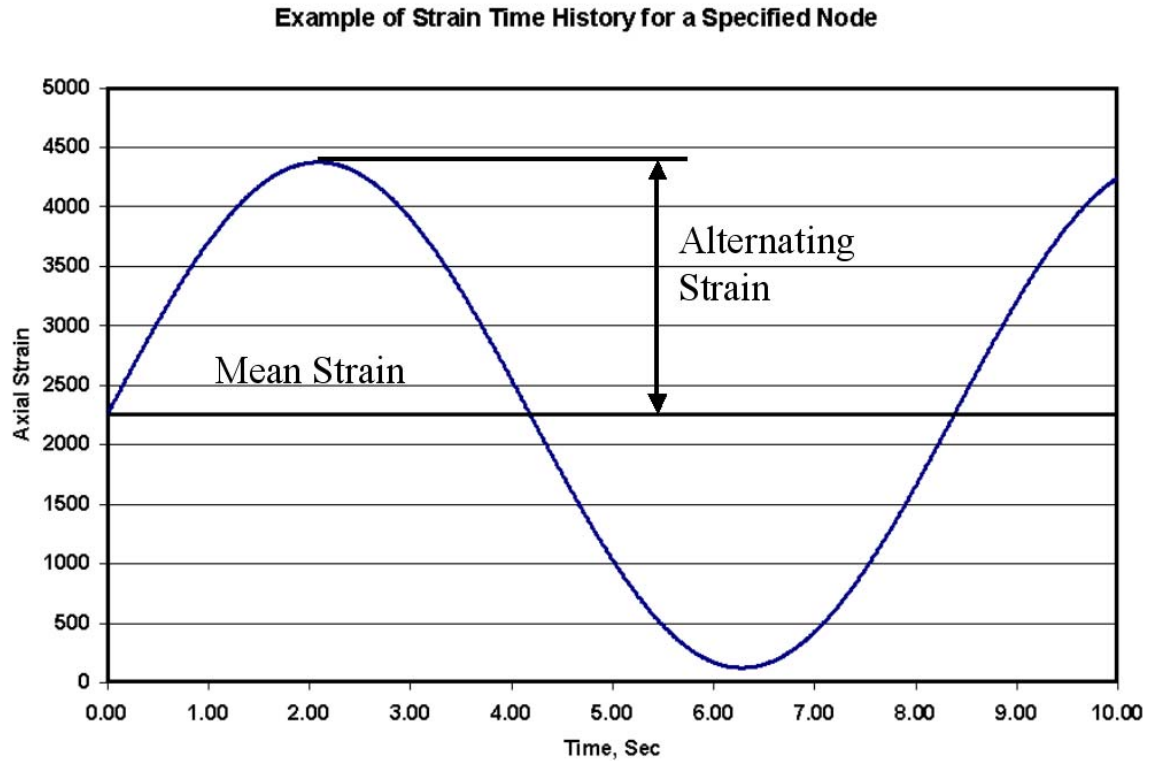
Figure 3-17. Strain time history for a specific node and phase angle

Since the mean and alternating strains at each node vary as a function of phase angle, the R-ratio (ratio between the minimum and maximum strain) is not constant. In order to compare the strains equally, an equivalent strain was calculated using a Goodman diagram. As shown in Figure 3-18, the Goodman diagram used for this analysis is a straight-line approximation of the material properties. It would be possible to use a more accurate representation of the material properties if this analysis were tailored to a specific blade. However, this analysis is meant to represent the response of a general wind turbine with generic material properties. So it is not practical to customize the Goodman diagram [107] for a specific material at this time. Since a straight line approximation has been used for this analysis, the equivalent strain can be calculated by applying a parallel line starting at the point derived from the mean and alternating strain values and ending for an equivalent alternating strain as shown below.

Figure 3-18. Goodman diagram and equivalent strain definition

Using the above technique, it is possible to calculate the equivalent strain at each node resulting from each phase angle. As shown by Figure 3-19, the phase angle can influence the range of alternating strains for a single node. But before this research project, it was not clear how different phase angles affect nodes distributed around the airfoil profile.
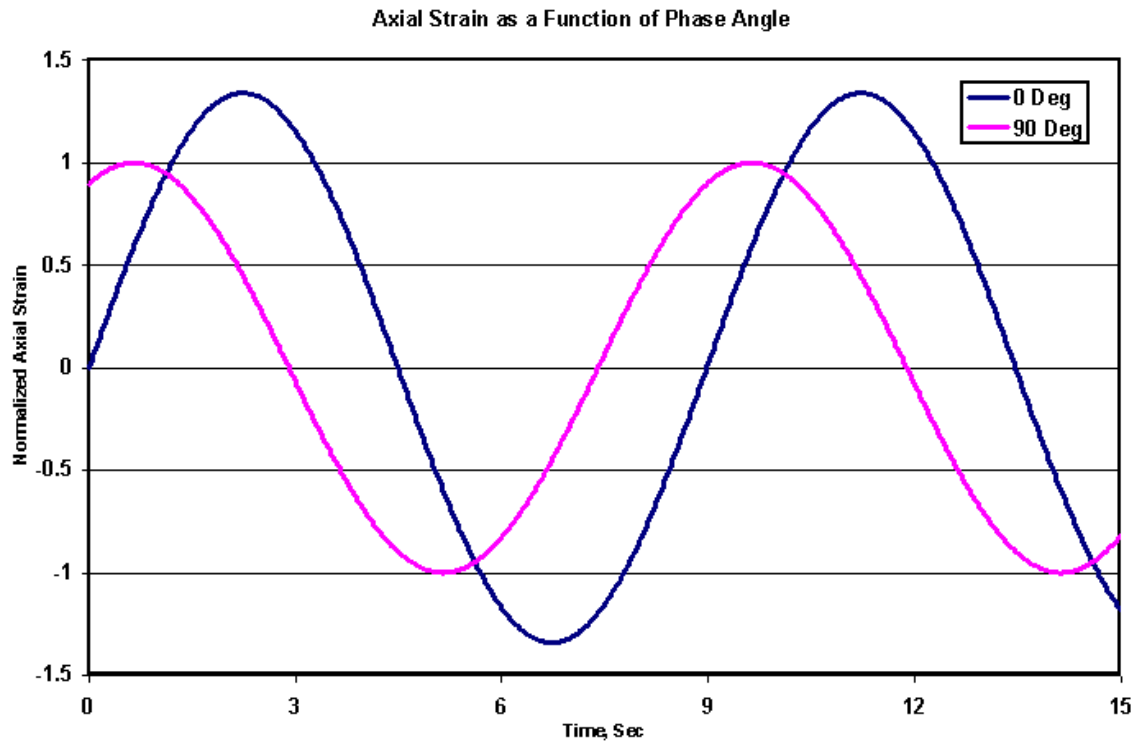
Figure 3-19. Axial strain as a function of time and load phase angle

Figure 3-20 shows that changing the phase angle impacts the strain at each node differently.
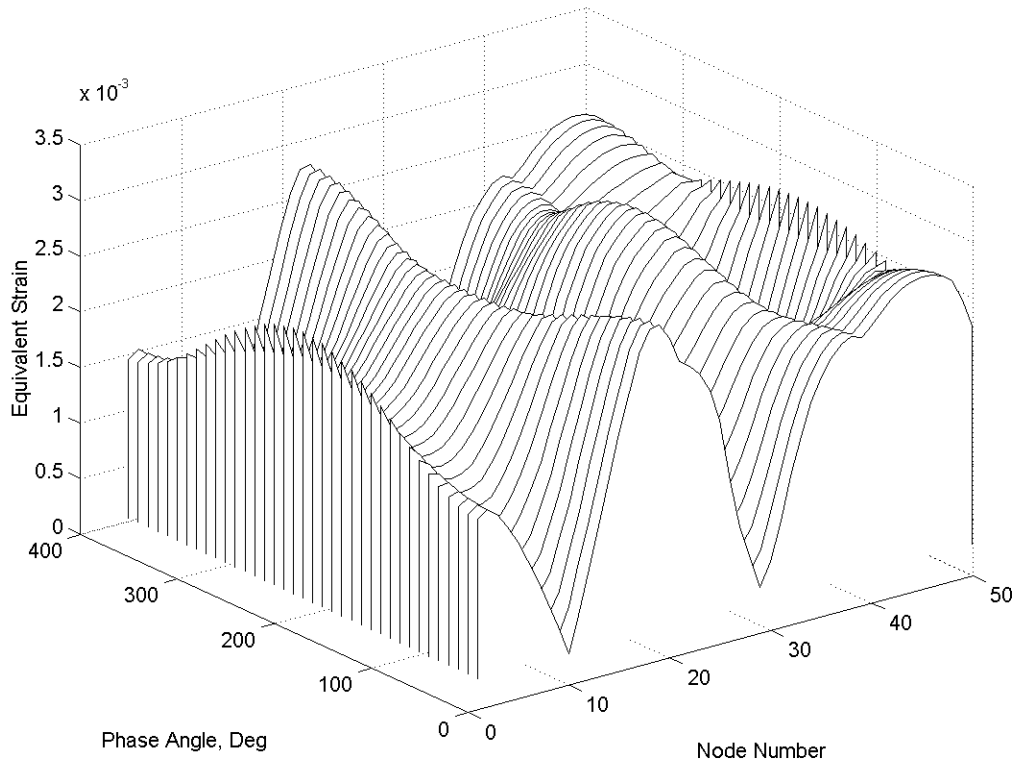
Figure 3-20. Equivalent strain at the 15.75-meter blade station

For the purpose of this analysis, most of the calculations were conducted at the 15.75-meter station. Analysis of the nodal data showed that the strain distributions outboard of the maximum cord location (6.3-meter station) have very similar strain distributions. As such, the 15.75-meter station is a good representative for the conditions over most of the blade. As shown in Figure 3-21, the difference in equivalent strain has a greater range for phase angles near zero degrees than for phase angles near 90 degrees. The phase angles of zero, 72 and 90 degrees were extracted for further analysis because these phase angles have been used for actual full structure fatigue tests.
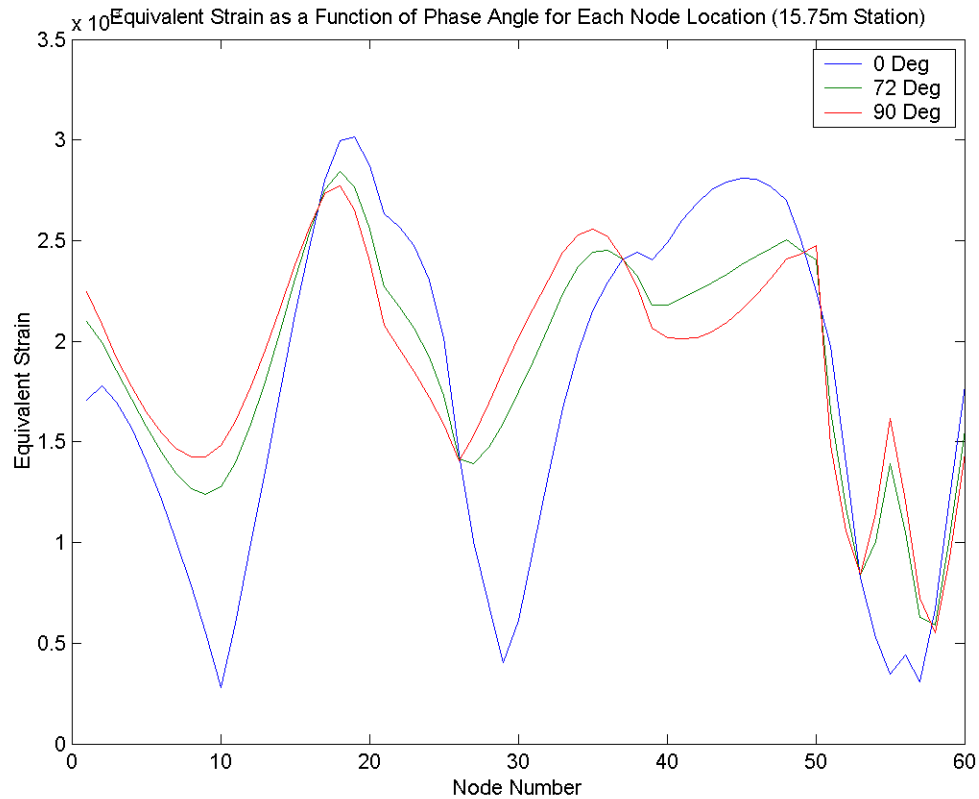
Figure 3-21. Equivalent strain at the 15.75-meter blade station (0, 72, 90 deg.)

The maximum strain occurred at the maximum chord location and this location has a unique strain profile. While analyzing the effects of phase angle on this location is of interest, it is not possible to draw much information on possible test improvements by analyzing this station, because the design and structure of the maximum chord station is dependent on individual blade designs. However, as shown by Figure 3-22, the strain distribution around the maximum chord station is influenced by changes in phase angle.
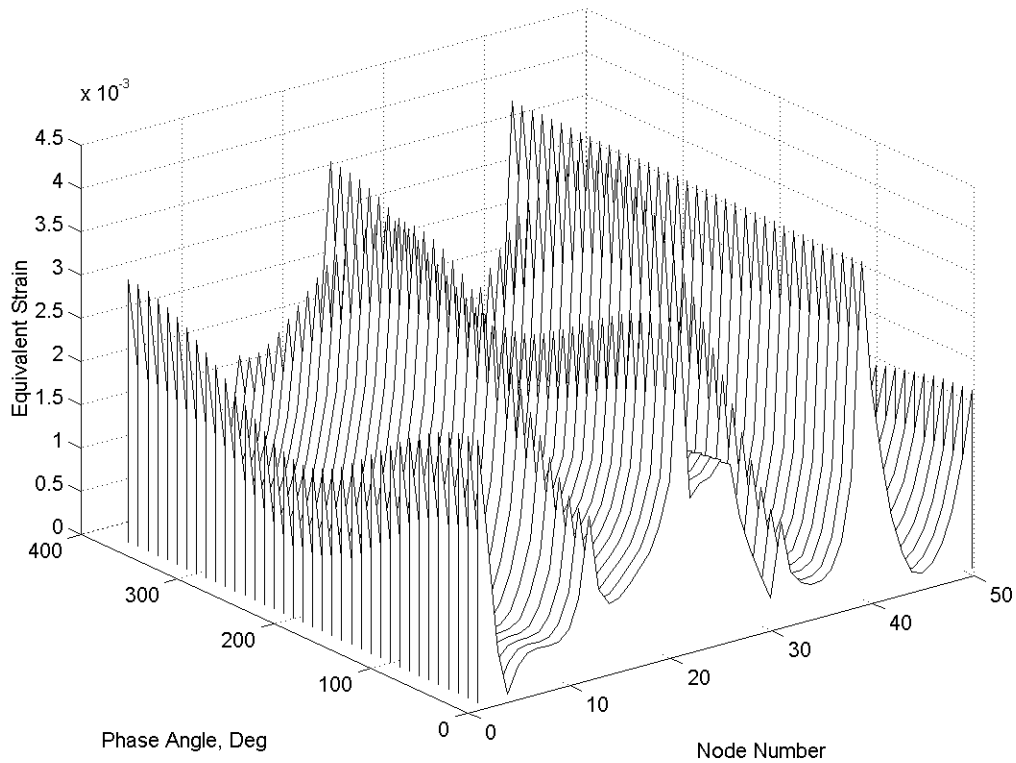
Figure 3-22. **Equivalent strain at the 6.3-meter blade station**

As shown in Figure 3-23, the difference in equivalent strain has a greater range for phase angles near zero degrees than for phase angles near 90 degrees. The strain distribution for the 6.3-meter station also shows that locations of peak strain are more concentrated than at other stations. Each of the locations of peak strain in Figure 3-23 corresponds to either the trailing edge or the connections of the spar to the skin.
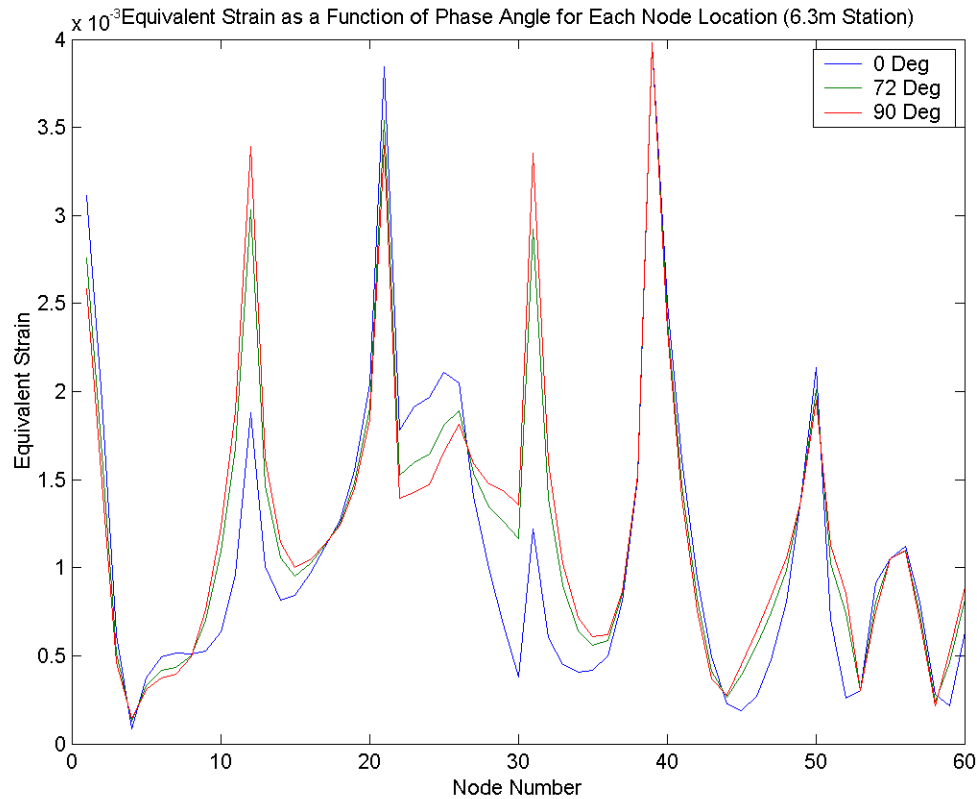
Figure 3-23. Equivalent strain at the 6.3-meter blade station (0, 72, 90 deg.)

3.5 Accumulated Damage

After calculating the influence of the phase angles on the strain of each node, it is possible to calculate the predicted life resulting from each test condition. While there are several models used to predict fatigue accumulation for composite material [108-110], it is still common to use Palmgren-Miner's Rule for general damage calculations. Since Miner's rule is a linear model of damage accumulation, it is not possible to use this method to evaluate all of the test conditions that are considered as part of this research. However, the simplicity and acceptance of Miner's rule make it advantageous to analyze some of the test conditions using this method.

3.5.1 Miner's Rule

Miner's rule assumes that damage is accumulated linearly throughout the life of a test specimen. From coupon tests, it is possible to determine the number of cycles required to fail a material sample at a specific strain level. Miner's rule assumes that the life subtracted from the initial value is simply the ratio of the number of cycles applied to the material to the number of cycles at which the material will fail for a specific strain level. As such this damage accumulation rule can be expressed by Equation 3.2.

$$D = \sum_i \frac{n_i}{N_i} \tag{3.2}$$

Where,

D = Total Accumulated Damage
i = Load Case Index

3.5.2 Material Properties

Regardless of which damage model is used to predict the life of the blade during various testing conditions, the material properties of the blade must be considered. Based on coupon tests and material standards, two strain-cycle curves have been used to calculate the material strength properties [84, 85].   As shown in Figure 3-24, the strain required to fail the skin material is higher than the strain required to fail the spar material (see Figure 3-13).
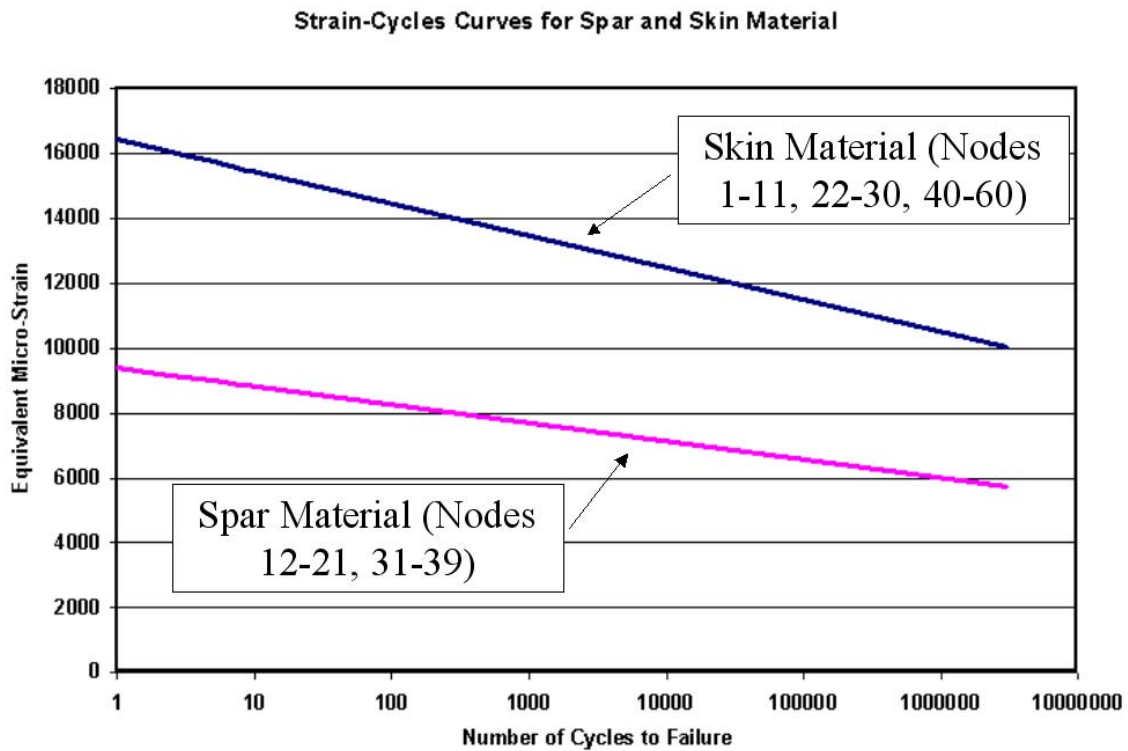
Figure 3-24. Strain-cycle curves for blade materials

3.5.3 Damage Accumulation for Constant Phase Angles

Using Miner's Rule and the material properties described above, it is possible to calculate the life expectancy of a wind turbine blade subjected to a specific set of loading conditions. As shown in Figure 3-25, a blade subjected to three million cycles at certain phase angles result in significantly different results than for other phase angles. For example, the damage accumulated at node 12 is significantly higher for phase angles around 180 degrees than for phase angles around 72 degrees. A constant amplitude fatigue test run at a 72-degree phase angle will not include any cycle at the much more damaging 180-degree phase angle.
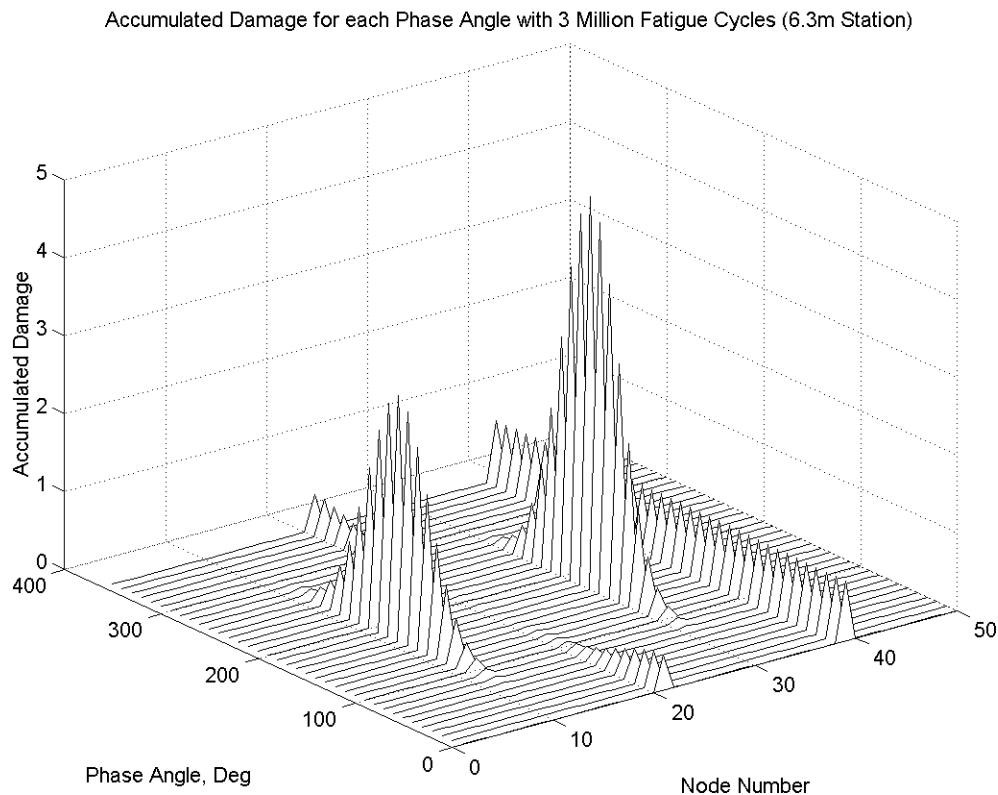
Figure 3-25. Damage as a function of phase angle for 6.3-meter station

Similar results were found for other blade stations. As shown by Figure 3-26, the damage accumulation for each node at the 15.75-meter station would be highly influenced by phase angle for a constant phase angle fatigue test.

Accumulated Damage for each Phase Angle with 3 Million Fatigue Cycles (15.75m Station)
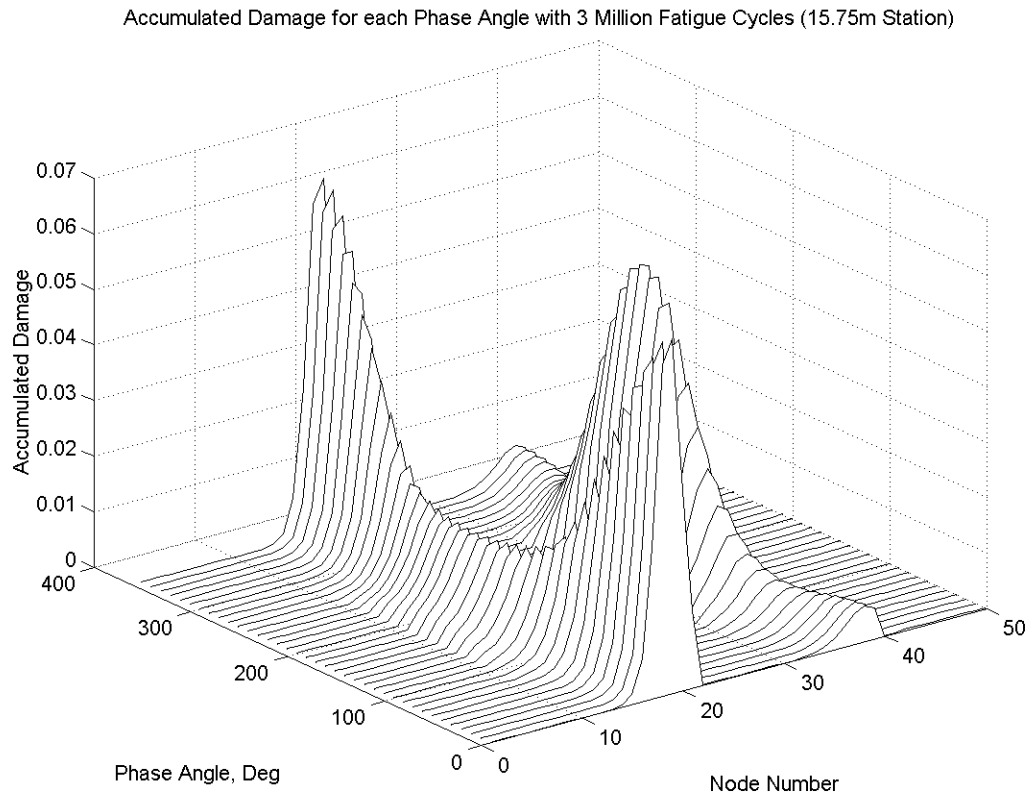
Figure 3-26. Damage as a function of phase angle for 15.75-meter station

These results are summarized for the 0 degrees, 72 degrees and 90 degrees situations in Figure 3-27. As shown, the zero degree phase angle case results in the most damage at node 19 but the 90-degree case results in the most damage at node 33. Clearly, certain phase angles are capable of producing a higher degree of damage than other phase angles at specific nodes.
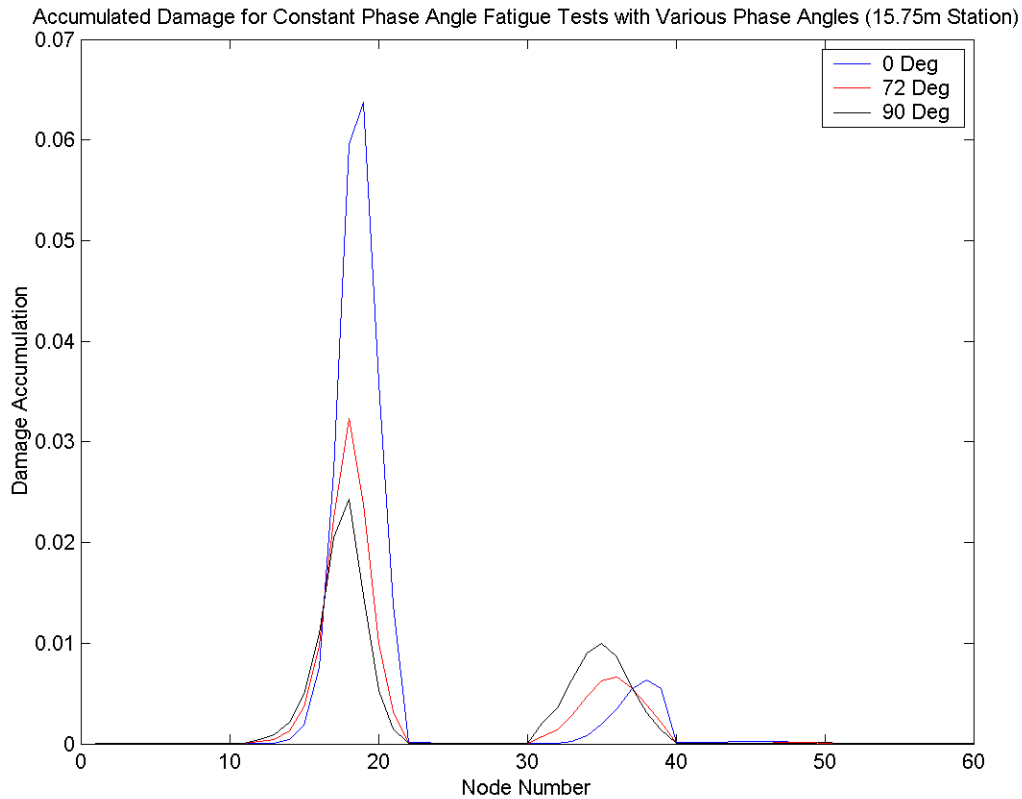
Figure 3-27. Damage for 15.75-meter station

3.5.4 Damage for Constant and Variable Phase Angles

The previous analysis shows that the damage accumulated at each node during a constant phase angle test can vary as a function of the phase angle. The analysis performed earlier shows that the phase angle during typical operating conditions is not constant but approximately Gaussian. To analyze the effect that varying the phase angle during testing could have on the accumulated damage, three phase angle distributions were compared. As shown in Figure 3-28, the three distributions considered for this stage of the analysis were a uniform distribution (equal probability for all phase angles), a Gaussian distribution and a constant phase angle distribution. The uniform distribution has been included because it represents a load case that could be easily tested. The Gaussian distribution is the same as the one derived earlier and represents the closest approximation to actual conditions. The constant 72-degree phase angle distribution represents the baseline and agrees with fatigue tests currently being conducted by NREL.
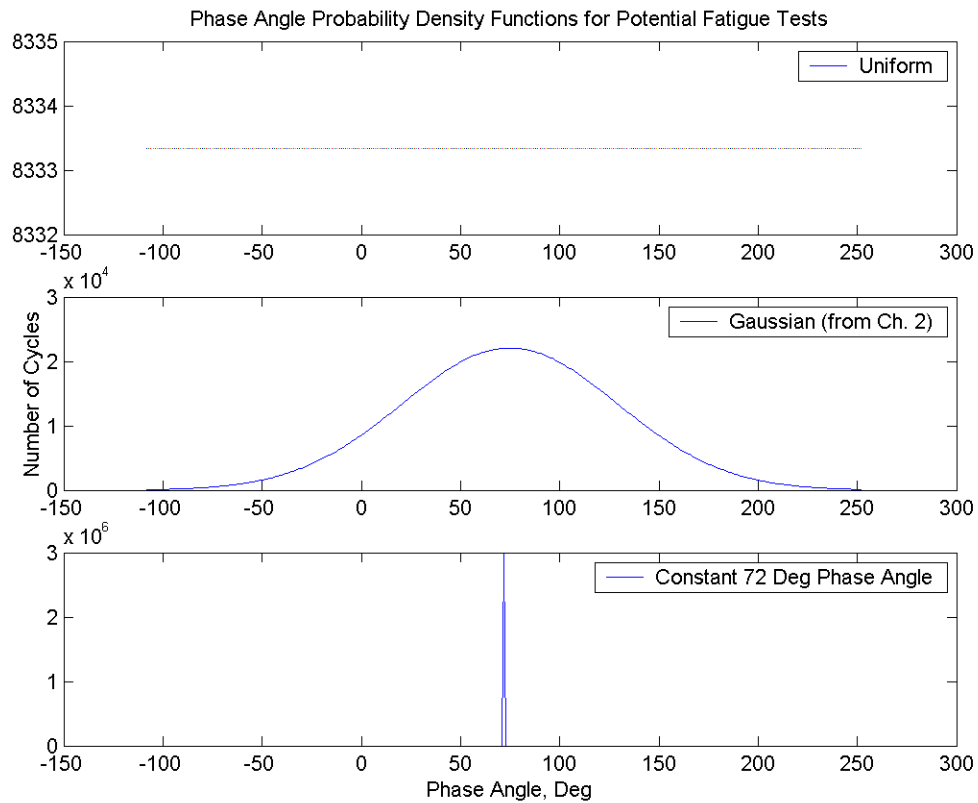
Figure 3-28. Phase angle histograms

When the above distributions are applied to the FEM strain data and distilled using Miner's Rule into an accumulated damage value, it can be seen in Figure 3-29 that the constant phase angle distribution results in the least amount of damage for node 33. The damage around node 19 remains approximately the same for all three cases but the location and magnitude of the second peak changes as a function of the distribution. The uniform distribution results in the highest damage accumulation for the second peak.
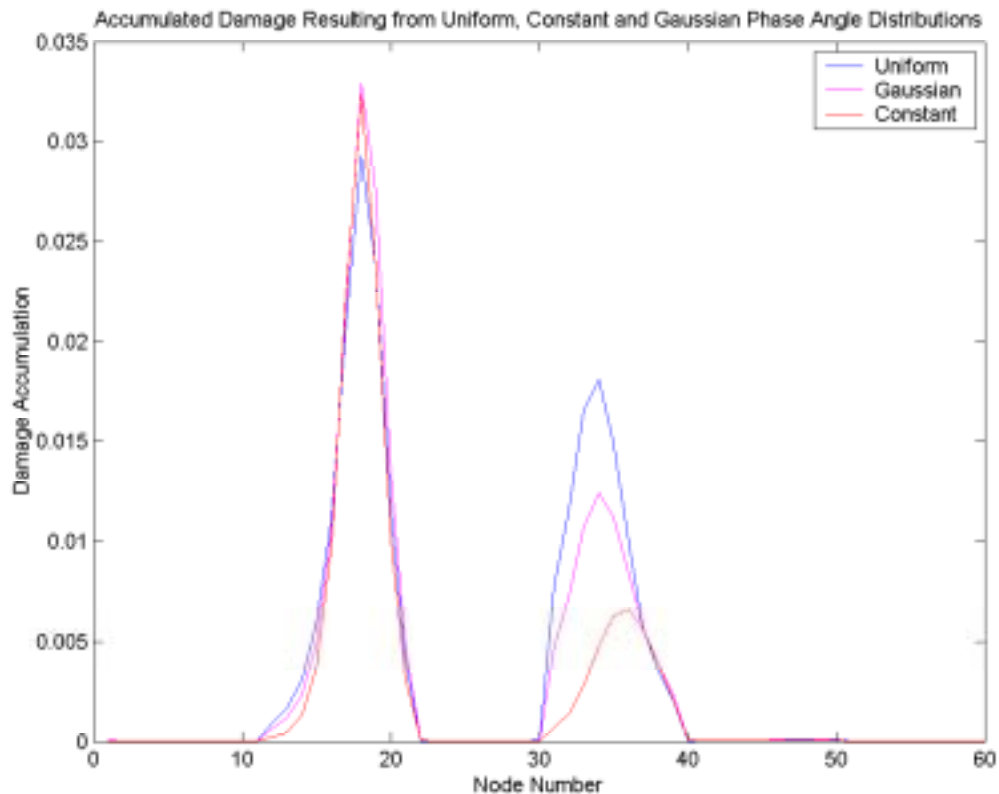
Figure 3-29. Total damage accumulation results from phase angle distributions (15.75m station)

Primarily, it is important to accurately represent operating conditions. While the uniform distribution results in the most damage for the second peak, this distribution does not represent the distribution of phase angles that would be observed during field operation. If the Gaussian distribution is the best representation of the operating conditions, then this analysis indicates that some of the blade is not being accurately fatigued by the constant phase angle tests.

3.5.5 Influence of Material Defects

Up to this point of this analysis, the wind turbine blade properties have been assumed to agree with the ECN standard [84, 85]. Thus, the analysis has assumed that the blade has been built exactly as designed. However, one of the primary purposes of performing a fatigue test is to find any flaws in the blade design or construction that may exist. In order to evaluate the influence that varying the phase angle during testing could have on a blade with a hidden manufacturing defect, defects were artificially added to six nodal locations. As shown in Figure 3-30, the material defects are arranged around the blade profile at the 15.75-meter blade station. In each case, Miner's Rule was used to calculate the damage accumulation.
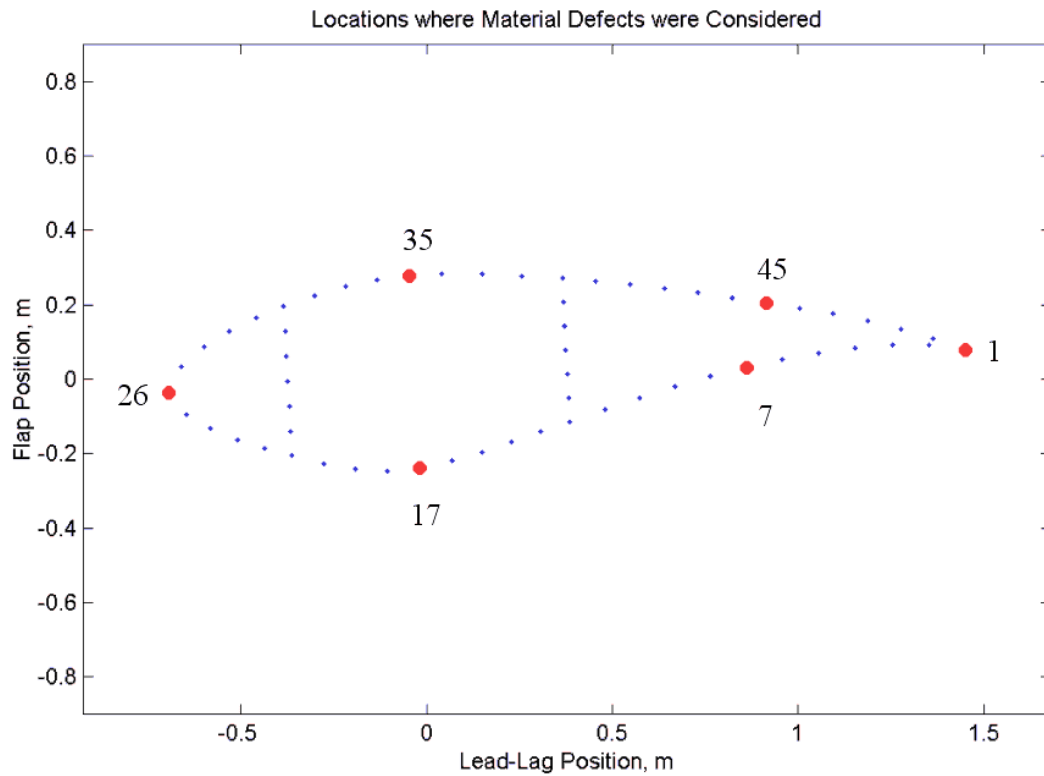
Figure 3-30. Locations of material defects

In each case, a stress concentration factor of 2.0 was used to represent the material defect [111]. This value is based on material testing conducted at Montana State University. As shown by Figure 3-31, the damage accumulation at each node is highly influenced by the phase angle. The material defect located at node 1 (trailing edge) also has a significant influence on the maximum damage accumulated. For this defect location, a phase angle of approximately 150 degrees will result in the maximum damage accumulations.

Accumulated Damage for each Phase Angle with Material Defect at Trailing Edge (15.75m Station)
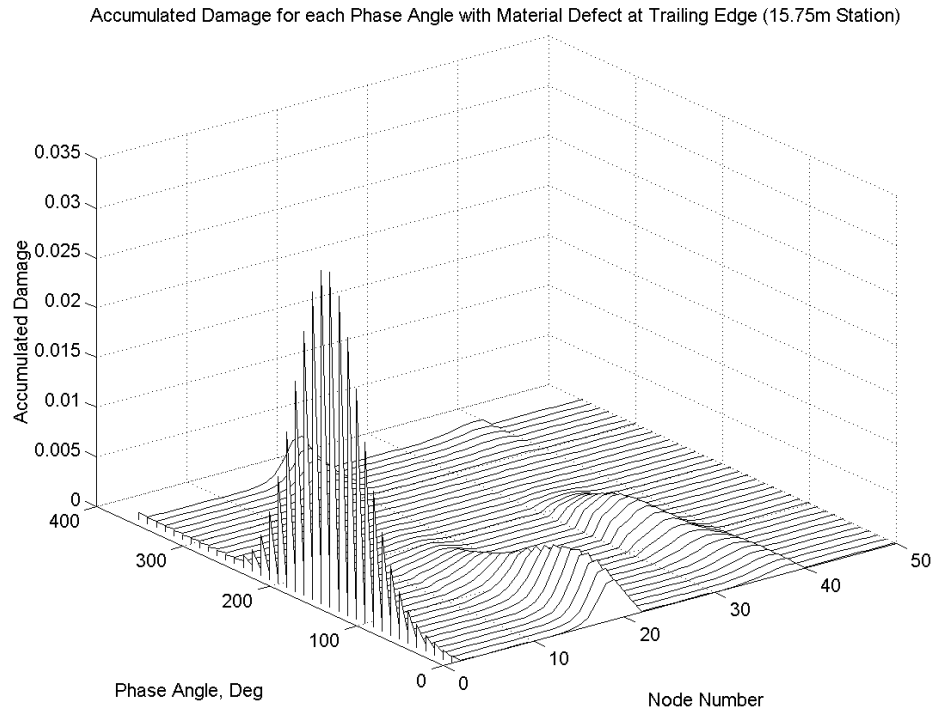
Figure 3-31. Damage as a function of phase angle with material defect at node 1

In Figure 3-32, the damage accumulation for a material defect located at node 7 results in a similar distribution as for a material defect at the trailing edge. The maximum damage at node 7 also occurs for a phase angle of approximately 150 degrees but unlike the node 1 material defect, the increase in damage is not sufficient to dominate the total damage.
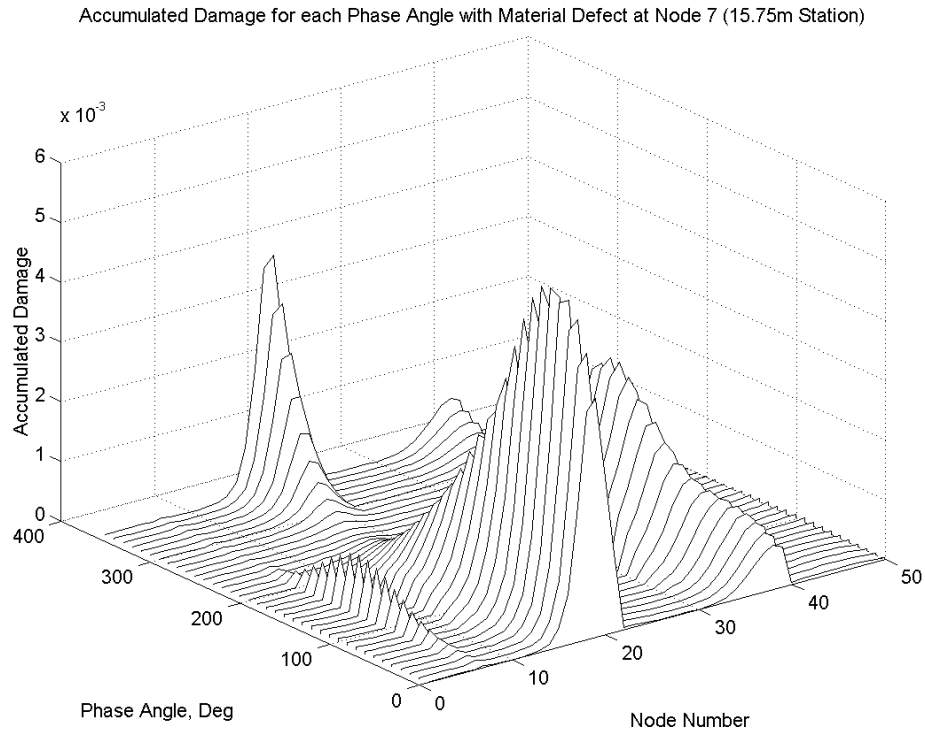
Figure 3-32. Damage as a function of phase angle with material defect at node 7

The defects occurring on the aft skin nodes each showed a similar dependence on phase angle. The defect occurring at node 17 (composed of spar material) does not share these properties. Change in the magnitude of the maximum damage is much greater. The damage accumulation at node 17 when a defect is present dwarfs the damage accumulation at all other locations. Additionally, the phase angle that results in the maximum damage is approximately 50 degrees, which is a significant change from the 150-degree phase angle that produced the maximum damage for defects at nodes 1 and 7.

Accumulated Damage for each Phase Angle with Material Defect at Node 17 (15.75m Station)
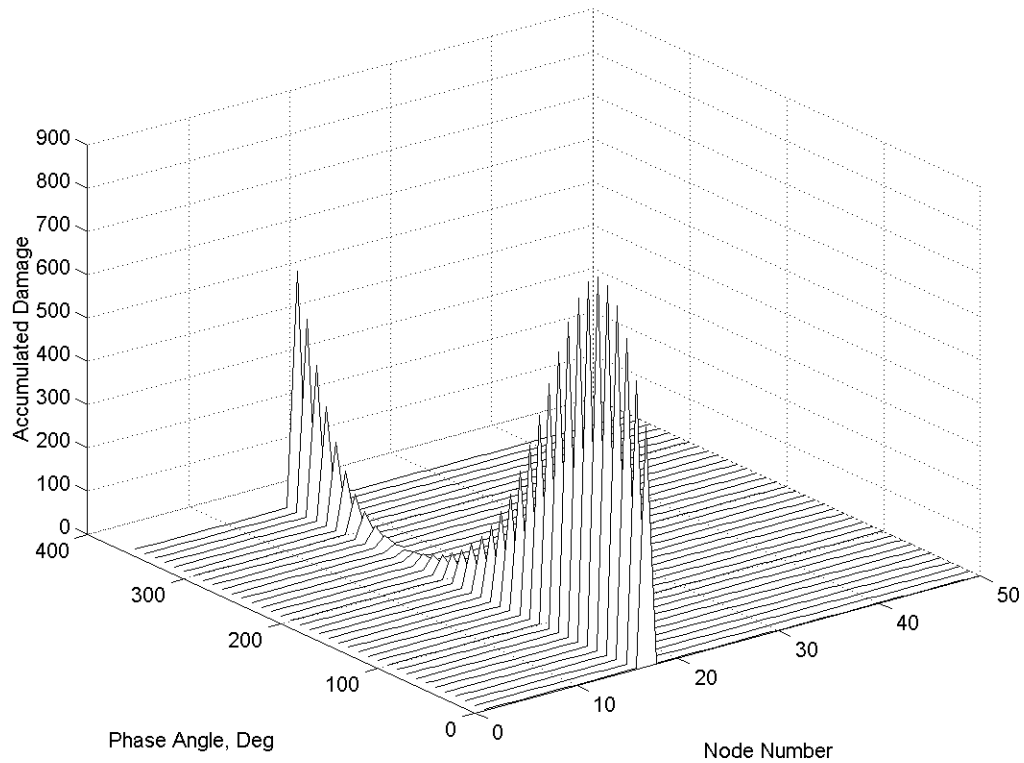
Figure 3-33. Damage as a function of phase angle with material defect at node 17

In contrast to the results for a material defect at the trailing edge, a material defect on the leading edge (node 26) results in a minimal damage accumulation, as shown in Figure 3-34. The phase angle resulting in the maximum damage accumulation also differs from that for the trailing edge. A phase angle of approximately 50 degrees results in the most damage at node 26.

Accumulated Damage for each Phase Angle with Material Defect at Node 26 (15.75m Station)
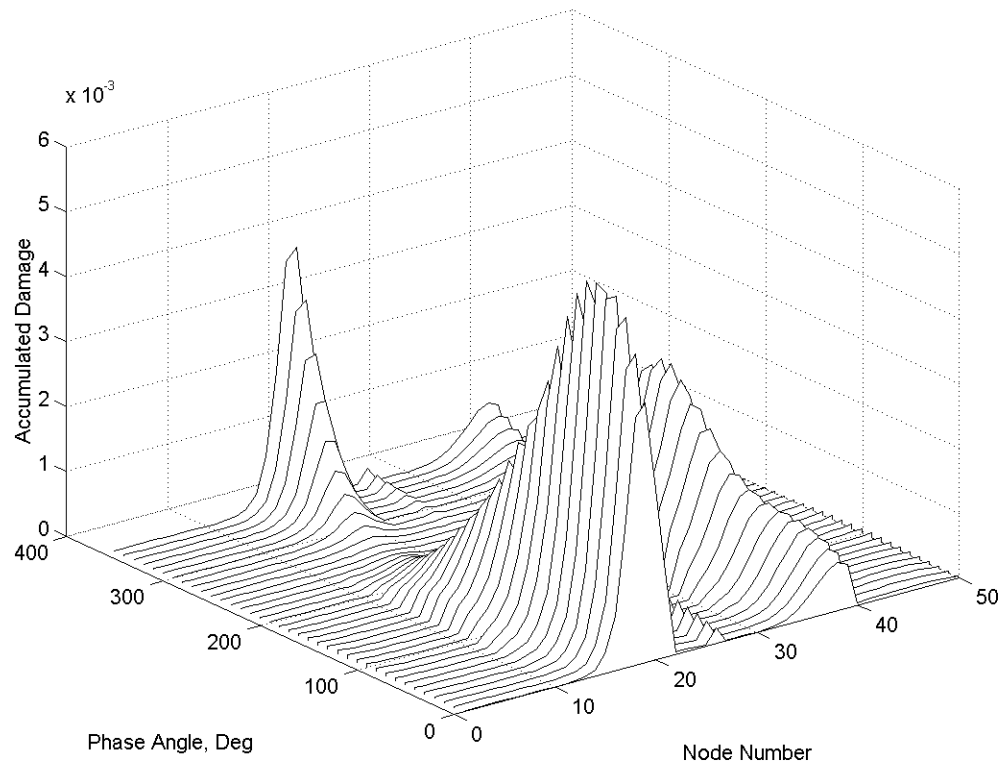
Figure 3-34. Damage as a function of phase angle with material defect at node 26

The damage accumulation for a defect on the upper spar material (node 35) has similar properties as the results for the lower spar material (node 17). As shown by Figure 3-35, a defect in node 35 results in relatively high damage values. Unlike the lower spar material, a defect in the upper spar has a maximum damage for a phase angle of approximately 150 degrees.

Figure 3-35. Damage as a function of phase angle with material defect at node 35

A material defect on the upper aft panel produces the most unique results, shown in Figure 3-36. The damage accumulation is significant compared to the damage at other nodes. The phase angle that results in the maximum damage for a defect at node 45 occurs at approximately 20 degrees in contrast to the other nodes considered.

Accumulated Damage for each Phase Angle with Material Defect at Node 45 (15.75m Station)
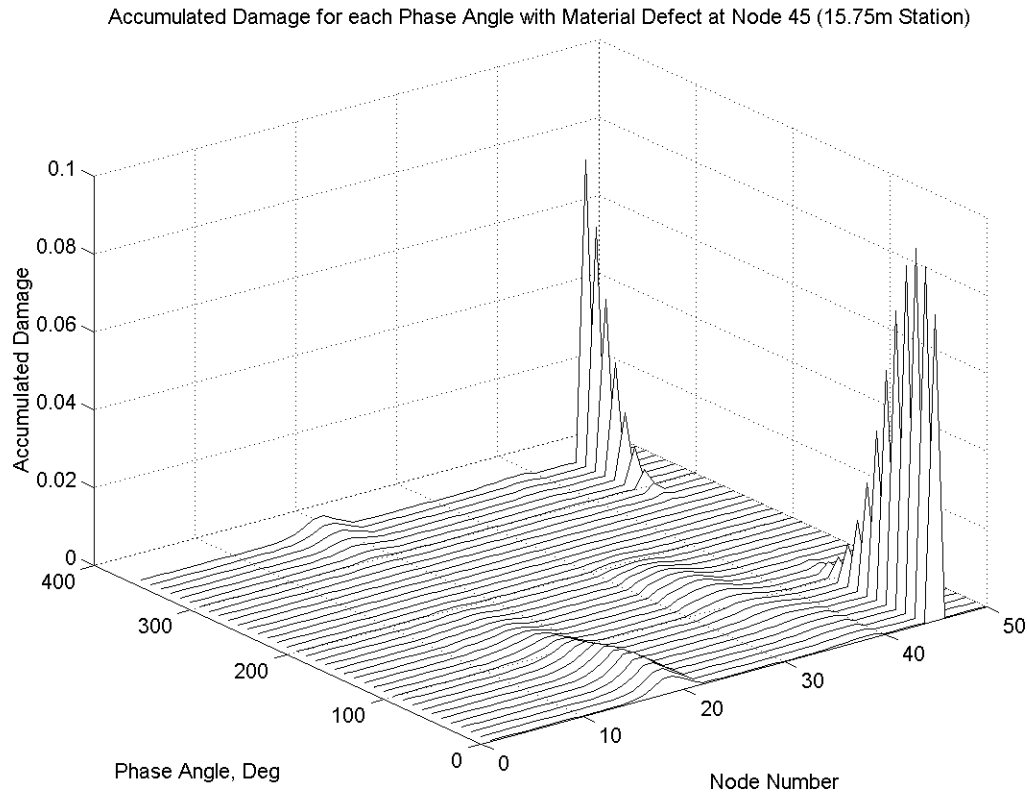
Figure 3-36. Damage as a function of phase angle with material defect at node 45

Observing how a material defect influences the damage accumulation of a particular node is important for understanding the underlying problem. However, of more importance for this analysis is the question of how the damage accumulation is affected by varying the phase angle when material defects are present. As shown by previous sections in this chapter, the constant phase angle fatigue test produces different strain and damage values at each node than the considered Gaussian distribution fatigue test. By applying the Gaussian distribution to the damage values for each defect and comparing that to the constant phase angle results, the relationships shown in Figure 3-37 have been derived. As shown, a varied phase angle test produced a significant change in the expected life compared to the constant phase angle test. In five of the six node locations, the damage was substantially higher for the varied phase angle test. This indicates that the varied phase angle test has a higher probability of finding a material defect than the constant phase angle test. In one case, the constant phase angle test results in higher damage.
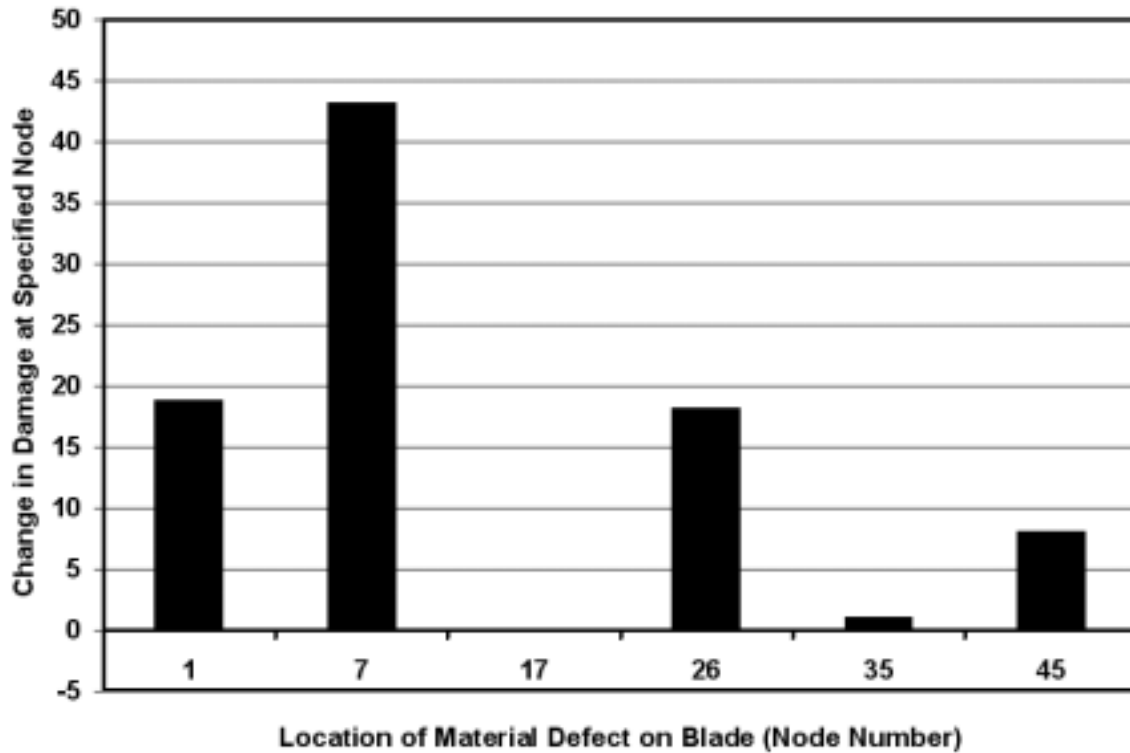
Figure 3-37. Effect of fixed and varied phase angle distributions on damage when a material defect is present

In general, a varied phase angle test seems to increase the probability of finding material defects on a blade during testing. Since one of the advantages of using full-structure fatigue testing over finite element modeling is the ability to find construction defects not present in computer models, it would be advantageous to employ varied phase angle testing.

3.6 Summary

For this analysis, a 3-D finite element model of a 1.5 MW wind turbine blade has been used to calculate the expected life of the blade under various testing conditions. The consequence of testing the blade with various constant phase angles have been analyzed and it has been determined that testing at certain phase angle can influence the time and location of a failure. A Gaussian distribution has been derived using data from the WindPACT program and used as part of a damage fatigue analysis. The fatigue results from using the Gaussian distribution have been compared to the current constant phase angle method. This comparison shows that the constant phase angle test may not accurately fatigue the blade at some locations and that the varied phase angle test is more likely to find defects at various locations around the airfoil.

Chapter 4. Non-linear Fatigue Damage Analysis

This chapter evaluates the effects on the fatigue life of a target wind turbine blade using a non-linear damage accumulation model. The non-linear model is required to evaluate the influence of sequence effects on fatigue damage. For this analysis, a non-linear damage accumulation model has been derived. The parameters for the model have been determined by curve fitting material test data that is part of the material database maintained by Montana State University for the Department of Energy. Since a fatigue test may be conducted in a number of different ways, it is important to evaluate how each method influences the accumulation of damage. For the analysis discussed in this chapter, the overall phase angle distribution is the same for each case when compared over the entire length of the fatigue test. Based on this analysis, changing the order in which the loads are applied to a test specimen has a substantial effect on the degree of damage accrued during a fatigue test and this effect must be taken into account when fatigue testing is performed.

4.1 Non-linear Damage Model

Since Miner's rule [64] is a linear model of the damage, it is not capable of accounting for sequence effects. It has been experimentally determined that applying loads in a high-low order or a low-high order will cause failure at different rates [94]. A non-linear damage model that is suited to this type of testing is required. The variety of possible failure and failure modes do not lead to the use of a failure specific damage model although failure specific modes are used to analyze damage in other cases [112, 113]. As such, a phenomenological model based on crack propagation theory was derived for this study. Once a model was successfully derived, its parameters were determined using the material properties database maintained at Montana State University [94]. The crack growth model is described by Figure 4-1 and Equation 4.1 (Paris Equation) [114]. Using Paris's Equation to represent the cumulative fatigue damage of composite materials is not new. Experimental studies conducted by Radon and Wachnicki [115] indicates that Paris's Equation is an effect method for predicting crack propagation in composite materials. Boniface and Ogin also applied Paris's Equation to the fatigue growth of transverse ply cracks [116].

4.1.1 Derivation
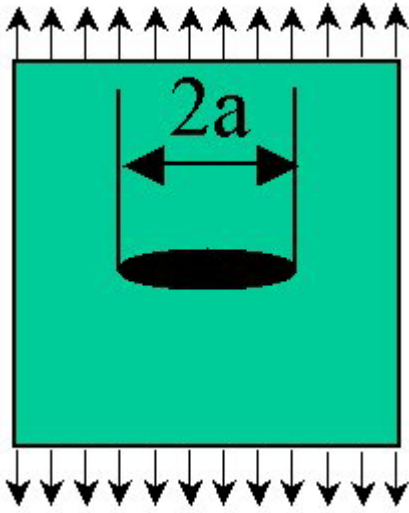
Figure 4-1. Crack length model

$$K = \sigma\sqrt{\pi a}$$

$$\frac{da}{dN} = CK^m \qquad (4.1)$$

Where,

K = Stress Intensity Factor
a = ½ Crack Length
N = Number of Cycles
m = Model Parameter
σ = Applied Stress
C = Model Parameter

In this case, the material is considered to have failed when the stress concentration factor amplifies the applied stress to equal the residual strength. The first step in deriving the model was to solve Equation 4.1 to explicitly have the stress concentration factor as a function of the number of cycles. Combining the two parts of Equation 4.1 results in the following non-linear differential equation shown by Equation 4.2.

$$\frac{da}{dN} = C\sigma^m \pi^{m/2} a^{m/2} \qquad (4.2)$$

Applying separation of variables to solve for the crack length as a function of the number of applied cycles results in Equation 4.3.

$$a(n) = \left[\left(1 - \frac{m}{2} \right) C\sigma^m \pi^{m/2} n + C_2 \right]^{\frac{2}{2-m}} \qquad (4.3)$$

By substituting the crack growth equation back into Equation 4.1, the stress concentration factor can be expressed explicitly as a function of the number of cycles. The constant of integration from Equation 4.3 has been combined with other terms and renamed to C_3 for Equation 4.4.

$$K(n) = \left[\left(1 - \frac{m}{2} \right) C\sigma^2 \pi n + C_3 \right]^{\frac{1}{2-m}} \qquad (4.4)$$

This equation can be simplified by grouping the model parameters and constants as shown by Equation 4.5.

$$K(n) = A\sigma^{2V} n^V + B \qquad (4.5)$$

Where,

$$A, B, V = \text{Model Parameters}$$
$$n \quad = \text{Number of Cycles}$$
$$\sigma \quad = \text{Applied Stress}$$
$$K \quad = \text{Stress Concentration Factor}$$

Typically, residual strength damage models are expressed in the form shown in Equation 4.6. The residual material strength varies from an initial value to final value as a function of the number of cycles applied. The function f(n) varies from zero at the beginning of the test to one at the time of failure.

$$S_r = S_0 - (S_f - S_0)f(n) \qquad (4.6)$$

For Miner's rule, the function f(n) is described by Equation 4.7.

(Miner's Rule) $$f(n) = \frac{n}{N} \qquad (4.7)$$

Where,

$$n = \text{Number of Applied Cycles}$$
$$N = \text{Number of Cycles at Failure}$$

The accumulated damage is calculated by summing the function f(n) for each applied stress level.

For the non-linear residual stress model, the stress concentration factor was used to derive a damage accumulation function. By dividing the stress concentration function (Eq. 4.5) by the critical stress concentration factor, the following expression, Equation 4.8, is derived.

$$f(n) = \frac{An^V + B}{AN^V + B} \qquad (4.8)$$

From Equation 4.5, it can be seen that the term B is approximately equal to one. Since the system in the problem is subject to high cycle fatigue, the number of cycles to failure, N, will have an order of magnitude of approximately one million. As such Equation 4.8 can be approximated by Equation 4.9. The damage accumulation model derived here coincides with the Marco-Starkey damage accumulation model [117], which is commonly used to describe damage accumulation for composite materials [118 - 120].

$$f(n) = \left(\frac{n}{N}\right)^V \qquad (4.9)$$

Where,

$$V = \text{Model Parameter}$$

The parameter V has been determined using the material database maintained by Montana State University for the Department of Energy. The material used for this analysis is designated as DD16 and is a typical material currently used in the construction of wind turbine blades. This material is composed of an E-glass and polyester matrix in a lay-up of $[90/0/\pm45/0]_s$ with a fiber volume fraction of 0.36. Coupons of the material were tested by Montana State up to 10^{10} cycles. Curve fitting this material fatigue test to the specified residual strength model results in a model parameter of V [94]. The experimental results show a very large amount of scatter but the parameter can be bounded between 0.265 and 1.0.

4.2 Comparison to Miner's Rule

The initial and final residual strengths of the non-linear model and Miner's Rule are the same. The difference between the two methods occurs in how the residual strength varies between the initial and final values. As shown in Figure 4-2, the strength for the non-linear model initially decreases at a faster rate than Miner's Rule but near the end of the material life, the rate of strength degradation is at a slower rate. The plot below uses a value of 0.74 for the model tuning parameter.
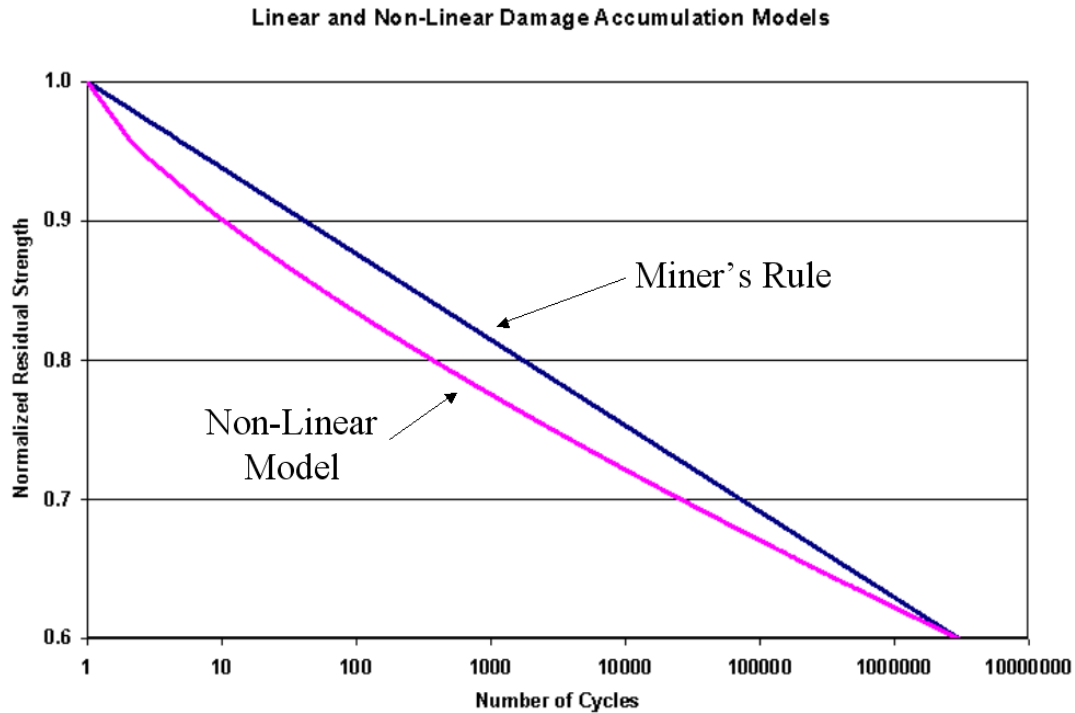
Figure 4-2. Residual strength for miner's rule and non-linear model

While the two damage models may appear closely related, the non-linear model should be more accurate since it is based on an interpretation of more fatigue samples. More importantly, the non-linear model is capable of capturing the effects of load sequence.

4.3 Load Sequence Effects

For constant phase angle fatigue tests, there are no load sequencing effects because the strain history at each location is the same for all cycles. Varying the phase angle throughout a fatigue test will result in variations in the time histories and load sequence can be a factor. Since load sequencing is believed to effect damage accumulation, the situation was studied as part of this analysis. As shown later in this chapter, the effects of the load sequence can be significant.

4.3.1 Proposed Phase Angle Progression

Since Miner's Rule is not sensitive to the effects of load sequence, it has been possible to use the Gaussian distribution in the previous chapter for any analysis up to this point. However, there are an infinite number of sequences that result in the same Gaussian distribution used above. For most of the load sequence analysis, the phase angle progression shown by Figure 4-3 was used. Since this progression has been derived from the Gaussian distribution, a histogram of the progression will result in the original Gaussian distribution. To generate this progression, the Gaussian distribution was multiplied by the total number of cycles in each sequence. Since the Gaussian distribution was originally normalized for an area of one, this amplification generates a

87

progression of the correct length. The progression array is then created by dwelling on each phase angle for the number of cycles specified by the amplified Gaussian distribution. This progression represents the smoothest and most implemental array that can be created from the Gaussian distribution. An additional advantage of this progression is that for a specified number of total cycles, this progression has a unique time history.
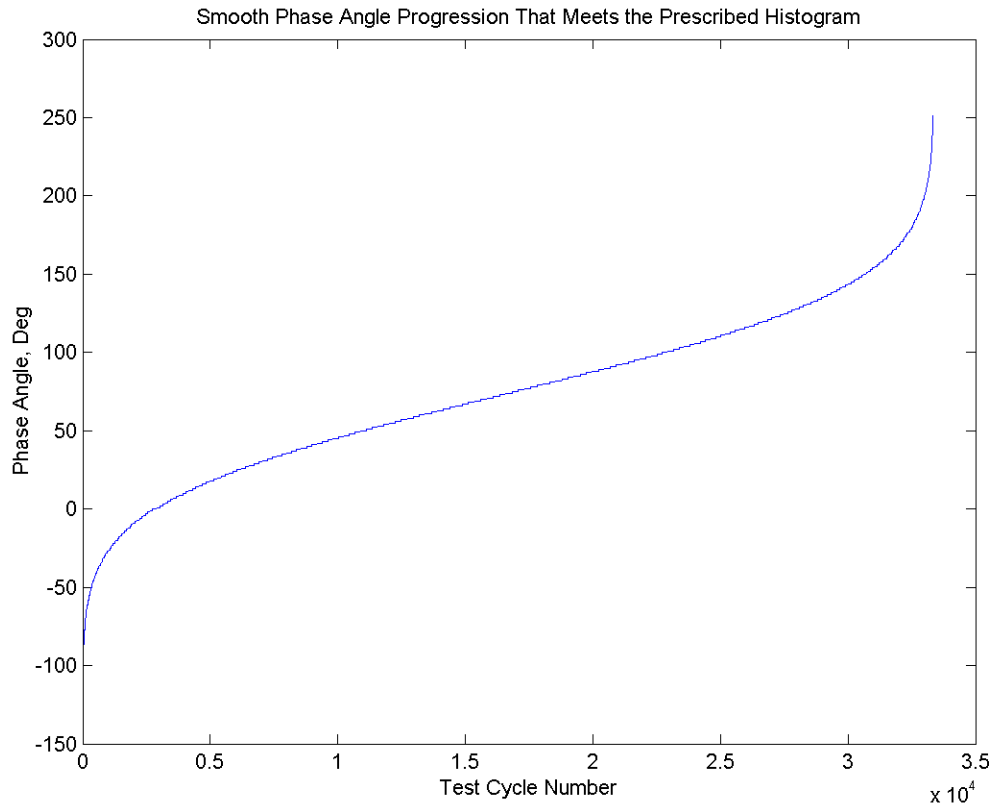
Figure 4-3. Proposed phase angle progression for each sequence

4.3.2 Effect of the Number of Repetitions

The number of cycles in a phase angle progression can be adjusted based on the number of times the repetition will be repeated. For example, if the phase angle progression will be repeated only once, the progression will contain 3-million cycles. If a progression will be repeated 10 times, each progression has 200,000 cycles, as shown by Figure 4-4. The number of times that a particular progression is repeated is of particular interest because these results may be easily verified by future testing. This analysis is intended to determine if there exists a specific number of repetitions that is most damaging and how much of an effect increasing/decreasing the number of may have on the total damage.
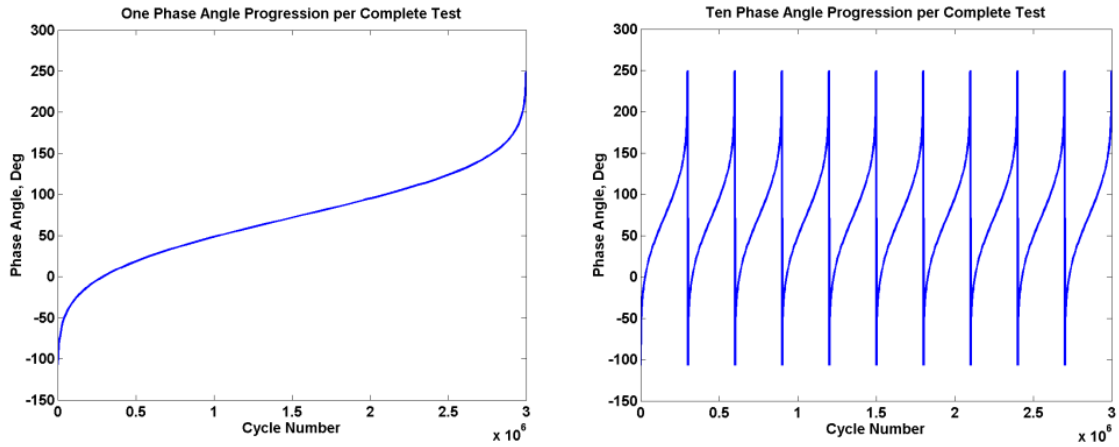
Figure 4-4. Comparison of one to ten load phase angle progressions

As discussed above, Miner's Rule is not capable of demonstrating the effects of load sequencing. Since this is an important consideration, this fact is further demonstrated by Figure 4-5. As shown below, the Miner's Rule is not capable of calculating the effects of load sequence.
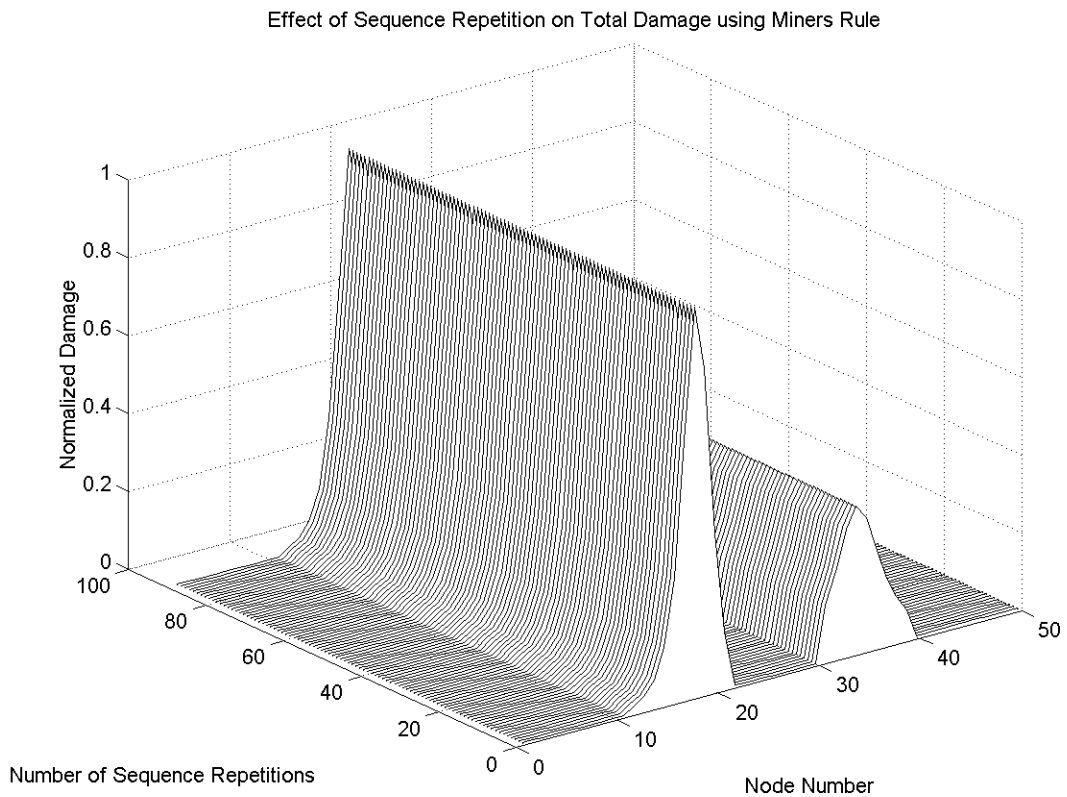
Figure 4-5. Effect of sequence repetition using Miners Rule

When the non-linear damage model is used, the effects of increasing the number of progressions become clearer. As shown by Figure 4-6, increasing the number of progression repetitions results in higher degrees of damage. Increasing the number of repetitions becomes less significant when the number of repetition is already large.
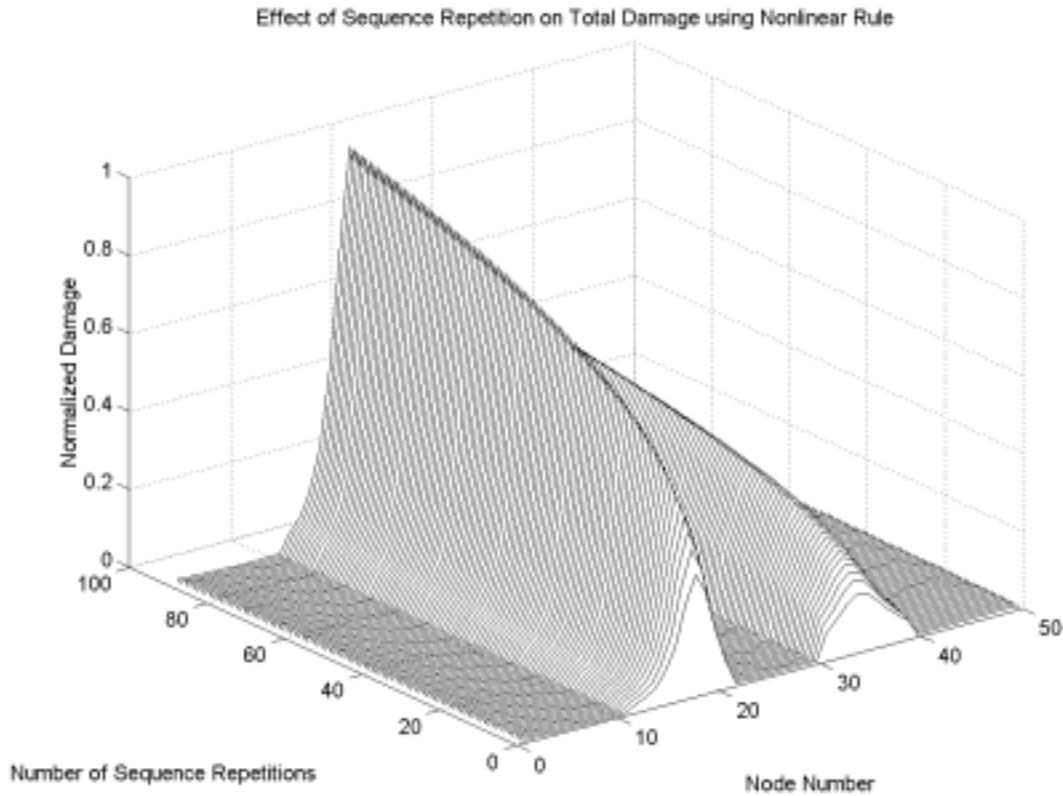
Figure 4-6. Effect of sequence repetition using non-linear model

The maximum damage continues to increase as the number of repetitions increase. As shown in Figure 4-7, the damage for 7300 repetitions is much higher than that for 100 repetitions. The profile of damage around the blade profile is generally unaffected by the number of phase angle sequence repetitions.
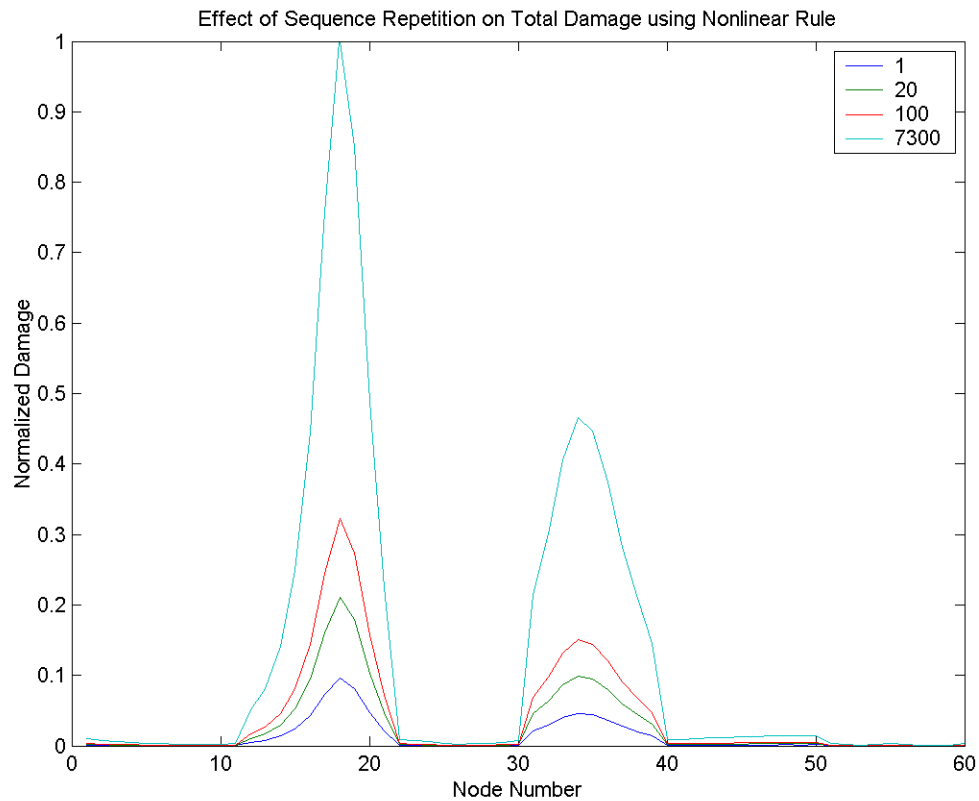
Figure 4-7. Damage accumulated for various numbers of sequence repetitions

Since the shape of the damage profile around the airfoil is not dependent on the number of sequence repetitions, the relationship between the maximum damage per repetition will be separately analyzed. As shown in Figure 4-8, the maximum damage monotonically increases as a function of the number of phase angle sequence repetitions.
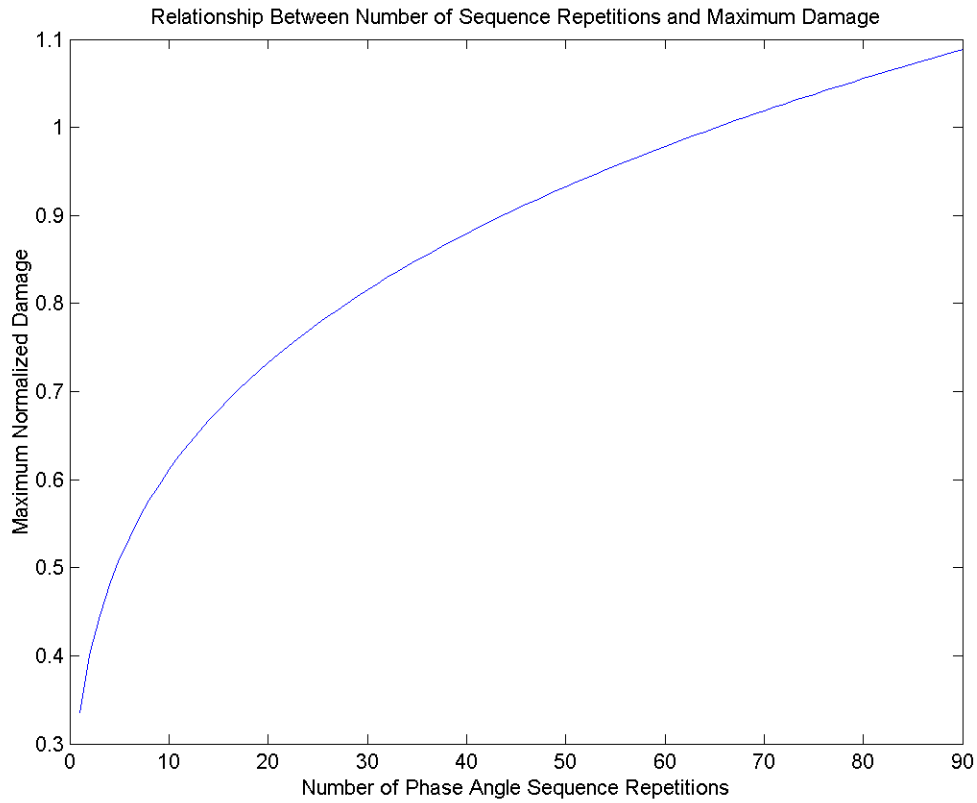
Figure 4-8. Maximum damage as a function of the number of repetitions

In an effort to further understand the relationship between the damage and the number of sequence repetitions, the data was curve fitted. Based on the shape of the function, a power equation was used. As shown by Equation 4.10, the damage occurring for any specified number of repetitions can be calculated based on the damage occurring for one repetition. The R-squared value for the function below was 1.0. It should be noted that the exponent for function 4.10 is equal to one minus the exponent used for the non-linear model. Since the number of sequence repetitions is inversely proportional to the number of cycles consecutively applied at a specific load, it makes sense that the exponent relating the damage to the number of repetitions is indirectly proportional to the exponent used for Equation 4.9.

$$D_R = (D_1)(R^{0.26})$$ (4.10)

Where,

R = Number of Sequence Repetitions
D_x = Damage for x Repetitions

As discussed earlier, the uncertainty for the exponent used in Equation 4.9 is large. For the purpose of this analysis, a value of 0.74 has been assumed for the exponent. Since the range of valid exponents is 0.26 to 1.0, the influence of sequence effects on damage is subject to a large range. Assuming 100 sequence repetitions, the accumulated of

92

damage at a specific location can vary from 1.0 for Miner's Rule (1.0 exponent) to 30.0 for an exponent of 0.26.

Results indicate that the more progressions that are used to achieve a given number of fatigue test cycles, the greater the damage will be. However, it is not realistic to vary the phase angle progression too quickly. The maximum number of repetitions that will achievable can be achieved will be dictated by the stability of the test system.

4.3.3 Upper and Lower Damage Bounds

The number of times the phase angle sequence is repeated for a given number of cycles has been shown to influence on the test results. However, the manner that the phase angle progresses through the sequence also has an effect. Originally, an optimization routine was to be used to determine the most damaging phase angle sequence but after the formulation of the optimization problem, it was determined that there was no unique solution. Two solutions are shown by Figure 4-9.
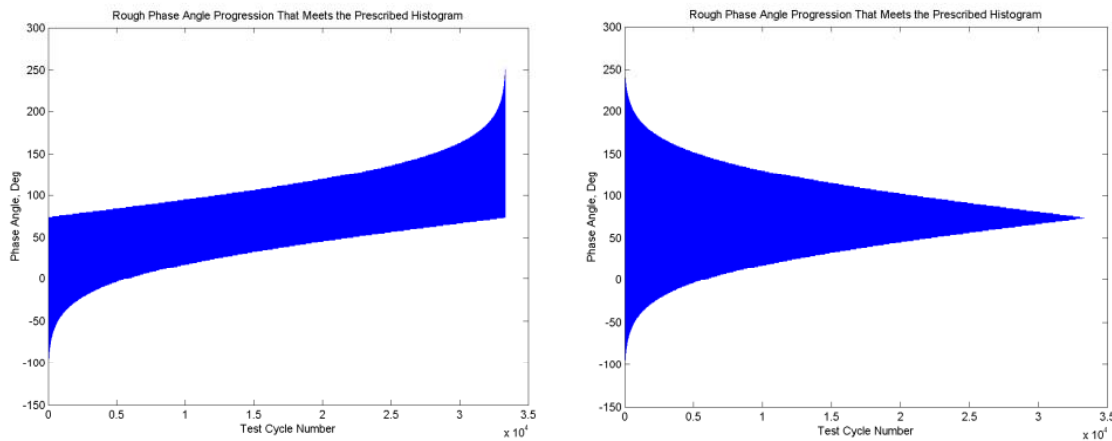
Figure 4-9. Most damaging phase angle progressions

Any phase angle progression that never repeats the same phase angle for two consecutive cycles and has a histogram that agrees with the Gaussian distribution from the previous chapter is a valid solution to the optimization problem. While it would be possible to add additional criteria that may result in a unique solution, such an analysis would provide no additional information. None of the most damaging phase angle sequences can be realistically employed on an actual test since the dynamic stability and accuracy of the test would be compromised. As such, this analysis can only be used to define the boundaries of the effects for the phase angle sequences. The phase angle sequence resulting in the least amount of damage will be the one shown in Figure 4-3 since this sequence has the maximum number of repetitive cycles at any given phase angle. The change in damage resulting from the most damaging sequences (Figure 4-9) and the least damaging sequence (Figure 4-3) can be seen in Figure 4-10. The change in the maximum damage is significant, with a factor of approximately 4.5 between the two cases.
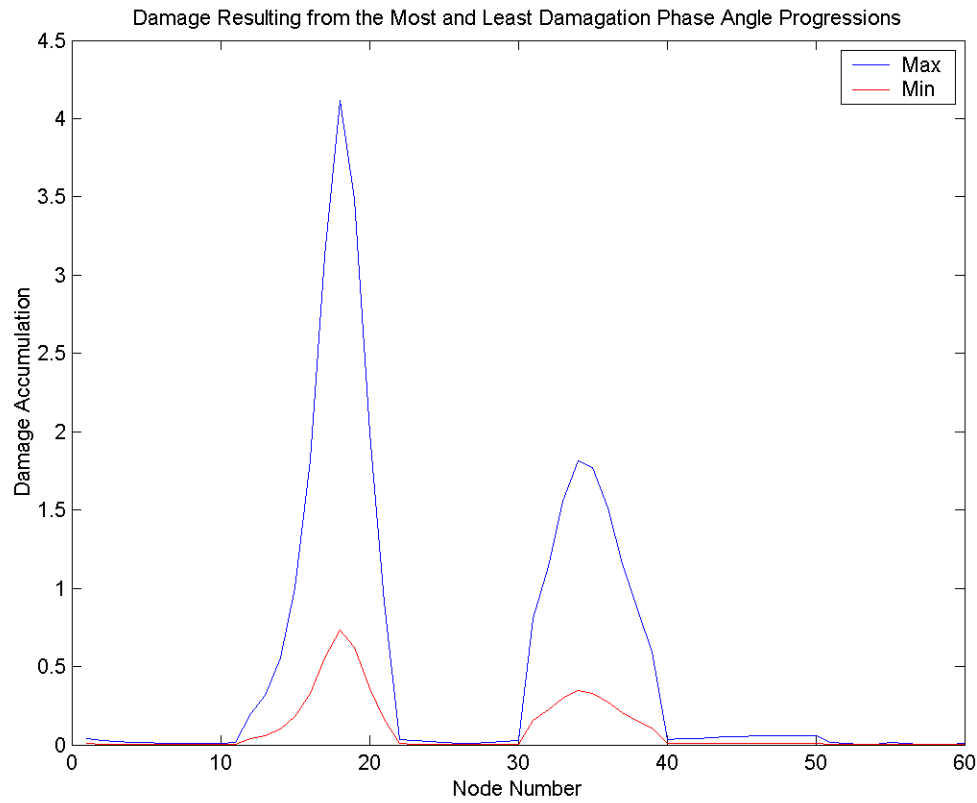
Figure 4-10. Max and min boundaries for the phase angle sequences

While the most damaging test case would normally be considered the most conservative case for testing a sample that cannot be achieved in this case. In this case, it is recommended that the least damaging sequence be used for testing but that the flap and lead-lag force magnitudes are increased to result in the same accumulated damage that would be generated by the most damage sequence.

4.4 Summary

A non-linear model has been derived to analyze the effects of load sequencing. The relationship between the number of sequence repetitions to achieve a given number of cycles and the total damage accumulation has been determined. Increasing the number of sequence repetitions will increase the amount of damage achieved. The effects of phase angle sequencing are predicted to be significant and should be accounted for during testing. Since the analysis conducted here indicates that sequencing effects are so significant, an experiment validation of these results should be conducted.

Chapter 5. Wind Turbine Blade Fatigue Testing Methods

This chapter describes three methods for fatigue testing wind turbine blades. The National Renewable Energy Laboratory (NREL) currently uses a common dual-axis forced-displacement method. Some other research institutes use a single-axis resonance excitation method. A new method that combines the best properties from the forced-displacement and resonance excitation methods has been evaluated, designed and built as part of this research project. The new test system is capable of accurately reproducing the results of the forced-displacement test system while reducing the energy required to performed a full-scale fatigue test on a wind turbine blade by over 60%. The new system is unique in that it is the first test system to ever apply excitation forces using resonance excitation and forced-displacement methods simultaneously. To maximize energy savings, the flap displacements will be controlled using the resonance excitation method but the edge displacements will be controlled using the forced displacement method. Prior to the research conducted for this project, it was thought that a combination of the two test methods was impossible because of issues with dynamic stability. The analysis in this and the following chapters show that the system is possible. Further, the system has been constructed and successfully tested. The results of which are shown in chapter 7. The new system will substantially reduce test durations, reduce test costs and will provide more accurate results than either of the existing test systems.

5.1 Overview of Testing Methods

Many of the latest technologies have been used in the design and analysis of wind turbine blades. Finite element models of the blades have been constructed to analyze the theoretical life expectancy for wind turbine blades before they are built [121]. Dynamic models using programs such as ADAMS and FAST have been created to simulate the blade's real-time response to wind conditions over the life of the blades [122]. Wind tunnel tests have been conducted to optimize the blade shape to capture the most energy [123]. Data have and continue to be collected from operating wind turbines in field use [124]. However, there is still a need to test wind turbine blades under controlled conditions. By precisely applying fatigue loads to the wind turbine blades, it is possible to compare the results of the actual blade to the finite element model, find manufacturing defects, and accelerate the fatigue test to take months instead of decades.

5.1.1 Test Facilities

There are four laboratories throughout the world that perform static and fatigue testing of wind turbine blades; RISO in Denmark, CRES in Greece, WMC at TU Delft in the Netherlands and NREL in the US. RISO National Laboratories (RISO) operates under the Danish Ministry of Science, Technology and Innovation. Static, fatigue and modal testing of wind turbine blades is conducted at the Sparkaer Blade Test Centre in Roskilde, Denmark. The Centre for Renewable Energy Sources (CRES) operates under the Greek Ministry of Development. CRES has testing facilities located in Attiki, Greece capable of testing wind turbines blades up to 25 meters in length. The Wind turbine Materials

95

and Constructions Knowledge Centre (WMC) is a new facility opening in 2003 in The Netherlands. The facility is a joint project between Delft University and the Energy research Centre of the Netherlands (ECN). This new facility will be capable of testing wind turbine blades up to 60 meters in length. In the U.S., the National Renewable Energy Laboratory (NREL), a Department of Energy Laboratory, is responsible for wind turbine blade testing.

NREL developed a wind turbine blade testing facility in 1989 at its National Wind Technology Center (NWTC). This facility, located in Golden, Colorado, is unique in the United States. More than 100 blades have been tested at this facility. Most of the tests have been conducted for commercial wind turbine manufacturers under various NREL development projects. NREL can currently perform static, fatigue and modal testing of blades up to 30 meters in length. Additional facilities may be created in the near future to test longer blades.

Each of the four test facilities has independently developed methods for performing blade tests. Over time some test methods have been replaced by newer methods and many of the test facilities now use similar equipment and procedures for fatigue testing. RISO performs fatigue tests on blades by applying cyclical loads in either the flap or lead-lag direction using an electric motor that rotates an eccentric mass. The average frequency of the vertical force approximates the first mode resonance frequency in the direction of the test. This test technique will be referred to as the single-axis resonance test for the remainder of this document. NREL, CRES and WMC have invested in hydraulic actuators and equipment to exercise the blades. The hydraulic actuators apply loads at a single spanwise station on the blade in both the flap and lead-lag directions. The technique will be referred to as the dual-axis forced-displacement method for the remainder of this document. For the past couple of years, NREL has been developing a new test method that combines the benefits of resonance excitation with the accuracy of dual-axis testing. This new method, its advantages, analysis and development are described below.

5.1.2 Dual-Axis Forced-Displacement Method

The dual-axis forced loading system, currently used by NREL and other research facilities, employs a servo-hydraulic system with actuators to exercise the blade in the flap and lead-lag directions [29, 68, 125]. Tests are conducted at frequencies well below the blade's first fundamental flap natural frequency. The primary advantage of this system is that biaxial loading creates strain profiles in the test article that more accurately agree with the service conditions, as compared to single-axis tests. The dual-axis test system used by NREL is shown in Figure 5-1.

96

Figure 5-1. NREL's dual-axis forced-displacement test system

While the dual-axis forced-displacement test is the most accurate test currently used to test wind turbine blades, this method has several drawbacks. The forced loading system requires large forces and displacements from hydraulic actuators. Consequently, new actuators must be specially designed and built each time a larger blade is tested. As the actuator size increases, the hydraulic pumping requirements also increase. Consequently, substantial equipment costs are incurred when increasing test capabilities for larger blades. For blade tests, the flap actuator has the greatest requirement for both displacement and force. The lead-lag actuator, which applies its load through the bell crank shown in Figure 5-1, has a lower force requirement, and a smaller displacement due to the higher blade stiffness in the lead-lag direction. These increased flow requirements have also created significant energy costs associated with running a fatigue test. Since the excitation frequency for this test does not equal the resonance frequency, it is possible to create unwanted blade dynamics. In order to mitigate these dynamics and to fit 'longer' blades into the test facility, the tips of the blades are typically removed before testing.

5.1.3 Single-Axis Resonance Method

The single axis resonance test, currently used by RISO, uses an electric motor to spin an eccentric mass in order to excite blade resonance in either the flap or lead-lag direction. Whereas the dual-axis test applied both flap and lead-lag bending moments during a fatigue test, the single axis resonance test applies each component independently in two

separate tests. As a result, this test method is less accurate for predicting blade life but it has several advantages over the dual-axis forced-displacement test. A single-axis resonance fatigue test with forces acting in the flap direction conducted at RISO's facility is shown prominently in Figure 5-2.

Figure 5-2. RISO's single-axis resonance test system

By adding masses to the blade, it is possible to tune the bending moment distribution along the blade length. So the mean and alternating bending moment distributions in the flap or lead-lag direction more closely approximate the actual bending moments for this test. While the added masses lower the system natural frequency, the test cycle frequency remains substantially higher for this method compared to the forced-displacement method. Since the excitation frequency is higher for this method, it takes less time to accumulate a specific number of cycles at a prescribed load level, making it possible to complete fatigue tests faster and to complete more tests per year.

By taking advantage of the displacement magnification that occurs near resonance, the force required to exercise the blade is substantially lower for this system. This results in lower energy consumption. Additionally, the test is conducted at the blade's natural frequency, which makes it possible to test the entire blade without creating unwanted structural dynamics. As a result, the blade tip does not need to be removed before testing. Resonance excitation demonstrates several advantages for larger blades including; lower testing costs, faster results, more efficient use of test space and the ability to test the entire blade. However, the system currently used by RISO has several limitations. As shown in Figure 5-3, the eccentric mass applies forces in the axial direction along the blade in addition to the desired testing direction. As blade become larger the test forces and unwanted axial forces also increase until the axial forces interfere with the accuracy of the test results.
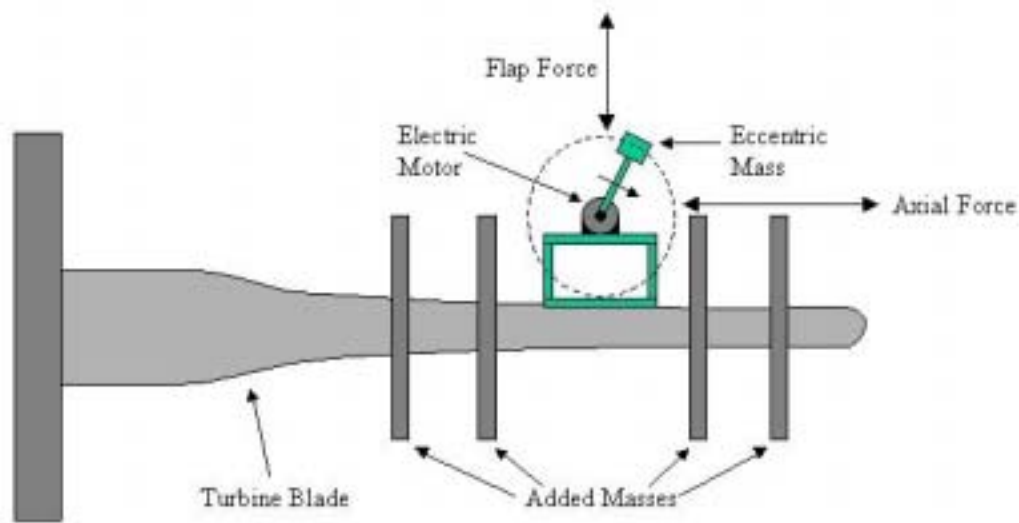
Figure 5-3. Schematic of RISO resonance test system

Since the RISO system uses the rotational speed of the eccentric mass to control the magnitude of the bending moment, the excitation frequency is not constant throughout the test. Without a constant excitation frequency, it is not possible to accurately apply dual-axis loading. The single-axis resonance test system provides a cheaper, and faster method for testing wind turbine blades but it is less accurate than dual-axis test methods may not be suitable for the next generation of large wind turbine blades.

5.1.4 Proposed Dual-Axis Resonance Method

In the proposed method for testing wind turbine blades, as much of the existing NREL test equipment and test experience has been used as possible. The blade will be cantilevered from the existing test stand. The lead-lag force component will be achieved using the same actuators and equipment currently used at NREL (see Figure 5-1). The new test method changes the technique used to apply the flap displacement but uses the same actuator technology and hydraulic equipment that NREL has developed during its wind turbine-testing program. A new control algorithm has been designed to allow the flap and lead-lag displacements to progressively change throughout a fatigue test based on the phase angle analysis conducted in this study. The phase angle progression and the development of the control algorithm will be discussed in later chapters of this text.

While current NREL fatigue tests rely on actuators with greater than 1.5 meters of stroke to apply loads of over 200 kN, the proposed method will use a much smaller actuator to apply a small harmonic force at the resonance frequency of the blade in the flap direction. The actuator will oscillate a steel mass linearly in the flap direction to generate the excitation force. The excitation force will be applied to the blade through a load frame

99

specifically design for this application. Figure 5-4 shows the proposed load frame design with actuator and excitation mass.
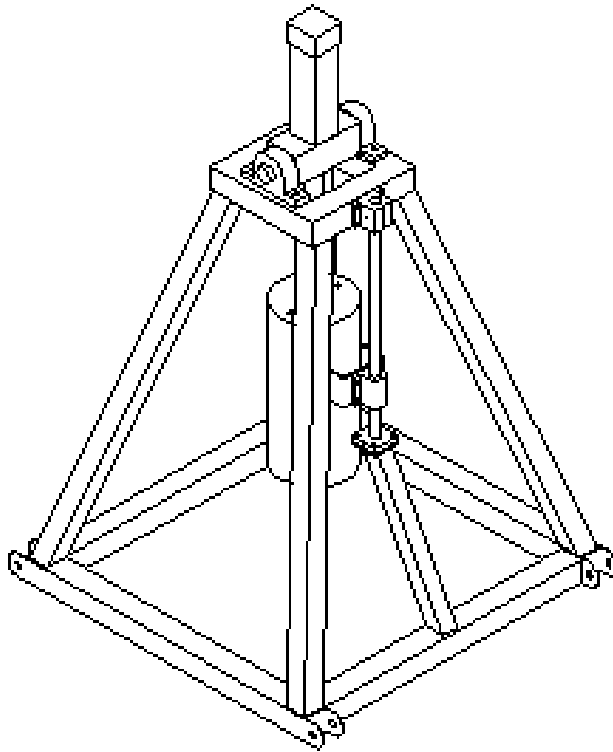
Figure 5-4. Load frame design for hydraulic resonance system

 As shown by Figure 5-5, the load frame assembly will sit on top of the blade during testing. The load frame will be attached to the blade using contoured saddles that clamp onto the blade. Soft rubber mounts are used to compensate for any bending that may occur between the two saddle locations during operation.
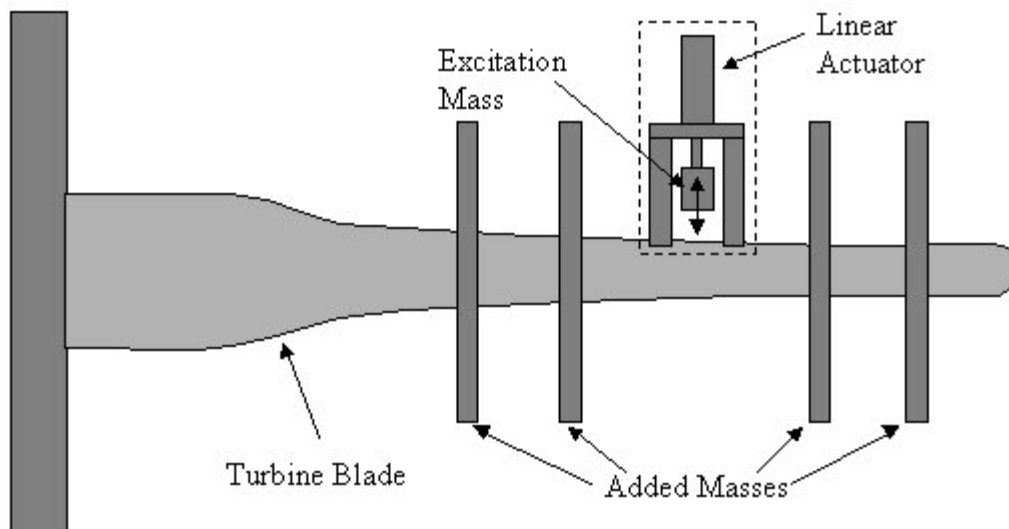
Figure 5-5. Schematic of proposed resonance test system

The control algorithm will change the displacement of the excitation mass to maintain constant blade flap displacements at a fixed control point. Stationary (with respect to the blade) masses will be added to the blade along its span to contour the shape of the bending moment distribution under first mode oscillations to match the desired equivalent damage fatigue load distribution and to pre-load the blade to the proper mean bending moment.

The new system has several advantages over existing test systems. This system uses linear motion only in the direction of blade displacement to apply the forces. Therefore, unwanted loads, such as axial loads, are minimized. Another advantage is that the frequency and magnitude of excitation are decoupled. Control of the excitation force is achieved by varying the stroke of the excitation mass at a constant excitation frequency, chosen to be very near the system's natural frequency in the flap direction. The constant excitation frequency makes it possible to accurately combine the flap resonance system with a forced lead-lag displacement.

Because the flap actuator is responsible for most of the hydraulic flow rate demand, the overall reduction in flow requirements is substantial. This will allow the testing of much longer blades without increasing the flow requirements of the NREL facility. Another big advantage is that the cycle rate of the new hydraulic resonance system will be approximately twice that of the forced-displacement method, allowing a faster turn around time for the facility.

The proposed system can provide a more accurate stress distribution than either the single-axis resonance system or dual-axis forced-displacement system. The new system

requires less energy, less expensive equipment, and less testing time than other dual-axis test methods.

5.2 Dual-Axis Resonance Method Design

To design the dual-axis test method the test blade properties were obtain and then verified experimentally, the mode shapes in the flap direction were calculated using finite element models and the stationary mass distribution was calculated using a steepest decent optimization routine. The stiffness (EI) distribution for a target blade was collected and verified by measuring the stiffness of the blade at the 23-meter station. The damping ratio of the blade was calculated using two methods; the log decrement method and calculated from the area within the hysteresis loop. Two codes were used for the FE calculations; an NREL finite element code called "MODES" [126] and a beam finite element model that I wrote in MATLAB. The two models were essentially the same but it was advantageous to use a model within MATLAB for the purpose of optimizing the stationary mass distribution and then verify the end result using MODES.

5.2.1 Blade Properties

For the target test blade, constant time (and spatially) invariant stiffness (EI) distributions were available in the flap and lead-lag directions. These values were used to create a beam finite element model of the blade that will be presented in the next section. In order to verify that the material properties of the blade are accurately represented, experimental values for the fundamental frequency and damping were measured using traditional methods [127, 128]. Since specific blade properties are proprietary to the blade manufacturer, it will not be possible to show the exact EI distribution or aggregate stiffness values. However, the methods used to verify these values are presented below. The EI distribution was initially verified by experimentally determining the stiffness of the blade at 23-meters. The EI distribution was further verified by calculating the fundamental flap frequency using MODES and experimentally verifying this frequency. The natural frequency was calculated by applying a step input to the blade and performing a frequency analysis on the response. In each case, the theoretical results agreed very closely with the experimental values.

Normalized Step Response for Target Wind Trubine Blade
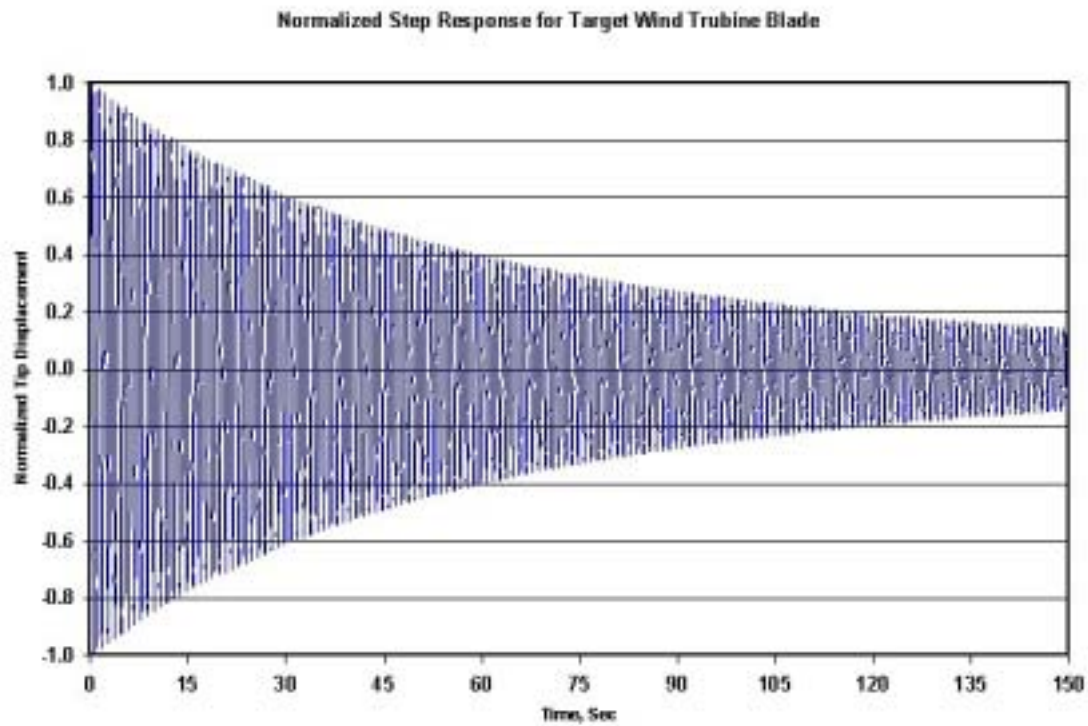
Figure 5-6. Time series for target wind turbine blade step response

The same data were used to confirm the natural frequency and subsequently the EI and mass distributions were used to calculate the damping ratio. First the data were decimated to include only the maximum value per cycle. The reduced data can be seen in Figure 5-7.
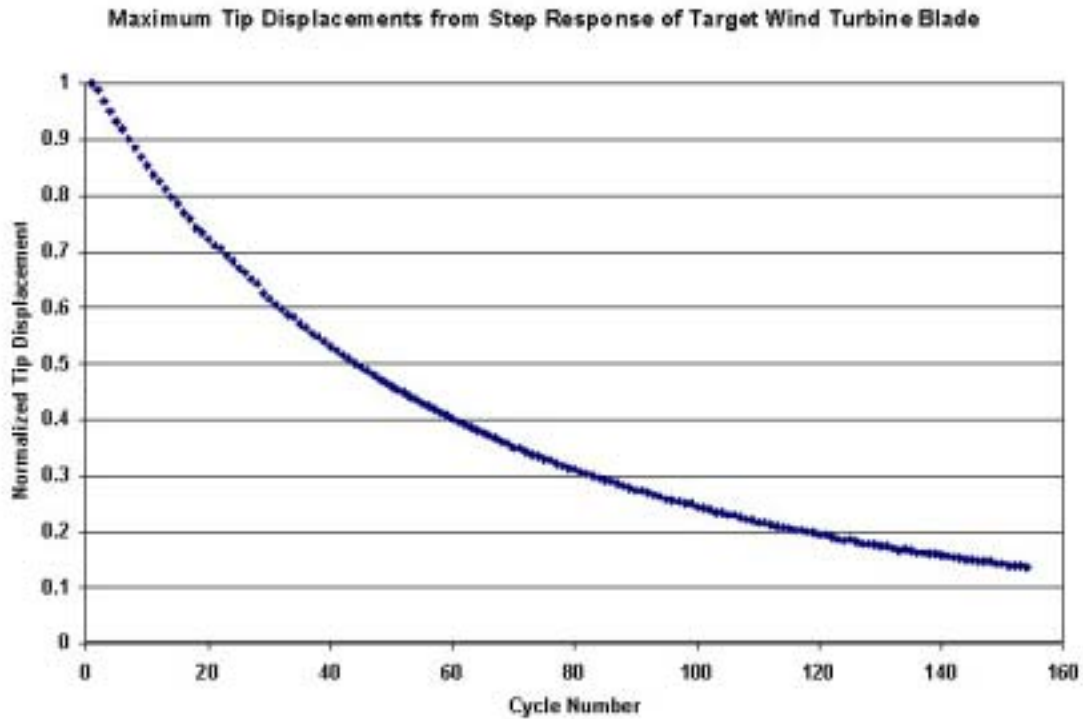
Figure 5-7. Reduced step response time series data

The damping ratio was calculated using each maximum value using the log decrement formula [129].

$$\frac{2\pi\zeta}{\sqrt{1-\zeta^2}} = \ln\left(\frac{x_n}{x_{n+1}}\right) \qquad (5.1)$$

Where,

ζ = Damping Ratio

X_n = Amplitude at cycle n

As shown in Figure 5-8, the damping ratio is not constant with tip displacement. This behavior is consistent with structural damping principles. It can also be seen that the step response was conducted at a much lower tip displacement that would be expected during testing. To calculate the displacement at the target displacement, a linear approximation of the damping ratio as a function of tip displacement was created. The damping ratio was extrapolated to be 1.1%. This value was verified by conducting an independent test of the blade properties at the target displacement.
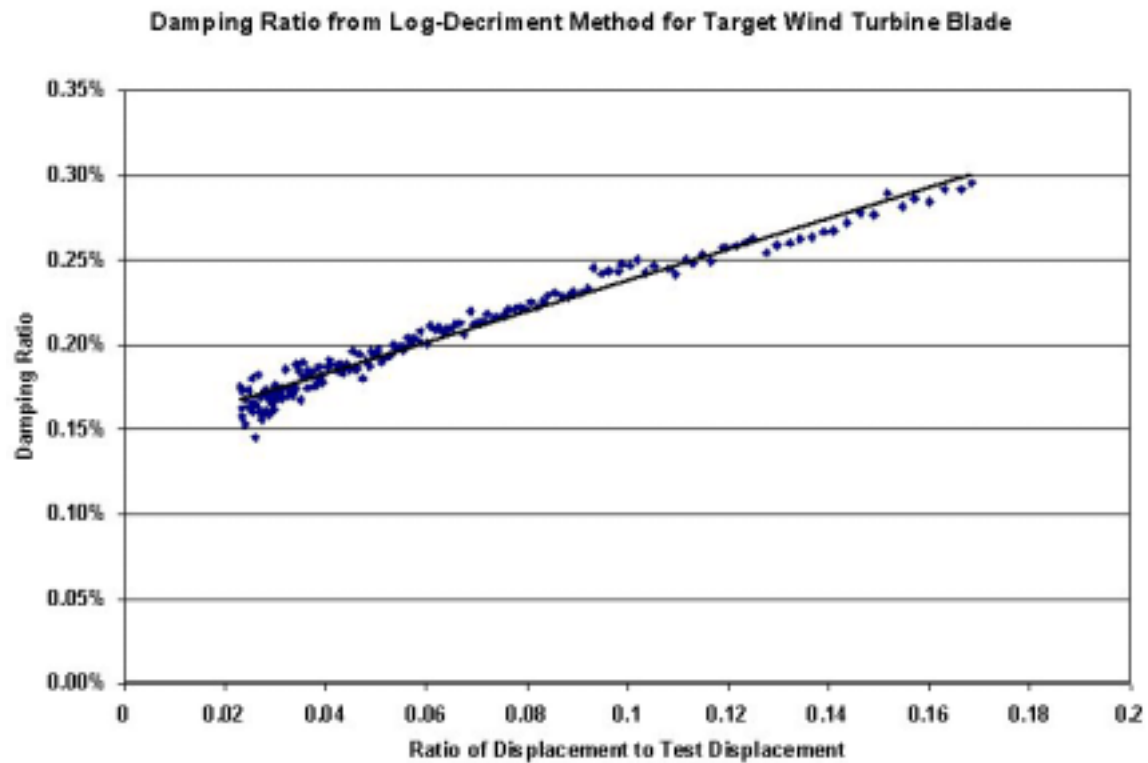
Figure 5-8. Damping ratio as a function of tip displacement

Since the system damping is associated with material (or hysteresis) damping rather than viscous damping, the hysteresis loop was measured for the target blade at the prescribed displacements. As shown in Figure 5-9, the system characteristics are not linear throughout the displacement range but the properties are very consistent. The data shown in Figure 5-9 represent roughly eight hysteresis cycles.

Normalized Hysterysis Loop for Target Blade
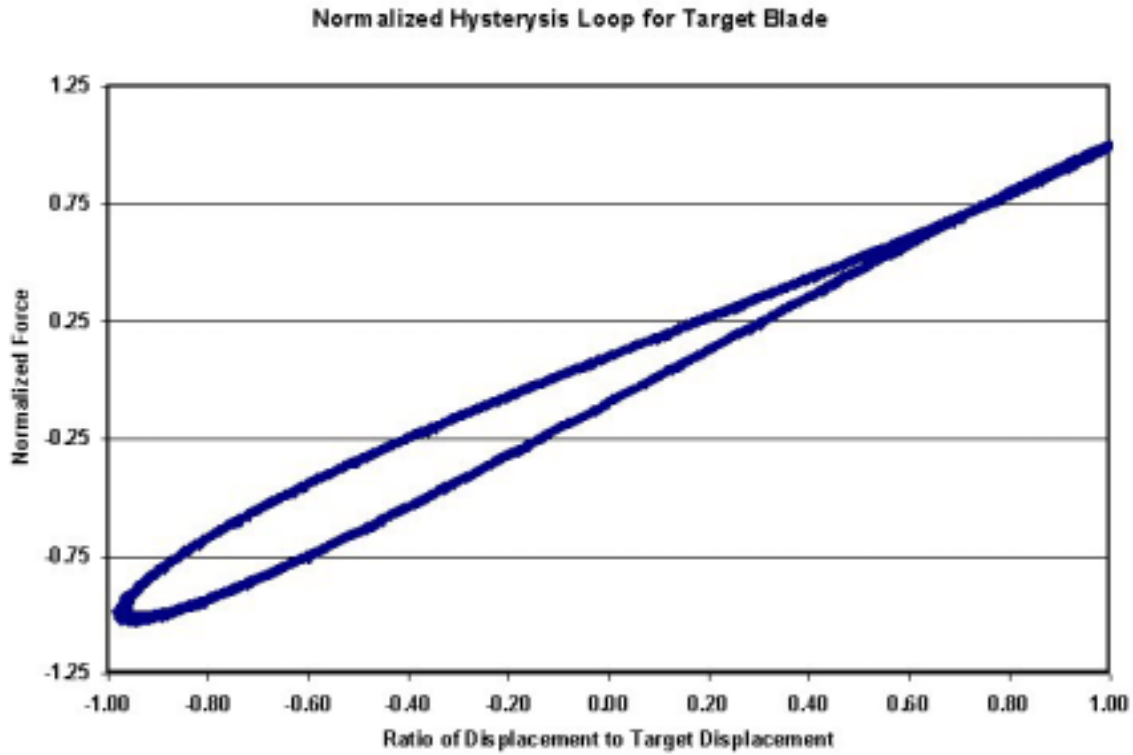
Figure 5-9. Normalized force-displacement curve for target blade

The energy dissipated-per-cycle is a function of the average area within the hysteresis loops. In order to convert to energy dissipation per cycle into the damping ratio, the maximum tip displacement, flap-bending stiffness, and the resonance to excitation frequency ratio were used, as shown in Equation 5.2 [130, 131].

$$\zeta = \frac{\Delta W}{4\pi^2 k X^2}\left(\frac{\omega_n}{f}\right) \tag{5.2}$$

Where,

ζ = Equivalent Viscous Damping Ratio
ΔW = Area of Hysteresis Loop (Energy Dissipated per Cycle)
k = Blade Flap Bending Stiffness
X = Maximum Tip Displacement
F = Excitation Frequency
ω_n = Fundamental Flap Frequency

The structural damping ratio was approximately equivalent to a viscous damping ratio of 1.0%. Since the extrapolated log decrement damping ratio and structural damping ratio are approximately equal, there was some confidence that this value was correct. As an additional precaution, the damping ratio calculated for this target blade was compared to

106

typical material damping ratios. As shown in Table 5-1, the target blade has similar damping characteristics to other common materials.

Table 5-1. Typical Material Damping Ratios

Material	Damping Ratio
Steel	0.002
Composite	0.003
Steel Structure	0.004
Composite Structure	0.006
Target Blade	**0.01**
Rubber	0.05

5.2.2 Mode Shape Calculation

The mode shapes in the flap and lead-lag directions were calculated using a beam finite element model from the EI data for the target blade and the stationary masses. A lumped mass finite element model was used so that the added stationary masses could be easily manipulated using an optimization algorithm. This model used to calculate the mode shape is described below.

5.2.2.1 Beam Finite Element Model

A beam finite element model was created to calculate the wind turbine blade's mode shapes in the loaded test condition. The finite element model was further used as part of an optimization algorithm (shown in Appendix A) to tune the mean and alternating bending moments observed by the blade during testing. Since damping has been experimentally determined to be small, it will be ignored for this calculation but not for the controller design described in chapter 6. The stiffness of the blade during operation will be assumed to be symmetrical for the purpose of this calculation even though the airfoil is nonsymmetrical. Similar analysis has been used to model the dynamics of airfoil structures as shown by Murri et al [132]. The assumption that the airfoils are symmetric reduces the system from a time-variant to a time-invariant stiffness matrix, which is important for the control theory used in chapter 6. Reducing the system to a time-invariant model guarantees that eigenvalues exist and that the eigenvectors are orthogonal [133]. While it is expected that a small error will be introduced by this assumption, it is important to recognize that the purpose of the fatigue test is to apply an alternating force onto the blade. The magnitude and distribution of the force can be adjusted based on experimental measurements. So small errors can be corrected by tuning the system response. The experimental measurements will be presented in chapter 7. The eigenvectors were calculated in the flap and lead-lag direction but not the torsional direction because no torsional stiffness data were available and the torsional fundamental frequency is approximately 20 times higher than the flap fundamental frequency. Since no torsional loads are applied to the blade, this aspect of the system

107

dynamics has been assumed to have a minimal influence. The elemental mass and stiffness matrices for a generalized beam element are shown by Equations 5.3 and 5.4 [134].

$$k_n = \left(\frac{8(EI)_n}{l^3}\right)\begin{bmatrix} 12 & -12 & 6l & -6l \\ -12 & 12 & -6l & -6l \\ 6l & -6l & 4l^2 & 2l^2 \\ 6l & -6l & 2l^2 & 4l^2 \end{bmatrix}\begin{bmatrix} V_n \\ V_{n+1} \\ \theta_n \\ \theta_{n+1} \end{bmatrix} \tag{5.3}$$

$$M_n = \begin{bmatrix} m_n & 0 & 0 & 0 \\ 0 & 0 & 0 & 0 \\ 0 & 0 & 0 & 0 \\ 0 & 0 & 0 & 0 \end{bmatrix}\begin{bmatrix} \ddot{V}_n \\ \ddot{V}_{n+1} \\ \ddot{\theta}_n \\ \ddot{\theta}_{n+1} \end{bmatrix} \tag{5.4}$$

Where,

k_n	= Elemental Stiffness Matrix
M_n	= Element Mass Matrix (Lumped Mass)
V_n	= Vertical Displacement at Node n
θ_n	= Rotational Displacement at Node n
l	= Element Length
E	= Modulus of Elasticity
I	= Moment of Inertia for Element (Flap or Lead-lag)

Each elemental matrix was combined to create global mass and stiffness matrices. These matrices were combined into a finite element model of the target wind turbine blade that was used to solve for the eigenvalues and eigenvectors in each direction. The finite element model

$$\begin{bmatrix} M_{11} & 0 \\ 0 & 0 \end{bmatrix}\begin{bmatrix} \ddot{V} \\ \ddot{\theta} \end{bmatrix} + \begin{bmatrix} K_{11} & K_{12} \\ K_{21} & K_{22} \end{bmatrix}\begin{bmatrix} V \\ \theta \end{bmatrix} = \begin{bmatrix} 0 \\ 0 \end{bmatrix} \tag{5.5}$$

Where,

M_{11}	= Global Mass Matrix (Lumped Mass Values on Diagonal)
K_{xx}	= Global Stiffness sub-Matrices

Before solving the eigenvalues problem, the order of the global stiffness matrix was reduced to eliminate the rotational degree of freedom. The reduced order finite element model is shown by Equation 5.6.

$$[M_{11}][\ddot{V}] + [K_{11} - K_{12}K_{22}^{-1}K_{21}][V] = [0] \tag{5.6}$$

The first two eigenvectors for the flap system and the first eigenvector in the edge direction are shown in Figure 5-10. The location where the harmonic force will be added to the blade is also shown on Figure 5-10. This location has been selected to be near the node of the 2nd eigenvector. This should minimize any excitation of this higher order mode.
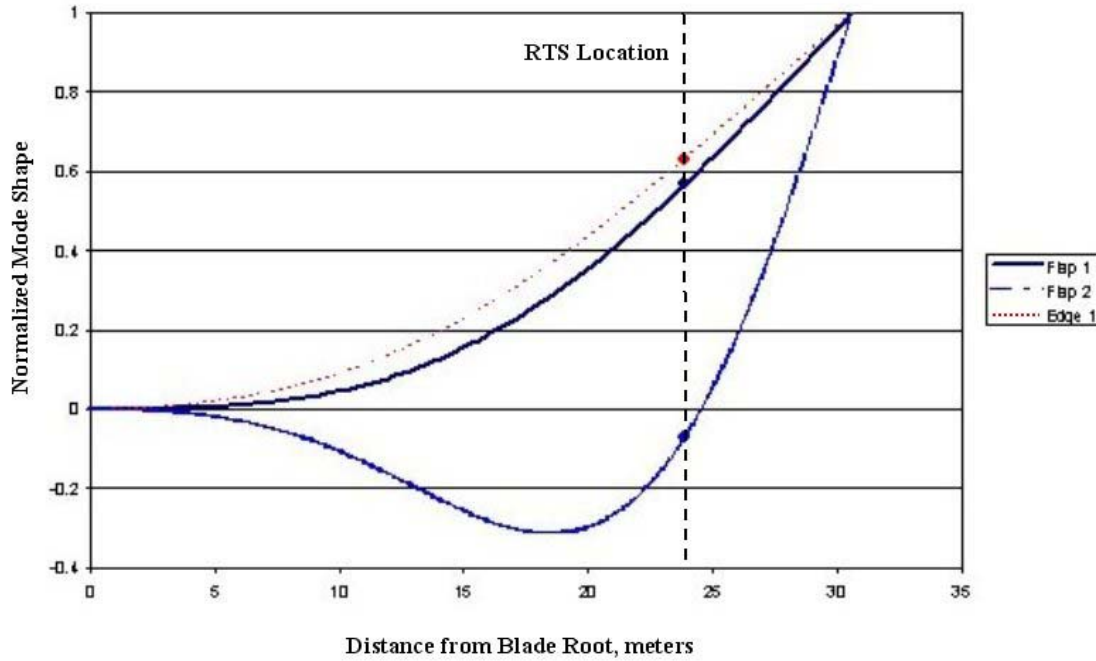
Figure 5-10. Normalized mode shapes for target blade

The mode shape was calculated many times during the stationary mass optimization process as discussed in section 5.2.4. The bending moment distribution along the blade is determined by the mode shape and stationary mass sizes.

5.2.3 Bending Moment Calculation

The alternating flap bending moment was calculated by multiplying the mass of each blade station by its acceleration and the distance from the mass to the current station. The mean bending moment is calculated in the same manner but using gravity in place of acceleration. These relationships can be seen in Equation 5.7.

$$BM_a = \sum_{i=1}^{N_a} mb_i L_{ai} \left[\omega^2 y_i + g \right] \qquad (5.7)$$

Where,

BM = Bending Moment (mean + alternating) at station a
mb = mass of blade element (i)
L = Length between station (a) and blade element (i)
ω = Excitation Frequency

$$y \qquad = \text{Displacement amplitude of blade element (i)}$$
$$g \qquad = \text{gravitational acceleration constant}$$

The acceleration at each blade station was calculated by assuming that all of the blade motion was contributed by the fundamental mode shape in the flap direction. Since the mode participation factor of the fundamental eigenvalue is approximately 98.5%, the error introduced by ignoring the other eigenvectors contribution to the blade response is small. As shown by Equation 5.7, the bending moment distribution is a function of both the added stationary masses and the mode shape. Since the terms are coupled an optimization routine was used to solve for the sizes of masses required to produce the best bending moment distribution. In this case, the routine determines the mass distribution that results in the closest relationship between the target bending moment distribution and the predicted bending moment distribution.

5.2.4 Bending Moment Optimization

The first step in the optimization process is to assume an arbitrary stationary mass distribution, which involves selection of the magnitude and position of the added masses, including the weight of the actuator and its support structure as shown in Figure 5-4. The blade's mass distribution is critical and must be included in the calculation. The system mass and distributions are input the beam finite element dynamic beam model discussed in section 5.2.2.1, which predicts the mode shapes of the blade/mass system. Equation 5.8 shows the global mass matrix with the optimization variables (s_1, s_2, s_3) highlighted.

$$M_{11} = \begin{bmatrix} m_1 & 0 & 0 & 0 & 0 & 0 & 0 & 0 & 0 & 0 \\ 0 & \ddots & 0 & 0 & 0 & 0 & 0 & 0 & 0 & 0 \\ 0 & 0 & s_1 = m_{70} & 0 & 0 & 0 & 0 & 0 & 0 & 0 \\ 0 & 0 & 0 & \ddots & 0 & 0 & 0 & 0 & 0 & 0 \\ 0 & 0 & 0 & 0 & M_{RTS} + s_2 = m_{85} & 0 & 0 & 0 & 0 & 0 \\ 0 & 0 & 0 & 0 & 0 & \ddots & 0 & 0 & 0 & 0 \\ 0 & 0 & 0 & 0 & 0 & 0 & s_3 = m_{95} & 0 & 0 & 0 \\ 0 & 0 & 0 & 0 & 0 & 0 & 0 & \ddots & 0 & 0 \\ 0 & 0 & 0 & 0 & 0 & 0 & 0 & 0 & m_{99} & 0 \\ 0 & 0 & 0 & 0 & 0 & 0 & 0 & 0 & 0 & m_{100} \end{bmatrix} \quad (5.8)$$

Using a conjugate gradient/steepest decent optimization routine [135], the stationary mass sizes were iteratively adjusted until convergence between the current bending moment distribution and target moment distribution was achieved. For this analysis, the target bending moment distribution was selected to be the bending moment distribution achieved by performing the forced-displacement fatigue test.
Figure 5-11 shows that by tuning the blade/mass mode shape by adjusting the size of the added masses, the flap bending moment for the resonance system can closely approximate the bending moment for the current forced-displacement test method. The adjustability of the bending moment distribution makes it possible for the resonance test

system to match more complex distributions than the one shown. This means that the dual-axis resonance test method will be the most accurate method for testing large wind turbine blades.
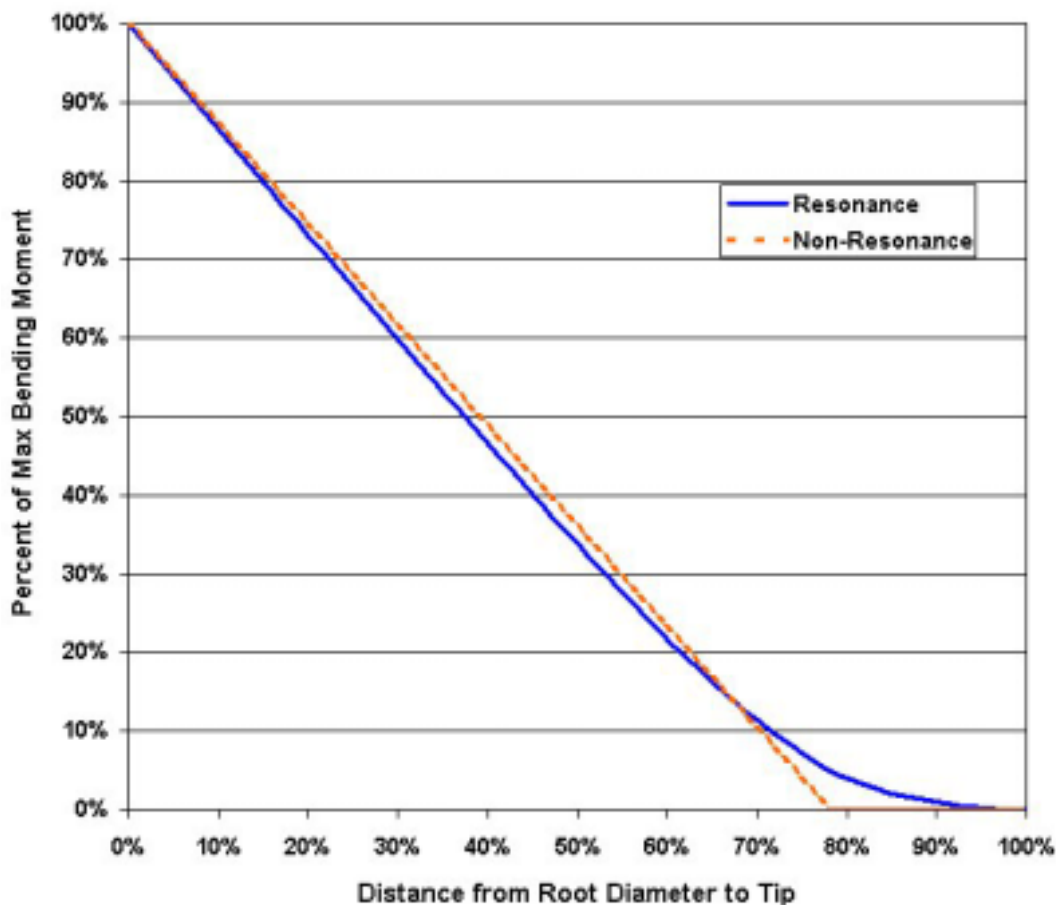
Figure 5-11. Bending moment distribution along blade

The dual-axis resonance system presents several advantages over both methods currently used to fatigue test wind turbine blades.

5.3 Comparison of Test Methods

When considering methods for fatigue testing wind turbine blades several factors are important. The accuracy of the test is arguably the most important evaluation criterion. The stress profile for single axis tests are generally considered to be the least accurate. Dual-axis test methods were developed specifically to improve the accuracy of the fatigue tests. However, forced-displacement tests have a very limited capability to adjust the moment distributions. The dual-axis resonance test provides not only the improved stress profile of dual-axis tests but also a much greater ability to adjust the flap bending moment distribution.

Other important criteria for evaluating wind turbine fatigue test methods are the time required to perform the test and the operating cost, which is largely determined by the energy consumption. The time required to perform the tests are dependent on a number

111

of factors and will be discussed below. The cost associated with performing a fatigue test on a wind turbine blade also includes many factors including setup time, material, equipment depreciation, labor costs and energy consumption. Several of the costs, such as material costs and setup time, will not be significantly affected by the method used for testing. Other costs, such as equipment depreciation and labor costs per test, depend on the number of tests conducted in a specific amount of time. As such, the time required to perform a fatigue test is an accurate metric for determining how the various test methods affect these costs. The remaining cost, energy consumption will be treated separately.

5.3.1 Test Duration

The amount of time required to perform a fatigue test using a resonance system depends on the resonance frequency. While adding stationary masses to the blade allows for greater bending moment adjustability, it also lowers the resonance frequency. In general, the loaded natural frequency of the blade is reduced by 25-30%, based on the research conducted for the project. The forced-displacement test frequency is limited by several factors. The large actuator forces and displacements required to perform the test, require very large hydraulic flow rates and cooling capacity. NREL's test facility currently has the ability to pump 250 GPM of hydraulic fluid. This allows blades to be tested at approximately 30% of the natural frequency. As shown in Figure 5-12, the single-axis and dual axis resonance tests require approximately half the time to complete a 3-million cycle fatigue test.
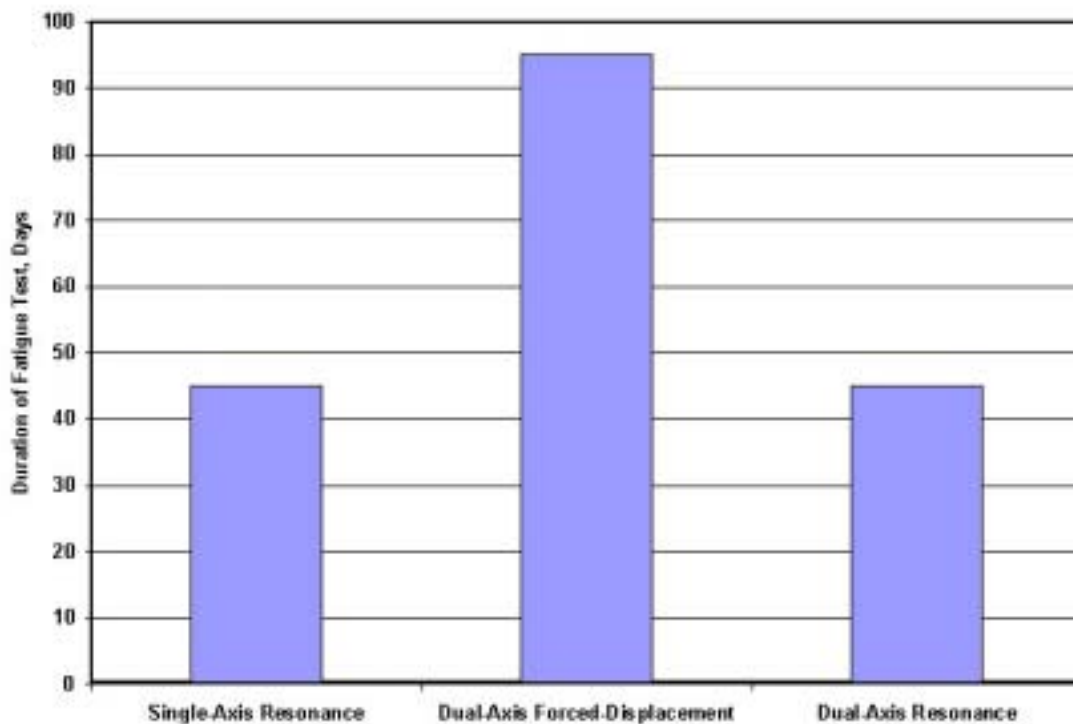
Figure 5-12. Duration of fatigue test using each method (1.5 MW blade)

5.3.2 Energy Requirements

The difference in energy consumption for the two hydraulic methods is a function of the amount of hydraulic fluid pumped through the actuator and externally cooled. The total system efficiency of using an electric motor operating around the resonance frequency compared to the efficiency of using a hydraulic actuator operating at the resonance frequency is difficult to determine. As such, the amount of work required to perform a fatigue test using each method will first be considered. The energy consumed using the two hydraulic methods will be considered separately.

5.3.2.1 Required Work

The force required to achieve the target blade displacement during testing is a function of material damping ratio and the frequency of excitation. The relationship between the excitation force and the displacement can be expressed using Equation 5.9 [134].

$$\frac{Xk}{F_0} = \frac{1}{\sqrt{\left[1-\left(\frac{\omega}{\omega_n}\right)^2\right]^2 + \left[2\zeta\left(\frac{\omega}{\omega_n}\right)^2\right]^2}} \tag{5.9}$$

The results of this equation for a range of frequencies are shown in Figure 5-13.
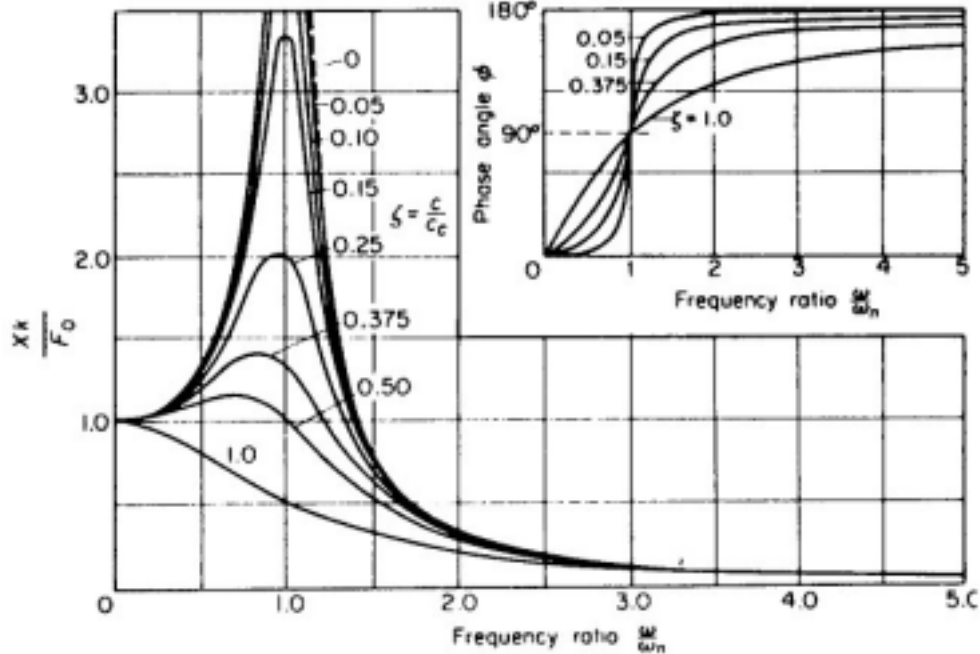
Figure 5-13. Theoretical frequency response for wind turbine blade [134]

By applying the information about the target blade to the displacement magnification equation, the ideal work required to perform a fatigue test using each method was calculated. It was assumed that the single axis resonance test could typically maintain an excitation frequency within 5% of the resonance frequency. As shown in Figure 5-14, the single axis resonance test required the least amount of energy to perform a fatigue test. Since the single axis test does not use any energy to test the blade in the lead-lag direction (in this example), the work required is less than the dual-axis test methods. In many cases, the single-axis resonance test is performed on a blade in each direction but at different times. Although, the energy consumption to perform two single axis resonance tests is still less than the dual axis tests, this method is less accurate and results in substantially longer test durations. Similarly, the dual-axis resonance test requires much less energy to perform a fatigue test than the forced-displacement test.

114
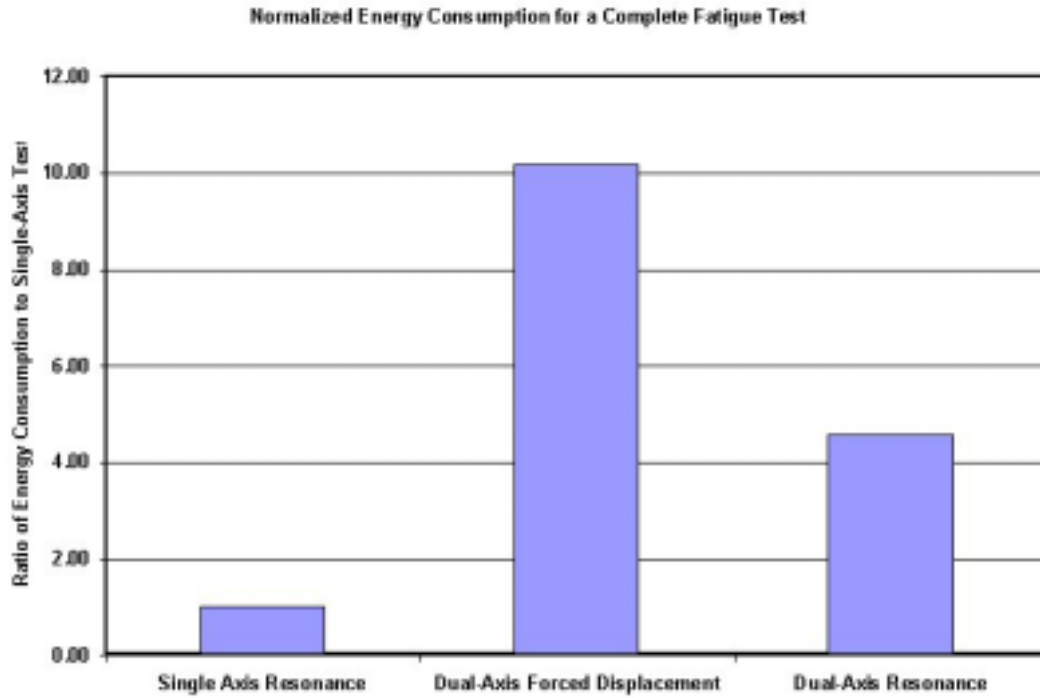
Figure 5-14. Relative energy consumption for each test method

Since a dual axis test is required to achieve the highest test accuracy, these methods will be evaluated further. In order to determine the actual energy consumption for the new resonance system, a flap actuator must be selected. The size of the actuator will greatly influence the amount of hydraulic fluid that will be pumped through the system. In order to optimize the system the smallest actuator bore that can meet the load requirements should be chosen. In order to determine the best actuator, the minimum forcing requirements were calculated as a function of the available stroke. The actuator must withstand several forces; the displacement of the mass, the acceleration of the excitation mass from the blade displacement and acceleration of the excitation mass from gravity. The actuator forces are summarized in Equation 5.10.

$$F = m\frac{\omega^2}{2}(S + R) + mg \qquad (5.10)$$

Where,

F　　= Total Actuator Force
ω　　= Excitation Frequency
S　　= Actuator Stroke
R　　= Blade Displacement Range
m　　= Excitation Mass

The size of the excitation mass is determined by the available stroke. As shown by Equation 5.11, the minimum excitation mass depends on the minimum excitation force, which in turn depends on the damping ratio.

$$m = \frac{2F_0}{S\omega^2} = \frac{4k\zeta}{S\omega^2} X \qquad (5.11)$$

Where,

F_0	= Minimum Excitation Actuator Force
ω	= Excitation Frequency
S	= Actuator Stroke
m	= Excitation Mass
k	= Blade Stiffness
ζ	= Damping Ratio
X	= Target Blade Displacement

Since each quantity in Equations 5.10 and 5.11 is a known value for the target blade, it is possible to calculate the required actuator force as a function of the available actuator stroke. As shown in Figure 5-15, several available actuators at NREL satisfy the force requirement. For compactness and future capacity, the smallest length actuator with the highest available force was selected. This actuator results in higher than optimal energy consumption but allows the same system to be used for longer blade lengths.
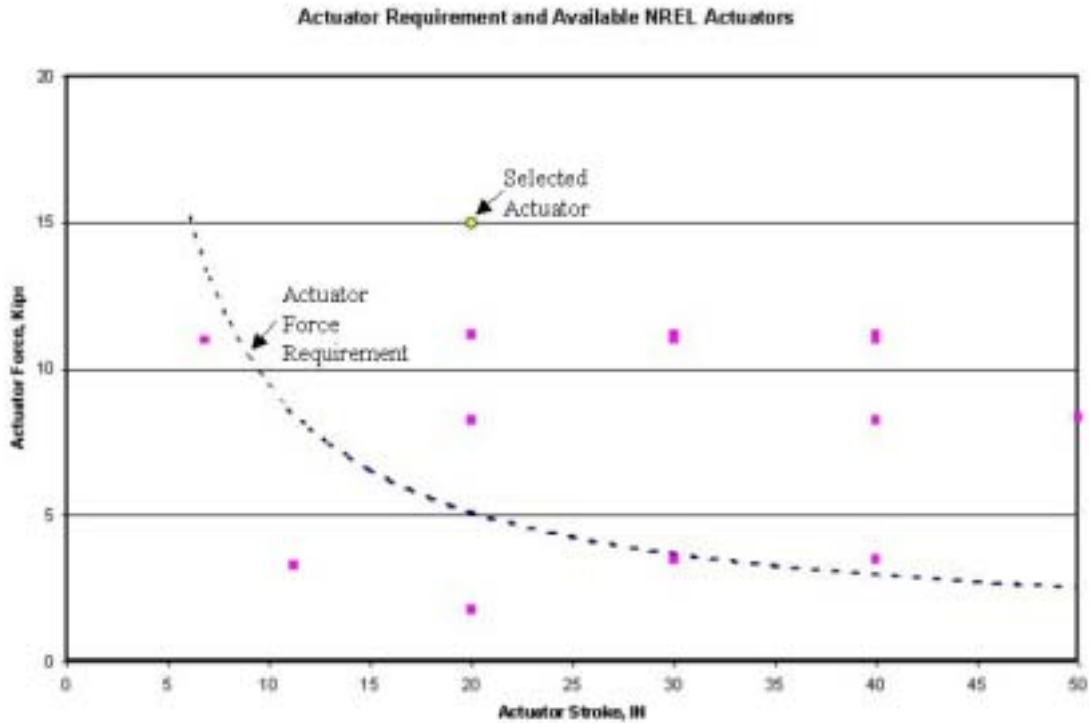
Figure 5-15. Resonance system flap actuator selection

With the properties of the selected actuator known, the hydraulic flow rates required to perform a fatigue test may be calculated. As shown in Equation 5.12, the hydraulic flow rate depends on the actuator piston diameter, actuator stroke and excitation frequency.

The maximum hydraulic flow rate capacity of NREL's test facility typically influences the excitation frequency because of this relationship.

$$FR = (PA)(S)(f) \qquad (5.12)$$

Where,

FR = Maximum Hydraulic Flow Rate
S = Maximum Actuator Stroke
f = Excitation Frequency

Using the selected actuator, the energy saving between the forced-displacement method and the resonance excitation method is less than the potential savings. As shown in Figure 5-16, the maximum flow rate for the resonance system is approximately 40% of the maximum flow rate for the current NREL test method. The average hydraulic flow rate for the resonance system is also approximately 60% lower than the flow rate for the forced-displacement system.
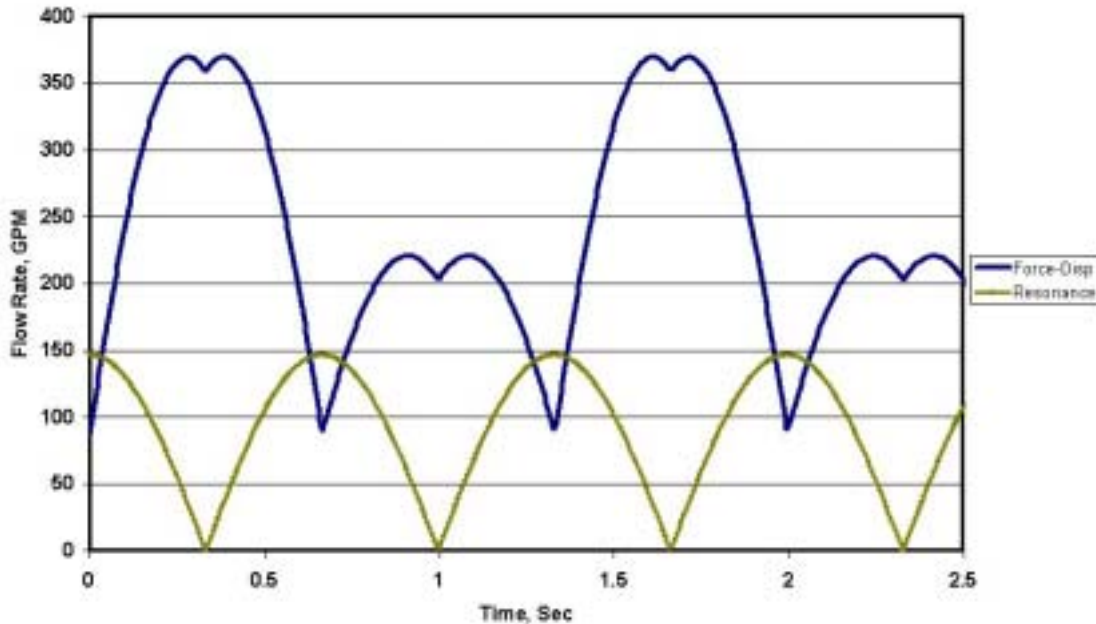
Figure 5-16. Hydraulic flow rate requirements for hydraulic test methods

Based on the analysis of the theoretical energy consumption and the hydraulic flow rate requirements for the selected actuators, the dual-axis resonance system will use approximately 60% less energy to perform a fatigue test on a 1.5 MW wind turbine blade than the forced-displacement method. This savings combined with the reduction in testing time will make testing large wind turbine blades more practical and economical.

5.3.3 Testing Efficiency as a Function of Blade Length

For current blade technologies, the resonance fatigue test method has advantages over the current force-displacement test method. As blades continue to grow larger, the advantages of the resonance test method should increase even further.

As shown in Figure 5-17, the flap actuator force for the force-displacement test method increases linearly as the blades become longer. While the blade bending moments increase at a higher rate, as the blade length increases the load application point moves further outboard from the root, which allows the force to increase at a slower rate.
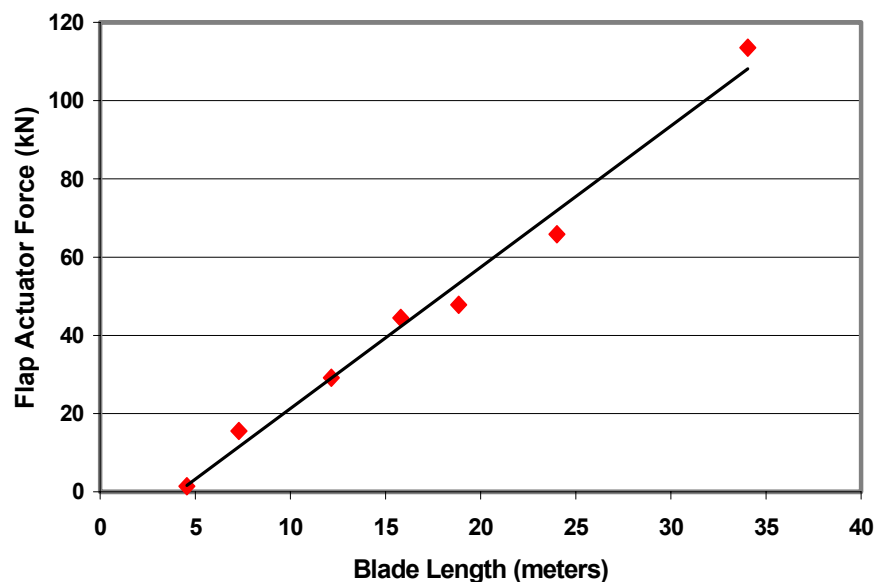
Figure 5-17. Force requirement for force-displacement test method

Although moving the actuator location further from the root mitigates the increase in force requirement, it results in higher actuator displacements. As shown in Figure 5-18, the actuator displacement increases at approximately a quadratic rate as blades become longer.
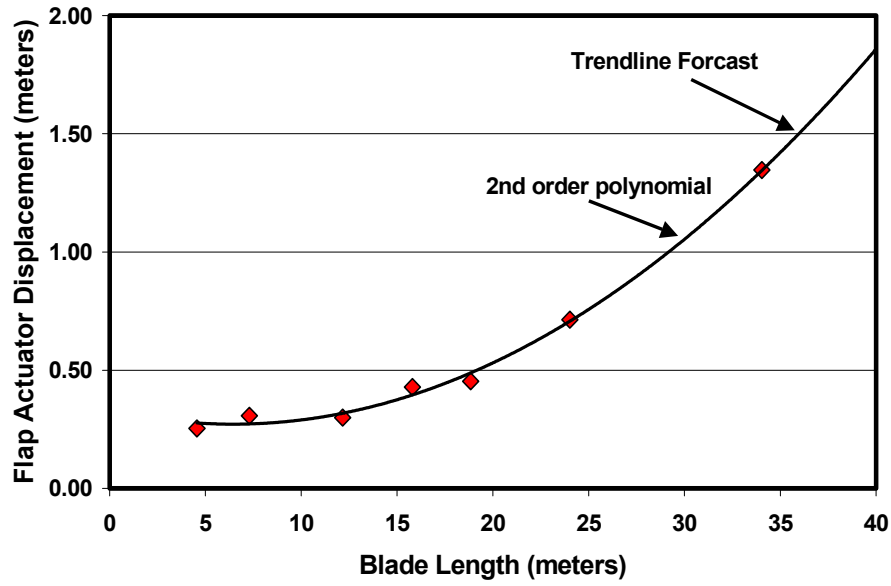
Figure 5-18. Actuator displacement requirement for force-displacement test

If the blade tests were conducted at the same frequency, the hydraulic flow rate requirement for the flap actuator for the forced-displacement test method would increase cubically. This relationship can be seen from Equation 5.12 and in Figure 5-19. This relationship would be predicted by calculating the strain energy. Since strain energy is influenced by the stiffness of the system as shown by Equations 5.13 and 5.14, its not surprising that the energy consumed to perform a fatigue test would depend on the cube of the blade length.

$$k = \frac{3EI}{l^3} \tag{5.13}$$

$$Strain\_Energy = \frac{1}{2}kx^2 = \frac{1}{2}k\left(\frac{F}{k}\right)^2 = \frac{F^2}{2k} = \frac{F^2}{2}\left(\frac{l^3}{3EI}\right) = \left(\frac{F^2}{6EI}\right)l^3 \tag{5.14}$$
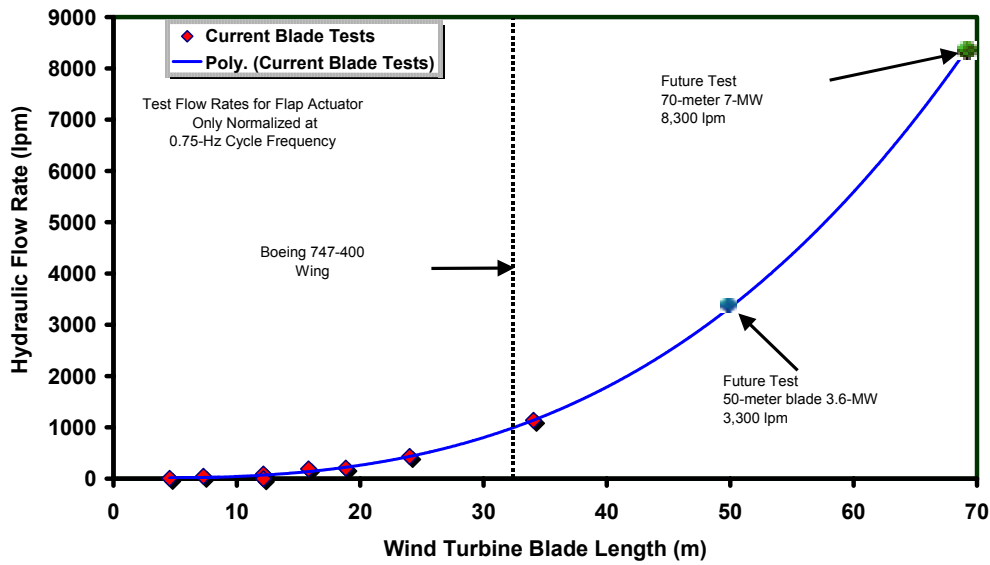
Figure 5-19. Flap actuator flow rate requirement for force-displacement test

The lead-lag actuator can be shown to have a similar trend as the flap actuator but the dual-axis resonance test method will have no impact on the hydraulic flow requirement for the edge actuator. As a result, all of the energy saving for the resonance system compared to the forced-displacement system can be demonstrated using the hydraulic flow rate for the flap actuator. As shown in Figure 5-20, the reduction in flow requirements increases substantially for larger wind turbine blades.

Reduction in Hydraulic Flow Requirement for Dual Axis Resonance Method
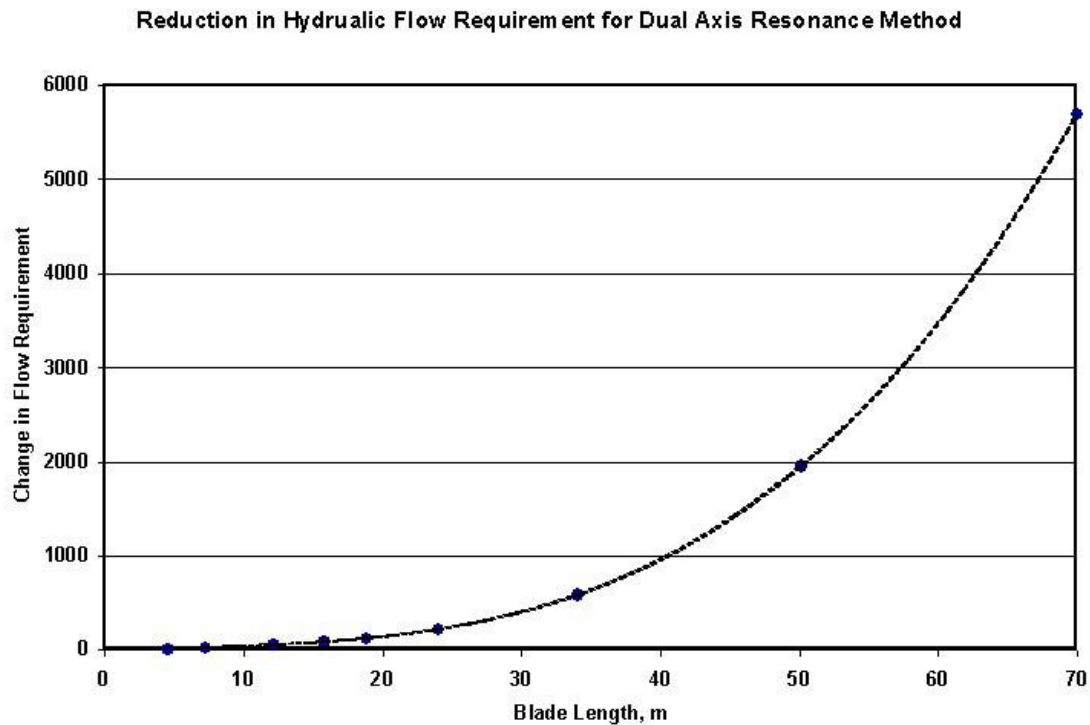
Figure 5-20. Hydraulic flow rate reduction (l/m) for resonance system

5.4 Summary

A new method for fatigue testing wind turbine blades has been evaluated and designed. The bending moment distribution for the new test method can equal or even improve upon current test systems. The forced-displacement test method is capable of generating only a straight-line approximation to the service bending moment and is capable of accurately reproducing service loads at only one location. Since the bending moment distribution for the resonance test system can assume an infinite variety of shapes depending on the stationary mass sizes, the resonance test system can reproduce service test loads at more than one location. The tip of the blade is typically removed for forced-displacement fatigue testing to avoid uncontrolled second mode vibrations. Since the second mode will be controllable for the resonance test system, it is not necessary to remove the blade tip. As such, the resonance test system is capable of testing the entire blade length. The new test method will substantially reduce the expense and time required to test large wind turbine blades. By increasing the test speed to approximately 200% of the forced-displacement system, the resonance test system will allow more blades to be tested in a shorter amount of time. By reducing the amount of hydraulic fluid used to perform fatigue tests, the resonance system will mitigate some of the hardware costs associated with testing increasing larger blades and make it cheaper to perform fatigue tests on current blade sizes. Using the resonance test system to perform a fatigue test on a 37-meter long blade will save enough energy to power over 100 houses for one year when compared to the forced-displace fatigue test commonly used.

121

Chapter 6. Controller Design and Analysis for Dual-Axis Resonance Test Method

This chapter describes a dynamic blade model to model the wind turbine blade's dynamic response and two methods to control the blade's response. The equations of motion for this system were developed using the beam finite element model presented in Chapter 5, section 5.2.2.1 and parameters that were experimentally validated for the target blade. A PID controller was designed and evaluated for the system under constant phase angle and progressive phase angle conditions. A full-state feedback controller was also designed and evaluated. It was determined that a PID controller is sufficient for the control of the system when a constant phase angle test is performed. If variable phase angle testing is implemented, a full-state feedback controller will be required. The current NREL testing software supports the use of PID controllers but not full-state feedback controllers. A software upgrade will be required if the full-state feedback controller is ultimately used.

6.1 Dynamic Blade Model

A wind turbine blade in the test configuration was modeled as a cantilever beam with lengthwise varying mass and stiffness properties, as presented in section 5.2.2.1. The finite model of the blade was used to calculate the mode shapes and natural frequencies in the flap and lead-lag direction for the blade in the loaded condition. The fundamental mode shape was modified using an optimization routine to size stationary masses that are added to the blade to achieve a target moment distribution. The tip displacement resulting in the best agreement between the target and the calculated moment distributions was also calculated. The fundamental eigenfrequency resulting from the beam finite element model has been used to calculate an equivalent mass and stiffness for the blade. The distinction between the eigenvalues and the equivalent natural frequencies in the flap and lead-lag directions is small but it must be noted that the beam finite element did not include damping but the dynamic model does include damping. As shown in chapter 5, the damping of the system is very small but measurable. By using the equivalent mass and stiffness values, it was possible to measure the system damping and include this in the dynamic calculations.

6.1.1 Equations of Motion

Since the natural frequency and blade stiffness at the tip have been determined both analytically and experimentally, it is possible to create a simplified dynamic model of the wind turbine blade that is very accurate for the to the first order approximation of the system. In this case, the nonlinear dynamics of the blade have not been included in the dynamic model. During testing, the blade will have very little damping and will be excited at or near the fundamental natural frequency. These characteristics are indicative of systems they may experience significant nonlinear behavior [133]. However, the tip displacements relative to the blade length are relatively small, less than 5%, and any non-linearity in the blade displacement will have little influence on the damage accumulation since most damage models require the data to be decimated using a peak-valley detection

algorithm [134]. As such, the dynamic model will be based on linear blade properties initially. If the blade stiffness increases or decreases as a function of the tip displacement (i.e., a spine curve), the excitation natural frequency will be adjusted manually before the fatigue test is conducted.

The wind turbine blade and test system are schematically shown in Figure 5-1. During testing, the blade is cantilevered from a very stiff load frame. The load frame introduces some small dynamic influence but these dynamics will be ignored for this analysis. The flap and lead-lag directions of the blade will be analyzed independently. This simplification is consistent with current modeling and control strategies used for dual axis fatigue testing [29]. For the purpose of creating a dynamic model, several blade properties have been determined. Using a finite element model of the blade, the natural frequency and blade stiffness for a point load at the tip have been calculated. These numbers have been confirmed experimentally as discussed in chapter 3. Additionally, the equivalent structural damping at the prescribed tip displacement (based on the target bending moment) has been empirically determined. Since the fundamental frequency and damping ratio were accurately known, an approximation for the actuator force was calculated using Equation 3.5.
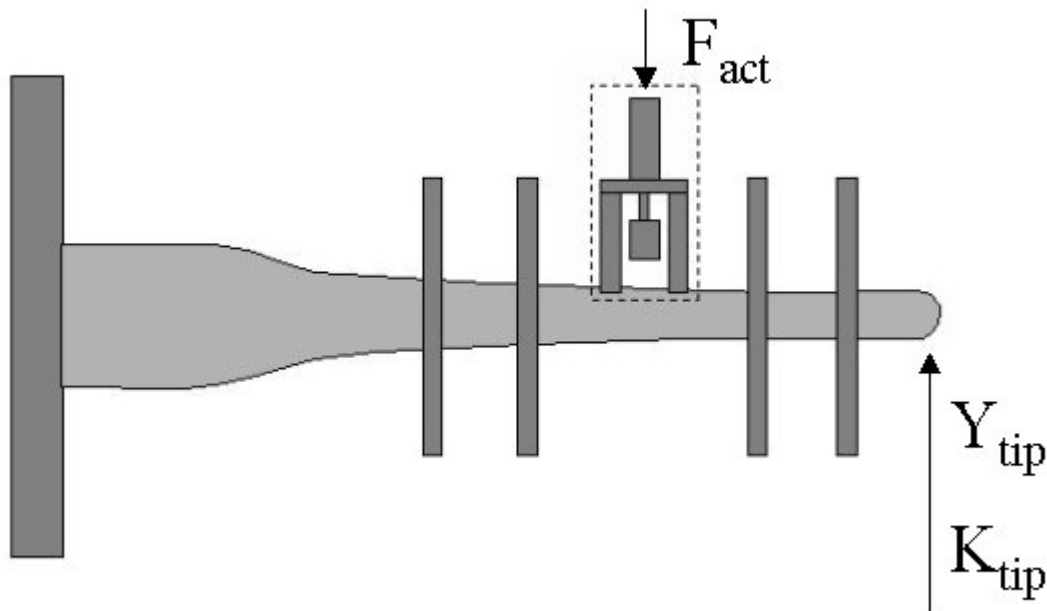
Figure 6-1. Cantilevered wind turbine blade with test system

The cantilever beam system was reduced to the simplified dynamic model shown using the eigenvalues from the beam finite element model discussed in chapter 5 and the measured damping discussed in section 5.2.1. This type of model was assumed for both the flap and lead-lag directions.

The equivalent stiffness and mass for the simplified blade model were calculated using Equations 6.1 through 6.3. The stiffness and natural frequency values for the flap and lead-lag blade deflections determined using the previously mentioned finite element model have been used for these calculations. Another beam finite element code developed by the National Wind Technology Center called 'Modes' (a significant part of the original source code was written by Oregon State University), was to verify the results of the beam finite element program discussed in chapter 5.

$$K_{eq} = K_{tip}$$
$$M_{eq} = K_{eq} / \omega_n^2 \qquad (6.1\text{-}6.3)$$
$$C_{eq} = 2M_{eq}\omega_n\zeta$$

Using the simplified dynamic model, the equations of motion were determined for this blade. As shown by Equations 6.4 and 6.5, the equations of motion for this dynamic system appear to be straightforward but additional considerations make the model more complex.

$$M_{eqx}\ddot{X} + C_{eq}\dot{X} + K_{eq}X = F_x$$
$$M_{eqy}\ddot{Y} + C_{eq}\dot{Y} + K_{eq}Y = F_y \qquad (6.4\text{-}6.5)$$

The lead-lag forces are added using a hydraulic actuator and are applied using a bell crank mechanism. This mechanism can be seen in Figure 6-2.

Figure 6-2. Dual-axis test using bell crank to apply lead-lag force

The direction of the load applied by the bell crank changes as a function of the blade flap displacement. As shown in Figure 6-3, the bell crank linkage will add forces in the flap and lead-lag direction at varying amounts throughout the fatigue cycle.
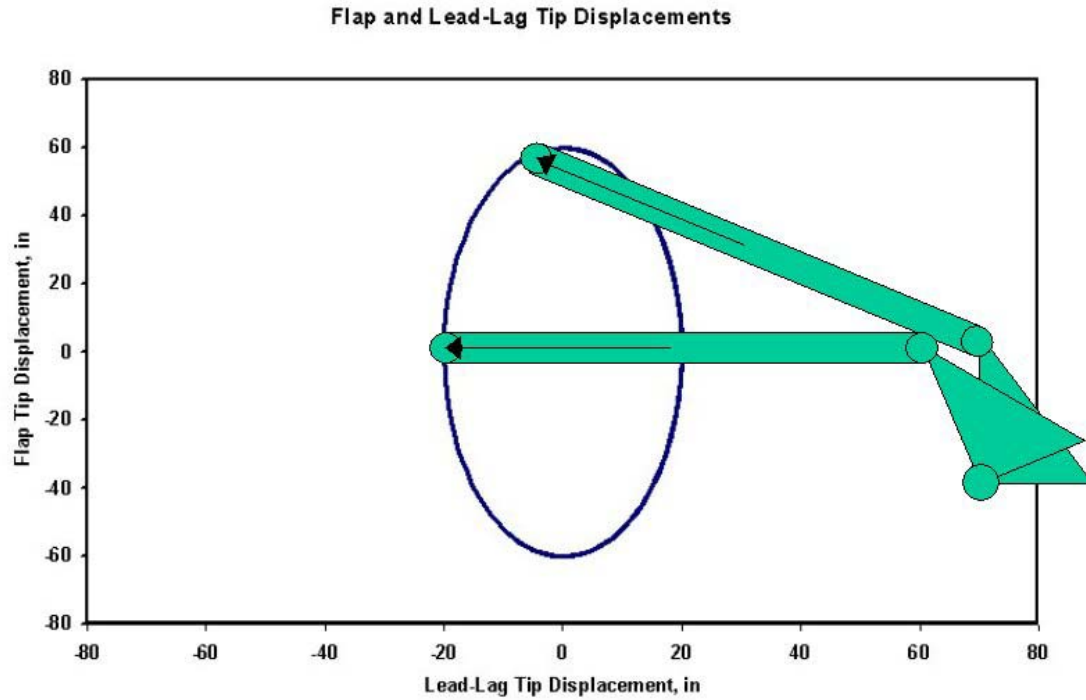
Figure 6-3. Effect of blade flap displacement on linkage position

The bell crank is intended to supply only the lead-lag forces during fatigue testing but it is not kinematically possible for the linkage to supply a force only in the lead-lag direction.

6.1.1.1 Bell Crank Influence

To analyze the influence that the bell crank has on the application of flap forces, the coordinate systems defined in Figure 6-4 have been used. In this case, x has been used to describe motion in the lead-lag (horizontal) direction and y has been used to describe motion in the flap (vertical) direction.

126
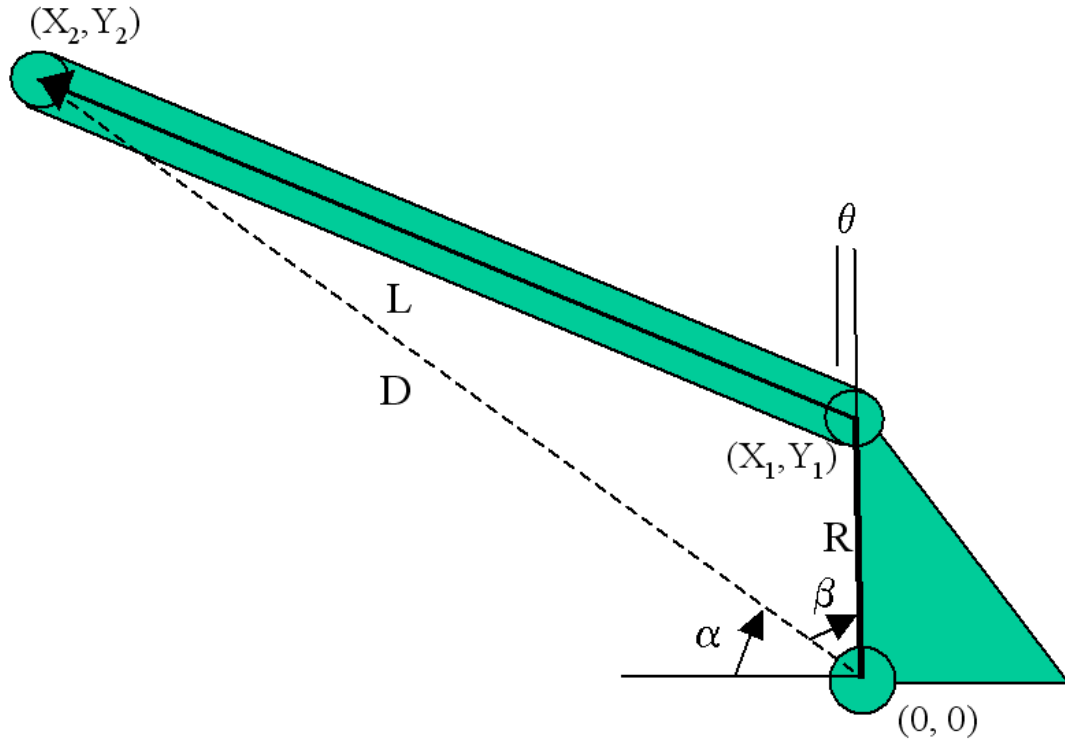
Figure 6-4. Bell crank coordinate systems

Using the above coordinate systems and knowledge about the test system, it is possible to write the following equations (Equations 6.6-6.10) about the bell crank kinematics. It should be recognized that the independent variables in these equations are the displacements of the blade in the flap and lead-lag direction (x_{LL} and y_F). The location of the endpoints of the push rod and the push rod slope are dependent variables.

$$x_1 = R\sin(\theta)$$
$$y_1 = R\cos(\theta)$$
$$x_2 = -L + x_{LL}$$
$$y_2 = R + y_F$$
$$\frac{f_F}{f_{LL}} = m_{pr} = \frac{(y_2 - y_1)}{(x_2 - x_1)}$$

(6.6-6.10)

Where,

X_1	= Lead-Lag position of Bell Crank
Y_1	= Flap position of Bell Crank
X_2	= Lead-Lag position of Blade
Y_2	= Flap position of Blade
X_{LL}	= Lead-Lag displacement of Blade
Y_F	= Flap displacement of Blade
θ	= Angle of Bell Crank
R	= Length of Bell Crank

$$
\begin{array}{ll}
L & = \text{Length of Push Rod} \\
m_{pr} & = \text{Slope of Push Rod} \\
f_{LL} & = \text{Force in the Lead-Lag direction} \\
f_F & = \text{Force in the Flap direction}
\end{array}
$$

The influence of the bell crank on the flap forces is clearly a function of the push rod slope. When the slope of the push rod is zero, no component of the lead-lag force is applied in the flap direction. To use the push rod slope effectively in future dynamic calculations, it is necessary to determine the slope as a function of the independent variables. As shown by Equation 6.11, the slope of the push rod can be expressed as a function of the independent variables plus the angle of the bell crank but the angle of the bell crank is not an independent variable.

$$
m_{pr} = \frac{y_F + R - R\cos(\theta)}{x_{LL} - L - R\sin(\theta)} \tag{6.11}
$$

To find the angle of the bell crank, several new equations were produced using the geometry of the bell crank mechanism and the designated coordinate system. Equations 6.12-6.15 show the calculations required to determine the angle of the bell crank as a function of the independent variables.

$$
\begin{aligned}
D^2 &= x_2^2 + y_2^2 = (x_{LL} - L)^2 + (y_F + R)^2 \\
\sin(\alpha) &= \left(\frac{y_F + R}{D} \right) \\
\cos(\beta) &= \left(\frac{L^2 - R^2 - D^2}{2RD} \right) \\
\theta &= 90 - \alpha - \beta
\end{aligned} \tag{6.12-6.15}
$$

Where,

$$
\begin{array}{ll}
D & = \text{Length of trapezium diagonal} \\
\alpha & = \text{Angle from diagonal to horizontal axis} \\
\beta & = \text{Angle from diagonal to Bell Crank}
\end{array}
$$

Combining Equations 6.12-6.15, results in Equation 6.16.

$$
\theta = 90 - \sin^{-1}\left(\frac{y_F + R}{(x_{LL} - L)^2 + (y_F + R)^2} \right) - \cos^{-1}\left(\frac{L^2 - R^2 - \left[(x_{LL} - L)^2 + (y_F + R)^2 \right]^2}{2R\left((x_{LL} - L)^2 + (y_F + R)^2 \right)} \right) \tag{6.16}
$$

The slope as a function of the independent variable is shown in Equation 6.17.

$$m_{pr} = \frac{y_F + R - R\cos\left[90 - \sin^{-1}\left(\frac{y_F + R}{(x_{LL} - L)^2 + (y_F + R)^2}\right) - \cos^{-1}\left(\frac{L^2 - R^2 - \left[(x_{LL} - L)^2 + (y_F + R)^2\right]^2}{2R\left((x_{LL} - L)^2 + (y_F + R)^2\right)}\right)\right]}{x_{LL} - L - R\sin\left[90 - \sin^{-1}\left(\frac{y_F + R}{(x_{LL} - L)^2 + (y_F + R)^2}\right) - \cos^{-1}\left(\frac{L^2 - R^2 - \left[(x_{LL} - L)^2 + (y_F + R)^2\right]^2}{2R\left((x_{LL} - L)^2 + (y_F + R)^2\right)}\right)\right]} \quad (6.17)$$

Although this is the exact slope of the push rod, the slope used for dynamic calculations was simplified by assuming that the length of the push rod, L, is long relative to the other terms. As shown by Equation 6.18, the simplified push rod slope equation is much easier to work with.

$$m_{pr} = \frac{y_F}{\sqrt{L^2 - y_F^2}} \quad (6.18)$$

To evaluate the amount of error introduced by using the simplified slope equation, the two equations (6.17 and 6.18) were compared. As shown by Figure 6-5, the approximation for the slope equation has an error of approximately 2% when compared to the exact slope equation. Since the error is small, the simplified equation will be used to evaluate the influence of the bell crank on the system dynamics.
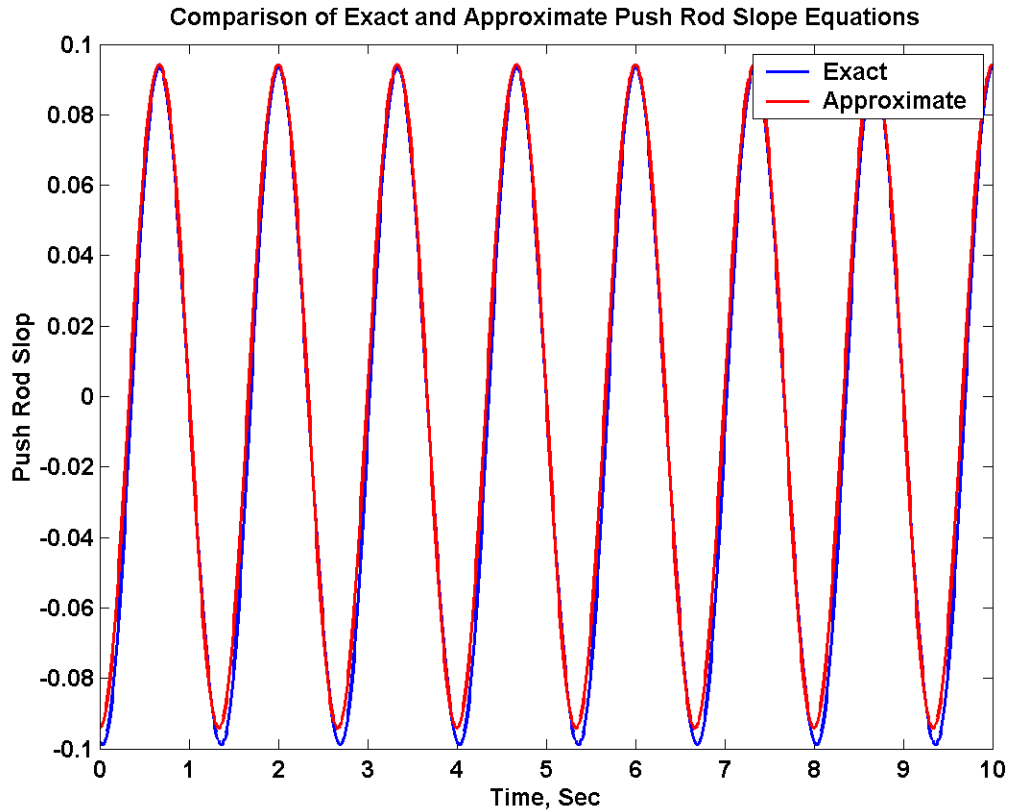
Figure 6-5. Exact and approximation push rod slope functions

As shown in Figure 6-6, a noticeable component of the bell crank force is transmitted to the blade in the flap direction. For the dual-axis forced displacement system discussed in Chapter 3, the flap forces produced by the bell crank are not significant compared to the flap forces because the system is operating away from the resonance frequency. Since the forced-displacement system controls the blade displacement directly, the bell crank load variation does not affect the fatigue test. Since the resonance test system relies on smaller flap forces to provide the target displacement, the flap force component contributed by the bell crank must be considered in the dynamic analysis of the system.
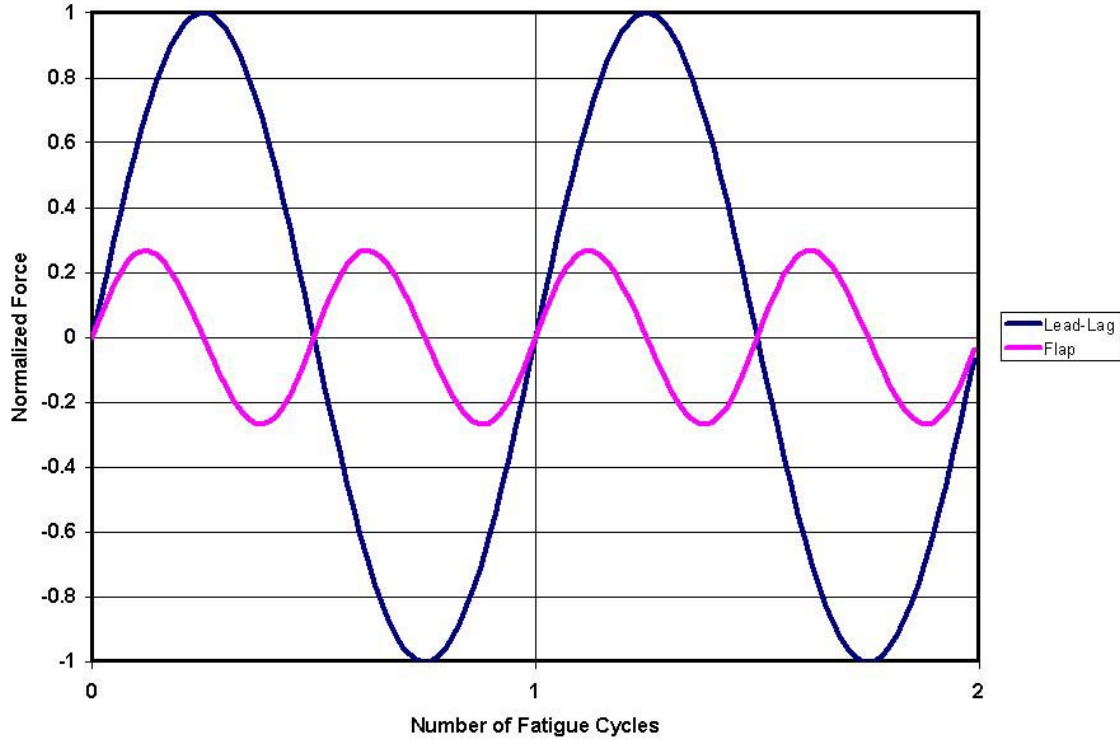
Figure 6-6. Relative alternating forces applied by the bell crank linkage

The influences of the bell crank have been added to the dynamic model. The system is shown in state space form in Equation 6.19. Note that the flap and lead-lag blade displacements are not coupled in the dynamic matrix but are coupled in the force matrix.

$$[\dot{x}] = \begin{bmatrix} 0 & 1 & 0 & 0 \\ -\omega_{nx}^2 & -2\zeta\omega_{nx} & 0 & 0 \\ 0 & 0 & 0 & 1 \\ 0 & 0 & -\omega_{ny}^2 & -2\zeta\omega_{ny} \end{bmatrix}[x] + \begin{bmatrix} 0 & 0 \\ \dfrac{\omega_{nx}^2}{k_x} & 0 \\ 0 & 0 \\ \dfrac{\omega_{ny}^2}{k_y}\left(\dfrac{x_4}{\sqrt{L^2 - x_4^2}}\right) & \dfrac{\omega_{ny}^2}{k_y} \end{bmatrix}\begin{bmatrix} f_x(t) \\ f_y(t) \end{bmatrix} \quad (6.19)$$

Where,

ω_{nx} = Blade Lead-Lag Fundamental Frequency

130

$$\zeta \qquad = \text{Blade Damping Ratio}$$

$$\omega_{ny} \qquad = \text{Blade Flap Fundamental Frequency}$$

$$k_x \qquad = \text{Lead-Lag Bending Stiffness at Blade Tip}$$

$$k_y \qquad = \text{Flap Bending Stiffness at Blade Tip}$$

$$f_x \qquad = \text{Target Lead-Lag Bending Force at Blade Tip}$$

$$f_y \qquad = \text{Target Flap Bending Force at Blade Tip}$$

$$\text{L} \qquad = \text{Length of Bell Crank Linkage}$$

6.1.2 Phase Angle Progression

As discussed in chapter 2 and in more detail in chapter 5, the phase angle between the flap blade displacement and the lead-lag blade displacement may vary for a variety of blade fatigue tests. As a result, the control system will be analyzed for two variations of the test. The first variation will have a constant phase angle between the flap and lead-lag input forces. The second variation will progressively vary the phase angle throughout the test. The target input forces are shown in Equations 6.20-6.21.

$$f_y(t) = A_x Sin(\omega t)$$

$$f_x(t) = A_y Sin(\omega t + \phi_i) \qquad (6.20\text{-}6.21)$$

Where,

$$\text{y} \qquad = \text{Flap Direction}$$
$$\text{x} \qquad = \text{Lead-Lag Direction}$$
$$f_x, f_y \qquad = \text{Target Force in the Flap and Lead-Lag Directions}$$
$$A_x, A_y = \text{Force Magnitude in the Flap and Lead-Lag Directions}$$
$$\omega \qquad = \text{Excitation frequency}$$
$$\phi_i \qquad = \text{Phase Angle for i}^{\text{th}} \text{ cycle}$$

Each phase angle will be a step change from the previous phase angle. For the controls analysis, a general phase angle progression based on the distribution in chapter 3 has been chosen. Since the dynamic response of the system is based on the step change in phase angle, the system response to the general distribution will be similar to the system response for the optimal distribution that will be described in chapter 5. The general phase angle progression was derived from the aggregate phase angle distribution described in chapter 2. For reference, the phase angle distribution from Figure 2-38 is shown again in Figure 6-7.
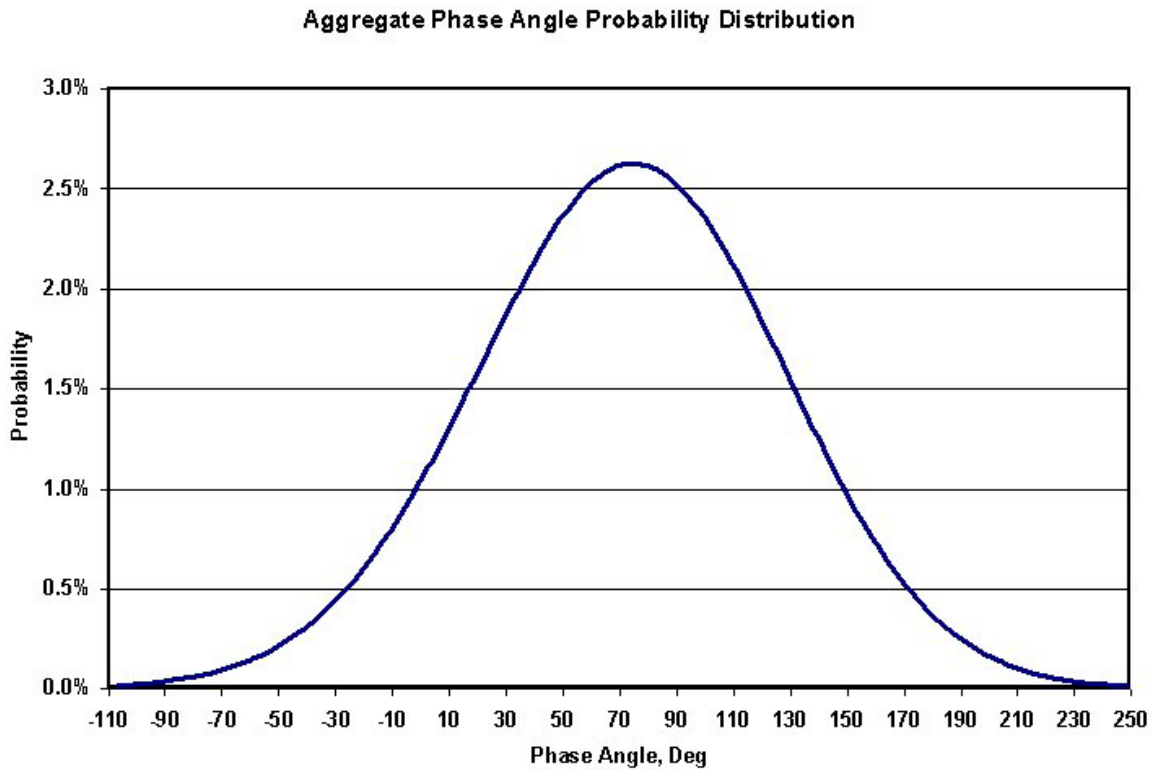
Figure 6-7. Target phase angle distribution for 1.5-MW turbine

The general phase angle progression was determined by weighting the above distribution by the total number of cycles. This distribution was divided by the desired number of repetitions for a fatigue test and then each bin was rounded to the nearest whole number of cycles. A phase angle time history was assembled by dwelling on each phase angle for the prescribed number of cycles before stepping to the next phase angle. The result of compilation is shown in Figure 6-8. This method for determining the phase angle history is useful for creating a generic phase angle history that results in the phase angle distribution shown in Figure 6-7.

One Phase Angle Progression per Complete Test
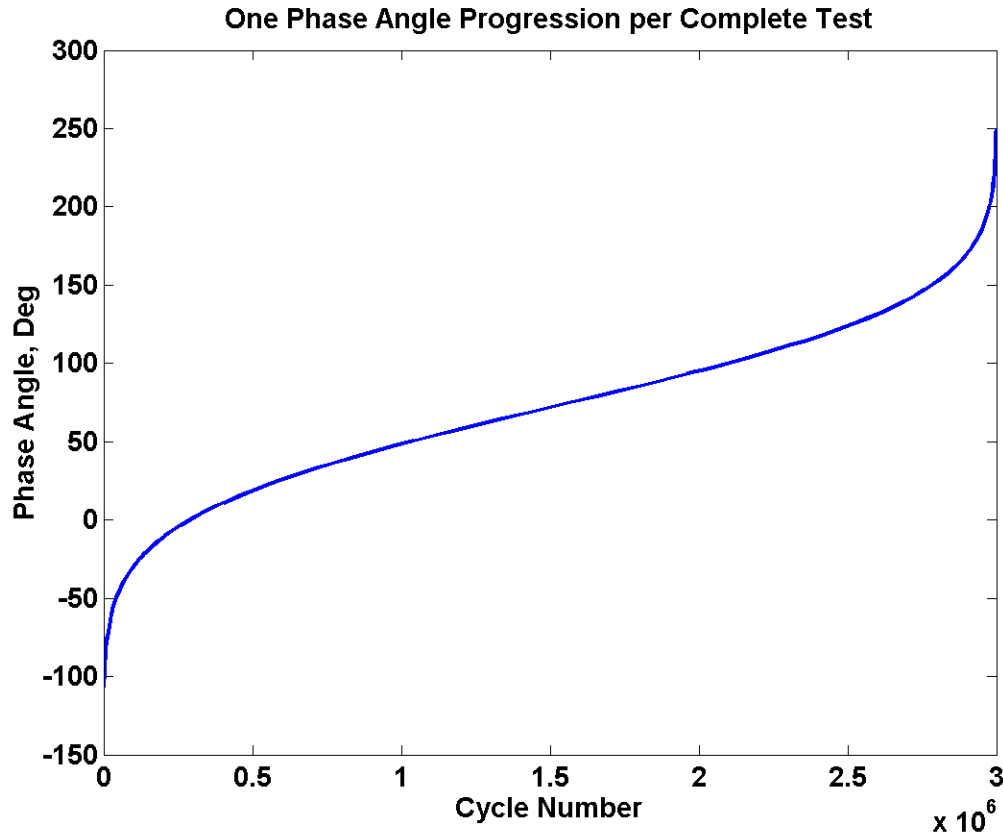
Figure 6-8. Sample phase angle progression for complete fatigue test

Having defined the system dynamics and input forces, controllers were designed to maintain system performance throughout a fatigue test. Both PID and full-state feedback controllers were designed.

6.2 PID Controller Design

NREL currently uses PID controllers [135] to maintain adequate test performance for the Dual-Axis Forced-Displacement test described in previous chapters. Current tests have a constant phase angle between the flap and lead-lag maximum displacements. For this study, a PID controller has been designed for the Dual-Axis Resonance Test system. The system response using a PID controller with constant and variable phase angles has been considered. Since NREL already has the software and working knowledge required to operate PID controllers, it would advantageous to continue using this type of controller for the Resonance Test System if the performance were adequate. The main purpose of this investigation is to determine which control strategies result in stable operation.

6.2.1 PID Dynamic Simulation

The dynamic system described above by Equations 6.22-6.24 was modeled using Matlab's Simulink. The block diagram for this system is shown in Figure 6-9. The values for the PID were determined experimentally.
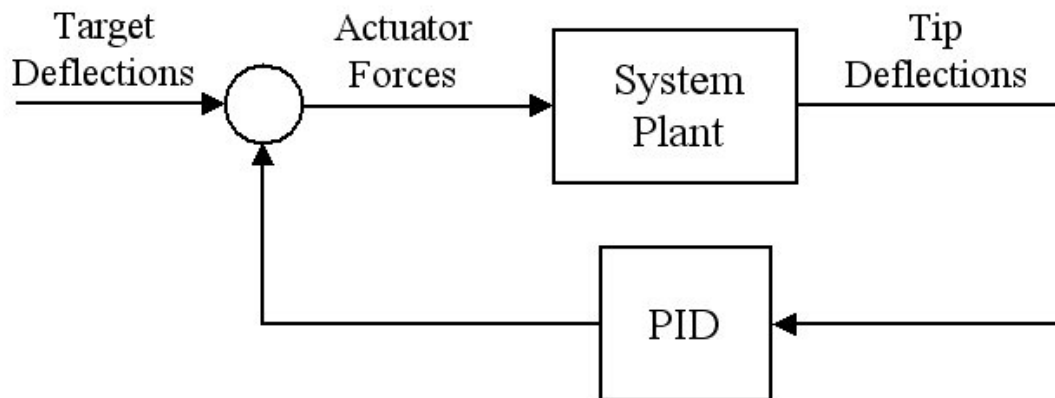
Figure 6-9. PID block diagram

The resulting Simulink model for this system is shown in Figure 6-10. The flap and lead-lag equations of motion are contained in separate blocks but the systems are coupled by the nonlinear interaction between the flap and the lead-lag forces. The delay between the controller signal and the actuator response has also been included. This delay was measured for a specific actuator and generalized as approximately 0.05 seconds for the entire system.
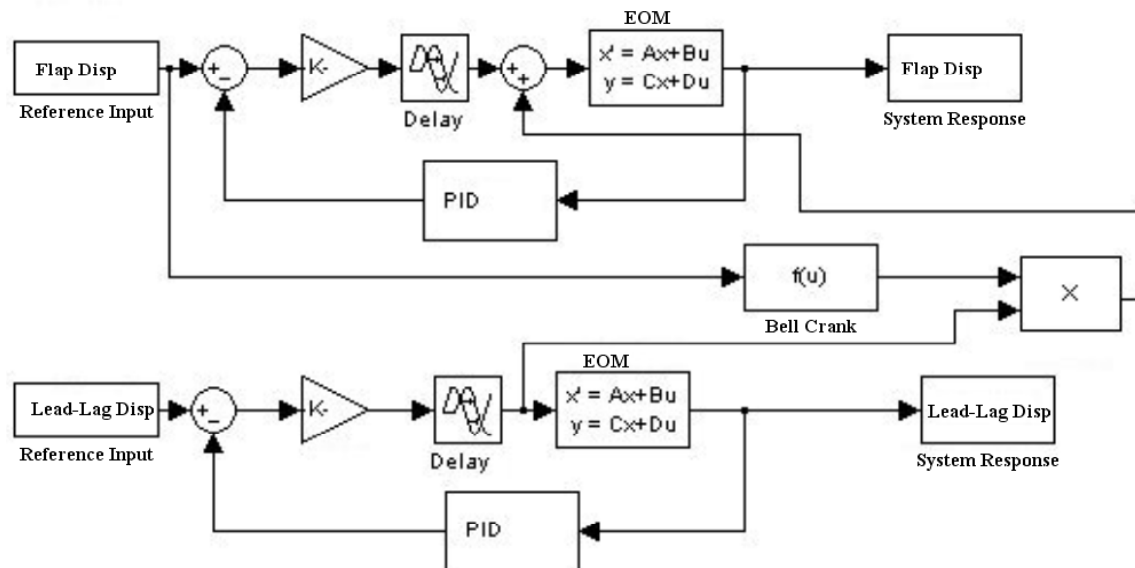
Figure 6-10. Simulink representation of resonance test system with PID controller

6.2.1.1 Constant Phase Angle Simulations

Current fatigue tests use a PID control to maintain system parameters but these tests are also conducted with a constant phase angle. While the phase angle is specified by the wind turbine blade manufacturer and depends on the force characteristics as described in chapter 2, the testing phase angle has traditionally been approximately 72 degrees for most large wind turbines. From the study discussed in chapter 2, it can be seen that 72 degrees is approximately the mean phase angle of the flap and lead-lag loads for the rated wind speed. Although it is believed to be more accurate to test wind turbine blades with a variation of phase angles, it is still important to consider the effectiveness of the controllers for the traditional fixed phase angle case.

As shown in Figure 6-11, the PID controller provides good dynamic performance for the flap displacement. For the purpose of fatigue testing, it is important that the maximum and minimum flap displacement consistently repeat throughout the test.
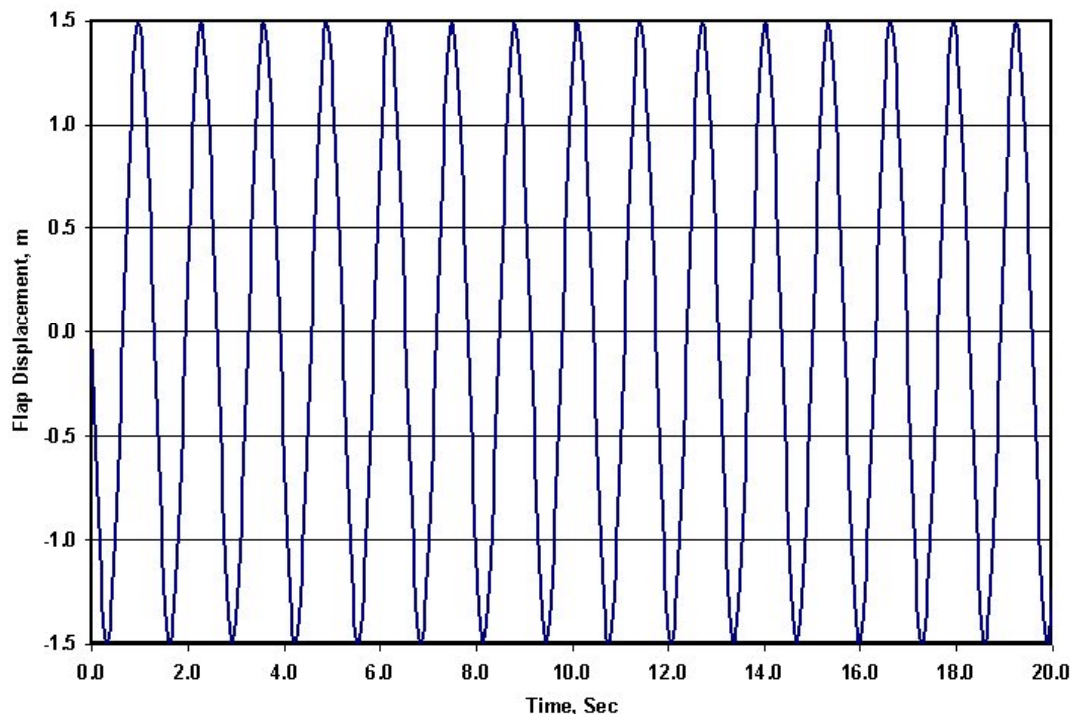
Figure 6-11. PID steady state blade flap displacement for constant phase angles

The performance of the PID controller was also sufficient for the lead-lag displacement. Figure 6-12 shows that the lead-lag displacement extrema are consistent when a fixed phase angle is maintained between the flap and lead-lag input signals.
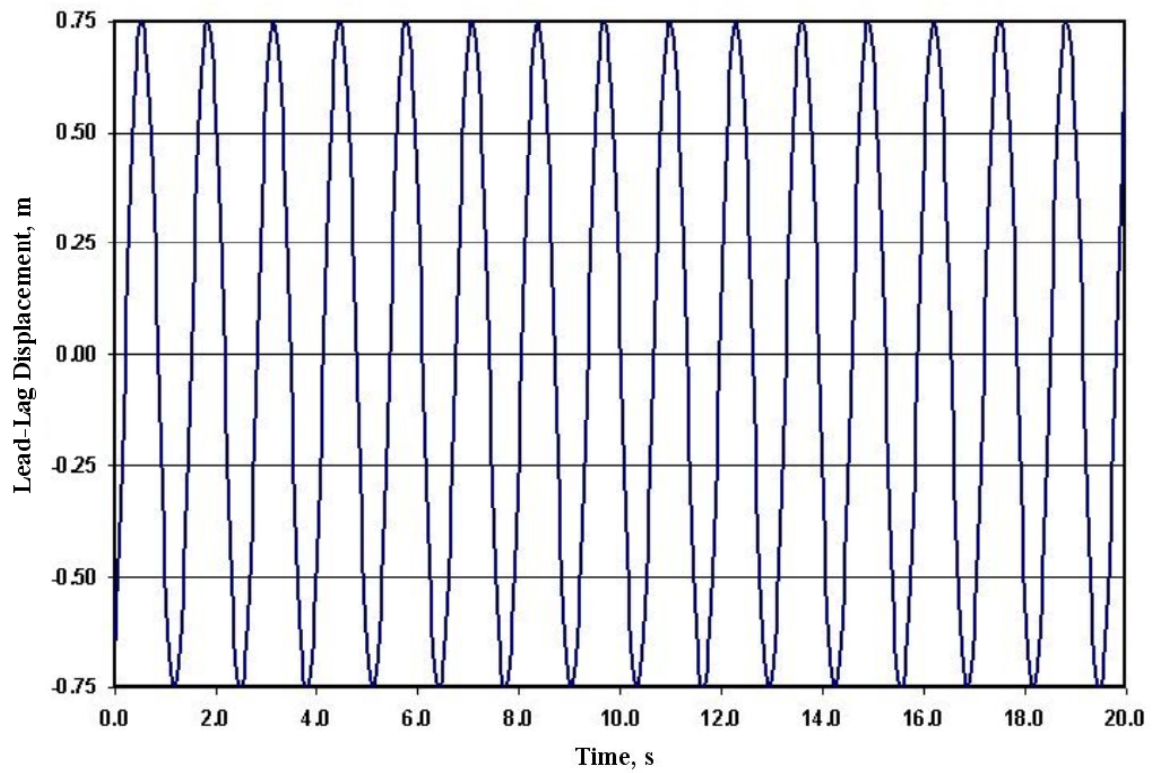
Figure 6-12. PID steady state lead-lag displacement for constant phase angles

6.2.1.2 Progressive Phase Angle Simulation

Since the phase angle between the flap and lead-lag displacements do vary during actual operation, it is believed that varying the phase angles during testing will result in a more accurate fatigue test. While the validity of this claim will be discussed in more detail in chapter 5, the variation in phase angle presents interesting dynamic challenges for the system controller. As such, the effect of applying step changes to the phase angle during testing has been considered in this study.

As shown in Figure 6-13, the change in phase angle causes an unstable displacement response for the blade. This behavior could be related to several of the system characteristics. The interdependence of the flap and lead-lag displacements make it possible for either of the 'systems' to cause instability for the entire blade.
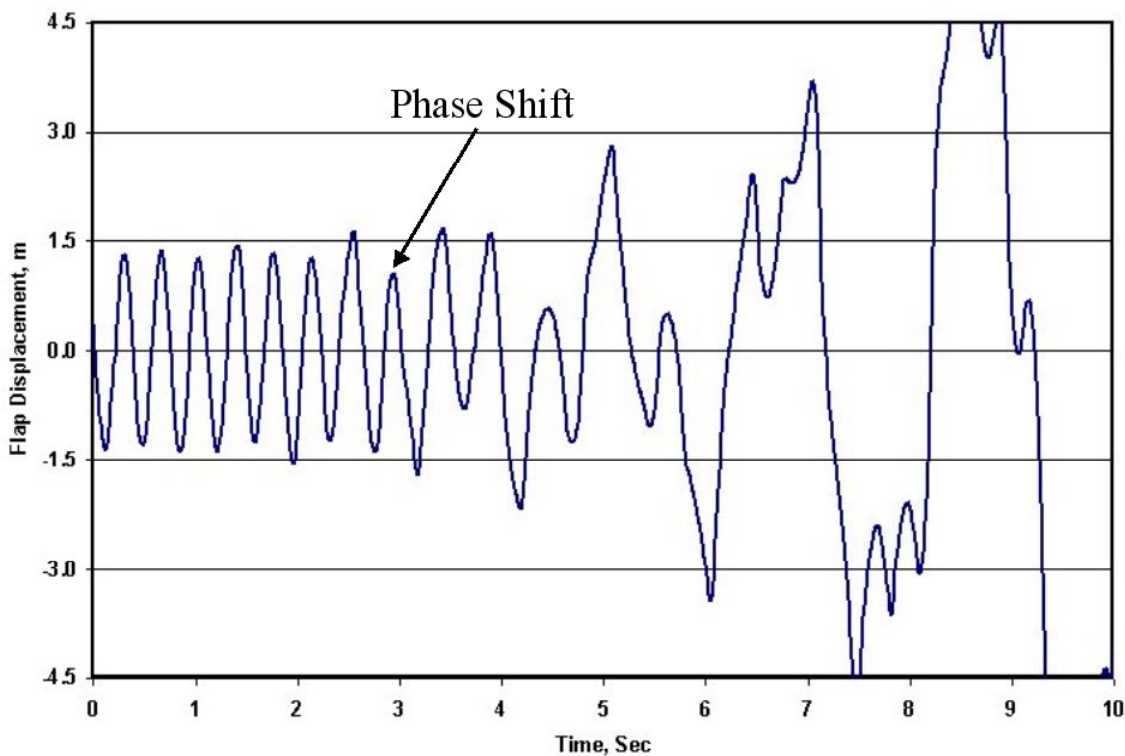
Figure 6-13. PID flap blade response for progressive phase angles

Since the lead-lag fundamental blade frequency is different from the flap fundamental frequency and therefore the excitation frequency, the amplification between the lead-lag force and lead-lag displacement is relatively small. As a result, any step response in the target lead-lag displacements will result in large lead-lag forces. While this behavior is undesirable, it is difficult to remove using the PID controller.

137

6.2.2 Summary

The PID controller is well suited to control the blade response during fatigue testing of wind turbine blades when a constant phase angle exists between the flap and lead-lag target displacements. When the phase angle between the flap and lead-lag target displacements is varied, the resulting blade response is less desirable. The nonlinear system may experience instability when a step shift in phase angle is applied to the target lead-lag displacement. While this behavior is undesirable, it should be noted that the blade system has been simplified for the purpose of this model. Nonlinear damping and stiffness characteristics not modeled may result in a different blade response than the one simulated. Although this study has shown that the PID controller is not well suited for controlling the blade response for a progressive phase angle fatigue test, it would still be advantageous to experimentally validate these findings.

6.3 Full-State Feedback Controller Design

While the PID controller has certain advantages, such as already being installed and well understood by NREL staff, it also has certain disadvantages. The PID parameters are largely determined by empirical methods. When a problem in the system response is detected, it may be difficult to determine the best set of parameters that result in the best performance. While it is possible to apply an optimization scheme such as LQR, the PID control has a limited degree of flexibility to improve the problem. For linear systems, a full-state feedback controller can be designed using more straightforward methods than the PID controller. For the purpose of this analysis, the blade/test plant was linearized about the mean operating condition and pole placement was used to contour the system response. The main purpose of this investigation is to determine if the full-state feedback controller can result in stable operation during fatigue testing.

6.3.1 Linear Equations of Motion

The nonlinear interaction between the flap and lead-lag forces was linearized around the mean blade response. In this case, the mean blade response has a value of zero for the lead-lag displacement. The resulting linearized blade equation of motion is shown in Equation 6.22.

$$[\dot{x}] = \begin{bmatrix} 0 & 1 & 0 & 0 \\ -\omega_{nx}^2 & -2\zeta\omega_{nx} & 0 & 0 \\ 0 & 0 & 0 & 1 \\ 0 & 0 & -\omega_{ny}^2 & -2\zeta\omega_{ny} \end{bmatrix} [x] + \begin{bmatrix} 0 & 0 \\ \dfrac{\omega_{nx}^2}{k_x} & 0 \\ 0 & 0 \\ 0 & \dfrac{\omega_{ny}^2}{k_y} \end{bmatrix} \begin{bmatrix} f_x(t) \\ f_y(t) \end{bmatrix} \quad (6.22)$$

To evaluate the system performance, the root locus of the linearized system was calculated. The pole locations for the target blade are shown in Figure 6-14.
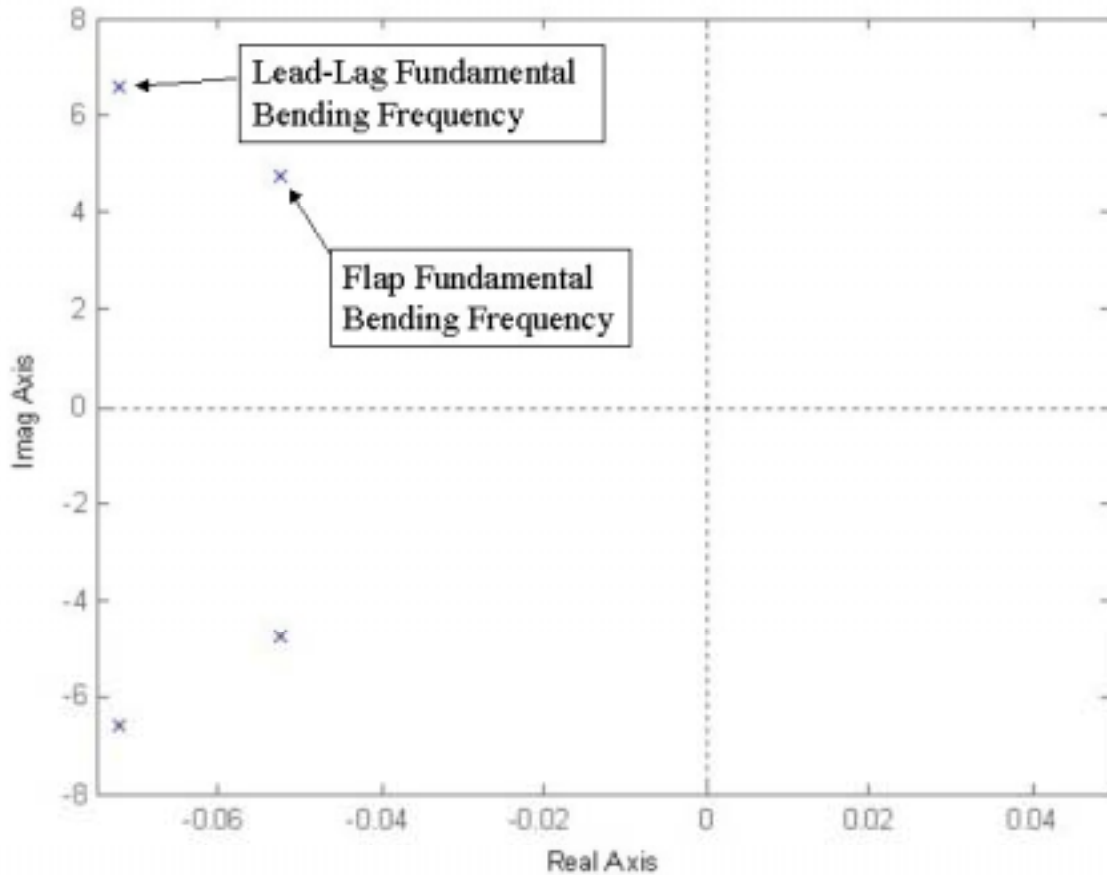
Figure 6-14. Root locus for linear blade model

6.3.2 Control Strategy

Pole placement was used to contour the blade dynamics. When using pole placement, some or all of the existing system poles are moved from an undesirable location to a more optimal location. The system dynamics are controlled by adding a set of zeros that cancel out the unwanted poles and a new set of poles at the desired location. In many cases, the poles are moved further into the left half plane to increase the overall system stability. In other cases, the poles are moved away from the frequency of excitation to avoid unwanted resonance excitation. In this case, a different pole placement strategy has been used.

As shown in Figure 6-15, the lead-lag poles have been moved to coincide with the excitation frequency. Effectively, the damped natural frequency of the controlled lead-lag equation of motion has been modified to coincide with the natural frequency of the flap equation of motion.

139
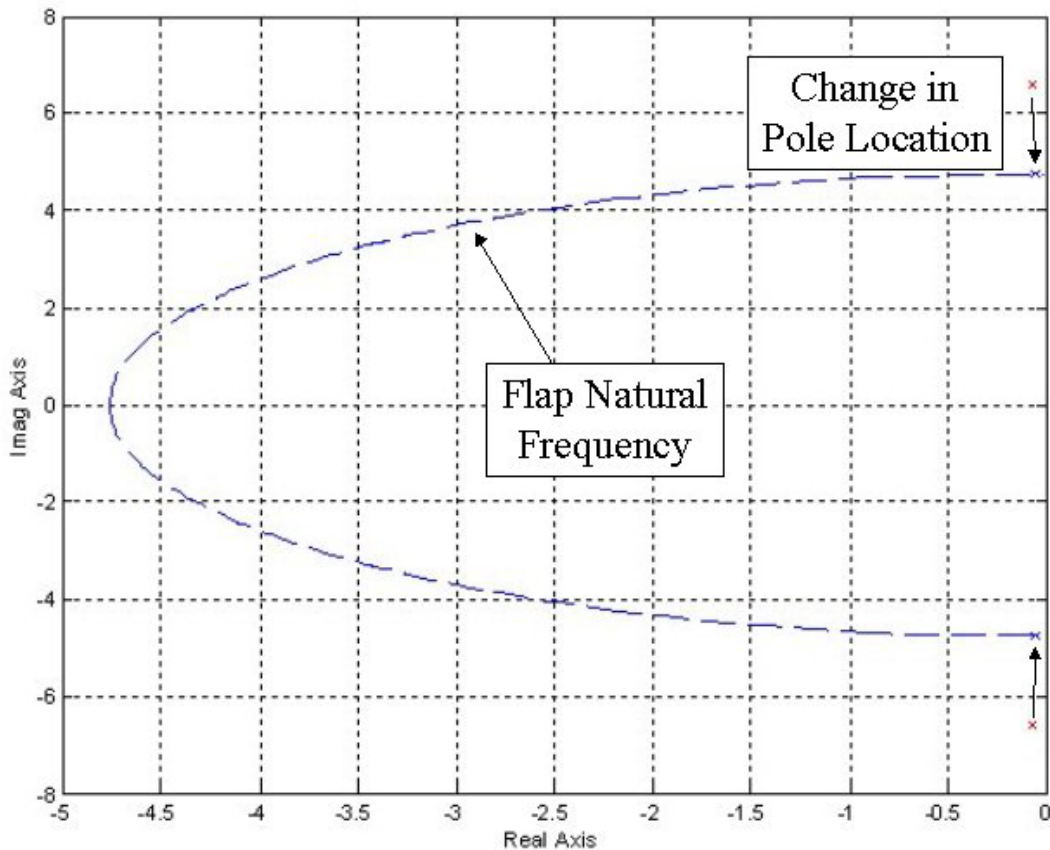
Figure 6-15. Pole placement control strategy for linear blade model

In most cases, it would be undesirable to change the resonance frequency to coincide with the excitation frequency. In this case, the primary target response of the blade agrees with the flap natural frequency. Any input forces that result in frequencies other than the flap resonance frequency are undesirable. By moving the lead-lag natural frequency to match flap natural frequency, the inputs from the lead-lag actuator are being weighted by the amplification ratio distribution shown in Figure 6-16. The forces generated by the lead-lag actuator in the flap direction are subsequently being attenuated by more than two orders of magnitude. So in this instance, placing the system poles on the excitation frequency is an effective way to mitigate input disturbances.
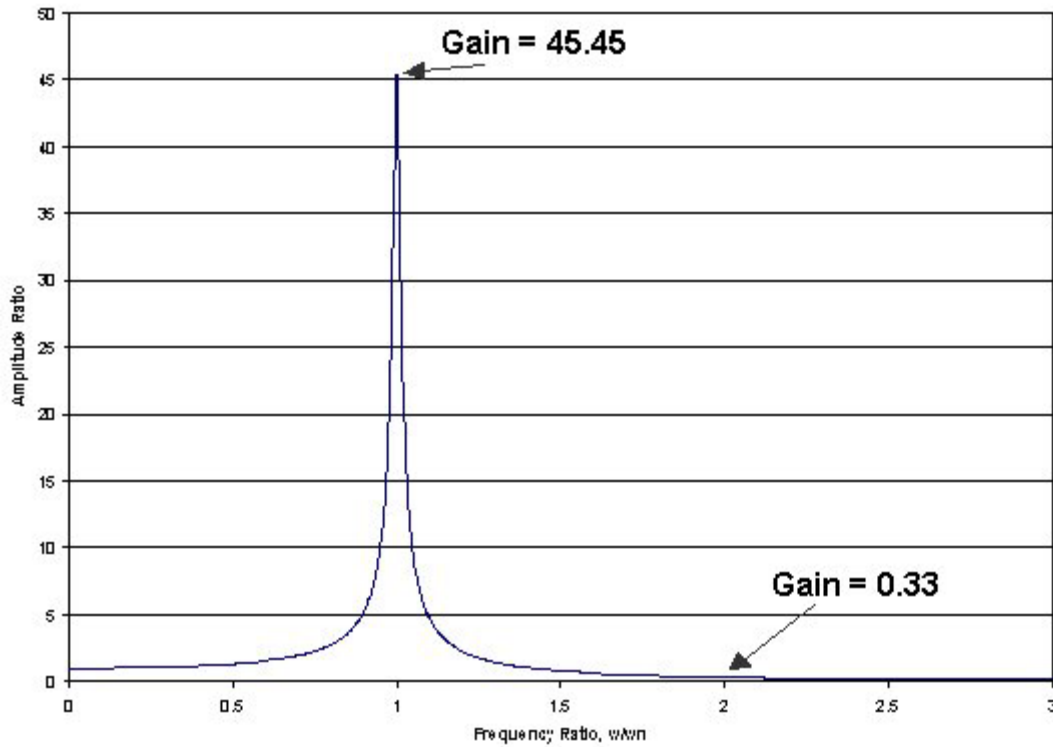
Figure 6-16. Amplification factor for SDOF system with target blade damping

The results of the control strategy illustrated above were evaluated for the linearized system for which it was designed and for the original nonlinear system.

6.3.3 Simulation of Linear Model with Control

The linear system described above was modeled in Simulink and evaluated with a constant phase angle (72 degrees) and the progressive phase angle distribution described earlier in this chapter. The Simulink model for the linear system with full-state feedback is shown below in Figure 6-17.

Figure 6-17. Simulink model for linearized blade and resonance test system

6.3.3.1 Simulation of Linear Model with Constant Phase Angles

The full-state feedback controller results in good dynamic performance for the blade. As shown in Figure 6-18, the flap displacement is fairly consistent when using the full-state feedback controller. There is actually more variation in the flap displacement extrema for the full-state feedback system than was present for the PID controller.
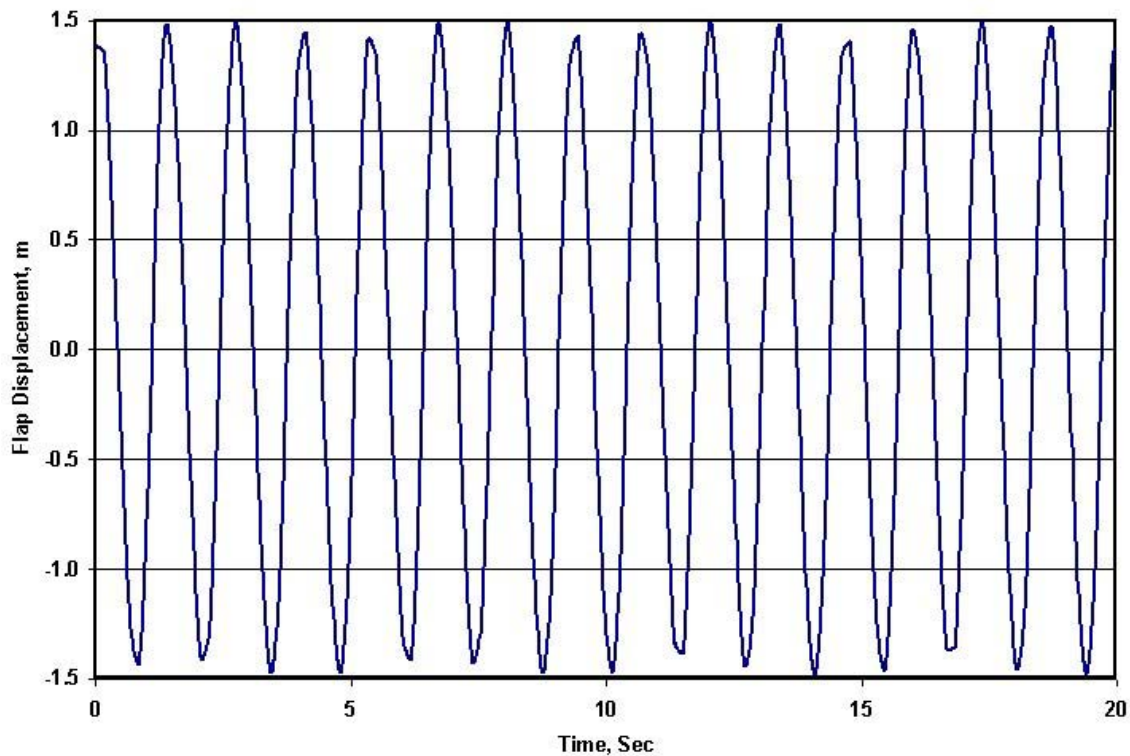
Figure 6-18. Full-state feedback blade flap response for constant phase angles

The lead-lag response using full-state feedback was very similar to the flap blade response. As shown in Figure 6-19, the performance for the lead-lag blade response was good but shows more variation than was present when using a PID controller.
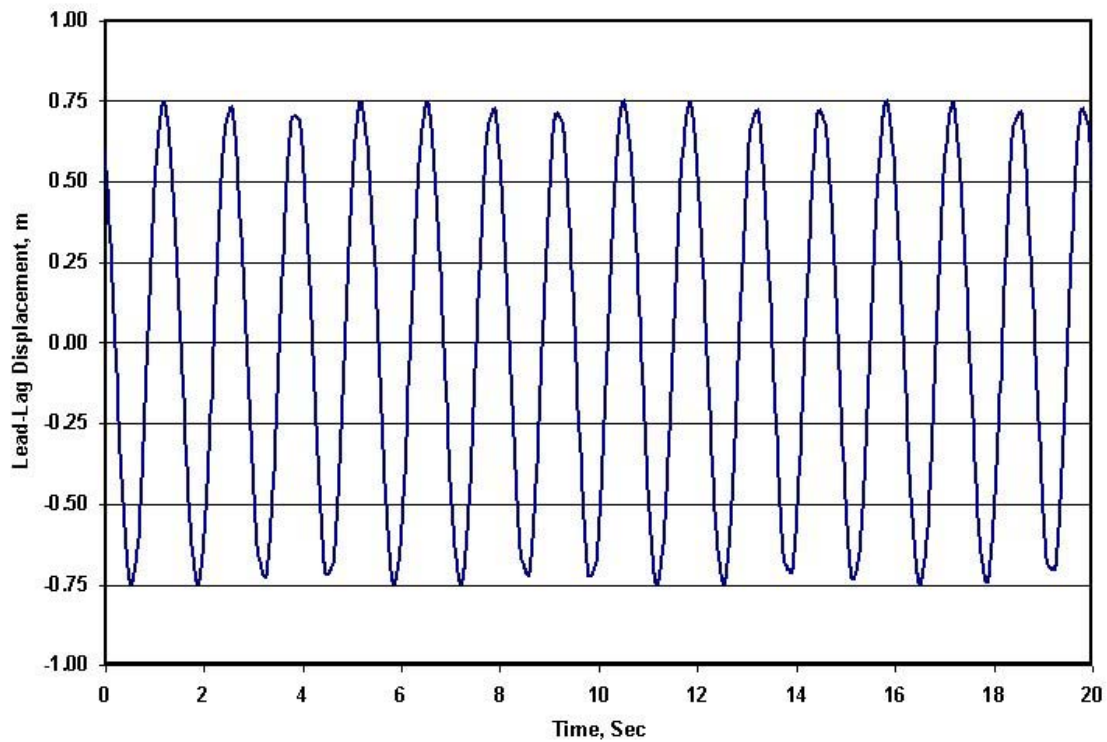
Figure 6-19. Full-state feedback lead-lag response for constant phase angles

In general, the full-state feedback performance was good for the linearized model. Since the model parameters were designed for the linear system, this result is not particularly surprising. Some variation in the displacement extrema was present but additional damping could be added to the system if desired.

144

6.3.3.2 Simulation of Linear Model with Progressive Phase Angles

The response of the linear system to a step change in phase angle was also investigated. The Simulink model used in the previous section was also used for this simulation. The blade's response was allowed to reach steady state and then the phase angle between the flap and lead-lag actuator forces was changed. The step change in actuator force takes place at approximately 4 seconds on Figures 6-20 and 6-21. Figure 6-20 shows very little variation in the flap displacement. Since linearizing the system also decoupled the flap and lead-lag blade responses, the flap actuator should not be affected by changes in the lead-lag actuator forces.
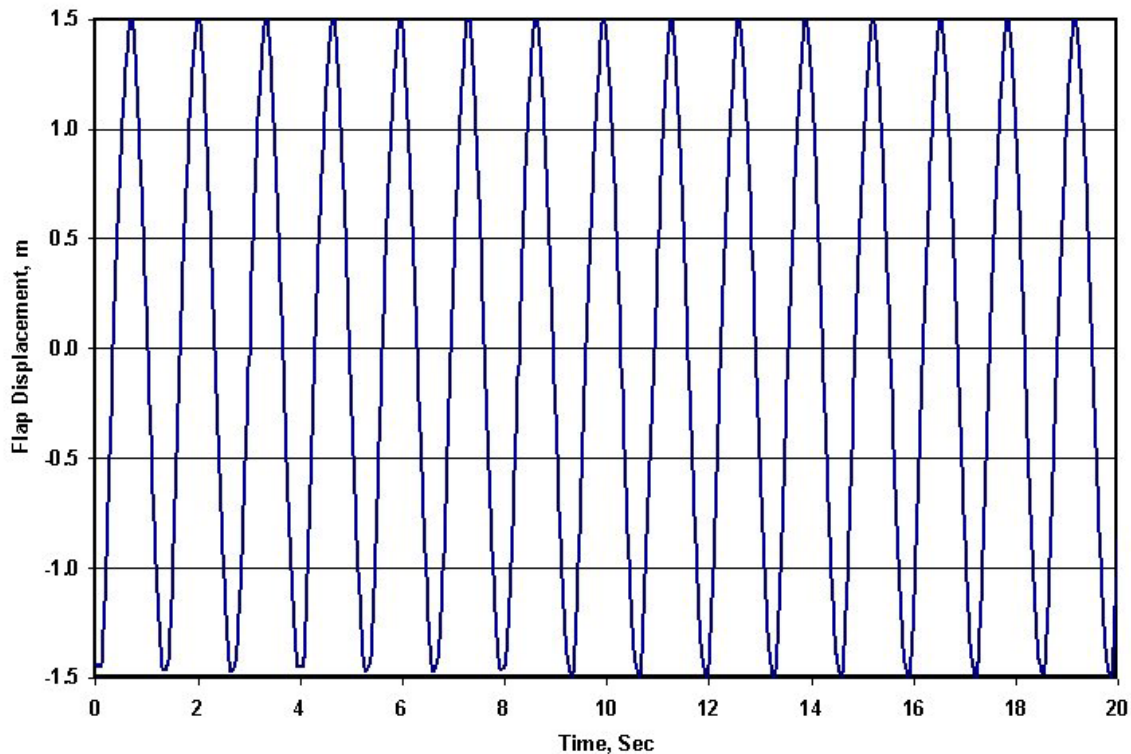
Figure 6-20. Full-state feedback blade flap response for progressive phase angles

As shown by Figure 6-21, the lead-lag displacement experiences higher extrema variations for several cycles after the shift in phase angle. The blade response remains stable and after a number of cycles (not shown) the extrema variations decrease.
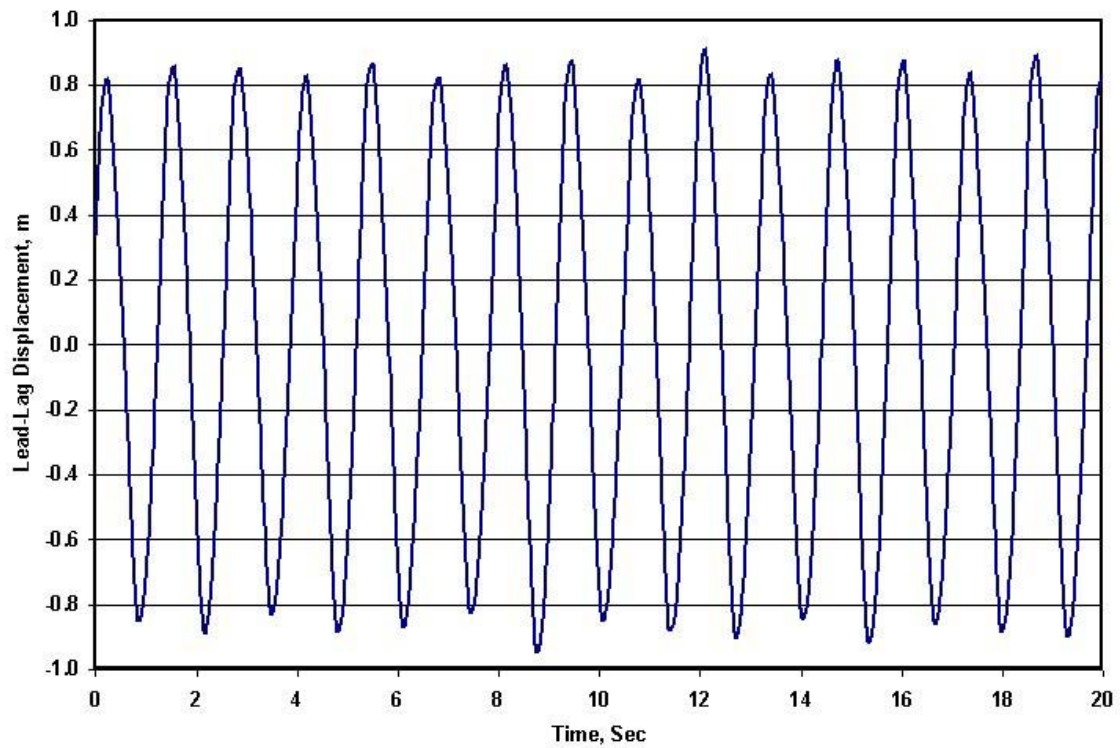
Figure 6-21. Full-state feedback lead-lag response for progressive phase angles

While the behavior of the linear system with full-state feedback are of interest, it is not possible to compare these results to the simulation for the PID controller since the PID control responses were for the nonlinear model.

6.3.4 Simulation of Non-linear Model with Control

The nonlinear interaction between the flap and lead-lag forces has been added to the Simulink model shown in Figure 6-22. The full-state feedback controller designed for the linearized system has been utilized for this study. The dynamic responses of the blade to a constant phase angle history and a progressive phase angle history have been investigated.

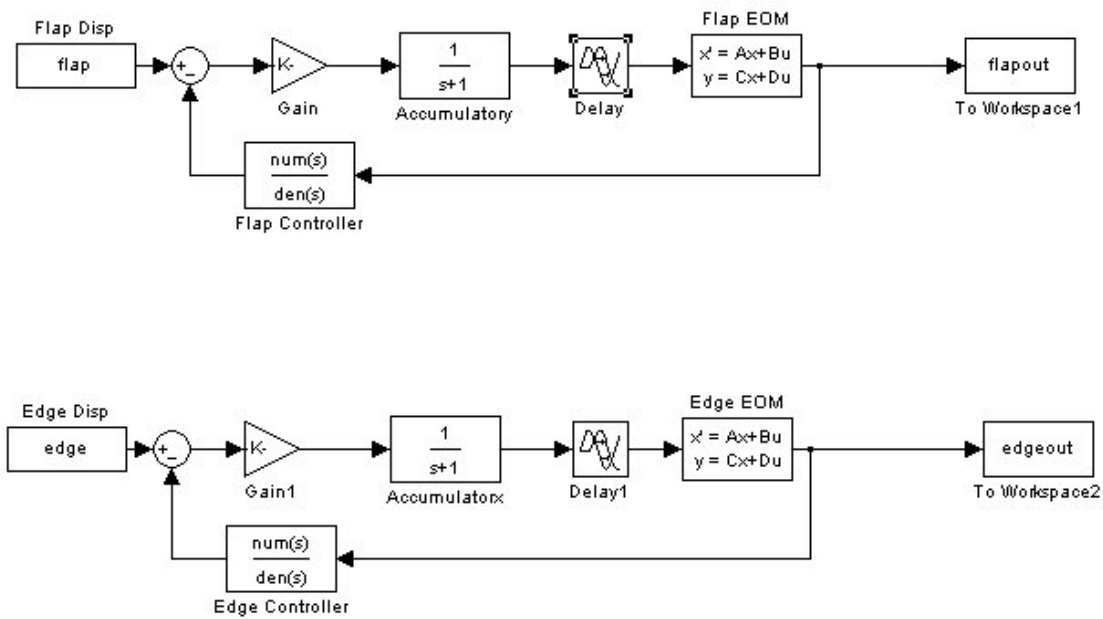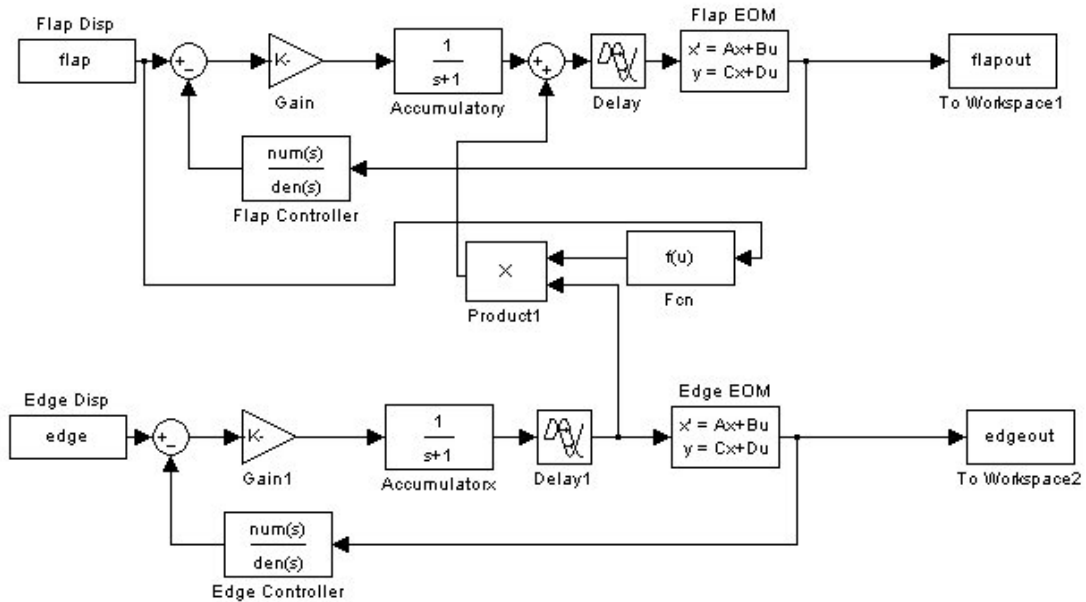**Figure 6-22. Simulink model for non-linear blade and resonance test system**

6.3.5 Simulation of Non-Linear Model with Constant Phase Angles

As shown in Figure 6-23, the flap displacement for the nonlinear system is fairly good. The variation in the flap displacement extrema is relatively small but still larger than the variation produced by the PID controller shown in Figure 6-11.
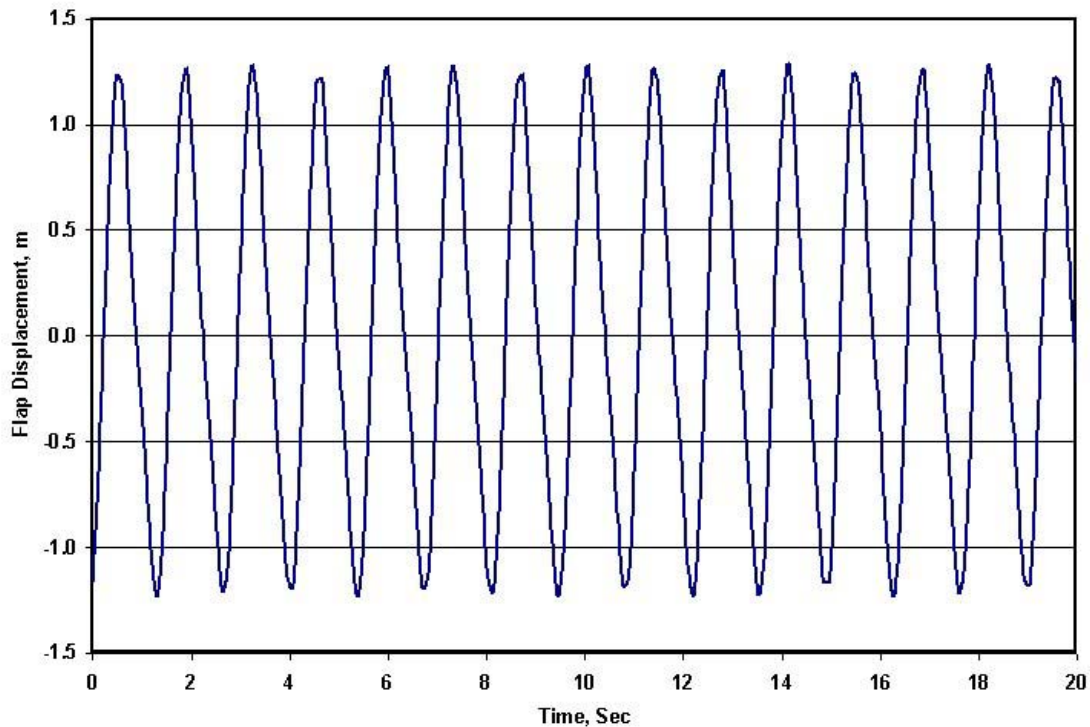
Figure 6-23. Full-state feedback blade flap response for constant phase angles

The variation in the lead-lag displacement extrema is also relatively small as shown by Figure 6-24. While moving the poles to add more damping to the system may result in better dynamic blade responses, it seems clear that both the full-state feedback and PID controllers provide adequate control for the nonlinear blade model with constant phase angles.
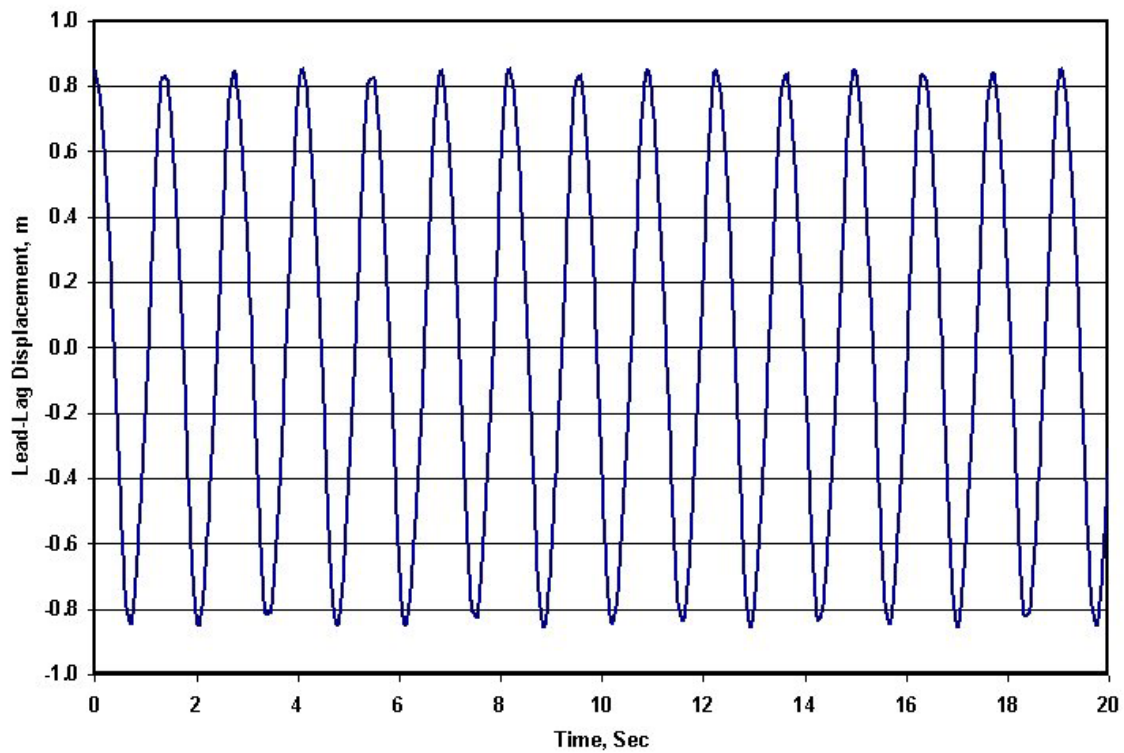
Figure 6-24. Full-state feedback lead-lag response for constant phase angles

6.3.6 Simulation of Non-Linear Model with Progressive Phase Angles

In general, the performance of the PID controller for constant phase angle loading is acceptable. As was shown above in Figure 6-13, the blade response for the PID controller with progressive phase angle loading was unstable. As a result, a full-state feedback controller has been designed. As shown in Figure 6-25, the full-state feedback controller designed using the control strategy described above results in stable operation. The flap displacement extrema for this controller are relatively small. As described previously, the lead-lag actuator force experiences a step change in the phase angle at approximately 4 seconds on Figures 6-25 and 6-26.

149
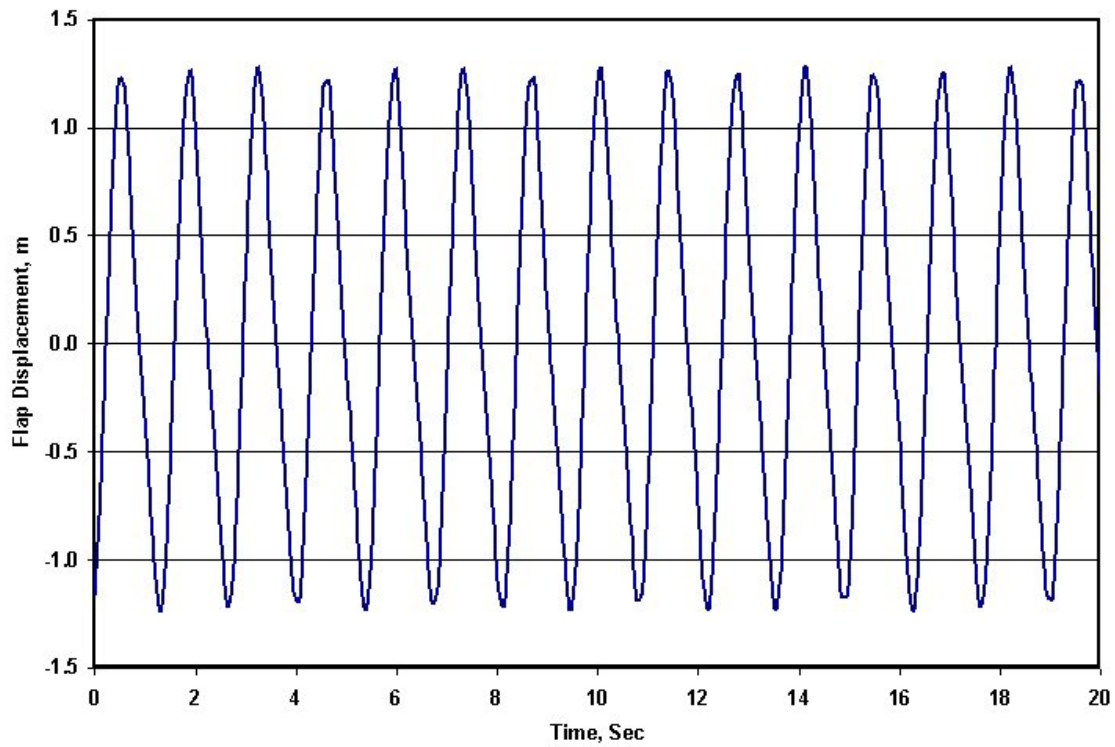
Figure 6-25. Full-state feedback blade flap response for progressive phase angles

The dynamic response of the blade in the lead-lag direction also shows stable operation as demonstrated in Figure 6-26. While the step change in phase angle results in an unstable system when using the PID controller, the full-state feedback controller provides stable operating conditions.
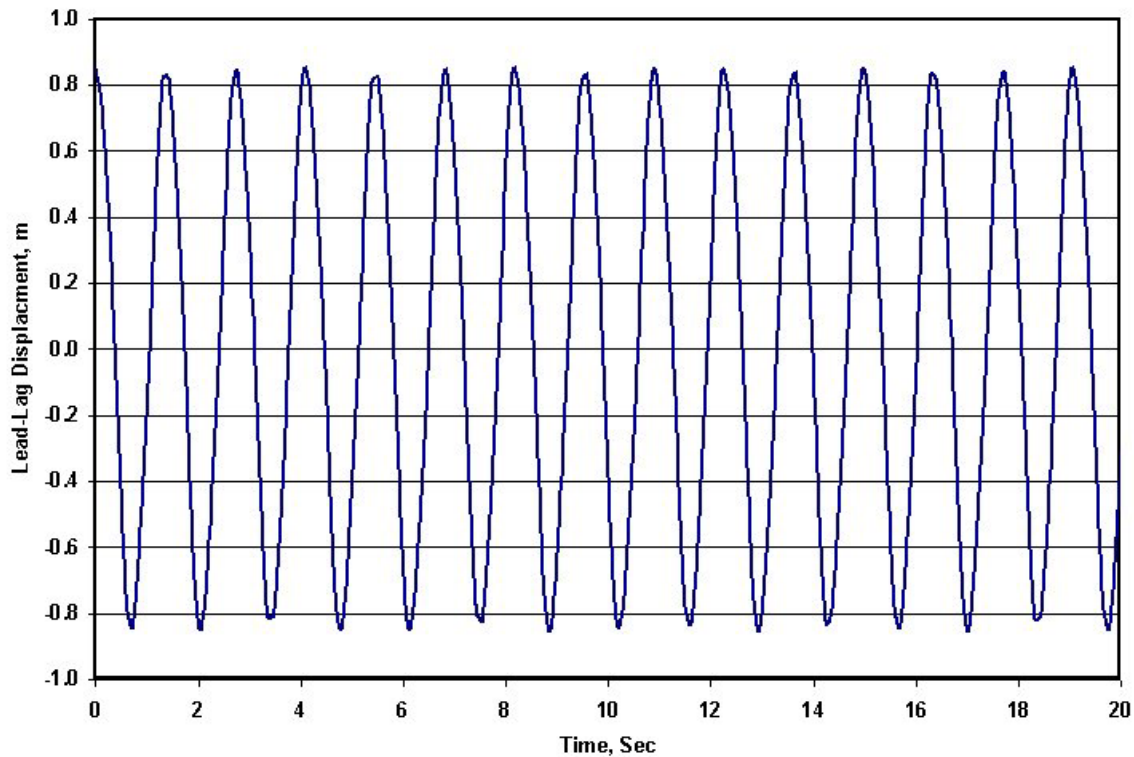
Figure 6-26. Full-state feedback lead-lag response for progressive phase angles

6.4 Summary

Although more analysis could be performed on both the PID and full-state feedback controllers, the objective of the controller design and analysis (i.e., the design of a controller capable of maintaining consistent and stable operation) has been achieved. The control capabilities of the current testing facility are limited by software considerations but the current software does support adaptive control. More analysis on how adaptive control could be used to optimize system performance should be conducted as part of a future research project. For this project, the advantages and limitation of the PID and full-state controllers have been identified. The PID controller is well suited to regulate the flap and lead-lag displacements for fatigue testing under current NREL loading conditions where the flap and lead-lag forces have a constant phase angle throughout the test. The PID controller is ill suited for regulating the blade response when step changes in the phase angle occur. A general design strategy has been described and evaluated that allows for the design of a full-state feedback controller capable of providing stable operation when the phase angle between the flap and lead-lag fatigue loads are allowed to vary. Additional control studies should be conducted on the actual blade and test system. Parameters not taken into account for this analysis, such as hydraulic line impulses, may prove to have a significant impact on the actual system performance. To implement the full-state feedback controller, additional control software must be installed on the test system.

151

Chapter 7. Experimental Validation of Resonance Test System

This chapter evaluates the accuracy of the modeling and analysis conducted in previous chapters. For this analysis, data was collected on a 1.5MW wind turbine blade subjected to single-axis and dual-axis excitations. Strain gauges were placed along the surface of the blade at regular intervals and used to compare the effects of using the resonance test system to the forced-displacement test system currently in use. The results show that the resonance test system can accurately reproduce the fatigue results of the current test system.

7.1 Objective of Experimental Evaluation

The analysis performed in previous chapters shows that it is possible to closely simulate the same fatigue test results using either a resonance test system or a forced-displacements system. Since this analysis was performed for a generic wind turbine blade, the results should be valid for a range of blade sizes and configurations. To demonstrate this point, a specific blade has been selected for testing. The same methods used to optimize the fatigue test conditions for the generic blade have been applied to the specific test blade. By subjecting the specified test blade to resonance testing and forced displacement testing, a comparison of the two methods has been made to demonstrate that validity of the previous chapter's analysis.

7.2 Test Blade

In order to obtain a test blade, the National Renewable Energy Laboratory submitted a solicitation for a Cooperative Research and Development Agreement (CRADA) to large blade manufacturers. GE Wind responded to the solicitation and agreed to supply a blade to be used to validate the new test method. As part of the CRADA, the proprietary material and structural properties of the wind turbine blade will not be published. Subsequently, the test results will be normalized so that propriety information cannot be derived from the results. Generally, the blade used for this test was a 37-meter long blade designated by GE Wind as 37a. The test blade is a good representation of blades currently being manufactured and is made entirely of composite material (fiber-reinforced plastic, balsa wood, etc.). This size of blade is sufficiently large to demonstrate the load accuracy, the test time savings and the energy cost reductions presented by the new test method.

7.3 Resonance Test System

As discussed throughout this document, a new test system has been developed to test large wind turbine blades. A significant amount of the effort required to complete this project has been used to create the test system. As such, the design and configuration of the test system will be described in this section. The most significant development of the

new resonance test system is the excitation load frame assembly. As shown in Figure 7-1, the load frame supports a 450 kg mass that is attached to the end of a 15 kip – 20-inch stroke hydraulic actuator. A 1.5-inch diameter chrome shaft is used to guide the 450 kg mass in a linear path.

Figure 7-1. RTS load frame assembly

The load frame is attached to the target blade using wooden saddles similar to the saddle shown in Figure 7-2. In the final configuration, the saddles are supported with steel beams and clamped to the blade using 5/8" diameter all-thread. Pouring a rubber compound between the saddle and blade controls the interface between the two surfaces and reduces stress concentrations that could be induced into the blade. A total of four saddles were attached to the target blade. Two of which were used to secure the load frame assembly.

Figure 7-2. Wooden blade saddle

The load frame assembly was attached to the saddles using rubber isolation mounts manufactured by Lord Corporation. As shown in Figure 7-3, the frame was attached to two blade saddles using a total of four rubber isolators. The rubber mounts have a voided center that reduces the mounts resistance to bending while retaining a high stiffness in the vertical direction.

Figure 7-3. Load Frame Assembly Mounts

Of the four blade saddles, two saddles were used to contour the blade's mode shape. In this case, the mode shape was modified to produce a bending moment distribution similar to the bending moment resulting from the forced-displacement test system. As shown in Figure 7-4, the amount of weight carried by the saddles can be easily adjusted by adding or removing steel bars attached to the saddles using 1.5-inch diameter all-thread.

Figure 7-4. Adjustable blade masses

7.4 Mode Shape Comparison

The mode shape for the test blade was modified by adding masses to the blade at specific locations based on the results of an optimization routine. The predicted mode shape and fundamental frequency of the blade were calculated using a finite element model. The actual mode shape was measured using two accelerometers placed along the blade. The acceleration at the two measurement locations was compared to the predicted accelerations. As shown in Figure 7-5, the measured accelerations agree very closely with the predicted values.
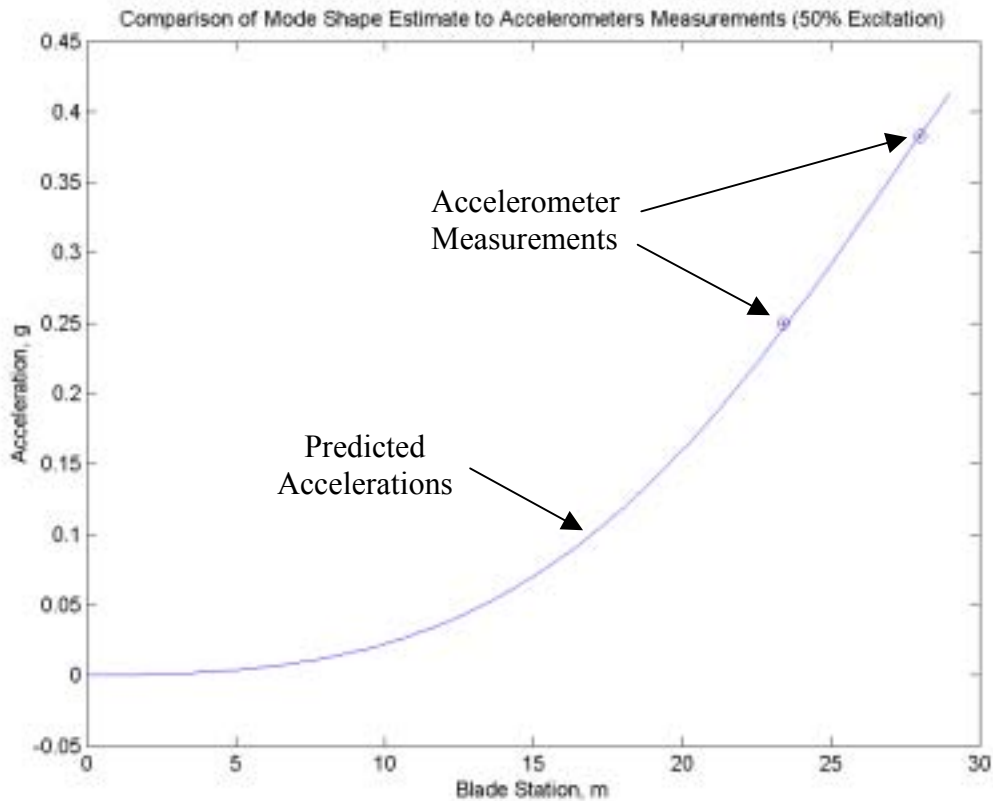
Figure 7-5. Comparison of predicted and actual blade accelerations

The close correlation between the measured and actual accelerations indicates that the finite element model, optimization routine and predicted blade properties accurately represent the actual blade system.

7.5 Single-Axis Strain Comparison

The blade mode shape determines the bending moment distribution applied along the blade during testing. However, other factors may influence the local strain at each point along the blade. In order to compare the influence of using the resonance test on the actual strain levels, strain gauges were applied to the blade at regular intervals along the blade length. The blade was then exercised in the flap direction to the target displacement levels using an actuator connecting the floor and blade, as shown in Figure 7-6. Note that the blade is turned over (top to bottom) for the resonance test system when compared to the forced displacement system. This change is required to apply the proper mean flap load during resonance testing.

Forced Displacement **Resonance Excitation**

Figure 7-6. Single axis test configurations

The extrema strain values for each strain gauge were collected for one hundred cycles for the forced-displacement and resonance tests. For the initial resonance test, the blade was intentionally excited less than required to damage the blade. As shown in Figure 7-7, the alternating strains for the resonance test were approximately 10% less than the strains for the forced displacement test. It should be noted that the forced displacement test has a different moment distribution than the resonance test system. As a result, the difference between the two test systems will never be zero for all points along the blade.
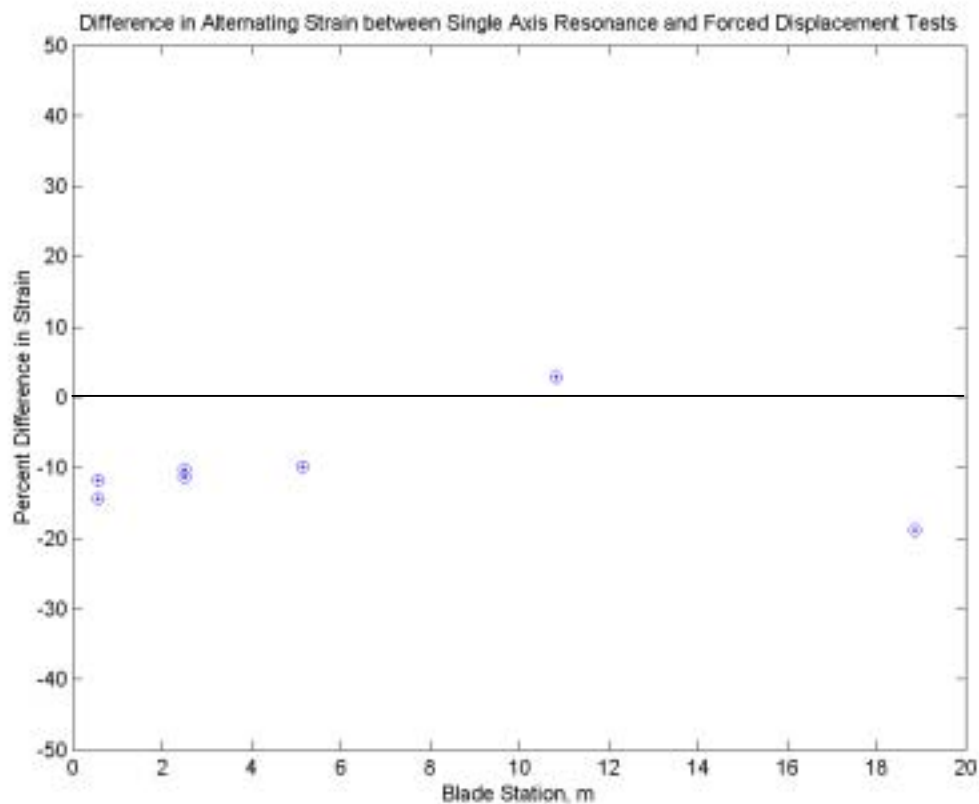
Figure 7-7. Comparison of blade strains (initial test)

The resonance test amplitude was increased by 10 percent to determine if the strain measurements increased linearly. As shown in Figure 7-8, a 10 percent increase in displacement results in a approximately a 10 percent increase in the blade strains. The mean difference in strains between the forced-displacement test and the second resonance test was approximately zero percent. As noted before, it is not possible for the forced-displacement test and resonance test to agree for every strain gauge.
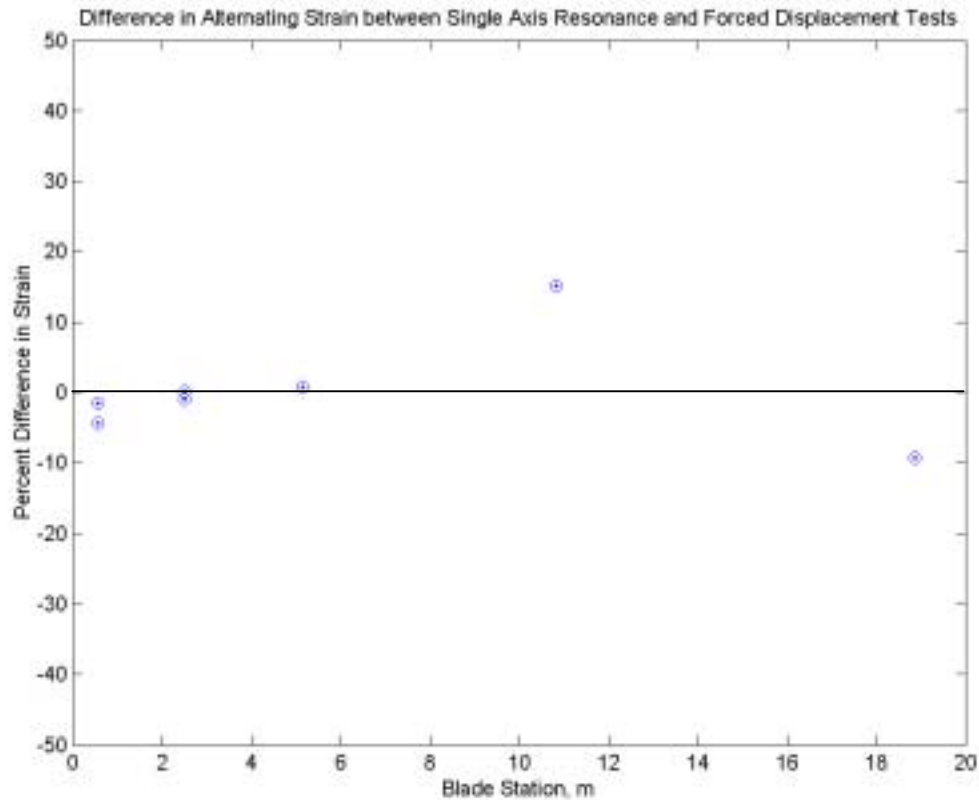
Figure 7-8. Comparison of blade strains (second test)

The ability of the test methods to consistently achieve the same strain levels is also important. As shown by Figure 7-9, each test method results in a little scatter in the strain gauge values for the strain gauge further from the root. The data shown represents approximately 200 cycles of operation.

158
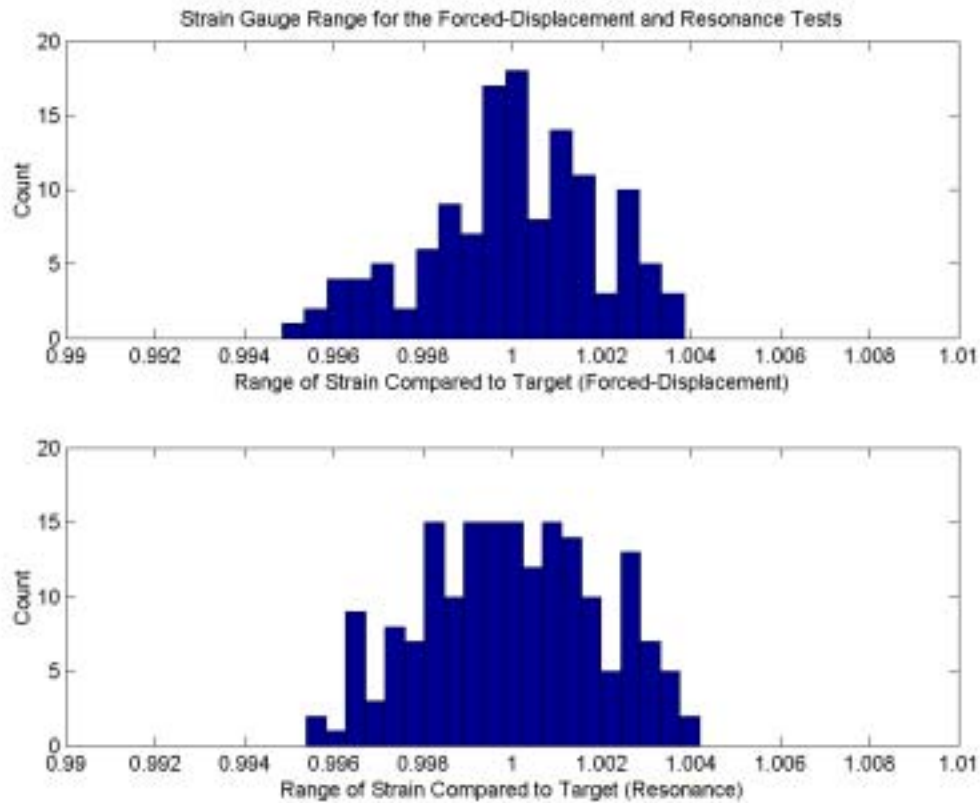
Figure 7-9. Strain range distributions for both test methods

The standard deviations for the two test methods were approximately the same but the resonance test system was able to maintain proper strains slightly better as shown by Figure 7-10. More advanced control strategies could result in better consistency for both test methods.

Difference in the Standard Deviation of the Alternating Strain between Single Axis Resonance and Forced Displacement Tes
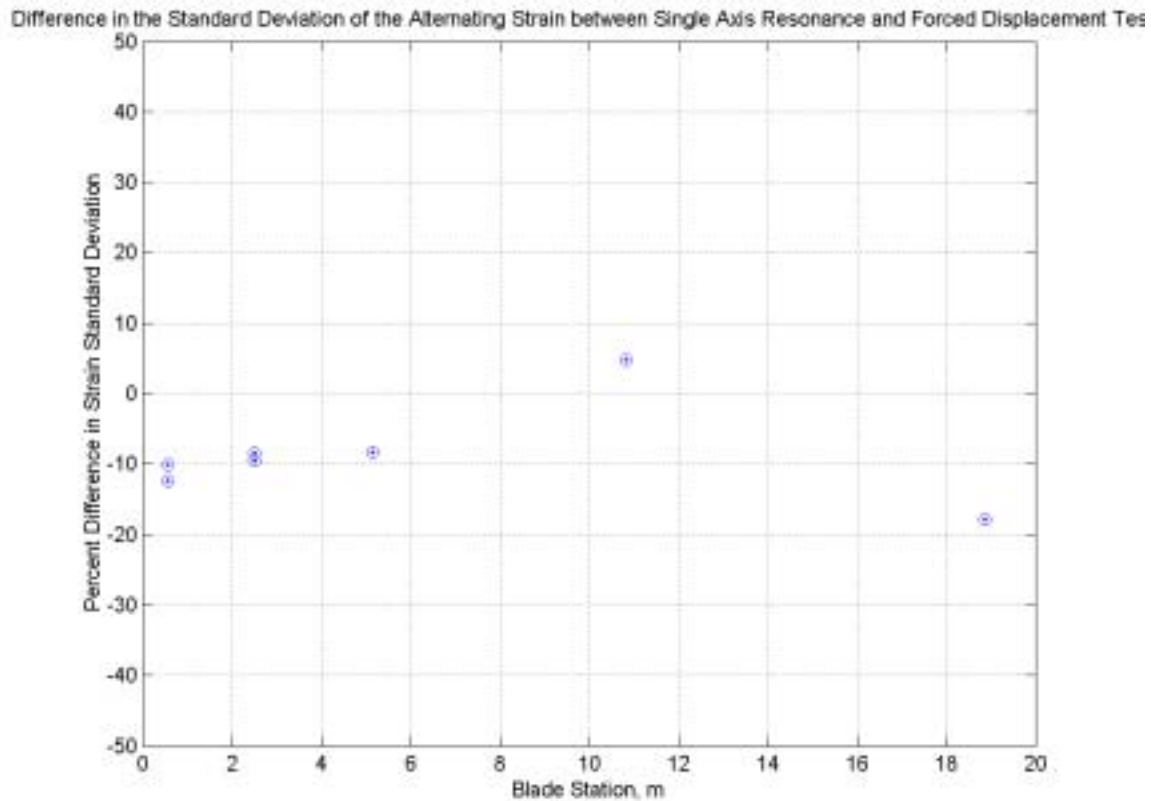
Figure 7-10. Comparison of blade strain STD for the single-axis tests

7.6 Dual-Axis Testing

In principle, the dual-axis system is simply the superposition of the individual flap and lead-lag forces. Since the displacements in the lead-lag direction are the same for both test systems, the differences in strain for the dual-axis test are completely dependent on the relationship of the strains in the flap direction. Since this difference was evaluated in the previous section, it will not be addressed again in this report. The main purpose of the testing the dual axis system is to demonstrate that the system exhibits stable operation.

As shown in Figure 7-11, the edge actuator applies a load to the blade through a bell crank. Due to space constraints, the edge actuator has been moved from the north side of the test facility to the south side for use with the resonance test system.

160

Figure 7-11. Dual-axis test configuration

The two dual-axis test methods were operated for a short time to determine the steady-state operating conditions for each configuration.

7.7 Operating Conditions

Maintaining testing accuracy is important to this project but the main object of this research is to create a test system capable of testing the next generation of wind turbine blades. In order to accomplish this, the new test system must be capable of cycling the blade at a much faster rate while using less energy. The actual result for the single-axis fatigue tests are shown in Table 7-1. As shown, the resonance test system provides are much more efficient methods for fatigue testing 37 meter blades. As blades become longer, the resonance test system will become an even more attractive method for fatigue testing.

Table 7-1. Single-Axis Operating Conditions

	Forced-Displacement	Resonance
Speed	0.3 Hz	0.75 Hz
Hyd. Flow	100 GPM	30 GPM

Since the edge actuator has the same restrictions in both cases, the advantages of the resonance system are somewhat blunted for dual-axis testing. As shown in Table 7-2, the advantages are still significant for the dual-axis resonance system even if they are less spectacular than the single-axis scenario.

161

Table 7-2. Dual-Axis Operating Conditions

	Forced-Displacement	Resonance
Speed	0.3 Hz	0.75 Hz
Hyd. Flow	200 GPM	100 GPM

7.8 Summary

The resonance test system is capable of duplicating the fatigue test results of the current forced-displacement test system. The advantages of the resonance test system are that it takes much less time to perform a complete fatigue test, the energy cost are significantly less and hardware costs will be mitigated when larger wind turbine blades need testing. Additional evaluation of the resonance system in combination with advanced controller designs and variable phase angle strategies should be conducted to further improve the testing capabilities of the system.

Chapter 8. Summary, Conclusions and Recommendations

This chapter provides a summary of the research presented in the previous chapters. It provides a description of the results as well as recommendations for future research related to the fatigue testing of utility scale wind turbine blades.

8.1 Summary and Conclusions

The research conducted for this project was designed to improve the overall state of wind turbine blade testing by creating a better understanding of how testing parameters effect the results of full-scale fatigue tests and by developing a new fatigue test method that is faster, cheaper and more accurate than any existing test method. The goals of this project can be divided into twenty items as shown in section 1.4:

1. Determine appropriate wind turbine size to be used in this analysis (section 2.2),
2. Obtain simulated wind turbine blade bending moment time histories in the flap and lead-lag directions (section 2.3),
3. Create a definition for the relationship between the two blade loads (section 3.3.1),
4. Evaluate the phase relationship between the flap and lead-lag bending moments for the target wind turbine blade size for various wind speeds and determine an aggregate phase angle distribution representative of general operating conditions (sections 3.3.2-3.3.4),
5. Use a finite element model of the target blade to evaluate the influence of the phase relationship between the bending moments on the nodal strains (section 3.4),
6. Use Miner's Rule to determine the possible impact on fatigue lifetime predictions of switching from the constant phase angle fatigue tests currently used by the wind turbine industry to a variable phase angle fatigue test representative of the phase angle distribution determined by this research project (section 3.5),
7. Determine an appropriate phenomenological fatigue damage model for composite blade material and determine the appropriate model parameters using the Department of Energy material database (sections 4.1-4.2),
8. Evaluate the influence of phase sequencing on the accumulation of fatigue damage (section 4.3),
9. Optimize the phase time history with respect to total damage accumulation using a conjugate method optimization routine (section 4.3.3),
10. Propose a phase time history for use with variable phase angle fatigue testing (section 4.4),
11. Analyze current blade fatigue testing methods and their performance (section 5.1),

12. Determine blade properties (EI, damping ratio, etc.) for target wind turbine blade and build a beam finite element model of the blade in the test configuration (section 5.2),

13. Analyze a new fatigue testing method that has been developed as part of this research project and compare its performance to current testing systems (section 5.3),

14. Perform an optimization of the new test system with respect to test bending moment distributions (section 5.3),

15. Create a dynamic model of the blade and test system (section 6.1),

16. Design and evaluate the performance of a PID controller for constant phase angle fatigue tests and for variable phase angle fatigue tests (section 6.2),

17. Design and evaluate the performance of a full-state feedback controller for constant phase angle fatigue tests and for variable phase angle fatigue tests (section 6.3),

18. Analyze, design and build the new test system and related hardware (section 7.3),

19. Evaluate the new test systems performance on an actual blade (sections 7.3-7.7),

20. Establish the limitation of this analysis and make recommendations for future analysis and testing improvements (sections 8.1-8.2).

Each goal was achieved during the course of this project as summarized below.

The analysis conducted for this project was for a specific wind turbine blade size. The methodology is valid for any blade but only the most relevant blade size has been analyzed in this project. The catalyst for this project is the constantly increasing size of wind turbine blades. As blades have gotten larger, traditional methods used to fatigue test blades have become less practical. At the same time, the operating loads applied to the blades have gone from predominately single axis loads (flap only) to multi-axis loads (flap and lead-lag). While test facilities have recently begun to apply dual-axis test loads to the blades, a detailed analysis of the how the phase relationship between the test loads effects the test results has not been conducted before this study. With these concepts in mind, a target blade was selected for this analysis. A 37-meter long blade, which corresponds to a 1.5-megawatt wind turbine, was selected for this study because it is the largest wind turbine blade that has subjected to a dual-axis fatigue test. While some prototype 50-meter blades do exist, the systems analysis and data collection required in order to perform this research project have not been completed on these blade sizes. Also, it was possible to obtain a 37-meter wind turbine blade for evaluating the new test system design as part of this project. The target turbine is described as a 1.5 MW variable-speed pitch-controlled wind turbine with 37-meter fiber-reinforced composite blades.

To perform the data analysis required by this project, it was necessary to obtain a time histories of the flap and lead-lag bending moments for a 1.5 megawatt wind turbine blade working during range of operating conditions. As described in chapter 2, a dynamic model of a generic 1.5 MW wind turbine was created as part of the WindPACT research

program. The flap and lead-lag bending moment time histories used for the research project presented in this dissertation were achieved by simulating the generic wind turbine's response to IEC class Ia wind conditions.

One goal of this project was to determine how the flap and lead-lag bending moments interacted with each other to cause fatigue damage on wind turbine blades and then to determine how best to account for this interaction during fatigue testing. Since this analysis had not been performed prior to this research project, what is meant by the interaction between the flap and lead-lag bending moment had to be defined. Since the dual-axis fatigue test system used by the wind industry is capable of having only one phase relationship between the test loads per applied test cycle and the spectral content of the flap and lead-lag bending moments indicate that the majority of operating loads are applied with a frequency of once per rotor revolution, it was decided that the load interaction analysis should result in a single value per rotor revolution. To accomplish this objective, the interaction between the operating loads was defined by a term called "phase angle" that is defined to be the change in rotor angle between the location of the maximum flap bending moment and maximum lead-lag bending moment as shown in chapter 3.

Using this definition, it was possible to quantify the relationship between the operating loads and to establish how this quantity varies during operating conditions. As shown in chapter 3, the variation of the phase angle is substantial for all wind speeds. The phase angle distribution for each wind speed was weighted by the IEC class Ia standard Rayleigh wind speed distribution to compile the distribution into a single aggregate distribution. As shown by this research project, the aggregate phase angle distribution has a mean of 72 degrees and a standard deviation of 54 degrees. This is a significant result considering that all dual-axis fatigue tests are conducted with a single constant phase angle.

To evaluate the impact that the phase angle has on fatigue damage accumulation, a three-dimensional wind turbine blade finite element model was used. This model was originally used as part of the WindPACT blade scaling studies but was modified to represent the blade in the as-tested condition. As shown in chapter 3, flap and lead-lag test loads were applied to the blade model at every phase angle. This analysis was used to produce time histories for the strain at each node. For the purpose of this analysis, three cross-sections of the blade were considered in detail. The three sections correspond to the root, maximum chord location and a mid-span airfoil cross-section.

The strain time histories for each node on each of the three cross-sections have been used to calculate the fatigue damage accumulation resulting from each phase angle. As shown in chapter 3, Miner's Rule has been used for most of the fatigue damage modeling. The strain time histories at each node have been used to calculate the alternating strain applied to each location for each phase angle. Using a strain-cycle curve experimentally determined by Montana State University for wind turbine blade composite material, the number of cycles that must be applied to the blade for failure to occur at each node for each phase angle induced time history has been calculated. This value has been used in

conjunction with Miner's Rule to calculate the actual fatigue damage that is accumulated for constant phase angle fatigue tests. As shown in chapter 3, this result has been compared to the fatigue damage accumulated at each node location if the phase angle distribution that was determined earlier in chapter 3 were applied during testing. This analysis indicates that constant phase angle testing is not representative of operating conditions. Constant phase angle testing, which is the industry standard, will not test certain areas of win turbine blades sufficiently and if material defects are present, constant phase angle testing has less of a probability of finding the defect (via blade failure) than variable phase angle testing.

Since full-scale fatigue tests have traditionally used constant amplitude loads with a constant phase relationship, the potential effect of sequencing the test loads was not relevant and has not been previously considered. Since the research presented in this document suggests using a variable phase angle between the test loads, the influence of phase sequencing is important. Since the fatigue damage accumulation law used for most of the analysis (Miner's Rule) is not capable of demonstrating the influence of sequences, a new damage accumulation model was derived and employed. As shown in chapter 4, the damage accumulation model was derived from Paris's Equation, which is commonly used to describe delamination for composite materials. The model's exponent was determined using material properties experimentally determined for composite blade material at Montana State University.

Using this nonlinear damage accumulation model, the influence of applying different sequences of phase angles that still result in the same overall phase angle distribution was evaluated. This analysis indicates that a sequence where the phase angles are grouped will results in less damage than a sequence where the phase angles are distributed. As shown in chapter 4, this relationship has been evaluated and it was shown that this characteristic is dependent on the damage model exponent and subsequently the material fatigue properties. As long as the fatigue properties of the material results in a fatigue damage accumulation model exponent of less than 1.0, a well dispersed phase angle sequence will result in the most damage. If blades are constructed of other materials in the future such as carbon fiber, this analysis should be considered.

In addition to evaluating the impact that different phase angle sequences have on the total damage accumulated, it was desirable to determine the most and least damaging sequence to bound this aspects influence. The influence of that phase angle sequencing has on damage accumulation been bounded but there exists no unique most damaging phase angle sequence. As shown in chapter 4, there are numerous phase angle sequences that can produce the most damaging scenario. This analysis also shows that different sequences of phase angles that have the same overall distribution result in different magnitudes of damage but not the relative distribution of damage around the airfoil.

Based on this analysis, a variable phase angle time history has been proposed for fatigue testing of wind turbine blades. This analysis was used to evaluate the capabilities of the different controllers in chapter 6. It was not in the scope of this project to implement

variable phase angle testing but clear the analysis conducted in this research suggests that this aspect must be considered for future full-scale fatigue testing.

At the heart of this project, is the need for a better understand and improved methods for performing full-scale fatigue tests on wind turbine blades. As described in chapter 1, wind turbine blade testing facilities face challenges that other industries do not. One solution to this problem would be to implement the types of testing systems that are used in the aerospace and automotive industries but the wind industry lacks the resources and market stability required for an investment of this enormity. The work conducted as part of this research project produces a solution to many of the problems facing wind industry testing facilities but before developing a new solution, the currently blade testing systems were analyzed and compared. As described in chapter 1 and chapter 5, there are two types of full-scale blade fatigue test systems: a single-axis system that doesn't accurately test the blade, and a dual-axis system that requires huge amounts of energy to operate. The power and equipment costs for the dual-axis test system substantially increase for larger blades making this system increasing less practical as the wind industry evolves. A new solution is warranted and because of this research project now exists.

As part of the design and evaluation of the new test system, a beam finite element model of the wind turbine blade in the test configuration was created. The model was created using stiffness (EI) data provided by the blade manufacturer in the flap and lead-lag directions. The torsional degree of freedom was not considered in this analysis because the torsional fundamental frequency is an order of magnitude higher than the excitation frequency (based on experimental results) and torsional stiffness data were not available. As discussed in chapter 5, the finite element model was used to calculate the beam's eigenvectors and eigenvalues in both the flap and lead-lag directions. The fundamental frequency in the flap direction was also experimentally determined and found to be within 2% of the analytical value. The damping ratio for the complete blade in the test configuration was also experimentally determined and found to be approximately 1% of the critical damping for this system.

The model of the new test system was used to compare its performance with the existing test methods. Based on the analysis shown in chapter 5, it was determined that the new test system could reduce energy consumption by at least 50% for the target 37-meter blade and can reduce the time required to perform a fatigue test by 50% as well. These results were confirmed on an actual blade as shown in chapter 7.

The beam finite element model was also used as part of an optimization algorithm designed to determine how closely the new test system can replicate existing dual-axis test systems. As shown in chapter 5, the new test system can reproduce the bending moment distribution for the current dual-axis test system to within a few percent depending on which blade station is being considered. The new test method also has additional flexibility in specifying the flap bending moment distribution that did not exist with the current dual-axis test method.

The eigenvalues calculated from the beam finite element model were used to create a dynamic model of the blade and test system. As shown in chapter 6, the dynamic model was created in Simulink and used to design both a PID controller and a full-state feedback control for tests subjected to constant phase angle time histories and variable phase angle time histories.

A PID controller was designed using the model shown in chapter 6 and its performance was analyzed under to two testing scenarios describe above. This analysis shows that a PID control is capable of maintaining a stable and consistent dynamics blade response for a constant phase angle fatigue test. Since only the constant phase angle test was implement for this project, the PID controller was used and as predicted it performance was adequate as shown in chapter 7. The analysis indicates that the PID controller's performance was not sufficient to be used with variable phase angle testing. When disturbances are introduced to the system associated with varying the phase angle during testing, the PID controlled system can go unstable even though the eigenvalues are always negative.

A full-state feedback controller was also designed using the dynamic model for the blade and test system. This analysis shows that a full-state feedback controller designed using the methodology described in chapter 6 is capable of maintaining stable controller for both the constant phase angle-testing scenario and the variable phase angle-testing scenario. These results were not experimentally evaluated because the current testing software available only supports PID controllers but this analysis shows that variable phase angle testing is viable if software upgrades are made.

Once the new testing system was analyzed and shown to be practical, feasible and controllable, the next step was to design and build the system. As shown in chapter 7, the new test system was design to sit on top of the test specimen. This presented certain challenges such as running the hydraulic lines along the top of the blade. None of the existing test system has hydraulic systems located on the blade (the single-axis test system uses an electric motor). Additional design challenges were: finding a way to isolate the test system from the blade without influencing the blades motion and determining a way to attached the masses required to tune the blades operational displacement shape that still allowed the masses to be adjustable. The solutions to each of these design challenges are shown in chapter 7.

After implementing the new test system, some preliminary analysis was conducted to verify assumptions made during the analysis. As shown in chapter 7, accelerometer measurements were taken to confirm that the actual displacement of the blade agrees with the predicted displacement. The system was successfully controlled using accelerometer feedback and a PID controller. Strain gauge data were collected and analyzed to show that the new test system can reproduce the results of the current dual-axis test. The new test system will require approximately 60% less energy for a complete fatigue test and is capable of performing the test at over twice the speed when compared to the current dual-axis test system. In each case, the results support the analysis that was conducted in chapters 5 and 6.

Overall, this research project has been highly successful. A new test system has been created that will help reduce the overall cost of wind energy, provide wind turbine blade designers with the fastest, most accurate information available, and reduce the energy consumed in performing full-scale fatigue testing. At the same time, this research project has shed light on a previously ignored aspect of fatigue testing. By analyzing the influence that the phase relationship between the flap and lead-lag test loads has on the accumulated fatigue damage, this research project has shown that it is not accurate to ignore the variations in load phasing that occur during turbine operation and this term should be considered when specify a blade test program.

8.2 Recommendations for Future Research

This research has analyzed all aspects of fatigue testing large wind turbine blades and implemented a new fatigue test method that is more efficient than current methods. Additionally, the project has highlighted some area where further improvements could be made. With the implementation of the new test system, it is now possible to apply more complex bending moment distributions than with the forced-displacement test system. As such, it would be advantageous to collect data for actual bending moments applied to the blades during operation. This data could be used to in conjunction with an optimization routine to create a more accurate fatigue test than is currently possible.

As part of the research presented in this document, the relationship between the flap and lead-lag bending moments has been analyzed. Additional work remains for the implementation of the variable phase angle testing. New control software may be required to fully implement the change. The tuning and analysis of the dynamic system response presents an excellent opportunity for additional research. A parametric analysis of the nonlinear influence contributed by the bell crank should be performed to determine the best method to reduce the control problems associated with variable phase angle testing (new bell crank design, a different mechanism, full-state feedback control, adaptive control, etc.).

While a phenomenological nonlinear model has been used as part of this analysis, a more accurate model of blade failure could be developed. Material testing performed by Montana State University indicate a very large amount of scatter when fitting the nonlinear models parameters. For this analysis, the failure mechanism is dependent only on the axial strain even though a 3-D finite element model was used. With sufficient research and testing, it may be possible to develop a more accurate phenomenological residual strength model based additional parameters available from the 3-D FEM.

As wind turbine blades become larger, new materials are being employed to reduce overall operating expenses or to make the design feasible. The impact of these new materials on the size and application of fatigue test systems should be analyzed. As part of this analysis, historic values for blade properties as a function of length have been used to project some of the requirements to test larger wind turbine blades. However, revolutionary changes in material properties may influence the overall blade properties at

unpredicted rates. A parametric study of this nature would benefit designers of future testing facilities.

Appendix A

Mass Optimization Code

RTS_MASS_OPTI.m

```
function [z,g] = RTS_MASS_OPTI(s);
%Load R (Blade Station), mpl (Station Masses per unit length), EI (Station Stiffness)
load blade.mat
%Linearly Interpolate Blade Data
[R,EI,mpl,MB] = expand(R,EI,mpl);
% Shorten Blade to proper length
[a,b] = min(abs(R-29));
R = R(1:b);
EI = EI(1:b);
mpl = mpl(1:b);
[R,EI,mpl,MB] = expand(R,EI,mpl);
%Target Moments: MS (Static Root Moment at Root), MD (Dynamic Root Moment at Root)
% Mean Root Moment 1104 kNm
% Alternating Root Moment 2699/2
MS = 1104;
MD = 2699/2;
xa = 23.37;
% R is from the end face
Mmean = MS*(xa-R)/2+abs(MS*(xa-R))/2;
Mmean = Mmean/23.37;
Malt  = MD*(xa-R)/2+abs(MD*(xa-R))/2;
Malt = Malt/23.37;
```

Driver_RTS.m

```
%Stationary Mass Optimization Driver
global numvar;
global numcon;
%Number of Stationary Masses
numvar=3;
%Number of Bending Moments Constraints(Mean, Alternating)
numcon=1;
% initial guess and bounds

s  = zeros(numvar,1);
su = zeros(numvar,1);
sl = zeros(numvar,1);

%Set Optimization Variable Bounds
%Mass of Stationary Weight in kg
sl = [1 1001 1];
su = [1000 1500 1000];

%Set Initial Optimization Variables
SI = sl/2+su/2;

% evaluation of initial design

[z,g]=RTS_MASS_OPTI(SI)
s = SI;

% sequential convex program

s = scp('RTS_MASS_OPTI','gradient',s',su',sl');

[z,g]=RTS_MASS_OPTI(s)

save stmp

freq
s
```

Phase Angle Analysis Code

<u>Phase_Angle.m</u>

```
for ii = 1:360
% pa = Phase Angle
pa = ii;
% Blade Cross-Section 1
% Load Unit-Load Results from FEM
load edge1;
sze = sz/21000;
load flap1;
szf = sz/21000;
t = [0:.01:2*pi+.01];
fm = 12500;
fm = 0;
fa = 15000;
f = fm+fa*sin(t);

em = 0;
ea = 13000;
e = em+ea*sin(t+pa/180*pi);

szt = sze*e+szf*f;
sz_peak(ii,:) = max(szt');
sz_val(ii,:) = min(szt');

[d(ii,:)]=strain_dam(nx,ny,szt);
end

for ii = 1:360
% pa = Phase Angle
pa = ii;
% Blade Cross-Section 2
load edge2;
sze = sz/21000;
load flap2;
szf = sz/21000;
t = [0:.01:2*pi+.01];
fm = 12500;
fm = 0;
fa = 15000;
f = fm+fa*sin(t);

em = 0;
ea = 13000;
```

```
e = em+ea*sin(t+pa/180*pi);

szt = sze*e+szf*f;
sz_peak(ii,:) = max(szt');
sz_val(ii,:) = min(szt');

[d(ii,:)]=strain_dam(nx,ny,szt);
end

for ii = 1:360
% pa = Phase Angle
pa = ii;
% Blade Cross-Section 3
load edge3;
sze = sz/21000;
load flap3;
szf = sz/21000;
t = [0:.01:2*pi+.01];
fm = 12500;
fm = 0;
fa = 15000;
f = fm+fa*sin(t);

em = 0;
ea = 13000;
e = em+ea*sin(t+pa/180*pi);

szt = sze*e+szf*f;
sz_peak(ii,:) = max(szt');
sz_val(ii,:) = min(szt');

[d(ii,:)]=strain_dam(nx,ny,szt);
end
```

References

1. Ackermann, T., Soder, L., Wind Energy Technology and Current Status: A Review *Renewable and Sustainable Energy Reviews*, 4, 315-374, 2000.

2. Dodge, D., Illustrated History of Wind Power Development, http://telosnet.com/wind, 2002.

3. Eldridge, F., *Wind Machines*, 2nd Edition, Van Nostrand Reinhold, New York, 1980.

4. Freris, L., *Wind Energy Conversion Systems*, Prentice Hall, New York, 1990.

5. Johnson, G., *Wind Energy Systems*, Prentice Hall, Englewood Cliffs, NJ, 1985.

6. Le Gourieres, D., *Wind Power Plants*, Pergamon Press, Oxford, 1982.

7. Nelson, V., *Wind Energy and Wind Turbines*, Alternative Energy Institute, Canyon, TX, 1996.

8. Hills, R., *Power from Wind*, Cambridge University Press, Cambridge, UK, 1994.

9. Inglis, D., *Windpower and Other Energy Options*, University of Michigan Press, Ann Arbor, MI, 1978.

10. Putnam, P., *Power From the Wind*, Van Nostrand Reinhold, New York, 1948.

11. Website of Danish Turbine Manufacturers, http://www.windpower.dk, 2001.

12. Gipe, P., *Wind Energy Comes of Age*, Wiley, New York, 1995.

13. Park, J., *The Wind Power Book*, Chesire Books, Palo Alto, CA, 1981.

14. Golding, E., *The Generation of Electricity by Wind Power*, E. & F. N. Spon, London, 1977.

15. Web site of the American Wind Energy Association - http://www.awea.org, Updated September 13, 2002; accessed December 19, 2002.

16. Berger, J., *Charging Ahead: The Business of Renewable Energy and What it Means for America*, University of California Press, Berkley, CA, 1997.

17. Harrison, R., Hau, E., Snel, H., *Large Wind Turbines: Design and Economics*, Wiley Chichester, 2000.

18. Eggleston, D., Stoddard, F., *Wind Turbine Engineering Design*, Van Nostrand Reinhold, New York, 1987.

19. Spera, D., *Wind Turbine Technology: Fundamental Concepts of Wind Turbine Engineering*, ASME Press, New York, 1994.

20. D.R.V. van Delft, J.L. van Leeuwen, "Full-Scale Testing of Wind Turbine Rotor Blades", EWEC 1994 Conference, Thessaloniki.

21. McLemon, K., Gibson, N., Graets, P., "Development of Blade Test Facility to Accommodate Flexible Blade Assembly for New MS4 Wind Turbine," BWEA 19, Edinburgh, 1997.

22. Philippidis, T., Bionis, P., Lekou, D., Fragoulis, A., "Rotor Blade Design Verification by means of Full-Scale Testing," EWEC 1997 Conference.

23. IEC 88/84/CD. *IEC 61400-23: Testing of Rotor Blades*. September 1998.

24. Website of the National Renewable Energy Laboratory blade testing facility, http://www.nrel.gov/research/wind/windpower.html , Accessed: October 2003.

25. Website of RISO National Laboratory – Spakaer blade testing facility, http://www.risoe.dk/rispubl/VEA/sparkaer/fatigue_tests.htm , accessed: October 2003.

26. Website of Delft University, http://www.duwind.tudelft.nl/ , accessed: October 2003.

27. Musial, W., et al., "A Photo-elastic Stress Analysis on a Phoenix 7.9 meter Blade," Windpower 1991 Conference and Exposition, Palm Springs, 1991.

28. Dutton, A., et al., "Damage Detection and Stress Measurement in Composite Wind Turbine Blades," EWEC 1994 Conference, Thessaloniki.

29. Hughes, S., Musial, W., (1999) "Implementation of Two-Axis Servo-Hydraulic System for Full-Scale Fatigue Testing of Wind Turbine Blades," WindPower '99, June 20-23, 1999.

30. van Delft, D., van Leeuwen, J., Noordhoek, C., Stolle, P., "Fatigue Testing of a Full Scale Steel Rotor Blade of the WPS-30 Wind Turbine," Journal of Wind Engineering and Industrial Aerodynamics, 27 (1988), Amsterdam.

31. D.R.V. van Delft, D.C. Corbet, J.L. van Leeuwen, "Full-Scale Fatigue Tests of Wood-Epoxy Blades", EWEC 1991 Conference, Amsterdam.

32. Jensen, P., Krogsgaard, J., Lundsager, P., Rasmussen, F., "Fatigue Testing of Wind Turbine Blades," European Wind Energy Conference, Rome. (1986)

33. Website of Defense Science & Technology Organization – Aircraft Structural Integrity and Fatigue Testing, www.dsto.defense.gov.au , Accessed: October 2003.

34. Website of the Nevada Automotive Test Center – Durability Test, www.natc-ht.com/header.phtml?page=durab.htm , Accessed: October 2003.

35. *Helicopter Fatigue Design Guide*, Advisory Group for Aerospace Research and Development, Report No. AGARD-AG-292.

36. Bleakney, W., "Fatigue Testing of Wing Beam by the Resonance Method," NACA TN-660, August 1938.

37. Swanson, S., "Random Load Fatigue Testing: A State of the Art Survey," MTS Systems Corporation – Materials Research and Standards, April 1968.

38. Schuster, S., "Testing the Structural Integrity of the Boeing 777," Sensors Magazine, January 14, 1995.

39. Grenier, G., Eisenlord, D., Leese, G., "Integration of Fatigue Analysis and Laboratory Simulation Requirements in the Field Data Acquisition Process," Society of Automotive Engineers Technical Paper Series, Paper No. 870805, April 1987.

40. Nelson, D., Fuchs, H., "Prediction of Cumulative Fatigue Damage Using Condensed Load Histories," Automotive Engineering Congress and Exposition, February 1975.

41. Tucker, L., Downing, S., Camillo, L., "Accuracy of Simplified Fatigue Prediction Methods," Automotive Engineering Congress and Exposition, February 1975.

42. Haver, S., "Application of Stochastic Methods in Structural Design – The Offshore Experience," 2001 ASME Wind Energy Symposium Collection, AIAA-2001-0043, January, 2001.

43. Bierbooms, W., SWING4 Stochastic Wind Field Simulation website, http://windenergy.citg.tudelft.nl/content/research/swing.shtml , Institute for Wind Energy, Accessed: October 2003.

44. Kelley, N., "Full Vector (3-D) Simulation in Natural and Wind Farm Environments Using an Expanded Version of the SNLWIND Turbulence Code," Wind Energy 1993, SED-Vol. 14, ASME, 1993.

45. Veers, P., "Three-Dimensional Wind Simulation," SAND 88-0512, Sandia National Laboratory, Albuquerque, NM.

46. Kelley, N., Buhl, M., *SNwind User's Manual*, NWTC Design Codes, http://wind/designcodes/snwind , Updated June 2003, Accessed October 2003.

47. Lumley, J., *Stochastic Tools in Turbulence*, Academic Press, 1970.

48. Lumley, J., Panofsky, H., *The Structure of Atmospheric Turbulence*, John Wiley and Sons, 1964.

49. Lungu, D., van Gelder, P., "Characteristics of Wind Turbulence with Applications to Wind Codes," Technical University of Civil Engineering, Bucharest, Romania.(2001)

50. Ten Have, A., "WISPER and WISPERX: A Summary Paper Describing Their Backgrounds, Derivation and Statistics," *Wind Energy 1995*, SED-Vol. 16, ASME 1995.

51. Ten Have, A., "WISPER and WISPERX: Final Definition of Two Standardized Fatigue Loading Sequences for Wind Turbine Blades," National Aerospace Laboratory NLR, Amsterdam, 1992.

52. Kelley, N., "A Comparison of Measured Wind Park Load Histories With the WISPER and WISPERX Load Spectra," *Wind Energy 1995*, SED-Vol. 14, ASME, 1995.

53. Madsen, P., Pierce, K., Buhl, M., "Predicting Ultimate Loads for Wind Turbine Design," 1999 ASME Wind Energy Symposium, 37th AIAA Aerospace Sciences Meeting and Exhibit, January 1999.

54. Manuel, L., Veers, P., Winterstein, S., "Parametric Modes for Estimating Wind Turbine Fatigue Loads for Design," 2001 ASME Wind Energy Symposium, 39th AIAA Aerospace Sciences Meeting and Exhibit, January 2001.

55. Fitzwater, L., Winterstein, S., Cornell, C., "Predicting the Long Term Distribution of Extreme Loads from Limited Duration Data: Comparing Full Integration and Approximate Methods," 2002 ASME Wind Energy Symposium, 40th AIAA Aerospace Sciences Meeting and Exhibit, January 2002.

56. Moriearty P., Holley, W., Butterfield, S., "Effect of Turbulence Variation on Extreme Loads Prediction for Wind Turbines," 2002 ASME Wind Energy Symposium, 40th AIAA Aerospace Sciences Meeting and Exhibit, January 2002.

57. Larsen, D., Ronold, K., Jorgensen, J., Argyriadis, K., de Boer, J., "Ultimate Loading of Wind Turbines," RISO-R-1111 (EN), RISO National Laboratory, Roskilde, Denmark, April 1999.

58. Veers, P., Winterstein, S., "Application of Measured Loads to Wind Turbine Fatigue and Reliability Analysis," 1997 ASME Wind Energy Symposium, 35th AIAA Aerospace Sciences Meeting and Exhibit, January 1997.

59. Manuel, L., Kasef, T., Winterstein, S., "Moment-based Probability Modeling and Extreme Response Estimation – The FITS routine Version 1.2," SAND99-2985, Sandia National Laboratories, Albuquerque, NM, November 1999.

60. Fitzwater, L., Cornell, C., Veers, P., "Using Environmental Contours to Predict Extereme Events on Wind Turbines," 2003 ASME Wind Energy Symposium, 41st AIAA Aerospace Sciences Meeting and Exhibit, January 2003.

61. D.R.V. van Delft, et al., "Fatigue Behavior of Fiberglass Wind Turbine Blade Material Under Variable Amplitude Loading", EWEC 1996 Conference, Gothenburg.

62. Poppen, M., "Fatigue Testing of Glass Fibre Reinforced Epoxy Using the WISPER Sequence," The Aeronautical Research Institute of Sweden, Report No.: FFA-TN-1989-45.

63. Kensche, Ch. W., Kalkuhl, T., "Fatigue Testing of GL-EP in Wind Turbine Rotor Blades," European Wind Energy Conference, Madrid, Spain, September 1990.

64. Miner, A., "Cumulative Damage in Fatigue," *Trans. ASME*, Vol. 67, 1945.

65. Ronold, K., Wedel-Heinen, J., Christensen, C., "Reliability-based Fatigue Design of Wind Turbine Rotor Blades," *Engineering Structures*, 1999.

66. Sutherland, H., "On the Fatigue Analysis of Wind Turbines," SAND99-0089, Albuquerque, NM, Sandia National Laboratories, 1999.

67. Dowling, N., "Fatigue Failure Predictions for Complicated Stress-Strain Histories," Journal of Materials, Vol. 7, 1972.

68. Larwood, S., Musial, W., Freebury, G., Beattie, A., "NedWind 25 Blade Testing at NREL for the European Standards Measurement and Testing Program," NREL/TP-500-29103, March 2001.

69. Web site of the American Wind Energy Association - http://www.awea.org, Updated September 13, 2002; accessed December 19, 2002.

70. Web site of U.S. Department of Energy Wind Energy - http://www.eren.doe.gov/wind, Updated Oct 11, 2001; last accessed December 19, 2002.

71. Worldwatch Institute, Vital Signs 2001 (New York: W.W. Norton & Co.), 2001, pp. 44-45, updated by Earth Policy Institute from BTM Consult, AWEA, EWEA, Windpower Monthly; -http://www.earth-policy.org/Updates/Update5_data.htm.

72. Griffin, D. A. (2001). WindPACT Turbine Design Scaling Studies Technical Area 1 - - Composite Blades for 80- to 120-Meter Rotor; 21 March 2000 - 15 March 2001. 44 pp.; NICH Report No. SR-500-29492.

73. Griffin, D. A, *WindPACT Turbine Design Scaling Studies Technical Area 1 -- Composite Blades for 80- to 120-Meter Rotor*; 21 March 2000 - 15 March 2001. 44 pp.; NREL Report No. SR-500-29492.

74. Manwell, J., McGowan, J. and Rogers, A., *Wind Energy Explained: Theory, Design and Application*, University of Massachusetts, Amherst, MA, 2002.

75. National Renewable Energy Laboratory Wind Resource Website - http://www.nrel.gov/wind/wind_map.html, Updated 2003, Accessed June 2003.

76. US Census Bureau Website - http://www.census.gov/geo/www/mapGallery/2kpopden.html, Updated September 17, 2001 , Accessed June 2003.

77. National Renewable Energy Laboratory; Renewable Energy Historical Cost Presentation - http://www.nrel.gov/analysis/docs/cost_curves_2002.ppt, Updated October 2002, Accessed June 2003.

78. Darrieus Wind Turbine Analysis website - http://windturbine-analysis.com/, Updated November 2002, Accessed June 2003.

79. National Renewable Energy Laboratory Wind Resource Website - http://www.nrel.gov/wind/animation.html, Updated 2003, Accessed June 2003.

80. National Renewable Energy Laboratory Wind Resource Website - http://www.nrel.gov/wind/windpact/, Updated 2003, Accessed June 2003.

81. Buhl, M., Jonkman, J., Wright, A., *FAST User's Manual*, NWTC Design Codes, http://wind/designcodes/fast/fast.pdf, Updated March 2003, Accessed June 2003.

82. Buhl, M., Wright, A., Pierce, K., "FAST_AD Code Verification: A Comparison to ADAMS", 2001 ASME Wind Energy Symposium, Reno, NV, January 2001.

83. Stohl, K., "Dynamic Modeling and Periodic Control of Horizontal-Axis Wind Turbines", University of Colorado, Boulder, CO, 2001.

84. Van Grol, H., Bulder, B., *Reference Procedure to Establish Fatigue Stresses for Large Size Wind Turbines: A State of the Art Report, Volume I: Main Body of the Report and Annexes*, Netherlands Energy Research Foundation ECN, the Netherlands, 1994.

85. Van Grol, H., Bulder, B., *Reference Procedure to Establish Fatigue Stresses for Large Size Wind Turbines: A State of the Art Report, Volume II: Tables and Figures*, Netherlands Energy Research Foundation ECN, The Netherlands.

86. Donaldson, K., "Field Data Classification and Analysis Techniques," MTS Systems Corporation, Report No. 820685.

87. Downing, S., Socie, D., "Simple Rainflow Counting Algorithms," University of Illinois at Urbana-Champaign, Ill.

88. Socie, D., "Fatigue Life Predictions Using Local Stress-Strain Concepts," 1975 SESA Spring Meeting, Chicago, Ill.

89. Kensche, Ch., Seifert, H., "Wind Turbine Rotor Blades under Fatigue Loads," ECCM-4 Conference, September 1990, Stuttgart.

90. Sutherland, H., Carlin, P., "Damage Measurements on the NWTC Direct-Drive Variable Speed Test Bed," Wind Energy 1998, Report No. AIAA-98-0064.

91. Sutherland, H., "Inflow and the Fatigue of the LIST Wind Turbine," Wind Energy 2002, Report No. AIAA-2002-0065.

92. Sutherland, H., Kelley, N., "Inflow and Fatigue Response of the NWTC Advanced Research Turbine," Wind Energy 2003, Report No. AIAA-2003-0862.

93. Thomsen, K., "The Statstical Variation of Wind Turbine Fatigue Loads," RISO-R-1063 (EN), Roskilde, Denmark: RISO National Laboratory, 1998.

94. Wahl, N., Samborsky, D., Mandell, J., Cairns, D., "Spectrum Fatigue Lifetime and Residual Strength for Fiberglass Laminates", AIAA-2001-0025.

95. Sutherland, H., "Fatigue Case Study and Loading Spectra for Wind Turbines", IEA Fatigue Experts Meetings, April 1994.

96. Manuel, L., Veers, P., Winterstein, S., "Parametric Models for Estimating Wind Turbine Fatigue Loads for Design", AIAA-2001-0047.

97. Sutherland, H., Veers, P., "Effects of Cyclic Stress Distribution Models on Fatigue Life Predictions", Wind Energy 1995, SED-Vol. 16.

98. Sutherland, H., Veers, P., "Fatigue Case Study and Reliability Analysis for Wind Turbines", ASME/JSME/JSES Int. Solar Energy Conference, 1995.

99. Veers, P., Sutherland, H., Ashwill, T., "Fatigue Life Variability and Reliability Analysis of a Wind Turbine Blade", Sandia National Laboratories, DOE Contract DE-AC04-76DP00789.

181

100. Sutherland, J., Carlin, P., "Damage Measurements on the NWTC Direct-Drive Variable Speed Test Bed", ASME/AIAA Wind Energy 1998, AIAA-98-0064.

101. Veers, P., Winterstein, S., "Application of Measured Loads to Wind Turbine Fatigue and reliability Analysis", ASME Wind Energy Symposium, January 6-9, 1997.

102. Sutherland, H., Osgood, R., "Frequency-Domain Synthesis of the Fatigue Load Spectrum for the NPS 100-kW Wind Turbine", WindPower '92, AWEA, Washington DC, 1992.

103. Sutherland, H., "Damage Estimates for European and U.S. Sites using the U.S. High-Cycle Fatigue Date Base", IEA R&D Wind Annex XI, February 1-2, 1996.

104. Sutherland, H., "Preliminary Analysis of the Structural and Inflow Data from the LIST Turbine", ASME/AIAA Wind Energy 2001, AIAA-2001-0041.

105. Curtis, P., Davies, A., "Fatigue Life Prediction of Polymer Composite Materials", Mechanical Sciences Sector, DERA, Farnborough, UK, June 200.

106. Web site of Sandia National Laboratories - http://www.sandia.gov/Renewable_Energy/wind_energy/NuMAD.htm, Updated April 8, 2003; Accessed June 2003.

107. Mayer, R., *Design of Composite Structures Against Fatigue: Applications to Wind Turbine Blades*, Mechanical Engineering Publications Limited, Suffolk, UK.

108. Degrieck, J., Van Paepegem, W., "Fatigue Damage Modeling of Fibre-Reinforced Composte Materials: Review", ASME Appl. Mech. Rev Vol. 54, NO. 4., July 2001.

109. Wahl, N., Samborsky, D., Mandell, J., Cairns, D., "Effects of Modeling Assumptions on the Accuracy of Spectrum Fatigue Lifetime Predictions for a Fiberglass Laminate", AIAA-2002-0023.

110. Sarkani, S., Michaelov, G., "Nonlinear Damage Accumulation in Stochastic Fatigue of FRP Laminates", 8th ASCE Specialty Conference on Probabilistic Mechanics and Structural Reliability, PMC2000-302.

111. Mandell, J., Samborsky, D., Scott, M., Cairns, D., "Effects of Structural Details on Delamination and Fatigue Life of Fiberglass Laminates", AIAA-1998-0061.

112. ASCE Committee on Fatigue and Facture Reliability, "Fatigue Reliability: Variable Amplitude Loading," Journal of the Structural Division, ASCE Vol. 108, January 1982.

113. Stoddard, F., Zuteck, M., "Composite Wind Turbine Blade Fatigue: Symptoms, Causes, Cures," 7th ASME Wind Energy Symposium, New Orleans, 1988.

114. Paris, P., "The Crack Growth of Fatigue Cracks Due to Variation in Load", PhD. Thesis, Lehigh University, Bethlehen (1962).

115. Radon, J., Wachnicki, C., "Biaxial Fatigue of Glass Fiber Reinforced Polyester Resin," *Multi-axial Fatigue*, ASTM STP 853, Philadelphia, 1985.

116. Boniface, L., Ogin, S., "Application of the Paris Equation to the Fatigue Growth of Transverse Ply Cracks," *Journal of Composite Materials*, 1989, 23(7).

117. Marco, S., Starkey, W., "A Concept of Fatigue Damage," *Transactions of the ASME*, 76(1), 1954.

118. Gamstedt, E., Andersen, S., "Fatigue Degradation and Failure of Rotating Composite Structures – Material Characteristics and Underlying Mechanisms," Materials Research Department Report Number RISO-R-1261 (EN), RISO National Laboratory, March 2001.

119. Paepegem, W., Degrieck, J., "Effects of Load Sequence and Block Loading on the Fatigue Response of Fibre-Reinforced Composites," *Mechanics of Advanced Materials and Structures*, 9(1).

120. Sarkani, S., Michaelov, G., (2000) "Nonlinear Damage Accumulation in Stochastic Fatigue of FRP Laminates," ASCE PMC2000-302, 1994.

121. Griffin, D. A, *WindPACT Turbine Design Scaling Studies Technical Area 1 -- Composite Blades for 80- to 120-Meter Rotor*; 21 March 2000 - 15 March 2001. 44 pp.; NREL Report No. SR-500-29492.

122. Kelley, N. D.; Wright, A. D.; Buhl, M. L.; Tangler, J. L, *Long-Term Simulation of Turbulence-Induced Loads Using the SNLWIND-3D, FAST, YawDyn, and ADAMS(TM) Numerical Codes*. Collection of the 1997 ASME Wind Energy Symposium Technical Papers Presented at the 35th AIAA Aerospace Sciences Meeting and Exhibit, 6-9 January 1997, Reno, Nevada. Washington, DC: American Institute of Aeronautics and Astronautics; pp. 74-85; NREL Report No. 23277.

123. Hand, M. M.; Simms, D. A.; Fingersh, L. J.; Jager, D. W.; Cotrell, J. R.; Schreck, S.; Larwood, S. M., *Unsteady Aerodynamics Experiment Phase VI: Wind Tunnel Test Configurations and Available Data Campaigns*. 310 pp.; NREL Report No. TP-500-29955.

124. Kelley, N. D.; Sutherland, H. J., *Damage Estimates from Long-Term Structural Analysis of a Wind Turbine in a U.S. Wind Farm Environment*. Collection of the 1997 ASME Wind Energy Symposium Technical Papers Presented at the 35th

AIAA Aerospace Sciences Meeting and Exhibit, 6-9 January 1997, Reno, Nevada. Washington, DC: American Institute of Aeronautics and Astronautics; pp. 170-179; NREL Report No. 23282.

125. Hughes, S., Musial, W., (2002) "Wind Turbine Blade Fatigue Test Plan for Enron 37B Rotor Blade," NWTC Document: NWTC-ST-EW-FAT-04-TP.

126. Buhl Jr., M.L. "A Simple Mode-Shape Generator for Both Towers and Rotating Blades." *NWTC Design Codes (Modes)*, http://wind.nrel.gov/designcodes/modes/. Last modified November 21, 2002; accessed December 31, 2002.

127. Larsen, G., Kretz, A., "Experimental Determination of Stiffness Distributions and Mode Shapes of Wind Turbine Blades," RISO Report R773 (EN), March 1995.

128. Larsen, G., Kretz, A., "Experimental Determination of Structural Properties by Non-Destructive Methods," RISO Report 1995.

129. Singiresu, R., *Mechanical Vibrations*, Purdue University, Addison-Wesley Publishing Company, Reading, MA, 1990.

130. British Laboratory for Advanced Dynamic Engineering website - http://mail.bris.ac.uk/~aemtak/damp/damping.html#hyst, Updated 2001, Accessed June 2003.

131. Website of the University of Iowa - http://twist.lib.uiowa.edu/vibrations/Lect1-24.pdf, last updated February 11, 2002; last accessed January 13, 2003.

132. Murri, G, Schaff, J., Dobyns, S., "Fatigue and Damage Tolerance Analysis of a Hybrid Composite Tapered Flexbeam", American Helicopter Society Forum, Washington DC, May 9-11, 2001.

133. Trefethen, L., Bau, D., *Numerical Linear Algebra*, Society for Industrial and Applied Mathematics, Philadelphia, 1997.

134. Thomson, W., *Theory of Vibration with Applications*, University of California – Santa Barbara, Prentice Hall Publishing Company, Englewood Cliffs, NJ, 1993.

135. Hjorteland, T., "The Action Variational Principle in Cosmology", pp. 40-47, University of Oslo – Institute of Theoretical Astrophysics, http://trond.gothamnights.com//Thesis/node26.html, last modified July 5, 1999.

136. Nayfeh, A., *Introduction to Perturbation Methods*, John Wiley, New York, 1973.

137. Degrieck, J., Van Paepegem, W., "Fatigue Damage Modeling of Fibre-Reinforced Composte Materials: Review", ASME Appl. Mech. Rev Vol. 54, NO. 4., July 2001. (Duplicate of 107).

138. Wolovich, W., *Automatic Control Systems*, Brown University, Saunders College Publishing, Fort Worth, TX, 1994.

REPORT DOCUMENTATION PAGE

*Form Approved
OMB NO. 0704-0188*

1. AGENCY USE ONLY (Leave blank)	2. REPORT DATE April 2004	3. REPORT TYPE AND DATES COVERED Technical Report

4. TITLE AND SUBTITLE
New Method for Dual-Axis Fatigue Testing of Large Wind Turbine Blades Using Resonance Excitation and Spectral Loading

5. FUNDING NUMBERS
WER4.3707

6. AUTHOR(S)
Darris White

7. PERFORMING ORGANIZATION NAME(S) AND ADDRESS(ES)
National Renewable Energy Laboratory
1617 Cole Blvd.
Golden, CO 80401-3393

8. PERFORMING ORGANIZATION REPORT NUMBER
NREL/TP-500-35268

9. SPONSORING/MONITORING AGENCY NAME(S) AND ADDRESS(ES)

10. SPONSORING/MONITORING AGENCY REPORT NUMBER

11. SUPPLEMENTARY NOTES

12a. DISTRIBUTION/AVAILABILITY STATEMENT
National Technical Information Service
U.S. Department of Commerce
5285 Port Royal Road
Springfield, VA 22161

12b. DISTRIBUTION CODE

13. ABSTRACT *(Maximum 200 words)*
The blades of a wind turbine are generally considered to be the most critical component of the wind turbine system. The fundamental purpose of performing fatigue tests on wind turbine blades is to demonstrate that a blade, when manufactured to a certain set of specifications, has the prescribed reliability and service life. The purpose of the research conducted for this project is the advancement of knowledge and capabilities in the area of wind turbine blade fatigue testing.

14. SUBJECT TERMS
wind turbine; blades; fatigue testing; wind energy

15. NUMBER OF PAGES

16. PRICE CODE

17. SECURITY CLASSIFICATION OF REPORT Unclassified	18. SECURITY CLASSIFICATION OF THIS PAGE Unclassified	19. SECURITY CLASSIFICATION OF ABSTRACT Unclassified	20. LIMITATION OF ABSTRACT UL